

# **Identification and Characterization of Small Molecules Inducing Cellular Reactive Oxygen Species Accumulation**

## **Dissertation**

zur Erlangung eines akademischen Grades  
des Doktors der Naturwissenschaften  
(Dr. rer. nat.)

der Fakultät der Chemie und Chemischen Biologie  
der Technischen Universität Dortmund

vorgelegt von

**Julian Wilke, M.Sc.**

geboren am 02.03.1990 in Bonn

Dortmund, den 11.11.2020



Die vorliegende Dissertation wurde im Zeitraum vom Februar 2016 bis Oktober 2020 unter der Anleitung von Prof. Dr. Dr. h.c. Herbert Waldmann und Dr. Slava Ziegler an der Fakultät für Chemie und Chemische Biologie der Technischen Universität Dortmund und dem Max-Planck-Institut für Molekulare Physiologie Dortmund verfasst.

1. Gutachter: Prof. Dr. Dr. h.c. Herbert Waldmann

2. Gutachter: Prof. Dr. Markus Kaiser



*Für Philipp.*



Results presented in this thesis contributed to the following publications:

J. Wilke, T. Kawamura, N. Watanabe, H. Osada, S. Ziegler, H. Waldmann: *‘Identification of cytotoxic, glutathione-reactive moieties inducing accumulation of reactive oxygen species via glutathione depletion’* *Bioorg Med Chem.*, 2018, **26**, 1453-1461

J. Wilke, T. Kawamura, H. Xu, A. Brause, A. Friese, M. Metz, D. Schepmann, B. Wunsch, A. Artacho-Cordón, F.R. Nieto, N. Watanabe, H. Osada, S. Ziegler, H. Waldmann: *‘Discovery of a novel  $\sigma_1$  receptor antagonist by combination of unbiased Cell Painting and thermal proteome profiling.’* *Cell Chem Biol.*, 2020, in revision





## Acknowledgements

At first, I would like to express my gratitude to Prof. Herbert Waldmann for the great opportunity to conduct my doctoral studies in his department, for his guidance throughout this exciting project and for providing an excellent research environment, which helped me to become the scientist I am today. In addition, I am deeply thankful to Dr. Slava Ziegler for the supervision of my project and proof-reading of this dissertation. Throughout this journey, she not only contributed helpful advice and ideas, but also motivating words in times of setbacks.

I am grateful to the *IMPRS for Living Matter* (formerly *IMPRS in Chemical and Molecular Biology*) for providing various opportunities to develop new skills useful both in- and outside of the laboratory. I would like to thank Dr. Lucia Sironi and Christa Hornemann for their support, as well as the members of my thesis advisory committee Prof. Konstanze Winklhofer and Prof. Markus Kaiser for their scientific input. Furthermore, I would like to thank Prof. Kaiser for being my second examiner.

As this project was conducted in collaboration with the *RIKEN Center for Sustainable Resource Science*, I would like to express my gratitude to Prof. Hiroyuki Osada and Dr. Nobumoto Watanabe not only for sharing their scientific expertise, but also for the great opportunity to join their lab in Japan. I am sincerely grateful to Dr. Tatsuro Kawamura, who guided me throughout this project and helped me to get familiar with my new role as a Chemical Biologist, especially during the first year as a PhD student. I enjoyed working with him both in Dortmund and Wako-shi. Furthermore, I would like to thank Dr. Makoto Muroi and Dr. Yushi Futamura for their scientific support, and my former colleagues at RIKEN for providing a warm welcome and a pleasant working atmosphere. ありがとうございました。

The *Compound Management and Screening Center Dortmund* provided the basis for this project by conducting a phenotypic screen and various follow-up experiments. I would like to thank Dr. Sonja Sievers, Dr. Gernot Hahne, Dr. Axel Pahl and Dr. Claude Ostermann for their support. Furthermore, I would like to thank Dr. Petra Janning for all mass spectrometry measurements and for the many scientific discussions, which helped me to elucidate different molecular targets. I am grateful to Jens Warmers, Malte Metz and Andreas Brockmeyer for conducting the respective measurements and to Dr. Elena Rudashevskaya for performing the phosphoproteome analysis. I would like to thank

Dr. Hao Xu, Dr. Houhua Li and Dr. Matthias Bischoff for great collaboration and for the synthesis of various research compounds. In addition, I am grateful to Dr. Alexandra Friese for the expression of  $\sigma$  receptor proteins and Alexandra Brause for conducting various biological experiments. Furthermore, I had the chance to supervise two highly motivated and dedicated bachelor students, Naomi Hönisch-Gravel and Daya Agne. Both are acknowledged for supporting me on this research project by providing valuable insights for the diaminopyrimidine project.

Additionally, I would like to thank our external collaboration partners for sharing scientific expertise in their respective fields: Prof. Bernhard Wünsch and Dr. Dirk Schepmann, *University of Münster*, for performing  $\sigma$  receptor binding studies, and Prof. Francisco R. Nieto and Antonia Artacho-Cordón, *University of Granada*, for conducting the mechanical allodynia assays. Prof. Dan Yang and Mingyang Lu, *University of Hong Kong*, are acknowledged for measuring reactive oxygen species using their sophisticated set of probes, and Dr. Matthias Baumann and coworkers, *Lead Discovery Center Dortmund*, for performing a redox cycling assay.

An integral part of the excellent research environment I worked in at the *Max Planck Institute* were of course my colleagues, who provided support, advice and sometime a little distraction when needed. I am especially thankful to Elisabeth Hennes, Beate Schölermann, Dr. Elena Reckzeh and Dr. Lea Kremer for their company, scientific input and moral support. Furthermore, I would like to thank the people I shared lab and office with: Tabea Schneidewind, Dr. Hélène Adihou, Dr. Sumersing Patil, Dr. Tim Förster, Dr. Nadine Kaiser, Dr. Guillaume Garivet, Dr. Peter t'Hart, Dr. Javier Ceballos, Aylin Binici, Dr. Mahyar Akbarzadeh, Adrian Krzyzanowski, Dr. Gregor Cremosnik, Dr. Michael Grigalunas and Dr. David Grill. I am grateful to all current and former members of Department 4 I got to know in the past years, for contributing to this great working atmosphere. I would also like to thank Brigitte Rose for her support with all administrative matters.

At last, I would like to express my gratitude to the people important in my non-scientific life: my partner, my family and my friends, who helped me to stay on track on this long and sometimes bumpy journey towards obtaining a PhD. Thank you.





## Table of contents

<b>1</b>	<b>Abstract / Zusammenfassung</b> .....	<b>1</b>
<b>2</b>	<b>Introduction</b> .....	<b>5</b>
2.1	Discovery of bioactive small molecules .....	5
2.1.1	Identification of bioactive small molecules .....	6
2.1.2	Target identification .....	7
2.1.3	Target validation .....	14
2.2	Reactive oxygen species .....	16
2.2.1	Cellular sources of ROS and antioxidant mechanisms .....	17
2.2.2	ROS as signaling molecules .....	19
2.2.3	Oxidative stress response .....	20
2.2.4	Role of reactive oxygen species in cancer .....	22
2.2.5	ROS induction as cancer therapy.....	26
<b>3</b>	<b>Aim of this thesis</b> .....	<b>31</b>
<b>4</b>	<b>Materials and methods</b> .....	<b>32</b>
4.1	Materials .....	32
4.1.1	Chemicals and reagents.....	32
4.1.2	Buffers .....	35
4.1.3	Cell culture media.....	38
4.1.4	Kits.....	39
4.1.5	Antibodies.....	39
4.1.6	Plasmids .....	40
4.1.7	Cell lines .....	40
4.1.8	Bacterial strains and insect cell lines .....	40
4.1.9	Devices.....	41
4.1.10	Software .....	42
4.1.11	Consumables.....	42
4.2	Methods .....	44
4.2.1	Cell culture methods.....	44
4.2.2	Phenotypic screening methods .....	51
4.2.3	Target identification methods .....	53
4.2.4	Target validation methods .....	63
4.2.5	Other methods.....	69
<b>5</b>	<b>Results</b> .....	<b>73</b>
5.1	Phenotypic screening for small molecule inducers of ROS accumulation .....	73
5.2	Identification of cytotoxic, GSH-reactive inducers of ROS accumulation .....	77
5.3	Diaminopyrimidines as novel inducers of cellular ROS accumulation .....	85

5.3.1	Structure-activity relationship study.....	85
5.3.2	Biological characterization.....	95
5.3.3	Target identification via photo-crosslinking beads .....	104
5.3.4	Target identification via thermal proteome profiling and Cell Painting assay .....	106
5.3.5	Target identification via affinity-based chemical proteomics .....	119
5.3.6	Target identification via <i>in situ</i> pulldown.....	133
5.3.7	Target identification via proteome profiling .....	136
5.3.8	Target identification via phosphoproteome profiling.....	138
5.3.9	Influence on cell viability.....	141
<b>6</b>	<b>Discussion .....</b>	<b>147</b>
6.1	DHMP and TCMP compounds as novel GSH-depleting ROS inducers.....	147
6.2	Chemical optimization of diaminopyrimidine-based ROS inducers.....	150
6.3	DP68 interferes with superoxide dismutation .....	152
6.4	ROS-inducing potency of DP68.....	154
6.5	DP68 as antagonist of the $\sigma_1$ receptor.....	156
6.6	Target identification using affinity-based chemical proteomics .....	158
6.7	Target identification via photoaffinity probes .....	164
6.8	Biological profiling of DP68 for target identification .....	165
6.9	Perspectives on the target identification of diaminopyrimidine-based ROS inducers .....	167
6.10	Cancer-selective cytotoxic effects of ROS-inducing compounds .....	169
<b>7</b>	<b>Conclusion and perspectives .....</b>	<b>174</b>
<b>8</b>	<b>References .....</b>	<b>177</b>
<b>9</b>	<b>Appendix .....</b>	<b>191</b>
9.1	Supplementary data.....	191
9.2	Abbreviations .....	224
9.3	Curriculum vitae .....	228
9.4	Publication list.....	229
9.5	Eidesstattliche Versicherung (Affidativ) .....	231

# 1 Abstract / Zusammenfassung

## Abstract:

The human cell is constantly confronted with reactive oxygen species (ROS), which are oxygen-containing chemical intermediates readily reacting with different biomolecules. ROS can originate from exogenous sources, but are also produced within cells, e.g. as part of their metabolism. Depending on the concentration, ROS can either act as important signaling molecules or induce oxidative stress, thereby harming cellular components. Thus, cells utilize a multitude of antioxidant mechanisms to maintain redox homeostasis. As ROS play an important role in the development and propagation of cancer, modulation of cellular ROS levels, e.g. via small molecules, may have the potential to induce cancer-selective cytotoxicity.

In the course of this thesis, novel fast-acting small-molecule inducers of cellular ROS accumulation were identified by means of phenotypic screening. A counter-screen for glutathione-reactive compounds led to the discovery of 4,5-dihalo-2-methylpyridazin-3-ones and 2,3,4,5(6)-tetrachloro-6(5)-methylpyridines as potent depleters of cellular glutathione. Furthermore, an in-depth characterization of a 2,4-diaminopyrimidine-based compound class was conducted to identify the molecular target and elucidate the mode of action. Structure-activity relationship studies improved both potency and water solubility of the original hit compound and eliminated bioactivities unrelated to its ROS-inducing properties. The optimized compound DP68 was found to strongly elevate cellular superoxide levels without affecting hydrogen peroxide concentrations, indicating an interference with superoxide dismutation. However, an inhibition of the enzymatic activity of superoxide dismutases by DP68 was not observed. Target identification studies of DP68 were conducted, using affinity-based chemical proteomics and different profiling techniques to investigate the compound's influence on cellular morphology, thermal stability of proteins and the (phospho)proteome. Thereby, DP68 was identified as novel antagonist of the  $\sigma_1$  receptor, which however does not mediate ROS induction. Furthermore, DP68 was found to interact with HEAT repeat-containing proteins, including phosphatidylinositol 3-kinase-related kinases. In addition, DP68 induced a phosphorylation of superoxide dismutase 1, which may influence its cellular localization. DP68 induced cytotoxicity in cancer cell lines and non-malignant primary cells, which may depend on its superoxide-inducing properties.

**Zusammenfassung:**

Die menschliche Zelle gerät dauerhaft mit reaktiven Sauerstoffspezies (ROS) in Kontakt. Dabei handelt es sich um sauerstoffhaltige chemische Intermediate, die spontan mit verschiedensten Biomolekülen reagieren können. ROS können sowohl aus exogenen Quellen stammen, aber auch in Zellen selbst, z.B. als Nebenprodukt ihres Metabolismus, entstehen. Abhängig von ihrer Konzentration können ROS sowohl als Signalmoleküle fungieren, oder oxidativen Stress auslösen und zelluläre Komponenten schädigen. Aus diesem Grund verfügen Zellen zur Erhaltung ihrer Redoxhomöostase über eine Vielzahl antioxidativer Mechanismen. Da ROS auch bei der Entstehung und Ausbreitung von Tumoren wichtige Rollen spielen, könnte ihre Modulation, zum Beispiel durch niedermolekulare Substanzen, das Potential zur Induktion krebsselektiver Zytotoxizität innehaben.

Im Rahmen dieser Doktorarbeit wurden mithilfe eines phänotypischen Screens neuartige schnellwirksame niedermolekulare Substanzen identifiziert, die die zelluläre ROS-Konzentration erhöhen. Ein weiterer Screen zur Detektion glutathionreaktiver Substanzen führte zur Identifizierung von 4,5-Dihalogen-2-methylpyridazin-3-onen und 2,3,4,5(6)-Tetrachlor-6(5)-methylpyridinen, die eine zelluläre Glutathiondepletion induzieren. Des Weiteren wurden ausführliche Studien einer 2,4-Diaminpyrimidin-basierten Substanzklasse durchgeführt, um das Zielmolekül zu identifizieren und den Wirkmechanismus aufzuklären. Die Untersuchung der Struktur-Aktivitätsbeziehung führte zur Verbesserung der Potenz sowie der Wasserlöslichkeit und zur Eliminierung von Bioaktivitäten, die nicht mit der ROS-induzierenden Eigenschaft in Verbindung stehen. Untersuchungen der optimierten Substanz DP68, zeigte eine starke Erhöhung zellulärer Superoxidlevel ohne Änderung der Wasserstoffperoxidkonzentration, welches darauf hinweist, dass die Substanz mit der Superoxiddismutation interferieren könnte. Eine Inhibition der enzymatischen Aktivität von Superoxiddismutasen durch DP68 wurde jedoch nicht festgestellt. Zur Identifizierung der molekularen Zielstruktur von DP68 wurden Studien mittels affinitätsbasierter chemischer Proteomik und verschiedener Profilingtechniken, die den Einfluss der Substanz auf die zelluläre Morphologie, die thermische Stabilität von Proteinen und das (Phospho)proteom untersuchen, durchgeführt. Dabei wurde DP68 als neuartiger Antagonist des  $\sigma_1$ -Rezeptors identifiziert, jedoch steht diese Interaktion nicht mit der ROS-Induktion in Verbindung. Desweiteren interagiert DP68 mit verschiedenen Proteinen, die „HEAT repeat“-Struktur motive enthalten, z.B. mit Kinasen der „Phosphatidylinositol 3-kinase-related kinase“-Familie. Zusätzlich wurde die eine Phosphorylierung der Superoxiddismutase 1 nach



Behandlung mit DP68 festgestellt, welches einen Einfluss auf dessen zelluläre Lokalisation haben könnte. DP68 induzierte Zytotoxizität sowohl in Krebszelllinien, als auch in nicht-malignen Primärzellen, welche auf seiner superoxidinduzierenden Eigenschaft beruhen könnte.



## 2 Introduction

The interdisciplinary field of Chemical Biology aims to probe biological systems by means of synthetic chemistry to manipulate and thereby investigate complex biological processes. A key objective in Chemical Biology research is the discovery of novel bioactive agents, especially small molecules.<sup>1</sup> Bioactive small molecules are an integral part of biomedical research, are used as tool compounds to dissect cellular processes, and are of course indispensable for drug discovery and disease therapy.

This doctoral thesis focusses on the role of redox regulation in cancer by identifying and characterizing small molecule inducers of cellular accumulation of reactive oxygen species (ROS). This chapter covers the principles of bioactive small-molecule discovery and provides an overview on redox biology with special emphasis on cancer.

### 2.1 Discovery of bioactive small molecules

Bioactive small molecules are defined as organic compounds, with molecular weight usually below 1 kDa, which can be both of natural or synthetic origin and have the ability to perturb a biological system, for example a living cell.<sup>2</sup> By interacting with biomolecules, such as proteins, nucleic acids, lipids or carbohydrates, small molecules can induce phenotypic changes in cells.<sup>3</sup> In contrast to a genetic perturbation, small molecule-mediated effects are in most cases fast and transient, i.e. after treatment termination, cells are often capable of restoring the original state, allowing to precisely control the perturbation time. Unlike a knock-out of a protein-encoding gene, which leads to a complete removal of a protein, small molecules do not necessarily interfere with all of a protein's functions. A small molecule might exclusively inhibit enzymatic activity or block a certain protein-protein interaction, thus allowing to dissect the various functions of a protein. Furthermore, the degree of such interference can often be controlled via compound concentration.<sup>4</sup>

The interaction of a small molecule with its target is however not as specific compared to e.g. the interaction between an antibody and its antigen. In a cell, every small molecule binds to various biomolecules, however with different affinity. The target whose modulation facilitates the bioactivity of a small molecule is termed 'on-target'. Biomolecules whose modulation is not related to the compound's biological activity is called 'off-target', accordingly.<sup>5</sup> Effects mediated by 'off-targets' can strongly influence the outcome of a biological experiment. Therefore, in-depth characterization and detailed target annotation are essential for the application of small molecules as research tool compounds.<sup>6</sup>

Awareness of 'off-targets' is even more important for the drug discovery process, as such interactions of small-molecule drugs may translate into severe side-effects.<sup>7</sup>

### 2.1.1 Identification of bioactive small molecules

A commonly applied method to identify bioactive small molecules is the screening of compound collections, often performed in a medium- or high-throughput manner. Two main strategies are to be distinguished: target-based and phenotypic screenings (Figure 1). Target-based (mainly biochemical or biophysical) screening aims to identify small molecules that modulate a (protein) target of interest. In phenotypic screening, a strategy applied in the course of this thesis, biologically more complex models such as cells, tissues or whole organisms are used to identify small molecules that induce or inhibit a certain phenotype of interest. The latter approach allows to identify not only novel bioactive molecules, but may also elucidate new links between cellular targets and the phenotype of interest. However, the biggest challenge in such approach arises after the actual screening, since a hit compound's target needs to be identified and validated, a laborious and time-consuming undertaking.<sup>8</sup>

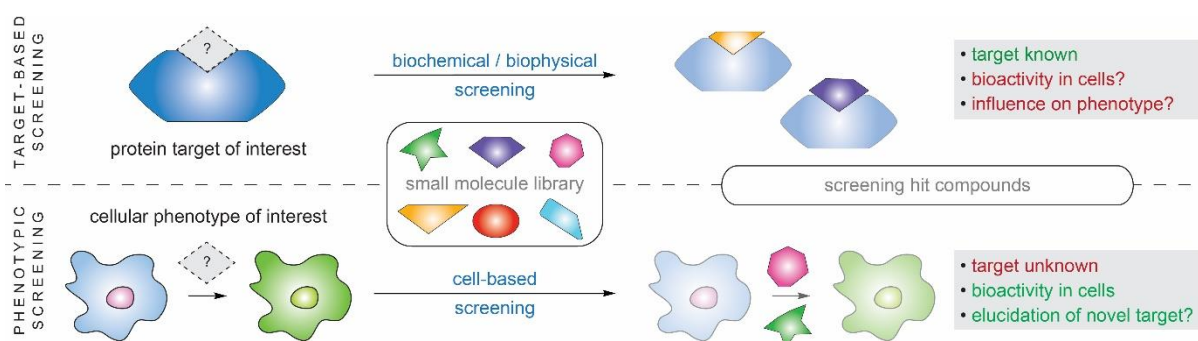


**Figure 1: Comparison of target-based vs. phenotypic screening.** Target-based screening is often based on a biochemical or biophysical assay to identify small molecule modulators of a protein of interest. This approach can detect potent interaction partners, which however may not be active in cells. Additionally, modulation of the chosen target may not always translate into a desired phenotype. In contrast, phenotypic screening utilizes cells or more complex models to identify small molecule modulators. Thus, these compounds are active in the respective model, but lack information on their molecular target. Subsequent target deconvolution may facilitate the discovery of novel targets relevant to the phenotype of choice.

In contrast, hits obtained in a target-based approach, are by default linked to a target already. However, this does not guarantee that such compounds also induce the desired effect in a cell or a whole organism. For instance, hit compounds may lack membrane permeability or sufficient solubility,

properties that need to be addressed by subsequent chemical optimization. In addition, the modulation of the chosen target may not always translate into the originally intended phenotypic change.<sup>9</sup>

Taken together, target-based screening approaches are a reliable source of novel small molecules tailored to a specific target, while phenotypic screening can deliver innovation regarding targets and modes of action. This is reflected in current drug discovery as reported in a study from 2011, which investigated the origin of all new molecular entities approved by the FDA between 1999 and 2008. The authors found the majority of all first-in-class drugs to be identified by means of phenotypic screening, while most follower drugs originated from target-based screening approaches.<sup>9</sup> However, a careful design of phenotypic screening campaigns is mandatory to ensure that identified hits successfully translate into candidate drugs. Fabien Vincent and colleagues therefore postulated the 'phenotypic screening rule of 3' defining optimal screening conditions for drug discovery:<sup>10</sup> The first criterion calls for a disease-relevant system, e.g. to favor the use of primary or induced pluripotent stem cells over cancer cell lines, or to consider three-dimensional models, like spheroids or organoids, instead of monolayer cultures. Secondly, a disease-relevant stimulus for phenotype induction need to be chosen, e.g. by using patient-derived cells that harbor genetic alterations causing the pathological condition. Finally, a suitable read-out closely related to the situation in patients should be chosen, ideally far downstream from the stimulus to cover a broad range of mode of actions.<sup>10</sup> Independent of the screening design, hit compounds originating from phenotypic screens need to undergo an in-depth characterization to identify their target in order to understand their underlying mode of action.

### **2.1.2 Target identification**

In the past, a plethora of target identification methods has been developed. The success of each approach depends on the target to be identified, which explains the absence of a universal target identification workflow.<sup>3</sup> In general, one can distinguish direct and indirect target identification approaches. Direct approaches aim to discover interaction partners of a small molecule, while indirect approaches, allow deriving a target hypothesis on the basis of certain compound characteristics, e.g. its chemical structure or influence on cellular transcriptome, proteome or morphology.<sup>11</sup>

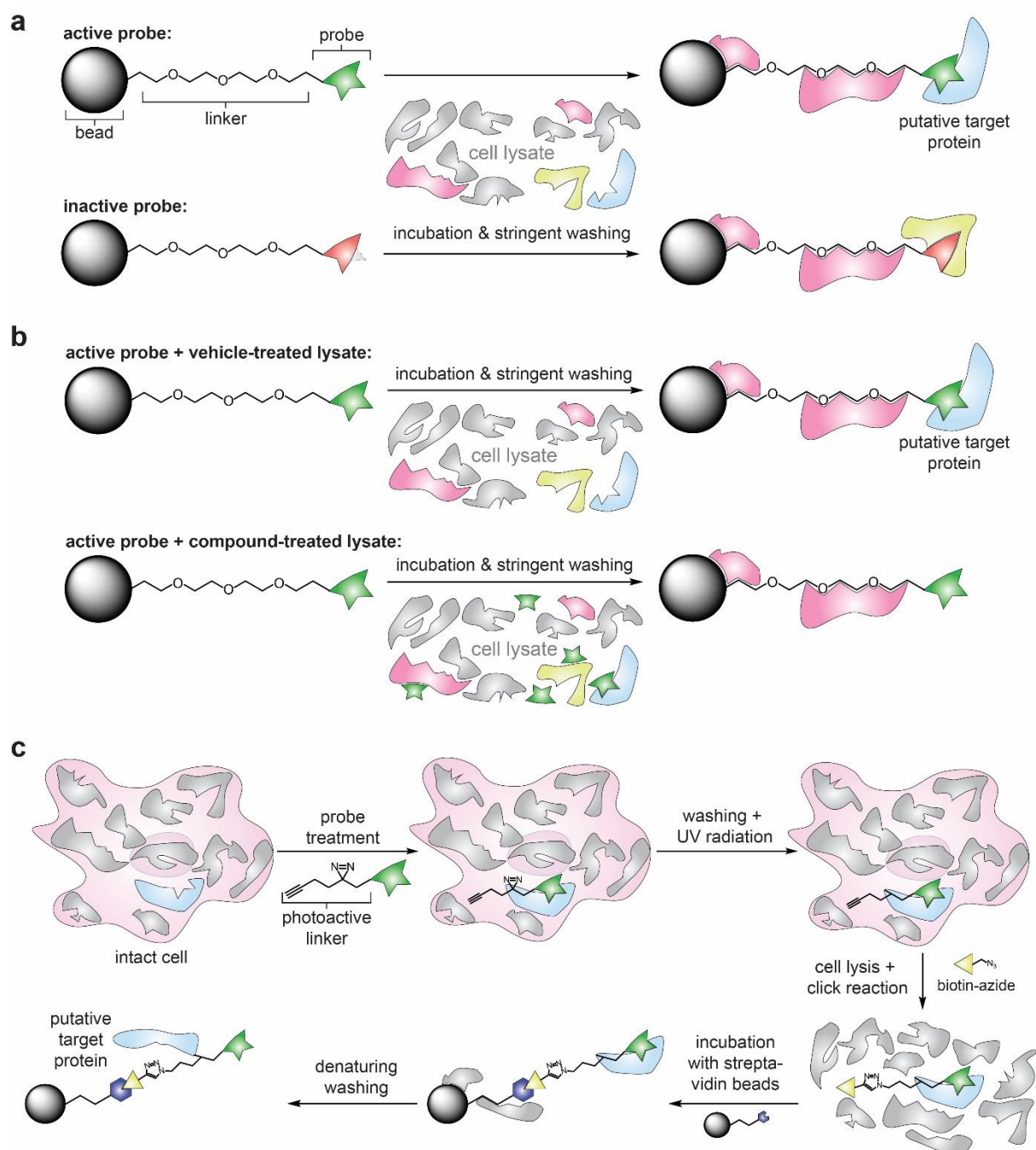


**Figure 2: Chemical proteomics approaches for target identification.** In affinity-based chemical proteomics (a and b) small molecules of interest are immobilized on a solid phase (bead), incubated with cell lysates, washed stringently followed by mass spectrometry to identify putative binding proteins. Two control strategies are available, i.e. to distinguish non-specific binders (pink) from actual interaction partners (blue): **(a)** the experiment is performed in parallel with an inactive derivative of the bioactive compound or **(b)** cell lysates are incubated with either a vehicle or an excess of the small molecule of interest prior to the binding reaction ('competition pull-down') **(c)** Photoaffinity labeling (PAL)-based 'in situ pull-down': the small molecule is attached to a photoactive linker containing an alkyne handle. Cells are treated with the probe, washed and UV-radiated to cross-link the probe with proteins in close proximity. Cells are lysed and cross-linked proteins are reacted with a biotin-azide. Biotin-tagged proteins are enriched on streptavidin beads, followed by denaturing washing steps and proteomics analysis.

Affinity-based chemical proteomics (ABP), is a broadly applied method to identify binding proteins of small molecules in cell lysates. In this approach, a small molecule of interest is immobilized on a solid phase (bead) and is subsequently incubated with cell lysate to enrich putative target proteins. After stringent washing steps, bound proteins are subjected to tryptic digestion and subsequent proteomics analysis (Figure 2a and 2b). Two common strategies are used to distinguish between proteins that interact specifically with the probe and those that bind non-specifically.

For the first strategy an inactive derivative of the bioactive compound is applied in a parallel experiment. Only proteins that are significantly enriched by the bioactive compound compared to its inactive counterpart are considered to be putative targets (Figure 2a). Alternatively, in two parallel experiments, lysates are preincubated with either free bioactive compound or its respective solvent prior to the binding reaction. In such 'competition pulldown', the free compound competes with the immobilized small molecule for protein binding sites and thereby interferes with the enrichment of the target protein on the beads. Thus, proteins that are significantly enriched on beads of lysates treated with solvent are considered as putative target proteins (Figure 2b).

A prerequisite for ABP is the synthesis of an affinity probe suitable for solid phase immobilization. Most importantly, the immobilization must not impede the interaction between the small molecule and its target protein. To ensure that this is the case, the underlying structure-activity relationship (SAR) needs to be explored. This is achieved by testing the bioactivity of chemical derivatives, which slightly deviate from the original structure, to identify positions that are susceptible to chemical modification, like the attachment of a chemical spacer.

Depending on the small molecule, such SAR study may be inconclusive or synthetically challenging, for example in case of large natural products for which synthesis routes are lacking. Compound immobilization on beads coated with photoaffinity-linkers, may provide remedy in such cases.<sup>12</sup> These beads are decorated with trifluoromethyl phenyl diazirine moieties, which form radical species upon UV irradiation and readily react with compounds in close proximity. Thereby small molecules can be immobilized without prior SAR study and chemical modification. However, the random orientation does not guarantee that immobilized small molecules can still bind to their target protein.<sup>12,13</sup>

All of the above-mentioned methods are performed in cell lysates, which however does not reflect cellular conditions in its entirety, as native lysates often lack certain membrane proteins or protein complexes. Therefore, target identification in intact cells may be advantageous, but extracting a small

molecule bound to its target protein may pose a problem, if the interaction is too weak. Therefore, different photo-affinity labeling (PAL) approaches have been developed to overcome this limitation (Figure 2c). PAL probes consist of a bioactive molecule, equipped with a photo-reactive moiety, e.g. benzophenone, aryl azide or diazirine, and a chemical handle, for instance a terminal alkyne.<sup>14</sup> Cells treated with PAL probes are washed and subsequently UV-irradiated to crosslink the probe to proteins in close proximity. After cell lysis, biotin or another affinity-tag is attached to the alkyne handle via click-reaction.<sup>14</sup> This facilitates the enrichment of probe-labeled proteins, e.g. via incubation with streptavidin beads, followed by denaturing washing steps. Finally, bound proteins are identified via mass-spectrometry.<sup>15</sup>

Although inactive analogs used as controls in pulldowns may not exert bioactivity, they might still bind to the target of the corresponding bioactive compound. In such case a qualitative detection of proteins is insufficient to identify the target. Thus, the enrichment of the target protein by the bioactive compound and the inactive analog needs to be quantified, which can be achieved by different methods. 'Label-free quantification' (LFQ) determines the intensities of a peptide between different samples by integrating its full mass spectrometric signal.<sup>16</sup> A more sensitive quantification method is the 'stable isotope labeling with amino acids in cell culture' (SILAC). In SILAC, two cell populations are cultured in growth media, which differ in the isotopic composition of selected amino acids, thereby allowing to distinguish between two sample sets in mass spectrometry.<sup>17</sup> To do so, cells are grown in 'light medium', containing  $^{12}\text{C}_6,^{14}\text{N}_2$ -L-lysine and  $^{12}\text{C}_6,^{14}\text{N}_4$ -L-arginine or 'heavy medium' with e.g.  $^{13}\text{C}_6,^{15}\text{N}_2$ -L-lysine and  $^{13}\text{C}_6,^{15}\text{N}_4$ -L-arginine for at least five cell divisions to ensure nearly complete incorporation of these amino acids into all proteins. The respective cell lysates are used for ABP experiments (Figure 2a and 2b). After enrichment and stringent washing, 'light' lysate-incubated beads decorated with the biologically active probe are pooled with 'heavy' lysate-incubated beads equipped with the biologically inactive analog and vice-versa. Each peptide identified in such combined sample can be traced back to its affinity matrix via mass differences in arginine and lysine. This allows to directly compare ion intensities of SILAC peptide pairs, making quantification more precise compared to LFQ.<sup>3,18,19</sup>

With the exception of the photo-crosslinking bead-based pulldown, all above-mentioned target identification methods require chemical modification of the bioactive small molecule, which may not always be possible. Therefore, different label-free approaches have been developed, which are based on the observation that a small molecule can influence the stability of its protein binding partner, for



example by altering its conformation. Examples for such approaches are 'drug affinity responsive target stability' (DARTS) or 'stability of proteins from rates of oxidation' (SPROX), which however did not find broad application in the scientific community.<sup>20,21</sup> A label-free method widely applied to study protein-ligand interaction is the cellular thermal shift assay (CETSA). In CETSA, compound- or vehicle treated cell lysates are split in ten fractions and each fraction is subjected to a short heat treatment at a different temperature within a temperature gradient, followed by ultracentrifugation to separate denatured from soluble protein. The latter is then analyzed via immunoblotting to obtain melting curves for the respective protein in the presence or absence of the compound. Shifts in the melting temperature indicate a protein-ligand interaction, as binding of a small molecule may increase or decrease the thermal stability of the respective protein.<sup>22</sup> Savitski and co-workers combined the technique with tandem mass tag (TMT) labeling to detect interacting proteins of small molecules in a proteome-wide manner, an approach named 'thermal proteome profiling' (TPP), as depicted in Figure 3. In TPP, each sample of sample set treated either with DMSO or compound is labeled with a different tandem mass tag, which corresponds to its respective treatment temperature. Samples of each set are pooled, subjected to tryptic digestion, prefractionation and tandem mass spectrometry analysis for protein identification and quantification. TMT labeling allows to determine melting curves for each corresponding protein of interest.<sup>23,24</sup>

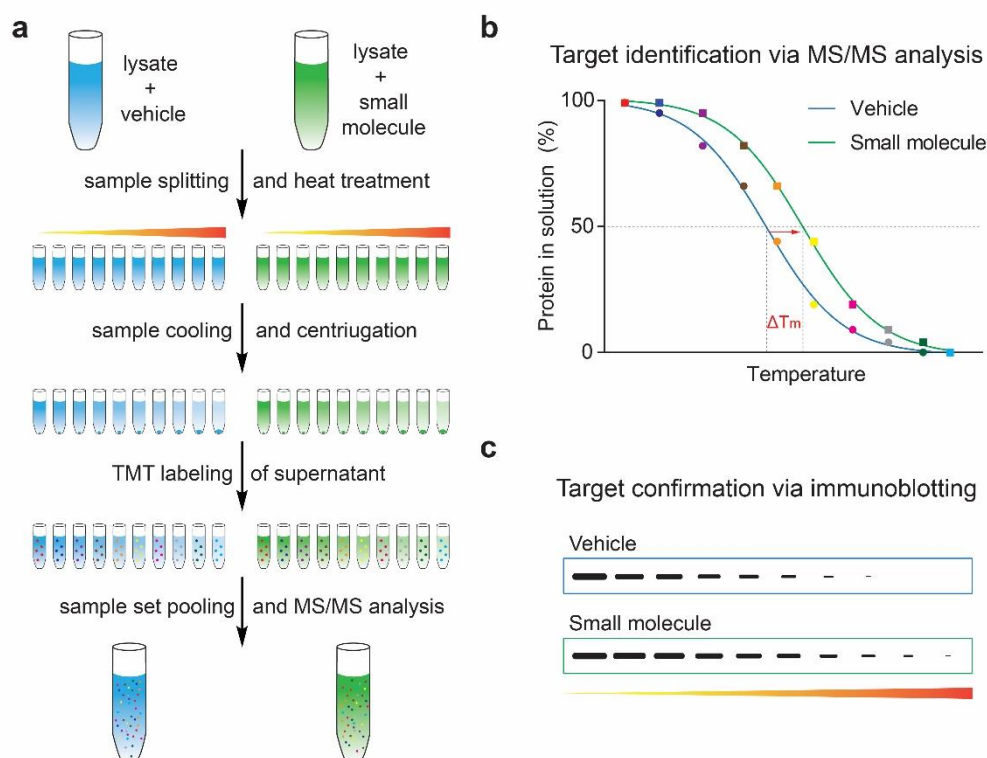


**Figure 3: Thermal Proteome Profiling (TPP) for target identification.** (a) General TPP workflow: cell lysates are treated with vehicle or compound and split into ten fractions, which are subjected to a short heat treatment with a temperature gradient for each sample. After cooling to 4 °C, aggregated proteins are separated by ultracentrifugation and the supernatant is subjected to tandem mass tag (TMT) labeling. Sample sets are pooled, subjected to tryptic digestion and analyzed via nano-HPLC-MS/MS. (b) Example quantification: the abundance of each protein in both samples is plotted against treatment temperature. For each protein identified, two melting curves (for vehicle or small molecule treatment) are determined. (c) Target candidates can be confirmed by subjecting supernatants derived after the ultracentrifugation step to immunoblotting. Adapted from Reckzeh et al.<sup>24</sup>

Indirect target identification methods aim to predict targets on the basis of certain compound characteristics. This includes *in silico* prediction methods, e.g. the ‘Similarity Ensemble Approach’ (SEA), which compares the chemical structure of a compound of interest with structures of annotated bioactive compounds.<sup>25</sup> Targets may also be predicted based on multi-parametric profiling. In these approaches, annotated compounds are applied to an assay system, yielding multiple read-outs, e.g. cell line sensitivity, transcription or protein expression, which can be summarized to a fingerprint.<sup>26–29</sup> Compounds with unknown targets are also subjected to such assay systems. Subsequent comparison of their profiles with profiles of annotated compounds may predict targets or mode of actions. Apart from their impact on transcriptome or proteome, bioactive small molecules may also change the outer appearance of cells, a property utilized by different phenotypic profiling methods. The high-content

profiling approach Morphobase identified novel tubulin inhibitors via nuclear staining and brightfield imaging.<sup>30</sup>

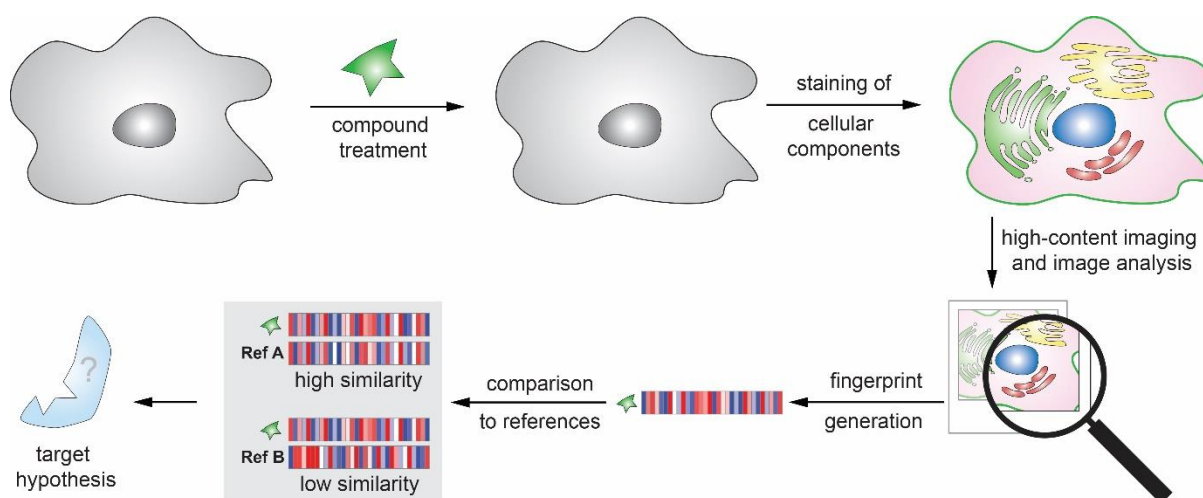


**Figure 4: Morphological profiling for target identification.** Cell Painting assay (CPA) workflow for target identification: Cells are treated with a compound for 20 h, followed by a multiplexed staining of different cellular compartments and high-content imaging. Image analysis quantifies hundreds of morphological features and compares these to the corresponding features of cells treated with solvent. Feature deviations are summarized in a compound fingerprint. Profile comparison with a reference set of characterized and target-annotated compounds allows to derive a target hypothesis.

Researchers at the Broad Institute developed a high-throughput phenotypic profiling approach called 'Cell Painting assay' (CPA), in which compound-induced morphological changes are visualized via multiplexed staining of different cellular components using six different dyes (Figure 4). Automated image analysis extracts hundreds of morphological parameters, such as size or staining intensity of a certain cellular compartment and compares these to parameters obtained from cells treated with solvent. Based on this data, morphological fingerprints were created for each compound.<sup>31</sup> The CPA was established at the Compound Management and Screening Center (COMAS), which led to the identification of bioactive small molecules and their respective targets in an unbiased manner.<sup>32–34</sup> Furthermore, by comparing fingerprints of bioactive small molecules to those of reference compounds molecular targets and modes of action can be predicted.<sup>35–37</sup>

Table 1 provides an overview on different target identification methods available. Whichever technique is used to identify a putative target of a bioactive small molecule, each target hypothesis needs to be thoroughly validated.

**Table 1: Overview on direct and indirect methods to identify small molecule targets.**

Technique	Principle	Type
Pulldown <sup>3,16</sup>	Enrichment of target proteins in cell lysates by solid phase-immobilized compounds. Comparison between resins with bioactive compound or inactive analog	Affinity-based chemical proteomics (direct approach)
Competition pulldown <sup>3</sup>	Pulldown; comparison between cell lysates treated with bioactive compound or vehicle	
Pulldown via photo-crosslinking beads <sup>12,13</sup>	Pulldown; compound immobilization on photo-activatable resin	
Pulldown via Kinobeads <sup>38</sup>	Competition pulldown using affinity resin to enrich ATP-binding proteins	
<i>In situ</i> pulldown <sup>14,15</sup>	Target binding in cells, enrichment via photoaffinity-labeling	
DARTS <sup>20</sup>	Assessment of protein stability after proteolysis	Label-free proteomics (direct approach)
SPROX <sup>21</sup>	Assessment of protein stability after chemical denaturation	
TPP <sup>23,24</sup>	Assessment of thermal protein stability	
SEA <sup>25</sup>	Prediction based on chemical similarity	<i>In silico</i> prediction (indirect approach)
SPIDER <sup>39</sup>	Prediction based on chemical similarity using artificial neuronal networks	
COMPARE Analysis <sup>26</sup>	Cytotoxicity profiling in various cancer cell lines	Multi-parametric profiling (indirect approach)
Connectivity Map <sup>27</sup>	Gene expression profiling	
ChemProteoBase <sup>28,29</sup>	Proteomic profiling, based on 2D-DIGE	
Morphobase <sup>30</sup>	Morphological profiling	
Cell Painting assay <sup>31,32</sup>	Morphological profiling using cellular dyes	

### 2.1.3 Target validation

Target validation confirms that modulation of a putative (protein) target by a small molecule actually mediates its bioactivity.<sup>40</sup> This is demonstrated ideally on three different levels: First, the compound's ability to interact with and, if applicable, functionally modulate the target protein should be confirmed *in vitro*, secondly the cellular target engagement should be demonstrated and thirdly chemical and genetic validation should link the target candidate with the observed bioactivity of the compound. An overview on the whole process is depicted in Figure 5.

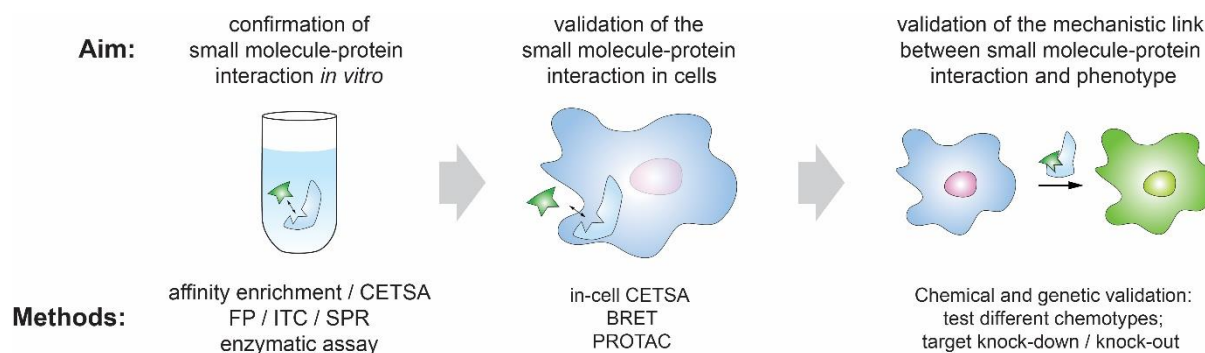


**Figure 5: Overview on the general target validation workflow.** BRET = bioluminescence energy transfer; CETSA = cellular thermal shift assay; FP = fluorescence polarization; ITC = isothermal titration calorimetry; PROTAC = proteolysis targeting chimera; SPR = surface plasmon resonance

The first level includes confirmation of e.g. ABP results via immunoblotting, ideally showing dose-dependent displacement of the putative target with free compound. CETSA may back-up the hypothesis, however not every interaction induces an alteration in the thermal stability. Biophysical techniques, such as fluorescence polarization (FP), surface plasmon resonance (SPR) or isothermal titration calorimetry (ITC), allow to monitor the protein-compound interaction directly.<sup>3</sup> These techniques, however, require purified protein and/or chemical modification of the small molecule. If the putative target is an enzyme or signaling protein, the bioactive compound (and its derivatives) can be tested for the influence on the enzymatic activity or the downstream signaling, respectively. This might further substantiate a target hypothesis, especially if the SAR based on such assay is largely congruent with the SAR obtained in the phenotypic assay in which the compound was originally discovered.<sup>40</sup>

In the second stage, cellular engagement can be demonstrated via CETSA in intact cells or bioluminescence resonance energy transfer (BRET).<sup>41</sup> For the latter technique, the protein of interest is expressed as a luciferase fusion protein and cells are treated with a fluorescent tracer based on the small molecule of interest. In case of an interaction between small molecule and protein, luciferase and fluorophore get into close proximity. Upon luciferase substrate addition, light emitted by the luciferase excites the fluorophore via resonance energy transfer. Thus, a fluorescent signal is indicative of the protein-small molecule interaction.<sup>41</sup> Alternatively, a small molecule-derived 'proteolysis targeting chimera' (PROTAC) can be used to test cellular engagement. Upon binding to its target protein, a PROTAC recruits an E3 ubiquitin ligase, which polyubiquitinylates the target protein, thereby triggering its proteasomal degradation.<sup>42</sup> In the third step, the relevance of a target-protein interaction for inducing a certain phenotype must be investigated. For chemical validation, known small molecule

modulators of the target protein with a different chemotype should be tested in the phenotypic assay, in which the bioactivity of the molecule of interest was originally discovered. Additionally, a genetic validation should be conducted, e.g. by determining the compound's bioactivity after decreasing or increasing the protein level of the putative target. This can be achieved e.g. via siRNA-mediated knock-down, CRISPR-Cas-mediated knock-out or overexpression. The last stage is the elucidation of the compound's mode of action, which should explain how modulating the target mechanistically translates into the observed phenotype. There are no general techniques to achieve this, since this procedure strongly depends on the target and the induced phenotype.

The target identification and validation of a small molecule is an important procedure to understand its mode of action. However, depending on the target of interest, it can be a very challenging endeavor, often including the application of multiple approaches.

## 2.2 Reactive oxygen species

'Reactive Oxygen Species' (ROS) is a collective term for various short-lived, radical or non-radical chemical species comprising oxygen. Prominent examples are superoxide ( $O_2^{\cdot-}$ ), hydrogen peroxide ( $H_2O_2$ ) or hydroxyl radicals ( $OH^{\cdot}$ ).<sup>43</sup> Cells are constantly confronted with ROS, as a multitude of cellular processes, such as mitochondrial respiration or oxidative protein folding, fuel their production.<sup>44,45</sup> In addition, various exogenous factors, e.g. UV radiation, tobacco smoke and exhaust gases, as well as (heavy) metal ions and oxidizing chemicals can induce ROS formation in cells.<sup>46–50</sup> In a cellular context, ROS are often regarded as a '*double-edged sword*': While low to moderate ROS levels fulfill second messenger functions or facilitate pathogen elimination, high concentrations damage biomolecules, cause oxidative stress and ultimately trigger cell death.<sup>51,52</sup> Thus, ROS are linked to a plethora of different pathological conditions, including cancer, neurodegenerative diseases, diabetes, ischemia and inflammation.<sup>53–57</sup> Furthermore, reactive oxygen species, especially those of mitochondrial origin, play a key role in the process of aging.<sup>58,59</sup> Hence, the maintenance of redox homeostasis is substantially important to prevent oxidative stress and associated cellular damage. Cells therefore employ a broad spectrum of antioxidant measures, to keep ROS levels low.

### 2.2.1 Cellular sources of ROS and antioxidant mechanisms

The cellular mechanisms involved in the formation, conversion or scavenging of ROS, are as diverse as the different reactive oxygen species themselves. The cellular antioxidant defense line consists of three major components: ROS-detoxifying enzymes, e.g. catalase, chemical antioxidants, such as glutathione, ascorbate or  $\alpha$ -tocopherol and various repair mechanisms, like the thioredoxin system (Figure 6).

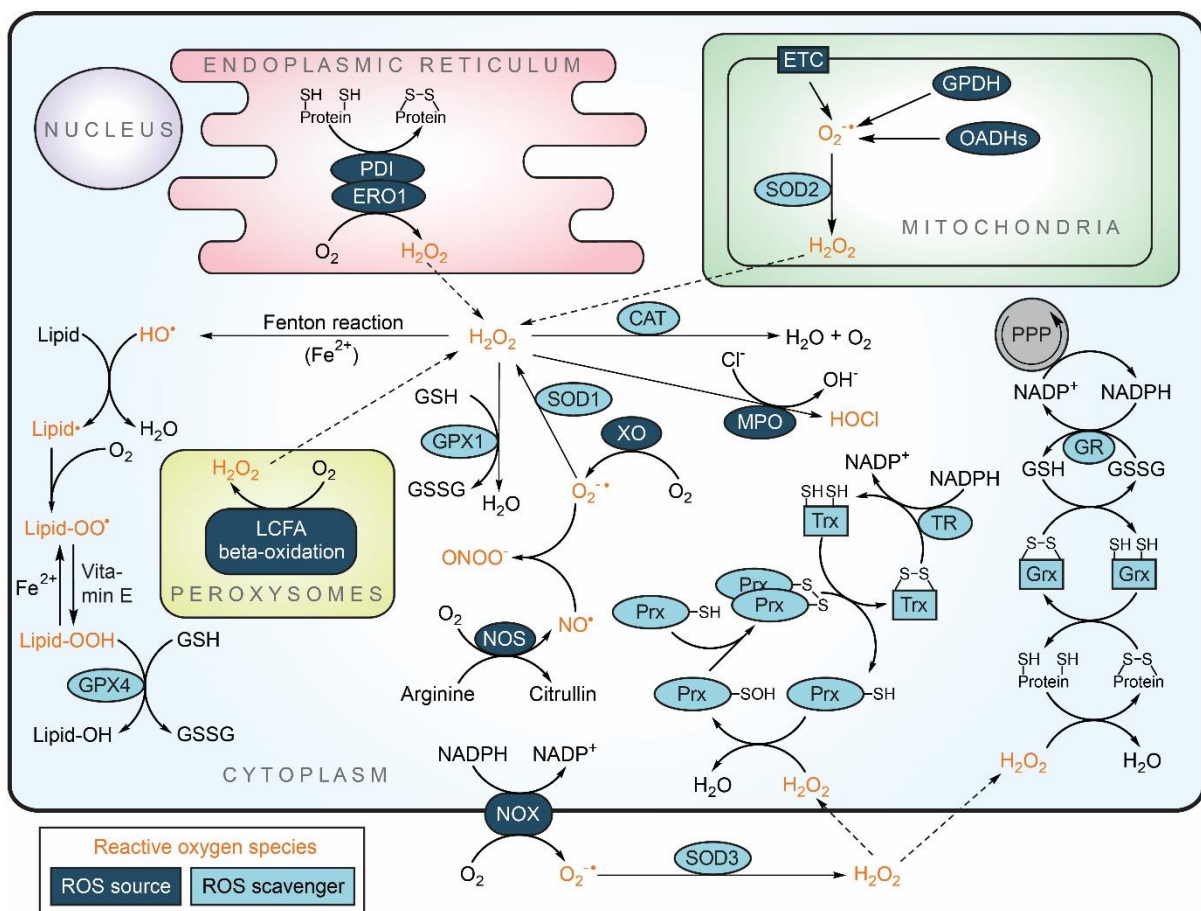


**Figure 6: Cellular sources and scavenging mechanisms of reactive oxygen species.** CAT = Catalase; ERO = ER oxidoreductin; ETC = electron transport chain; GPDH = glycerol-3-phosphate dehydrogenase; GPX = glutathione peroxidase; GR = glutathione reductase; Grx = Glutaredoxin; LCFA = long-chain fatty acid; MPO = myeloperoxidase; NOS = nitric oxide synthase; NOX = NADPH oxidase; OADHs = 2-oxoacid dehydrogenases; PDI = protein disulfide isomerase; PPP = pentose phosphate pathway; Prx = peroxiredoxin; SOD = superoxide dismutase; Trx = thioredoxin; TR = thioredoxin reductase; XO = xanthine oxidase

A major source of cellular ROS are mitochondria.<sup>60</sup> During ATP production, the mitochondrial electron transfer chain (ETC), especially at complex I and III, is known to produce high levels of superoxide by electron leakage.<sup>61</sup> In addition, glycerol-3-phosphate dehydrogenase (GPDH) and different 2-oxoacid

dehydrogenases (OADHs), like the pyruvate dehydrogenase, further contribute to the mitochondrial superoxide pool.<sup>62,63</sup> Superoxide is unable to permeate lipid bilayers and is considered to be the 'primary reactive oxygen species', which is converted to other reactive oxygen species.<sup>64,65</sup> For instance in mitochondria, superoxide dismutase (SOD) 2 converts superoxide radicals into the more stable hydrogen peroxide, which can diffuse through membranes e.g. into the cytoplasm.<sup>66</sup>

Apart from mitochondria, hydrogen peroxide is formed during  $\beta$ -oxidation of long-chain fatty acids (LCFA) in peroxisomes and during oxidative folding of proteins in the endoplasmic reticulum (ER).<sup>45,67</sup> In the latter process, the protein disulfide isomerase (PDI) forms disulfide bridges in misfolded substrate proteins via oxidation of cysteine residues. The thereby reduced cysteine residues within the active site of PDI are subsequently oxidized by the ER oxidoreductin 1 (ERO1), which in turn produces hydrogen peroxide.<sup>45</sup> Two antioxidant enzymes mainly facilitate the hydrogen peroxide detoxification in the cytoplasm: glutathione peroxidase (GPX) 1, which utilizes glutathione (GSH) as reductant, and catalase (CAT) that transforms hydrogen peroxide into water and oxygen.<sup>68</sup> Alternatively, myeloperoxidase (MPO), an enzyme mainly expressed in neutrophils, can transform hydrogen peroxide and chloride into hypochlorous acid.<sup>69</sup> In the presence of ferrous iron, hydrogen peroxide can undergo the so-called 'Fenton reaction', which leads to the formation of the highly reactive hydroxyl radicals. These radicals readily react with lipids, e.g. in the plasma membrane, to form lipid radicals, which further react with oxygen to lipid peroxide radicals. These can react with other lipids to form lipid radicals and lipid peroxides. This self-propagating process is termed lipid peroxidation, which poses a serious threat to the cellular membrane integrity. The lipophilic antioxidant vitamin E scavenges the lipid peroxide radical, forming a lipid peroxide. However, such peroxide can also undergo a Fenton reaction to form lipid peroxide radicals again. This is prevented by conversion of lipid peroxide into a lipid alcohol by GPX4, thereby preventing further propagation of lipid peroxidation.<sup>70</sup> In general, a high degree of lipid peroxidation can compromise the cell membrane integrity and can trigger a distinct type of cell death, termed ferroptosis.<sup>71</sup>

The reactive nitrogen species (RNS) nitric oxide ( $\text{NO}^{\bullet}$ ), which acts as an important signaling molecule, is formed during the conversion of arginine to citrulline by the NO synthase (NOS).<sup>72</sup>  $\text{NO}^{\bullet}$  can further react with superoxide, e.g. originating from the xanthine oxidase (XO), to form the highly reactive peroxynitrite ( $\text{ONOO}^-$ ).<sup>73</sup> An additional origin of superoxide is the family of NADPH oxidase (NOX) enzymes which are membrane-bound protein complexes and important for cellular signaling events and



pathogen elimination. Superoxide produced by NADPH oxidation can be liberated both intra- and extracellularly.<sup>74</sup> In the cytosol, SOD1 converts superoxide into hydrogen peroxide, while extracellular superoxide is converted by SOD3 and the resulting hydrogen peroxide can diffuse back into the cell.<sup>75</sup> Hydrogen peroxide can oxidize redox-sensitive proteins and thereby form disulfide bridges, which may alter protein conformation and interfere with the biological function of the protein.<sup>76</sup> Irreversibly oxidized proteins are subjected to proteasomal degradation to avoid protein aggregation.<sup>77</sup> The antioxidant enzyme peroxiredoxin (Prx) prevents oxidation of other proteins via direct hydrogen peroxide scavenging. Prx has a conserved cysteine residue that can be oxidized by hydrogen peroxide to form sulfenic acid. The sulfenic acid subsequently reacts with the cysteine of another Prx molecule to form a disulfide bridge.<sup>78</sup> Reversibly oxidized proteins can be reduced by two types of small redox proteins, namely thioredoxin (Trx), and glutaredoxin (Grx), which in turn get oxidized. Trx reduces intermolecular disulfide bridges in Prx dimers and or intramolecular disulfide bridges in other proteins, and is subsequently enzymatically reduced by the Trx reductase (TR).<sup>79</sup> In contrast, oxidized Grx is reduced by GSH.<sup>80</sup> The oxidized glutathione (GSSG) is reduced by glutathione reductase (GR).<sup>81</sup> Both TR and GR use NADPH as reductant, underlining the significance of NADPH for the peroxi-, glutathione- and thioredoxin system.<sup>80,81</sup> The cellular NADPH pool is mainly replenished via the pentose phosphate pathway (PPP), which therefore is an important metabolic pathway for maintaining the cellular redox homeostasis.<sup>82</sup>

### 2.2.2 ROS as signaling molecules

Physiological concentrations of ROS influence various cellular signaling events that are mediated for instance by reversibly oxidizing redox-sensitive cysteine residues. From all proteinogenic amino acids, cysteines are most prone to oxidation and therefore play a special role in redox biology. As shown in Figure 7, reduced cysteine residues (R-SH), can be gradually oxidized to sulfenic acid (R-SOH), a reversible posttranslational modification important for cellular signaling.<sup>83</sup> These reactions are mostly mediated by hydrogen peroxide, which has a comparably high stability among different ROS and the ability to freely diffuse through membranes, rendering it a suitable signaling molecule. Such redox-mediated signaling events involve local, low ROS concentrations, e.g. the before-mentioned thiol oxidation is hypothesized to occur at nanomolar hydrogen peroxide concentrations.<sup>84</sup>

Sulfenic acid readily reacts with other thiols to form disulfide bridges, however in the absence of such reaction partners it gets overoxidized to sulfinic acid (R-SOH) and finally sulfonic acid (R-SO<sub>3</sub>H). Both products cannot be reduced back into thiols within the cell. Also, disulfides (R-SS-R') are prone to oxidation and form thiosulfates (R-SOS-R') and thiosulfonates (R-SO<sub>2</sub>S-R').<sup>76</sup>

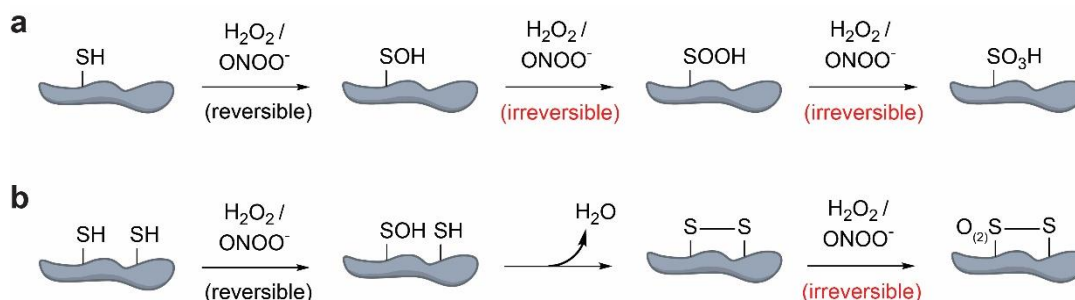


**Figure 7: Oxidation of cysteine residues by hydrogen peroxide or peroxynitrite.** Overoxidation of (a) a single thiol or (b) two thiols in close proximity.

A prominent example of ROS-mediated signaling is the cellular response to growth factors, such as the epidermal growth factor (EGF) or the platelet-derived growth factor (PDGF). The stimulation of cells with EGF or PDGF, leads to a rapid increase in hydrogen peroxide.<sup>85,86</sup> Such growth factor receptor-mediated signaling induces ROS via to the activation of the PI3K-AKT pathway, which in turn activates Rac-GTPases. Subsequently, Rac activates the superoxide production via NOX. Superoxide dismutases convert superoxide into hydrogen peroxide, which oxidizes various redox-sensitive protein targets, including 'phosphatase and tensin homolog' (PTEN).<sup>87</sup> PTEN is a phosphatase that antagonizes the effect of PI3K by dephosphorylation of phosphoinositoltriphosphate (PIP<sub>3</sub>). Oxidation by hydrogen peroxide inactivates PTEN, which in turn enhances AKT activation downstream of PI3K.<sup>88</sup> Hydrogen peroxide-mediated signaling occurs in close proximity to membrane and NOX enzymes. This local restriction is achieved by the action of Prx proteins, which eliminate hydrogen peroxide and prevent its diffusion further into the cell.<sup>78</sup>

### 2.2.3 Oxidative stress response

The term 'oxidative stress' describes a severe cellular redox imbalance caused by an excess of reactive oxygen species. High ROS levels affect various biomolecules and have devastating consequences for cells: Oxidation of DNA may lead to mutations and genomic instability, irreversible oxidation can lead

to protein aggregation and lipid peroxidation can compromise the integrity of the cell membrane.<sup>70,71,89–92</sup> Due to these detrimental effects of oxidative stress, cells take different antioxidative measures to counteract such imbalance and ensure cell survival as described in chapter 2.2.1. Cells utilize various mechanisms to monitor their cellular redox status, e.g. via proteins that contain redox-sensitive cysteine residues. An example for such protein is the Kelch ECH associating protein 1 (KEAP1), which is part of the KEAP1-NRF2 system, a key cellular antioxidant defense system.<sup>93</sup> Under normal redox conditions, KEAP1 forms a complex with the nuclear factor erythroid 2-related factor 2 (NRF2) and the E3 ubiquitin ligase CUL3, which constantly mediates the polyubiquitination and subsequent proteasomal degradation of NRF2 (Figure 8).

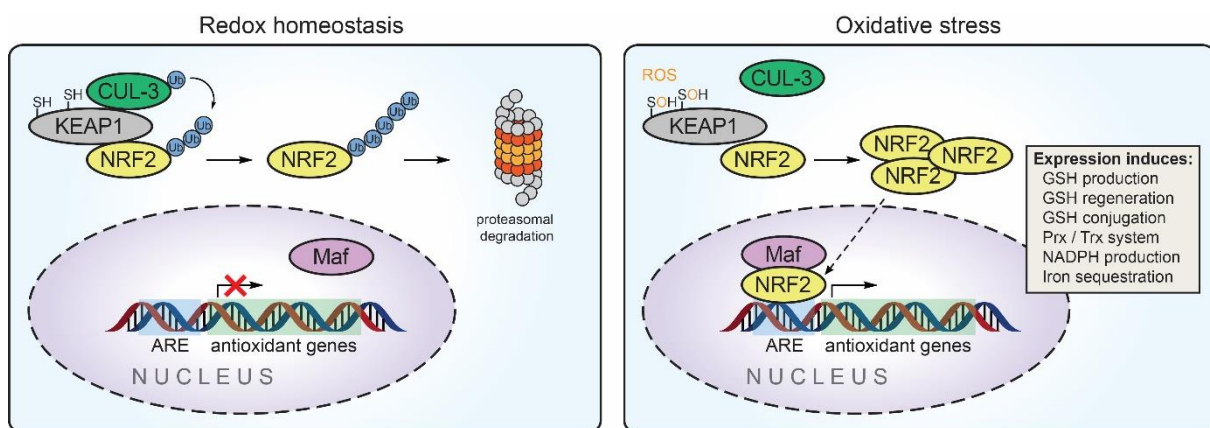


**Figure 8: KEAP1-NRF2 antioxidant pathway.** Schematic drawing of the NRF2-mediated antioxidant response. Under normal conditions, NRF2 is constitutively degraded, but accumulates under oxidative stress. The exact mechanism of NRF2 accumulation under oxidative stress is yet to be elucidated. ARE = antioxidant response element; CUL-3 = Cullin-3; KEAP1 = Kelch-like ECH-associated protein 1; NRF2 = Nuclear factor erythroid 2-related factor 2; Maf = musculoaponeurotic fibrosarcoma; Ub = ubiquitin

Upon cellular ROS accumulation, reactive cysteine residues in KEAP1 are oxidized, which results in the dissociation of CUL3 from KEAP1. This prevents the constant degradation of NRF2 and induces its translocation into the nucleus, where it heterodimerizes with a Maf protein. This complex binds to the antioxidant response element (ARE) and facilitates the expression of various antioxidant and cytoprotective proteins.<sup>94</sup> NRF2 signaling increases GSH production via elevated expression of the cystine/glutamate antiporter (xCT) and the glutamate-cysteine ligase (GCL) complex subunits GCLM and GCLC, as well as increased GSH recycling via increased expression of the glutathione reductase (GR).<sup>95–97</sup> The expression of various glutathione-S-transferases, which facilitate the GSH-conjugation

of xenobiotics, as well as GPX2, which scavenges organic hydroperoxides, is also elevated by NRF2.<sup>98,99</sup> Further antioxidative effects are mediated by upregulation of Prx, Trx and TR and key enzymes that control NADPH production, such as glucose-phosphate dehydrogenase (G6PD), phosphoglycerate dehydrogenase (PHGDH) and malic enzyme (ME).<sup>98,100,101</sup> In addition, the expression of proteins involved in iron sequestration and quinone detoxification is also enhanced.<sup>99,102</sup> Apart from NRF2, two other transcription factors participate in the oxidative stress response: p53 and FOXO. The tumor suppressor p53 is best known as 'guardian of the genome' and induces growth arrest and apoptosis upon DNA damage.<sup>103</sup> In addition, p53 exerts antioxidative effects by upregulating the expression of GPX1, SOD2 as well as Sestrin-1 and -2, which reduce overoxidized peroxiredoxins.<sup>104</sup> Furthermore, p53 induces the expression of TIGAR, a fructose-2,6-bisphosphate-degrading enzyme, which lowers the glycolytic activity of cells and promotes the activity of the pentose phosphate pathway, thereby enhancing NADPH regeneration.<sup>105</sup> The FOXO transcription factors also contribute to the antioxidant defense, by increasing SOD2, Prx3, Prx5 and TR2 expression.<sup>106</sup> Additionally, the tumor suppressor BRCA1, a protein mutated in approximately half of all hereditary breast cancer cases, is involved in DNA damage control and induces upregulation of antioxidants via NRF2, thereby ensuring genome integrity.<sup>107,108</sup>

#### **2.2.4 Role of reactive oxygen species in cancer**

Cancer is a collective term for a variety of diseases with defined characteristics: Cancer cells divide in an uncontrolled manner, due to aberrant, continuous growth signaling and evasion of growth suppressors. Unlike healthy cells, cancer cells inherit the potential to proliferate indefinitely and to circumvent cell death mechanisms. The growing tumor promotes angiogenesis to assure nutrient supply, invades into the surrounding tissue and ultimately metastasize into other areas within the body. These properties of cancerous diseases were defined 20 years ago as the 'Hallmarks of Cancer' by Douglas Hanahan and Robert A. Weinberg.<sup>109</sup> Later, additional properties, namely evasion from the immune system, induction of metabolic changes, inflammation and genomic destabilization were added to this list.<sup>110</sup> Although a tumor arises from a small number of aberrant cells with few genetic mutations, it is not a genetically and phenotypically uniform accumulation of cells.<sup>111</sup> Tumor cells undergo clonal evolution - they gain mutations, which can promote proliferation or trigger cell death.<sup>112</sup> During tumor

progression, cancer cells that survive within the current tumor microenvironment are selected and can clonally expand, which renders cancer a highly dynamic disease.<sup>111</sup>

Reactive oxygen species are involved in cancerous diseases on multiple levels. A healthy cell in the state of redox homeostasis produces few ROS, an adequate amount of antioxidants and is able to repair damages in its DNA and other cellular components. In contrast, cancer cells often display higher levels of ROS in comparison to their healthy counterparts.<sup>113,114</sup> These higher ROS levels may result from the activation of certain oncogenes, inactivation of tumor suppressors or from alterations in cellular metabolism.<sup>115</sup> Due to their DNA-damaging and mutagenic properties, elevated ROS levels promote genomic instability and tumorigenesis, however, ROS levels exceeding a certain threshold may lead to cell death. During tumor progression, those cancer cells are selected that maintain ROS levels high enough to induce tumor-driving mutations but low enough to survive their damaging effects. Thus, cancer cell signaling often leads to the activation of measures that increase both ROS and antioxidant levels. For example, oncogenic Ras protein can promote tumorigenesis by both pro- and antioxidant mechanisms.<sup>116</sup> On the one hand, HRas<sup>G12V</sup> induces strong elevation of superoxide levels by upregulation of NOX1 and NOX4, which was shown to be a prerequisite for transformation.<sup>117,118</sup> Furthermore, NRas<sup>G13D</sup> was found to downregulate the expression of sestrins, which reduce overoxidized peroxiredoxins, leading to elevated ROS levels and increased DNA oxidation.<sup>119</sup> On the other hand, KRas<sup>G12D</sup> was found to suppress ROS by increasing the transcription of the NRF2 protein, which increases the activity of the NRF2-dependent antioxidant program.<sup>120</sup>

Reactive oxygen species strongly influence various signaling pathways in cancer cells (Figure 9). Aberrant activation of the PI3K/AKT pathway was shown to increase both mitochondrial and NOX-mediated superoxide production via AKT, which indirectly elevates hydrogen peroxide levels.<sup>121</sup> Hydrogen peroxide maintains PI3K/AKT activity by inactivation of protein tyrosine phosphatases (PTPs), which dephosphorylate and inactivate RTKs, and PTEN.<sup>122</sup> However, AKT also inhibits FOXO, which mediates expression of antioxidative proteins.<sup>123</sup> Furthermore, AKT indirectly promotes survival by inhibition of proapoptotic proteins, such as Bad or caspase 9.<sup>124</sup> Taken together, the PI3K/AKT pathway establishes a persistent elevation of ROS levels that promotes survival, proliferation, and tumor growth.

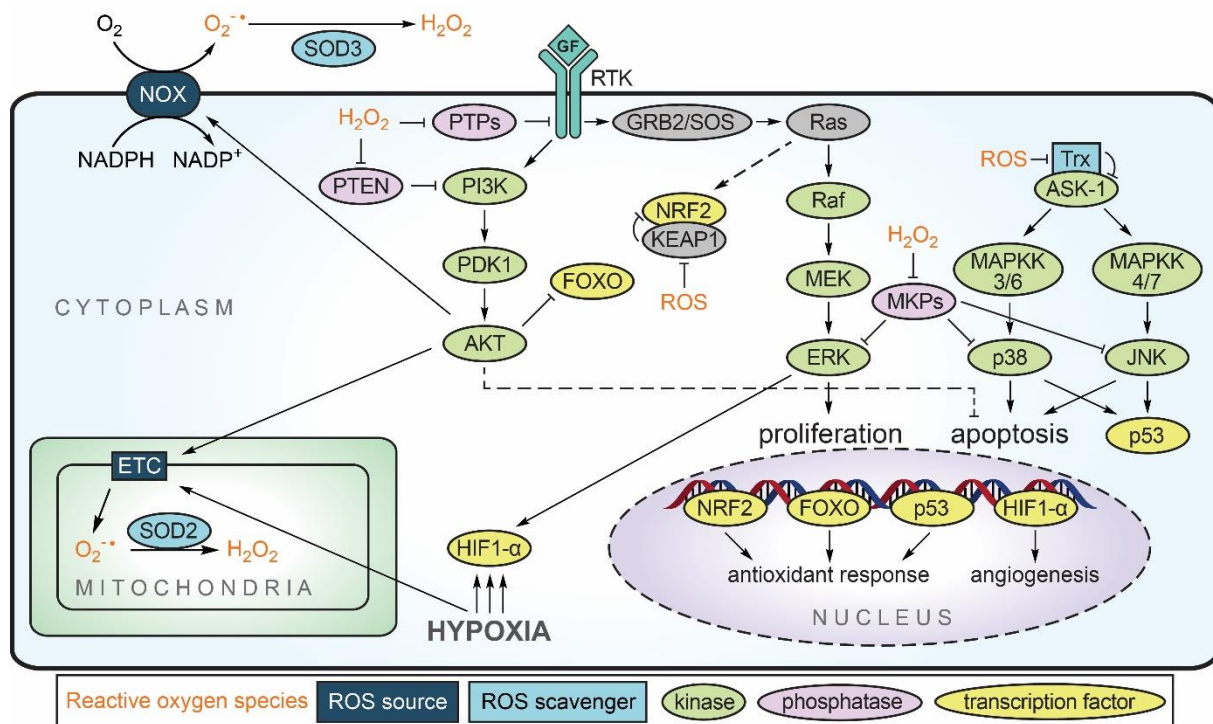


**Figure 9: Influence of ROS on signaling pathways in cancer cells.** Schematic drawing of PI3K/AKT and MAP kinase signaling pathways, which are regulated by ROS, mainly via inhibition of regulatory phosphatases. ASK-1 = Apoptosis signaling-regulating kinase 1; ERK = Extracellular signal-related kinase; FOXO = Forkhead box protein O; GF = growth factor; GRB2 = Growth factor receptor-bound protein 2; HIF1- $\alpha$  = Hypoxia-inducible factor 1-alpha; JNK = c-Jun N-terminal kinase; KEAP1 = Kelch-like ECH-associated protein; MAPKK = Mitogen-activated protein kinase kinase; MKP = MAP kinase phosphatase; NRF2 = Nuclear factor erythroid 2-related factor 2; PDK1 = 3-phosphoinositide-dependent protein kinase 1; PTEN = Phosphatase and tensin homolog; PTP = protein tyrosine phosphatase; RTK = Receptor tyrosine kinase; SOD = superoxide dismutase; SOS = Son of sevenless homolog; Trx = thioredoxin

It was also observed that oxidative stress can indirectly lead to the activation of the pro-proliferative ERK, either by the above-mentioned ROS-mediated activation of RTKs or by hydrogen peroxide-induced inactivation of MAP kinase phosphatases (MKP).<sup>125</sup> MKPs additionally inhibit the MAP kinases p38 and c-Jun N-terminal kinase (JNK) and mediate induction of apoptosis and p53 activation in response to high ROS levels.<sup>126</sup> Such elevated ROS levels are detected by a complex consisting of apoptosis signal-regulating kinase 1 (ASK-1) and Trx. Upon oxidation of Trx, ASK-1 can dissociate and activate different MAP kinase kinases (MAPKK), which subsequently activate p38 and JNK.<sup>127</sup> JNK- and p38-mediated apoptosis, however, might be counteracted by the before-mentioned antiapoptotic activity of AKT.

Progressing tumor growth often leads to an uneven distribution of oxygen and nutrients among cancer cells and cause starvation and hypoxia in cells located most remotely from blood vessels. Hypoxic

conditions induce the stabilization of Hypoxia-inducible factor 1-alpha (HIF1- $\alpha$ ), a transcription factor that is constitutively subjected to ubiquitination and proteasomal degradation during normoxia. HIF1- $\alpha$  controls the expression of over 60 proteins, including the vascular endothelial growth factor (VEGF), which stimulates angiogenesis.<sup>128</sup> ROS and hypoxia mutually influence each other, as hypoxia increases mitochondrial ROS production.<sup>129</sup> ROS in turn can promote the transcriptional activity of HIF1- $\alpha$  via ERK activation.<sup>130</sup> Angiogenesis triggers further vascularization, thereby ensuring a sufficient nutrient and oxygen supply for the growing tumor.

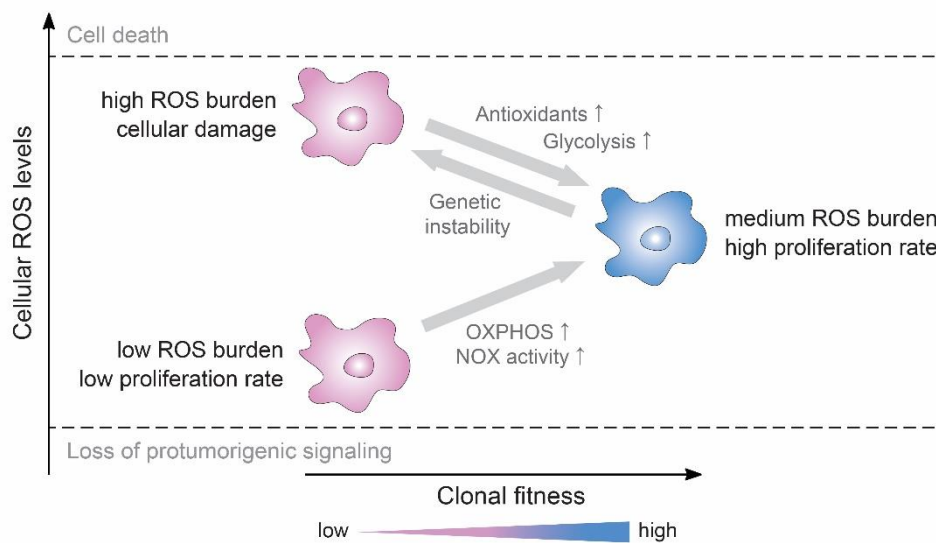


**Figure 10: Reactive oxygen species as important determinant of a cancer cell's clonal fitness.** The fitness of cancer cells may also be determined by their cellular ROS levels. To maintain high rates of proliferation, ROS levels need to be high enough to maintain pro-tumorigenic signaling, however also low enough to avoid ROS-mediated cell death. The metabolic phenotype may therefore be adapted to maintain such optimal ROS levels.

The metabolic phenotype of cancer cells is also heavily influenced by ROS. Almost a century ago, Otto Warburg described a high glycolytic rate in cancer cells, even in the presence of oxygen - an observation later termed 'Warburg effect' or 'aerobic glycolysis'.<sup>131</sup> During aerobic glycolysis, pyruvate is not shuttled into the citric acid cycle, but is instead fermented into lactate, which is subsequently secreted. In regard to its ATP yield this procedure is highly inefficient, but in comparison to oxidative phosphorylation hardly increases ROS levels.<sup>132</sup> To outlast the strong clonal selection within a tumor, cancer cells need to tune their metabolism towards optimal fitness. It is hypothesized by Rodic and Vincent that the cellular ROS level is the decisive factor to determine fitness and thereby also the

metabolic phenotype of cancer cells (Figure 10).<sup>133</sup> In case of very high ROS levels, the cancer cell might be forced to switch mainly to glycolysis, to avoid ROS production from oxidative phosphorylation. However, cancer cells also need to maintain a basal ROS level for pro-proliferative signaling processes. Thus, a drop in cellular ROS levels might induce oxidative phosphorylation or activation of NOX to increase ROS levels again. Taken together, in addition to the availability of oxygen and nutrients, ROS heavily influences a cancer cell's metabolic circuitry.

### 2.2.5 ROS induction as cancer therapy

Many cancer therapy approaches aim to induce proliferation reduction and cytotoxicity in cancer cells. Commonly used chemotherapeutics suppress cell division by targeting cellular components that are crucial in both cancer and healthy cells, which leads to a broad range of severe side effects. Typical modes of action are crosslinking of DNA (e.g. by cisplatin), microtubule stabilization (e.g. by paclitaxel) or by inhibition of topoisomerases (e.g. by camptothecin).<sup>134–136</sup> Thus, a main goal in the development of novel therapeutic approaches in oncology is to selectively target cancer cells in order to minimize side-effects. This endeavor requires the identification of features that distinguish cancer cells from healthy cells. A prominent example of a drug used in targeted cancer therapy is the kinase inhibitor Imatinib that inhibits the tyrosine kinase BCR-ABL, a fusion protein found in the majority of patients with chronic myelogenous leukemia (CML).<sup>137</sup> Another example is Trastuzumab, a monoclonal antibody against the human epidermal growth factor receptor 2 (HER2), an oncogene that is overexpressed in certain types of breast cancer.<sup>138</sup> These two therapeutic agents target proteins that are exclusively expressed or overexpressed in cancer cells, thereby providing selectivity over healthy cells. Although both drugs are successfully used as anti-cancer agents and regarded as essential medicines by the World Health Organization, they also evoke side effects and clonal selection for mutations in their respective main target and cause drug resistance.<sup>139</sup> Thus, other strategies to selectively address cancer cells are still highly demanded.

The redox status of tumor cells might be a property that allows to distinguish cancer cells from its healthy counterparts, as elevated ROS levels were found in many different cancer cell lines and cancer biopsies.<sup>113,114</sup> This sparked the investigation of cancer therapeutic redox modulation, considering both pro- and antioxidant interventions. Today, the latter approach is largely rejected, as dietary antioxidative supplementation for cancer prevention has been shown to be ineffective, if not protumorigenic.<sup>140–142</sup>



In addition, antioxidants have been found to lower the efficacy of many classical cancer therapies, including radiotherapy, as these take effect via ROS induction.<sup>143</sup>

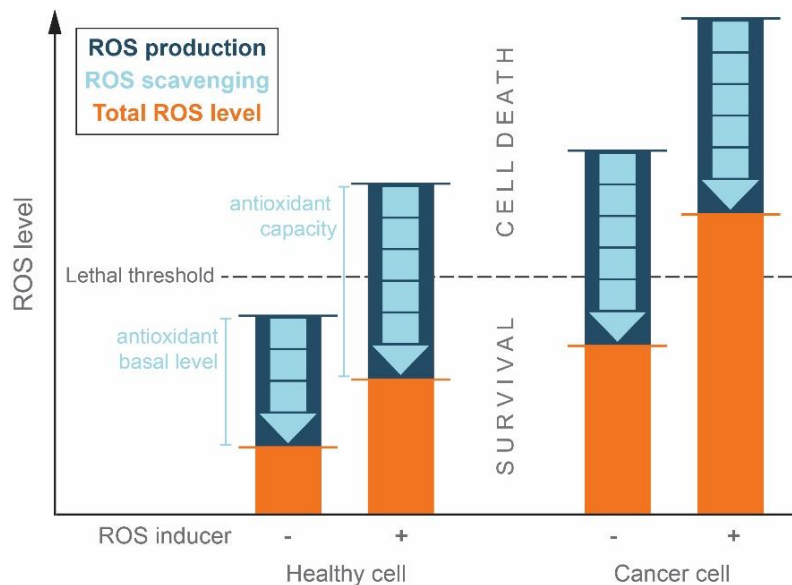


**Figure 11: ROS-inducing compounds may selectively kill cancer cells.** Healthy cells only partly exploit their antioxidant capacity to keep ROS levels low. Addition of a ROS-inducing compound, e.g. that increases ROS production, leads to antioxidant adaptation to keep ROS levels below the lethal threshold. Cancer cells constantly exploit their antioxidant capacity to counterbalance their comparably high basal ROS levels. Thus, exogenously induced ROS may not be compensated for and may induce cell death. Figure based on Trachootham et al.<sup>43</sup>

Twenty years ago, Kong *et al.* proposed a 'threshold concept for cancer therapy', thereby suggesting to elevate ROS levels in order to kill cancer cells.<sup>144</sup> Trachootham et al. hypothesize that healthy cells are able to counterbalance the effects of ROS-inducing compounds by upregulation of antioxidant measures, while cancer already exploits their antioxidant capacity and thus is unable to compensate for the additional ROS burden. Therefore, ROS-inducing compounds may selectively kill cancer cells (Figure 11).<sup>43</sup> Kong *et al.* highlight the importance of reaching local ROS concentrations within the cancer lesion that is high enough to effectively kill the cancer cells, as ROS levels below such toxic threshold would drive tumor proliferation. Due to the toxic nature of reactive oxygen species to all cells, they propose to combine ROS-enhancing therapeutics with a drug-delivery approach and systemic administration of antioxidants to minimize the damage to healthy cells.<sup>144</sup>

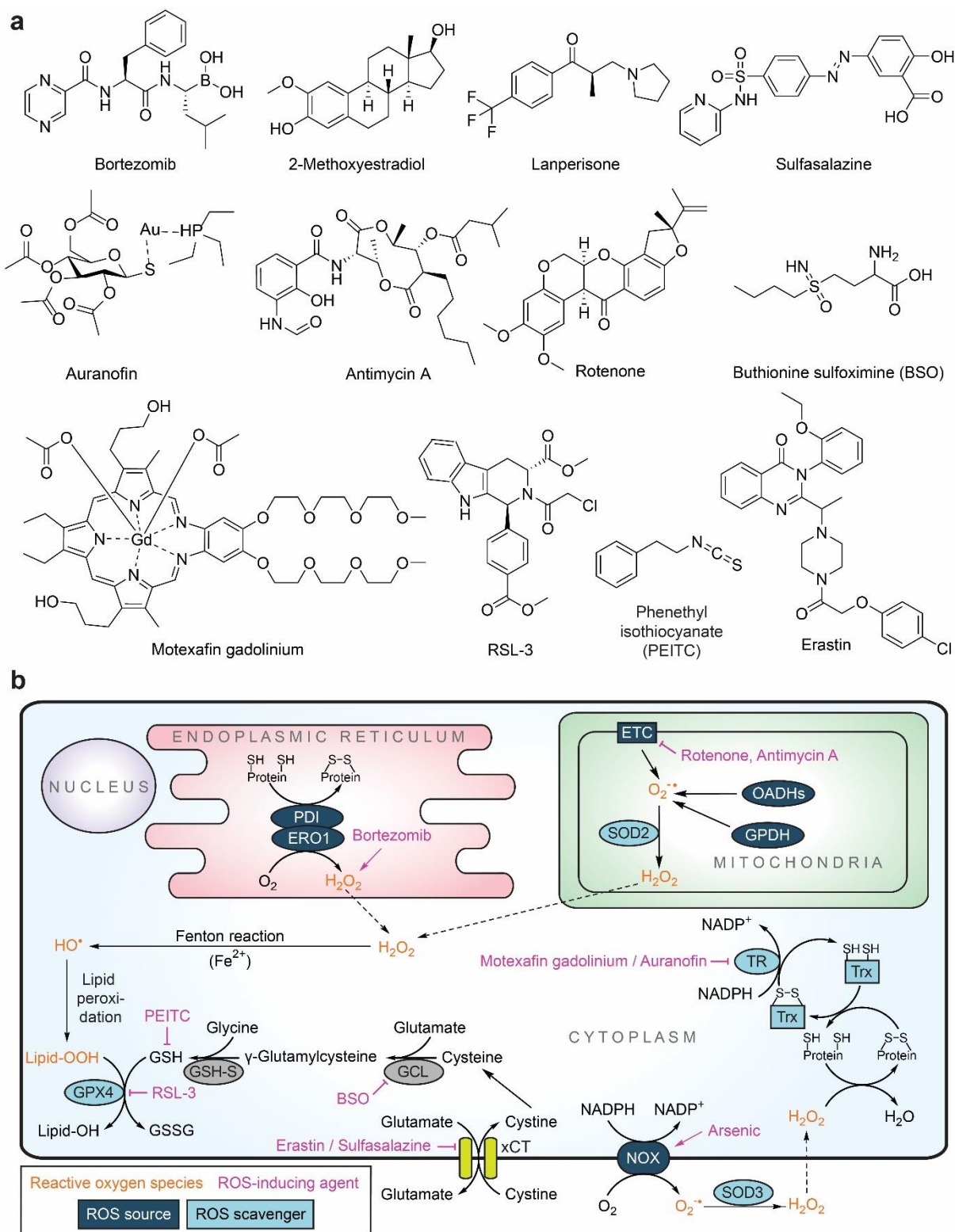


**Figure 12: ROS-inducing compounds. (a)** Chemical structures and **(b)** mode of action of different ROS-inducing compounds. Arsenic and Bortezomib induce ROS production by causing NOX activation or ER stress, respectively. BSO, Erastin, Sulfasalazine, RSL-3 and PEITC influence glutathione-mediated ROS clearance. Motexafin gadolinium and Auranofin inhibit TR. BSO = Buthionine sulfoximine; ERO = ER oxidoreductin; ETC = electron transport chain; GCL =  $\gamma$ -glutamylcysteine ligase; GPDH = glycerol-3-phosphate dehydrogenase; GSH-S = glutathione synthase; OADHs = 2-oxoacid dehydrogenases; PDI = protein disulfide isomerase;

PEITC = Phenethyl isothiocyanate; SOD = superoxide dismutase; TR = thioredoxin reductase; Trx = thioredoxin; xCT = cysteine-glutamate antiporters

Until today, various studies investigated this approach by developing ROS-inducing agents to selectively target cancer cells (Figure 12). An early example is arsenic, which induces cellular ROS accumulation via activation of NADPH oxidases and performed well in clinical trials for treatment of acute promyelocytic leukemia.<sup>145,146</sup> In immortalized Ras-transformed ovarian epithelial cells, which display elevated ROS levels in comparison their parental cell line, the GSH-depleting natural product phenethyl isothiocyanate (PEITC) caused dose-dependent cytotoxicity, while hardly affecting the viability of the parental cell line.<sup>147</sup> A high-throughput screen for small molecules that selectively induce cytotoxicity in K-Ras<sup>G12D</sup> mouse embryonic fibroblasts (in comparison to wild-type K-Ras cells) identified the muscle relaxant lanpersione, which exerts its effect in a ROS-dependent manner.<sup>148</sup> Erastin and RSL-3, both classical inducers of ferroptosis, an iron-dependent type of cell death that is caused by lipid peroxidation, originate from high-throughput screens for compounds that selectively induce cytotoxicity in engineered tumorigenic cell lines.<sup>71,149,150</sup> Erastin exhibits its selective toxicity towards Ras-transformed cells through GSH depletion via inhibition of the xCT.<sup>151</sup> RSL-3 inhibits GPX4, which reduces lipid peroxides into lipid alcohols, an important step in the containment of lipid peroxidation.<sup>152</sup> Sulfasalazine, an FDA-approved drug for the treatment of inflammatory bowel disease, was also found to inhibit xCT.<sup>153</sup> A more direct approach to deplete glutathione is the use of buthionine sulphoximine (BSO) that inhibits gamma-glutamylcysteine synthetase, which catalyzes one of the two steps in GSH biosynthesis.<sup>154</sup>

A different example for selective targeting of cancer cells with a ROS-inducing compound is Motexafin gadolinium, an inhibitor of TR1/2 and redox-cycler, which selectively localizes in tumors.<sup>155</sup> The antirheumatic agent Auranofin induces apoptosis in Cisplatin-resistant ovarian cancer cells also via ROS induction through TR inhibition.<sup>156</sup> Rotenone, a well-characterized inhibitor of complex I and mitochondrial respiration, induces apoptosis in a human leukemia cell line via induction of mitochondrial superoxide.<sup>157</sup> Antimycin A, which induces ROS via inhibition of complex III, also triggers apoptosis in this cell line, however in a ROS-independent manner.<sup>158</sup> The naturally occurring estrogen metabolite 2-methoxyestradiol (2-ME) was found to induce apoptosis and lipid peroxidation in an Erwing sarcoma tumor cell line, which could be suppressed by antioxidants.<sup>159</sup> In primary human tissue culture, 2-ME induced cytotoxic effects in ovarian carcinoma, but not in normal ovarian tissue.<sup>160</sup> The FDA-approved

proteasome inhibitor Bortezomib induces apoptosis in human non-small cell lung cancer cell line via induction of reactive oxygen species.<sup>161</sup>

As mentioned before, many of the widely used chemotherapeutics elevate ROS levels in addition to their primary mode of action, e.g. anthracyclins, vinca alkaloids, cisplatin, 5-fluorouracil and taxanes.<sup>162–166</sup> However, it is questionable, whether these compounds can achieve a ROS-dependent cancer-selective cytotoxicity. For example, doxorubicin-induced cardiac toxicity, which is one of this anthracycline's major site effects, is, among other mechanisms, caused by excessive ROS elevation.<sup>167</sup>

### 3 Aim of this thesis

Reactive oxygen species play major roles in the development and progression of cancer and heavily influence treatment outcome, however, the underlying mechanisms are often hardly understood. The short half-life of ROS makes their detection difficult. Furthermore, the fact that the term 'ROS' subsumes a variety of chemically diverse species leads to confusing or even contradictory reports about their biological effects. Both circumstances therefore hamper research on general redox biology and ROS-related cancer therapy approaches, like those based on the '*threshold concept for cancer therapy*' proposed by Kong *et al.*

In the past, Chemical Biology-driven approaches shed light on various cellular redox mechanisms. For instance, ferroptosis, a ROS-dependent form of cell death, was originally discovered by elucidating the mode of action of the small molecules erastin and ferrostatin-1, which trigger or inhibit ferroptosis, respectively.<sup>71</sup> These discoveries initiated various studies investigating novel concepts to exploit ferroptosis for cancer therapy.<sup>168</sup> This example highlights the power of ROS-modulating small molecules for research on cellular redox biology.

This thesis aimed to identify and characterize novel, fast-acting small-molecule inducers of cellular ROS accumulation by means of phenotypic screening. Subsequently, potent screening hits should be selected for hit confirmation and in-depth analysis. An SAR study should improve compound activity and identify a position susceptible to chemical alteration enabling target identification via affinity-based chemical proteomics. Different profiling methods should be applied to investigate the compound's influence on the thermal stability of proteins, cellular morphology and the (phospho)proteome in order to form a target hypothesis. Finally, the interaction of the small molecule with the proposed target candidate should be confirmed *in vitro* and *in cellulo*, and the relevance of the target for the compound's bioactivity should be validated chemically and genetically.

Such novel ROS-inducing compounds may pose a starting point for the development of innovative cancer therapy approaches, e.g. by discovering new potential drug targets, and could further deepen our understanding of redox regulation in cancer cells.

## 4 Materials and methods

### 4.1 Materials

#### 4.1.1 Chemicals and reagents

Compounds DP01-55 were purchased from Chemical Diversity (ChemDiv, USA). All other compounds mentioned in this thesis that are not listed in this chapter have been synthesized by chemists of the Chemical Biology department of the Max Planck Institute of Molecular Physiology or the Compound Management and Screening Center Dortmund.

Name	Supplier	Catalog number
<sup>12</sup> C <sub>6</sub> , <sup>14</sup> N <sub>2</sub> -L-lysine	Sigma-Aldrich	L5626
<sup>12</sup> C <sub>6</sub> , <sup>14</sup> N <sub>4</sub> -L-arginine	Sigma-Aldrich	11039
<sup>13</sup> C <sub>6</sub> , <sup>15</sup> N <sub>2</sub> -L-lysine	Sigma-Aldrich	608041
<sup>13</sup> C <sub>6</sub> , <sup>15</sup> N <sub>4</sub> -L-arginine	Sigma-Aldrich	608033
1-Chloro-2,4-dinitrobenzene (CDNB)	Sigma-Aldrich	237329
2-[4-(2-hydroxyethyl)piperazin-1-yl]ethanesulfonic acid (HEPES)	Gerbu	1009.025
3-Azido-1-propanol	Sigma-Aldrich	776130
5/6-TAMRA-Azide-Biotin	Jena Bioscience	CLK-1048-5
5-Carboxytetramethylrhodamine (5-TAMRA)	Sigma-Aldrich	C2734
Acetonitrile	Fisher Chemical	A998-212
Acrylamide / Bisacrylamide solution	AppliChem	A3626,0500
Alkyne agarose beads	Jena Bioscience	CLK-1032-2
Aminoguanidine	Sigma-Aldrich	396494
Ammonia	VWR	5330030050
Ammonium bicarbonate	Fisher Scientific	10207183
Ammonium persulfate (APS)	Serva	13375
Bathocuproinedisulfonic acid	Sigma-Aldrich	146625
Benperidol	Prestwick	Prestw-484
Biotin-PEG <sub>3</sub> -azide	Biomol	ABD-3019
Bovine serum albumine (BSA)	Serva	11945.03
Bromophenol blue	Carl Roth	A512.1
Bromperidol	Prestwick	Prestw-509
Buthionine sulfoximinine (BSO)	Sigma-Aldrich	B2515
Calcein	Sigma-Aldrich	C0875
Carbetapentane	Prestwick	Prestw-387
Cell dissociation solution	Sigma-Aldrich	C5914
Chloroacetamide	Sigma-Aldrich	22790
Chloroquine	Sigma-Aldrich	C6628

<b>Name</b>	<b>Supplier</b>	<b>Catalog number</b>
Chlorpromazine	Alfa Aesar	J63659
Clemastine	Sigma-Aldrich	C8903
CM-H <sub>2</sub> DCFDA	Thermo Fisher	C6827
cOmplete™ protease inhibitor cocktail	Sigma-Aldrich	11873580001
Concanavalin A/Alexa-488	Thermo Fisher	C11252
Copper(II) sulfate (CuSO <sub>4</sub> )	Sigma-Aldrich	C1297
D-(+)-Glucose	Carl Roth	6887.1
Deferoxamine (DFO)	Sigma-Aldrich	D9533-1G
Dibenzocyclooctyne (DBCO) agarose beads	Jena Bioscience	CLK-1034-2
Dimethyl sulfoxide (DMSO)	Sigma-Aldrich	D8418
Disodium phosphate (Na <sub>2</sub> HPO <sub>4</sub> )	Merck	1065800500
Dithioerythritol (DTE)	Gerbu	1007.0025
Dithiotreitol (DTT)	Gerbu	1008.0005
DNAse I	Serva	18535.01
Dynabeads Streptavidin C1 magnetic beads	Thermo Fisher	65001
Ethanol (EtOH)	VWR	153386F
Ethanolamine	Sigma-Aldrich	E9508
Ethylene diamine tetraacetic acid (EDTA)	Gerbu	1034
Fetal bovine serum (FBS)	Gibco	10500-084
Fetal bovine serum, dialized	Thermo Fisher	26400044
Fluoxetine	Sigma-Aldrich	F132
Fluphenazine	Sigma-Aldrich	F4765
Formaldehyde	AppliChem	A3592
Formic acid	J.T. Baker	6037
GE NHS magnetic beads	Sigma-Aldrich	GE28-9440-09
GlutaMAX	Thermo Fisher	35050061
Glutathione (reduced)	Sigma-Aldrich	G4251
Glycerol	Carl Roth	3783.1
Glycine	Carl Roth	3790.2
Glycolic acid	VWR	1041060100
Guanidine hydrochloride (GndHCl)	VWR	M110
Haloperidol	Sigma-Aldrich	H1512
Hoechst-33342	Invitrogen	H1399
Hydrochloric acid (HCl)	AppliChem	13378.1211
Hydroxylamine	Fluka	55460
Imidazole	Carl Roth	3899.2
Imipramine	Sigma-Aldrich	I7379
IncuCyte® Caspase-3/7 Green Reagent	EssenBio	4440

<b>Name</b>	<b>Supplier</b>	<b>Catalog number</b>
Iodoacetamide	AppliChem	A1666.0025
Iron(II) sulfate	Sigma-Aldrich	215422
L-687,384	Sigma-Aldrich	L8539
Lauryl maltose neopentyl glycol (LMNG)	Anatrace	NG310
Lys-C endoproteinase	Wako Chemicals	125-05061
LysoTracker Red DND-99	Thermo Fisher	L7528
MagReSyn TiO <sub>2</sub> microparticles	PELOBiotech	MR-TID005
MEM non-essential amino acids	PAN Biotech	P08-32100
Methanol (MeOH)	Sigma-Aldrich	32213
Milk powder, non-fat dry	AppliChem	A0830
MitoSOX Red	Thermo Fisher	M36008
MitoTracker Deep Red	Thermo Fisher	M22426
Monopotassium phosphate (KH <sub>2</sub> PO <sub>4</sub> )	Fisher Chemical	0240
N-acetylcysteine (NAC)	Sigma-Aldrich	A9165
NHS magnetic Sepharose beads	Sigma-Aldrich	GE28-9440-09
NP-40 alternative	Calbiochem	492016
PBS tablets	Jena Bioscience	AK-102P-L
PBS-based Odyssey® Blocking buffer	Li-COR Biosciences	927-40000
Penicillin / Streptomycin solution	PAN Biotech	P06-07100+
Pepstatin A	Sigma-Aldrich	P5318
Pierce™ NHS magnetic beads	Thermo Fisher	88826
Phalloidin/Alexa-568 solution	Thermo Fisher	A12380
PhosSTOP phosphatase inhibitors	Sigma-Aldrich	4906837001
Pierce NHS magnetic beads	Thermo Fisher	88827
Pimozide	Sigma-Aldrich	P1793
Piperazine-N,N'-bis(2-ethanesulfonic acid) (PIPES)	Sigma-Aldrich	P6757
Polysorbate 20 (Tween-20)	Sigma-Aldrich	P2287
Potassium chloride (KCl)	J.T. Baker	0509
Propidium iodide solution	Sigma-Aldrich	P4170
Protease inhibitor mix HP PLUS	Serva	39107.01
Rapamycin	Selleckchem	S1039
Sera-Mag™ SpeedBead™ Carboxylate-modified magnetic particles (hydrophilic)	GE Healthcare	45152105050250
Sera-Mag™ SpeedBead™ Carboxylate-modified magnetic particles (hydrophobic)	GE Healthcare	65152105050250
Sertraline	Sigma-Aldrich	S6319
Sodium acetate	J.T. Baker	0258
Sodium ascorbate	Sigma-Aldrich	A4034
Sodium chloride (NaCl)	VWR Chemicals	27810.295
Sodium dodecylsulfate (SDS)	Gerbu	1012



Name	Supplier	Catalog number
Sodium pyruvate solution	PAN Biotech	P04-43100
Staurosporine	Enzo	ALX-380-014-M001
SYTO 14	Thermo Fisher	S7576
Tamoxifene	Sigma-Aldrich	T5648
tert-butylhydroquinone (t-BHQ)	TCI	B0833
Tetramethylethylenediamine (TEMED)	Carl Roth	2367.3
TMT10plex™	Thermo Fisher	90110
Triethanolamine	Sigma-Aldrich	90279
Triethylammonium bicarbonate (TEAB) 1.0 M buffer	Sigma-Aldrich	T7408
Triethylene glycol diamine tetraacetic acid (EGTA)	VWR Chemicals	437013D
Trifluoroacetic acid (TFA)	Sigma-Aldrich	106232
Trifluoroethanol (TFE)	Fisher Scientific	10051560
Tris((1-hydroxy-propyl-1H-1,2,3-triazol-4-yl)methyl)amine (THPTA)	Sigma-Aldrich	762342
Tris(2-cyrcoxyethyl)phosphine) (TCEP)	Thermo Fisher	20491
Tris-HCl	Carl Roth	4855.2
Triton X-100	Serva	39795.02
Trypsin, recombinant	Sigma-Aldrich	3708969001
Trypsin/EDTA solution	PAN Biotech	P10-023100
Urea	J.T. Baker	0345
Wheat germ agglutinin/Alexa-555	Thermo Fisher	W11262
α-Tocopherol (α-Toc)	Sigma-Aldrich	T3251
β-mercaptoethanol (β-ME)	Serva	28625.01

#### 4.1.2 Buffers

Name	Composition
Affinity enrichment lysis buffer	50 mM PIPES, pH 7.4 50 mM NaCl 5 mM MgCl <sub>2</sub> 5 mM EGTA 0.1 % (v/v) NP-40 alternative (optional) 0.1 % (v/v) Triton X-100 (optional) 0.1 % (v/v) Tween-20 (optional) 0.1 % (v/v) β-ME
Affinity enrichment wash buffer	50 mM PIPES, pH 7.4 50 mM NaCl 75 mM MgCl <sub>2</sub> 5 mM EGTA 0.1 % (v/v) NP-40 alternative (optional) 0.1 % (v/v) Triton X-100 (optional) 0.1 % (v/v) Tween-20 (optional) 0.1 % (v/v) β-ME

<b>Name</b>	<b>Composition</b>
Fluorescence polarization buffer	20 mM HEPES, pH 7.5 150 mM NaCl 10 % (v/v) Glycerol 1 mM DTE 0.005 % (w/v) LMNG
In-gel digestion alkylation solution	55 mM Iodoacetamide 25 mM NH <sub>4</sub> HCO <sub>3</sub>
In-gel digestion digestion buffer	0.01 µg/mL Trypsin (proteomics grade) 25 mM NH <sub>4</sub> HCO <sub>3</sub>
In-gel digestion fixation solution	40 % (v/v) EtOH 10 % (v/v) Acetic acid
In-gel digestion reducing buffer	50 mM DTT 25 mM NH <sub>4</sub> HCO <sub>3</sub>
In-gel digestion wash buffer 1	25 mM NH <sub>4</sub> HCO <sub>3</sub> 25 % (v / v) Acetonitrile
In-gel digestion wash buffer 2	25 mM NH <sub>4</sub> HCO <sub>3</sub> 50 % (v / v) Acetonitrile
NHS blocking buffer A	0.5 M Ethanolamine 0.5 M NaCl pH 8.3
NHS blocking buffer B	0.1 M Sodium acetate 0.5 M NaCl pH 4.0
NHS coupling buffer	0.15 M Triethanolamine 0.5 M NaCl pH 8.3
PAL lysis buffer	PBS 0.4 % (v/v) NP-40 alternative 1 tablet / 10 mL cOmplete™ protease inhibitor cocktail
PAL wash buffer	4 M Urea 150 mM NaCl 0.5 % (v/v) SDS
Phosphate-buffered saline (PBS)	2.7 mM KCl 1.5 mM KH <sub>2</sub> PO <sub>4</sub> 136.9 mM NaCl 8.1 mM Na <sub>2</sub> HPO <sub>4</sub> pH 7.4
Phosphate buffer	27 mM KCl 15 mM KH <sub>2</sub> PO <sub>4</sub> 1.37 M NaCl 81 mM Na <sub>2</sub> HPO <sub>4</sub> pH 7.0
PBS-T	PBS 0.1 % (v/v) Tween-20
Phosphoproteomics digestion buffer	100 mM Ammonium bicarbonate 10 % TFE (v/v)
Phosphoproteomics loading buffer	1 M Glycolic acid 80 % (v/v) Acetonitrile 5 % (v/v) TFA

<b>Name</b>	<b>Composition</b>
Phosphoproteomics lysis buffer	6 M GndHCl 100 mM Tris-HCl, pH 8.5 10 mM TCEP 40 mM Chloroacetamide
Phosphoproteomics wash buffer 1	80 % (v/v) Acetonitrile 1 % (v/v) TFA
Phosphoproteomics wash buffer 2	10 % (v/v) Acetonitrile 0.2 % (v/v) TFA
Protein expression lysis buffer 1	20 mM HEPES, pH 7.5 250 mM NaCl 10 % (v/v) Glycerol 2 mM $\beta$ -ME 2 mM MgCl <sub>2</sub> DNAse I Protease inhibitor mix HP plus
Protein expression lysis buffer 2	20 mM HEPES, pH 7.5 250 mM NaCl 10 % (v/v) Glycerol 2 mM $\beta$ -ME 1 % (w/v) LMNG Protease inhibitor mix HP plus
Protein expression size exclusion buffer	20 mM HEPES, pH 7.5 150 mM NaCl 10 % (v/v) Glycerol 1 mM DTE 0.01 % (w/v) LMNG
Protein expression wash buffer 1	20 mM HEPES, pH 7.5 150 mM NaCl 10 % (v/v) Glycerol 2 mM $\beta$ -ME 5-10 mM Imidazole 0.1 % (w/v) LMNG
Protein expression wash buffer 2	20 mM HEPES, pH 7.5 150 mM NaCl 10 % (v/v) Glycerol 2 mM $\beta$ -ME 5-10 mM Imidazole 0.01 % (w/v) LMNG
SDB-RPS Equilibration buffer	30 % (v/v) MeOH 0.2 % (v/v) TFA
SDB-RPS Wash buffer	0.2 % (v/v) TFA
SDB-RPS Elution buffer	80 % (v/v) Acetonitrile 5 % (v/v) Ammonia
SDS running buffer (10x)	250 mM Tris-HCl 2.5 M Glycine 35 mM SDS

Name	Composition
SDS sample buffer (5x)	0.5 M Tris-HCl, pH 6.8 40 % (v/v) Glycerol 277 mM SDS 400 mM DTE 0.3 mM Bromophenol blue
SDS Separating gel buffer	1.5 M Tris-HCl, pH 8.8
SDS Stacking gel buffer	1.0 M Tris-HCl, pH 6.8
SOD assay lysis buffer	PBS 0.5 % (v/v) Triton-X 100 1 tablet / 10 mL cOmplete™ protease inhibitor cocktail
Stage-tip Elution buffer (buffer B)	80 % (v/v) Acetonitrile 0.1 % (v/v) formic acid
Stage-tip Wash buffer (buffer A)	0.1 % (v/v) Formic acid
TPP alkylation solution	200 mM TEAB 375 mM Iodoacetamide
TPP lysis buffer	PBS 0.4 % (v/v) NP-40 alternative
TPP reducing buffer	200 mM TEAB 200 mM TCEP
TPP tryptic digestion solution	100 mM TEAB 0.75 mM HCl 0.03 µg/mL Trypsin (proteomics grade)
Transfer buffer	25 mM Tris-HCl 188 mM Glycine 20 % (v/v) MeOH
Tris-buffered saline (TBS)	50 mM Tris-HCl 150 mM NaCl pH 7.5
TBS-T	TBS 0.1 % (v/v) Tween-20

#### 4.1.3 Cell culture media

Name	Supplements	Product number	Supplier
DMEM-based growth medium	10 % (v/v) FBS 1 mM sodium pyruvate 100 U/mL penicillin 0.1 mg/mL streptomycin MEM non-essential amino acids	P04-03550	PAN Biotech GmbH, Germany
DMEM-based growth medium (SILAC)	10 % (v/v) FBS 1 mM sodium pyruvate 100 U/mL penicillin 0.1 mg/mL streptomycin MEM non-essential amino acids 0.1 µg/mL <sup>12</sup> C <sub>6</sub> , <sup>14</sup> N <sub>2</sub> -L-lysine or <sup>13</sup> C <sub>6</sub> , <sup>15</sup> N <sub>2</sub> -L-lysine 0.1 µg/mL <sup>12</sup> C <sub>6</sub> , <sup>14</sup> N <sub>4</sub> -L-arginine or <sup>13</sup> C <sub>6</sub> , <sup>15</sup> N <sub>4</sub> -L-arginine	A33822	Thermo Fisher Scientific Inc., USA

Name	Supplements	Product number	Supplier
IMDM-based growth medium	10 % (v/v) FBS 100 U/mL penicillin 0.1 mg/mL streptomycin	P04-20150	PAN Biotech GmbH, Germany
MEM-based growth medium	10 % (v/v) FBS 1 mM sodium pyruvate 100 U/mL penicillin 0.1 mg/mL streptomycin MEM non-essential amino acids	P04-08500	PAN Biotech GmbH, Germany
Opti-MEM™		11058-021	Thermo Fisher Scientific Inc., USA
Sf-900™ III serum-free medium		12658019	Thermo Fisher Scientific Inc., USA
XF Assay Medium (DMEM)	25 mM glucose 2 mM GlutaMAX™	103335-100	Agilent Technologies Inc., USA

#### 4.1.4 Kits

Name	Supplier
Bio-Rad Protein Assay	Bio-Rad Laboratories, Inc., USA
Cathepsin D Inhibitor Screening Kit	BioVision, Inc., USA
Glutathione Assay Kit	Cayman Chemical, USA
Glyoxalase I Activity Assay Kit	BioVision, Inc., USA
GSH/GSSG-Glo™ Assay Kit	Promega Corporation, USA
MycoAlert™ mycoplasma detection kit	Lonza Group AG, Switzerland
Nano-Glo® Dual-Luciferase® Reporter Assay Kit	Promega Corporation, USA
Superoxide Dismutase Assay Kit	Cayman Chemical, USA
SuperSignal™ West Femto Maximum Sensitivity Substrate	Thermo Fisher Scientific Inc., USA
SuperSignal™ West Pico PLUS Chemiluminescent Substrate	Thermo Fisher Scientific Inc., USA

#### 4.1.5 Antibodies

Antigen	Origin	Supplier	Blocking	Dilution	Product number
CTSD	mouse	Thermo Fisher	LI-COR (PBS)	1:1000 (IB)	MA1-26773
GLO1	mouse	Santa Cruz	LI-COR (PBS)	1:1000 (IB)	sc-133214
mouse (680RD)	donkey	LI-COR		1:5000 (IB)	926-68072
mouse (800CW)	goat	LI-COR		1:5000 (IB)	926-32210
mouse (HRP)	goat	Thermo Fisher		1:10000 (IB)	Pierce 31430
NQO1	mouse	Santa Cruz	LI-COR (PBS)	1:100 (IB)	sc-271116
mTOR	rabbit	Cell Signal	LI-COR (PBS)	1:1000 (IB)	7C10
PPP2R1A	rabbit	Thermo Fisher	LI-COR (PBS)	1:250	703567
rabbit (680RD)	donkey	LI-COR		1:5000 (IB)	926-68073

Antigen	Origin	Supplier	Blocking	Dilution	Product number
rabbit (HRP)	goat	Thermo Fisher		1:10000 (IB)	Pierce 31460
SIGMAR1	mouse	Santa Cruz	LI-COR (PBS)	1:1000 (IB)	sc-166392
SOD1	mouse	Thermo Fisher	LI-COR (PBS)	1:1000 (IB)	MA1-105

IB = immunoblotting

#### 4.1.6 Plasmids

Name	Supplier	Backbone	Insert
pGL4.37[luc2P/ARE/Hygro]	Promega Corporation, USA	pGL4	luc2P/ARE/Hygro
pNL1.1TK[Nluc/TK]	Promega Corporation, USA	pNL1	Nluc/TK
pFL <sup>169</sup>	Imre Berger (University of Bristol)	pFL	His-6

#### 4.1.7 Cell lines

Name	Description	Culture conditions	Source
A549	Human lung carcinoma cells	DMEM-based growth medium, 5 % CO <sub>2</sub> , 37 °C	DSMZ GmbH, Germany
HAP-1 WT	Human chronic myelogenous leukemia cells	IMDM-based growth medium, 5 % CO <sub>2</sub> , 37 °C	Horizon Discovery Ltd., UK
HAP-1 SIGMAR1-K.O.	Human chronic myelogenous leukemia cells with SIGMAR1 knock-out	IMDM-based growth medium, 5 % CO <sub>2</sub> , 37 °C	Horizon Discovery Ltd., UK
HCT 116	Human colon carcinoma cells	DMEM-based growth medium, 5 % CO <sub>2</sub> , 37 °C	DSMZ GmbH, Germany
HeLa	Human cervix carcinoma cells	DMEM-based growth medium, 5 % CO <sub>2</sub> , 37 °C	DSMZ GmbH, Germany
MCF7	Human breast adenocarcinoma cells	DMEM-based growth medium, 5 % CO <sub>2</sub> , 37 °C	DSMZ GmbH, Germany
MDA-MB-231	Human breast carcinoma cells	DMEM-based growth medium, 5 % CO <sub>2</sub> , 37 °C	DSMZ GmbH, Germany
PANC-1	Human pancreas epithelioid carcinoma	DMEM-based growth medium, 5 % CO <sub>2</sub> , 37 °C	ATCC, Manassas, Virginia, USA
U-2 OS	Human osteosarcoma cells	DMEM-based growth medium, 5 % CO <sub>2</sub> , 37 °C	CLS Cell Lines Service GmbH, Germany

#### 4.1.8 Bacterial strains and insect cell lines

Name	Description	Source
One Shot OmniMAX™ 2 T1	<i>Escherichia coli</i>	Thermo Fisher Scientific Inc., USA
DH10EMBaCY	<i>Escherichia coli</i>	Imre Berger, University of Bristol
Sf9 cells	<i>Spodoptera frugiperda</i>	Thermo Fisher Scientific Inc., USA
BTI- <i>Tnao38</i>	<i>Trichoplusia ni</i>	Hashimoto <i>et al.</i> <sup>170</sup>

## 4.1.9 Devices

Description	Name	Supplier
Automated Fluorescence Microscope	Axiovert 200M	Carl Zeiss AG, Germany
	5810R	
	5417R	
Centrifuge	5424R	Eppendorf AG, Germany
	5430	
	Minispin	
Chromatography column	HisTrap HP	GE Healthcare GmbH, Germany
	HiLoad 16/600 Superdex 200 pg	
Chromatography system	ÄKTAprime Plus	GE Healthcare GmbH, Germany
Clean Bench	NU-437-400E	ibs tecnomara GmbH, Germany
	MSC-Advantage 1.2	Thermo Fisher Scientific Inc., USA
Extracellular Flux Analyzer	Seahorse XFp	Agilent Technologies Inc., USA
Fluorescence microscope	Observer Z1	Carl Zeiss AG, Germany
Gel and blot documentation system	ChemiDoc™ MP	Bio-Rad Laboratories, Inc., USA
Gradient thermal cycler	Mastercycler ep gradient	Eppendorf AG, Germany
High-content imaging system	Image Xpress XL	Molecular Devices, LLC, USA
HPLC-MS/MS system	LCQ Fleet	Thermo Fisher Scientific Inc., USA
Incubator	Nuair NU-5500E	Integra Biosciences Deutschland GmbH, Germany
	MCO-230AICUVH	PHC Europe B.V., Netherlands
	IPP-300	Memmert GmbH + Co. KG, Germany
Inverted microscope	DM IRB	Leica Microsystems GmbH, Germany
Liquid dispenser	Echo 520	Labcyte Inc., USA
Magnetic rack	MagRack6	GE Healthcare GmbH, Germany
Mass spectrometer	Q Exactive™ Plus	Thermo Fisher Scientific Inc., USA
	Q Exactive™ HF Hybrid Quadrupole-Orbitrap	
Nano-HPLC system	Ultimate™ 3000 RSLC nano-HPLC system	Thermo Fisher Scientific Inc., USA
Plate reader	Infinite M200	Tecan Group AG, Switzerland
	Spark	
	Envision	PerkinElmer, Inc., USA
Plate shaker	Monoshake	Thermo Electron LED GmbH, Germany
Precision scale	Analytical Plus	Sartorius AG, Germany

Description	Name	Supplier
Real-time live-cell analyzer	IncuCyte ZOOM	Sartorius AG, Germany
	IncuCyte S3	
Roll mixer	TRM 50	IDL GmbH & Co KG, Germany
Sample rotator	SB3	Cole-Parmer, UK
Spectrophotometer	Nanodrop 2000c	Thermo Fisher Scientific Inc., USA
Thermomixer	Comfort 1.5 mL	Eppendorf AG, Germany
Tip centrifuge	Tomy mini personal	Sonation GmbH, Germany
UHPLC-MS/MS system	VelosPro	Thermo Fisher Scientific Inc., USA
Ultracentrifuge	Optima™ MAX-XP	Beckman Coulter Inc., USA
UV irradiation system	BLX-365	Vilber Lourmat Deutschland GmbH, Germany
Vacuum concentrator	Concentrator plus	Eppendorf AG, Germany

#### 4.1.10 Software

Description	Name	Supplier
Chemical analysis software	ChemDraw	PerkinElmer, Inc., USA
Data analysis software	Prism	GraphPad Software, USA
	Excel	Microsoft Corporation, USA
Extracellular flux analyzer software	Wave Desktop	Agilent Technologies Inc., USA
Gel / Immunoblot analysis software	ImageLab	Bio-Rad Laboratories, Inc., USA
Image analysis software	Fiji ImageJ	<i>Open source</i> <sup>167</sup>
	CellProfiler	<i>Open source</i> <sup>168</sup>
Live-cell imaging system software	IncuCyte ZOOM	Sartorius AG, Germany
	IncuCyte S3	
Mass spectrometry analysis software	Xcalibur	Thermo Fisher Scientific Inc., USA
Microscopy & image analysis software	ZEN	Carl Zeiss AG, Germany
	MetaMorph	Visitron Systems GmbH, Germany
	MetaXpress	Molecular Devices, LLC, USA

#### 4.1.11 Consumables

Name	Supplier
384-well plate, black, flat bottom	Greiner Bio-One, Germany
384-well plate, black, flat, clear bottom	Greiner Bio-One, Germany
384-well plate, clear, flat bottom	Greiner Bio-One, Germany
3M™ Empore™ high performance extraction disks, C18	3M Bioanalytical Technologies
3M™ Empore™ extraction disks, SDB-RPS	3M Bioanalytical Technologies



<b>Name</b>	<b>Supplier</b>
6-well plate, clear, flat bottom	Sarstedt AG & Co, Germany
96-well plate, black, clear flat bottom	Corning Inc., USA
96-well plate, black, non-binding	Greiner Bio-One, Germany
96-well plate, clear, conical bottom	Sarstedt AG & Co, Germany
96-well plate, clear, flat bottom	Sarstedt AG & Co, Germany
96-well plate, clear, flat bottom, UV-transparent	Santa Cruz Biotechnology Inc., Germany
96-well plate, white, flat, clear bottom	Corning Inc., USA
Cannula, G30 0.3 x 13 mm	Terumo Deutschland GmbH, Germany
Cell culture dish, 10 cm / 15 cm	Sarstedt AG & Co, Germany
Cell culture flask T25 / T75 / T175	Sarstedt AG & Co, Germany
Cell scraper	Corning Inc., USA
Cryovials	VWR International GmbH, Germany
Micro reaction tube, 0.5 mL / 1.5 mL / 2.0 mL	Sarstedt AG & Co, Germany
Micro reaction tube, 1.5 mL / 2.0 mL / 5.0 mL, protein low-binding	Eppendorf AG, Germany
Parafilm® M	Bemis Company Inc., USA
Pipette tips, 10 µL	Sarstedt AG & Co, Germany
Pipette tips, 10 µL / 20 µL / 100 µL / 1000 µL, protein low-binding	Sorenson Bioscience Inc., USA
Pipette tips, 100 µL / 1000 µL	Diagonal GmbH & Co. KG, Germany
Polycarbonate ultracentrifugation tubes, 0.5 µL	Beckman Coulter Inc., USA
Polyvinylidene difluoride (PVDF) membrane	Merck KGaA, Germany
Sample tube, 15 mL / 50 mL	Sarstedt AG & Co, Germany
Seahorse XFe96 or XFp cell culture microplates	Agilent Technologies Inc., USA
Seahorse XFe96 or XFp sensor cartridges	Agilent Technologies Inc., USA
Serological pipette, 1 mL / 5 mL / 10 mL / 25 mL	Sarstedt AG & Co, Germany
Syringe, 1 mL	B. Braun Melsungen AG, Germany
Whatman® 3MM filter paper	Whatman GmbH, Germany

## 4.2 Methods

### 4.2.1 Cell culture methods

#### 4.2.1.1 Cell culture and cell seeding

For long-term cultivation, cell lines were incubated in a 37 °C humidified atmosphere with 5 % CO<sub>2</sub>. Cell lines were grown in the respective growth medium until cells were approximately 80-90 % confluent. For subcultivation, the medium was removed, cells were washed with prewarmed PBS, followed by the addition of trypsin/EDTA (2 mL for T75, 4 mL for T175 flasks) and a subsequent 4-minute incubation at 37 °C and 5 % CO<sub>2</sub>. Afterwards, 8 or 16 mL of growth medium was added to a T75 or T175 cell culture flask, respectively, and the cell suspension was transferred into a 50 mL falcon tube.

To assess the cell number, 10 µL of cell suspension were transferred into a slot of a *Neubauer improved* cell counting chamber. Cells were counted under an inverted light microscope with 10x magnification. For seeding of cells into cell culture plates or dishes, or for further cultivation in cell culture flasks, the cell suspension was diluted with growth medium to the desired cell number and an appropriate volume of the suspension was transferred into the respective culturing vessel. All cells cultured were tested monthly for mycoplasma infections, using the MycoAlert™ Mycoplasma Detection Kit according to the protocol of the manufacturer.

#### 4.2.1.2 Cyro-conservation of cells

Cells were cryo-conserved for long-term maintenance of cell lines. Cryovials containing 50 µL DMSO were prepared and 1 mL of cell suspension of approximately  $5 \times 10^5$  cells was added and mixed. The cryovials were transferred into a freezing container, which was stored at -80 °C overnight, before placing the vials into the vapor phase of a liquid nitrogen tank for long-term storage.

To thaw cryo-conserved cells, a T75 flask containing 25 mL of prewarmed growth medium was prepared. Frozen aliquots were thawed quickly in a 37 °C water bath and the cell suspension was immediately transferred into the prepared flask. Incubation at 37 °C and 5 % CO<sub>2</sub> in a humidified incubator overnight allowed attachment of cells to the surface of the flask. Subsequently, the medium was exchanged for fresh, prewarmed growth medium and cells were cultured as described.

#### 4.2.1.3 Image-based cellular ROS accumulation assays

For the general detection of cellular ROS accumulation induced by compounds, 5'/6'-chloromethyl-2'-7'-dichlorodihydrofluorescein diacetate (CM-H<sub>2</sub>DCFDA) was used, which is a cell-permeable, non-fluorescent derivative of fluorescein. In cells, CM-H<sub>2</sub>DCFDA is deacetylated by cellular esterases and its chloromethyl moiety readily reacts with cellular thiols, both facilitating a high cellular retention. In the presence of various ROS, this indicator dye gets oxidized, thereby yielding 2'-7'-dichlorofluorescein, whose fluorescent properties allow to estimate cellular ROS levels by means of fluorescence microscopy.

For this assay, the respective number of cells (Table 2) was seeded in 100  $\mu$ L of growth medium in a black 96-well cell culture plate with clear flat bottom and incubated at 37 °C and 5 % CO<sub>2</sub> overnight to allow attachment of cells. For HAP1 cells, plates were coated with poly-L-lysine solution according to the manufacturer's protocol prior to seeding to increase cell adhesion. The supernatant was exchanged for 100  $\mu$ L of compound-containing growth medium and cells were incubated for 1 h at 37 °C and 5 % CO<sub>2</sub>. For long-term treatments, cells were incubated with the compounds for 24 - 72 h. Afterwards, the medium was exchanged for supplement-free growth medium containing the respective concentration of CM-H<sub>2</sub>DCFDA and 5  $\mu$ g/mL Hoechst-33342, which is a cell-permeable DNA-intercalating dye allowing the visualization of cell nuclei. After 30 min of incubation at 37 °C and 5 % CO<sub>2</sub>, cells were partially fixed in 0.5 % formaldehyde in PBS for 10 min at ambient temperature in the dark. Cells were washed thrice with 100  $\mu$ L PBS, followed by a final addition of 100  $\mu$ L PBS for image acquisition. For determination of the minimal compound treatment time, cells were stained first, then compounds were added to the cells over a 1 h time course in 5-10 min intervals, followed by fixation and washing steps as described before.

**Table 2: Seeding densities and ROS indicator concentrations used for CM-H<sub>2</sub>DCFDA-based assays.**

Cell line	Seeding density [cells/well]	Dye concentration [ $\mu$ M]
HeLa	1.5 x 10 <sup>4</sup>	5
U-2 OS	1.0 x 10 <sup>4</sup>	2.5
HAP1 WT	4.0 x 10 <sup>4</sup>	1
HAP1 S1R KO	3.0 x 10 <sup>4</sup>	1

Cells were imaged immediately in an automated fashion using an automated fluorescence microscope at 10x magnification in combination with the MetaMorph 7.7.8.0 software. The fluorescence of Hoechst-33342 and CM-H<sub>2</sub>DCFDA was recorded in the DAPI or FITC channel, respectively. For each

well, four images were acquired, using the DAPI channel for focusing. The acquired images were analyzed using the 'Multi wavelength cell scoring' function of the MetaMorph software, which determines the integrated intensity of the CM-H<sub>2</sub>DCFDA staining per cell. The obtained values were averaged per image and the obtained values were again averaged for all four images acquired per well. Each treatment condition was tested in technical quadruplicates, including control cells that were treated with DMSO or 10  $\mu$ M of 1-chloro-2,4-dinitrobenzene (CDNB). The obtained staining intensity values were normalized to values of the DMSO (= 0 %) and the CDNB (= 100 %) control. For the determination of the half-maximal effective concentration (EC<sub>50</sub>), normalized intensity values were plotted against various compound concentrations using GraphPad Prism. A non-linear regression with a four-parameter fit was performed and the EC<sub>50</sub> values were determined by extrapolation of the compound concentration causing 50 % of the normalized integrated staining intensity.

#### **4.2.1.4 Image-based mitochondrial superoxide assay**

To detect the accumulation of mitochondrial superoxide in cells, the indicator dye MitoSOX Red was used. This indicator is a dihydroethidium derivative carrying a triphenylphosphonium moiety, which facilitates its accumulation in the mitochondria. Like dihydroethidium, MitoSOX Red is a non-fluorescent compound, which can be oxidized by superoxide, yielding the fluorescent 2-hydroxyethidium.

For this assay,  $1.5 \times 10^4$  HeLa cells were seeded into black 96-well cell culture plates with clear bottom and incubated at 37 °C and 5 % CO<sub>2</sub> overnight. The supernatant was exchanged for prewarmed growth medium without supplements containing 5  $\mu$ M MitoSOX Red and 5  $\mu$ g/mL Hoechst-33342 and cells were incubated for 30 min at 37 °C and 5 % CO<sub>2</sub>. Afterwards, the staining medium was exchanged for compound- containing growth medium, followed by 1 h of incubation at 37 °C and 5 % CO<sub>2</sub>. Afterwards cells were fixed and washed, using the same procedure as for the CM-H<sub>2</sub>DCFDA-based assay. Data analysis was performed as described above.

#### 4.2.1.5 Flow cytometry-based cellular ROS accumulation assays

*These experiments were performed by Mingyang Lu under the supervision of Prof. Dan Yang, University of Hong Kong.*

To further investigate which reactive species are formed upon compound treatment, a set of reactive oxygen species-selective fluorescent ROS indicators were used in a flow cytometry-based assay (Table 3).

**Table 3: Overview on ROS indicators selective for different reactive oxygen species.**

ROS indicator	Reactive species detected	Dye concentration [ $\mu\text{M}$ ]
HKSOX-1r <sup>171</sup>	O <sub>2</sub> <sup>•-</sup> (cytosolic)	2 $\mu\text{M}$
HKSOX-1m <sup>171</sup>	O <sub>2</sub> <sup>•-</sup> (mitochondrial)	2 $\mu\text{M}$
HKSOX-2L <sup>172</sup>	O <sub>2</sub> <sup>•-</sup> (lysosomal)	2 $\mu\text{M}$
HKGreen-4 <sup>173</sup>	ONOO <sup>-</sup>	5 $\mu\text{M}$
HKPeroX-1 <sup>174</sup>	H <sub>2</sub> O <sub>2</sub>	10 $\mu\text{M}$

HeLa cells were seeded and incubated at 37 °C and 5 % CO<sub>2</sub> overnight. Cells were treated with compounds for 1 h, washed with HBSS and incubated with the respective indicator for 30 min at 37 °C and 5 % CO<sub>2</sub>. Cells were washed with PBS, detached via trypsination, collected and analyzed via flow cytometry. For calculation of fold changes, fluorescence values were normalized to values obtained from untreated cells (= 1). For EC<sub>50</sub> determination, values were normalized to values from untreated cells (= 0%) and cells treated with 10  $\mu\text{M}$  CDNB (= 100%). EC<sub>50</sub> values were calculated as described in chapter 4.2.1.3.

#### 4.2.1.6 Real-time live-cell analysis

To monitor the influence of compounds on cell growth and viability, real-time live-cell analysis was performed using the IncuCyte ZOOM and IncuCyte S3 devices, which were located in a cell culture incubator with 37 °C and 5 % CO<sub>2</sub> and humidified atmosphere. Cells were seeded with respective density (Table 4) into clear 96-well cell culture plates and incubated in an IncuCyte device and monitored via phase-contrast imaging in a 2-hour interval at 10 x magnification overnight. Seeding medium was exchanged for compound-containing medium and monitoring was continued for 48 h. Optionally, the compound-containing medium was additionally supplemented with 25  $\mu\text{M}$  of propidium iodide to detect loss of cell membrane integrity or 5  $\mu\text{M}$  Caspase-3/7 reagent to detect apoptosis. Cells were then additionally imaged in the red or green fluorescent channel, respectively.

**Table 4: Seeding densities for IncuCyte-based real-time live-cell analysis for 48 h compound incubation.**

Cell line	Seeding density [cells/well]	IncuCyte device
HeLa	$4.0 \times 10^3$	ZOOM / S3
U-2 OS	$4.0 \times 10^3$	S3
MCF-7	$1.0 \times 10^4$	S3
PANC-1	$6.0 \times 10^3$	S3
A549	$3.0 \times 10^3$	S3
HCT 116	$7.5 \times 10^3$	ZOOM

Images were analyzed using the respective IncuCyte analysis software. Cellular confluence was determined from the phase-contrast images as a measure of cell growth. The number of cell membrane integrity loss or apoptosis events was derived from the respective fluorescent images. The half-maximal inhibitory concentration (IC<sub>50</sub>) for cytotoxicity was determined by normalizing all end-point confluence values to the value for control cells treated with DMSO (= 100 %), using non-linear regression curve fit with four parameters using GraphPad Prism.

#### 4.2.1.7 Spheroid cell culture

To test the effects of compounds on cell growth or viability in a three-dimensional culturing model, spheroids were generated using the 'forced floating method'. For this,  $2.5 \times 10^3$  A549 or HCT 116 cells were seeded in each well of a 96-well ultra-low attachment cell culture plate and incubated in the presence of 25  $\mu$ M propidium iodide in the IncuCyte S3 device for 72 h to monitor spheroid formation in the bright-field and red fluorescent channel. For compound treatment, half of the seeding medium was exchanged for compound in propidium iodide-containing growth medium and spheroids monitored in the IncuCyte S3 for 72 h. For data analysis, the red integrated fluorescence intensity of each spheroid was determined and normalized to the size of each spheroid directly before the compound addition. Misshaped spheroids were excluded from the analysis.

#### 4.2.1.8 Extracellular flux assay

*Parts of these experiments were performed by Dr. Yushi Futamura, co-worker of Prof. Hiroyuki Osada, RIKEN CSRS, Japan, using an XFe96 analyzer. All other experiments of this kind were performed at the Max Planck Institute Dortmund using an XFp analyzer.*

To determine the influence of compounds on glycolysis and mitochondrial respiration, 'Mito Stress Test' assays using the Seahorse XFe96 or XFp analyzer were performed. On the day prior to the assay,

10,000 HeLa cells were seeded in into each well of an XFe96 or XFp cell culture plate, including two wells filled with growth medium as background control. Outer moats of the plate were filled with PBS to minimize medium evaporation. Cells were incubated overnight at 37 °C and 5 % CO<sub>2</sub>. XFe96 or XFp sensor cartridges were hydrated with XF calibrant and incubated at 37 °C overnight.

Growth medium was exchanged for prewarmed assay medium and cells were incubated at 37 °C for 45-60 min. XF assay medium was prepared freshly and used for suitable dilutions of compounds, oligomycin, FCCP and rotenone / antimycin A. The injection ports of the sensor cartridges were loaded with compound dilutions and subjected into the XFe96 or XFp analyzer for calibration. Afterwards the cell plate was loaded into the device for the 'Mito Stress Test' assay.

The device measured the oxygen consumption rate (OCR) and extracellular acidification rate (ECAR) every 6 min with a total of 24 measuring intervals. After the first 5 intervals, the compounds were injected, followed by 10 measurement intervals. Sequentially, oligomycin, FCCP and rotenone / antimycin A were injected followed by 3 measuring intervals each. Data were background-subtracted and normalized to the last value before compound injection.

For each well, the obtained data were background-subtracted by subtracting the value of the first measurement after the injection of rotenone and Antimycin A. Then, the degree of mitochondrial respiration was calculated by dividing the value of the last measurement before the Oligomycin injection (60 min after test compound injection) by the value of the last measurement before the test compound injection (baseline), multiplied by 100. Data were averaged over all technical replicates and normalized to values from cells treated with DMSO. For the determination of IC<sub>50</sub> values, data were plotted against various compound concentrations and a non-linear regression with a four-parameter fit was performed using GraphPad Prism.

#### **4.2.1.9 NRF2-dependent reporter gene assay**

To assess the influence of compounds on the NRF2-driven expression of proteins involved in the cellular antioxidant response, an antioxidant response element (ARE) reporter gene assay was performed. For this, cells were transfected with the pGL4.37 [Luc2P/ARE/Hygro] plasmid, which encodes a firefly luciferase under the control of four ARE sites, and with the pNL1.1TK [Nluc/TK] plasmid, which encodes the NanoLuc® luciferase under the control of a constitutive HSV-thymidine kinase promoter.

For transfection, 1.5 µg pGL4.37 [Luc2P/ARE/Hygro] DNA and 75 ng pNL1.1TK [Nluc/TK] DNA were mixed with 7.9 µL of Fugene HD transfection reagent in OptiMEM with a total volume of 500 µL. This mixture was incubated at ambient temperature for 30 min. HeLa cells were harvested via trypsination, as described in chapter 4.2.1.1, and the cell suspension was centrifuged at 200 x g for 5 min prior to removal of the supernatant and resuspension in growth medium. After a 30-minute incubation, 10<sup>6</sup> cells in 10 mL growth medium were added to the transfection mixture and mixed carefully by pipetting. Cells were seeded into clear 96-well plates with 100 µL cell suspension per well (approximately 10<sup>4</sup> cells), including a row of non-transfected cells, and monitored with the IncuCyte ZOOM device over 24 h. Supernatants were discarded, 70 µL of prewarmed growth medium containing compounds was added and live-cell-monitoring was continued for 23 h.

The activities of firefly and NanoLuc® luciferases were determined using the Nano-Glo® Dual-Luciferase® Reporter assay kit, according to the manufacturer's instructions. The cell plate was equilibrated to ambient temperature for 1 h. To each well, 70 µL of ONE-Glo™ EX solution was added followed by a 3-minute incubation on an orbital shaker at ambient temperature and subsequent luminescence read-out using the Tecan Spark plate reader. Afterwards, 70 µL of NanoDLR™ Stop & Glo solution was added to each well. The plate was incubated on an orbital shaker for 10 min at ambient temperature, followed by luminescence measurement. Each luminescence value was background-subtracted before calculating the ratio of the firefly to NanoLuc® luciferase signal for each well. Mean values of technical replicates were normalized to values of transfected, cells treated with DMSO to obtain fold-change values.

#### 4.2.1.10 Autophagy assays

*These experiments were performed by COMAS, Dortmund.*

To measure autophagy-inhibitory properties of compound, 4,000 eGFP-LC3-expressing MCF7 cells/well were seeded into black 384-well plates with clear bottom in 25 µL medium and incubated overnight at 37 °C and 5 % CO<sub>2</sub>. Cells were washed with PBS thrice by means of a plate washer. After aspirating the supernatant, 25 nL of compound were added, using an acoustic dispenser. Autophagy was induced by addition of 25 µL of either medium containing 100 nM rapamycin and 50 µM chloroquine ('rapamycin-induced autophagy') or EBSS containing 50 µM chloroquine ('starvation-induced autophagy'). After incubation for 3 h at 37 °C and 5 % CO<sub>2</sub>, 25 µL of 7.5 % formaldehyde in PBS (v/v)



containing 2 µg/mL Hoechst-33342 were added and cells were incubated at ambient temperature in the dark for 20 min. Cells were washed thrice with PBS and imaged using a high-content imaging system at 20x magnification. The number of fluorescent eGFP-LC3 punctae per cell was quantified using the MetaXpress Software. Data were normalized to values of cells treated with DMSO (= 0 %).

To detect induction of autophagy, the same assay procedure was used, but compound incubation was carried out either in cell culture medium optionally containing 50 µM chloroquine.

#### **4.2.1.11 Lysosomotropy assay**

To determine whether compounds accumulate in the lysosomes, a lysosomotropy assay, using the lysosomotropic dye LysoTracker Red DND-99, was performed. 7,500 HeLa cells/well were seeded into black 96-well plates with clear bottom and incubated overnight at 37 °C and 5 % CO<sub>2</sub>. The growth medium was exchanged for medium containing the compounds. Cells were incubated for 1 h at 37 °C and 5 % CO<sub>2</sub>. Afterwards, growth medium containing LysoTracker Red DND-99 and Hoechst-33342 was added, yielding final concentrations of 500 nM and 5 µg/mL, respectively. Cells were incubated for 30 min at 37 °C and 5 % CO<sub>2</sub>. Subsequently, cells were washed thrice with PBS and fixed in 4 % paraformaldehyde for 5 min at ambient temperature. Cells were imaged using an automated fluorescence microscope at 10x magnification. Image analysis was performed using CellProfiler.<sup>175</sup> Cells were identified via the nuclear Hoechst-33342 staining and the LysoTracker Red DND-99 staining intensity was quantified per cell and averaged per image and well. The obtained values were normalized to the value for cells treated with DMSO (=100 %).

## **4.2.2 Phenotypic screening methods**

*All experiments described in this chapter were performed by COMAS, Dortmund.*

### **4.2.2.1 Phenotypic screen for inducers of cellular ROS accumulation**

To identify novel, fast-acting inducers of cellular reactive oxygen species accumulation, a phenotypic screening based on the assay using CM-H<sub>2</sub>DCFDA described in chapter 4.2.1.3 was performed. For this, 2 x 10<sup>3</sup> U-2 OS cells were seeded in 25 µL growth medium into black 384-well cell culture plates with clear bottom and incubated for 24 h at 37 °C and 5 % CO<sub>2</sub>. Screening compounds were directly added into the seeding medium using an acoustic dispenser, followed by 30 min of incubation at 37 °C and 5 % CO<sub>2</sub>. 25 µL of growth medium containing 2.5 µM CM-H<sub>2</sub>DCFDA and 5 µg/mL Hoechst-33342

were added and cells were incubated for 60 min at 37 °C and 5 % CO<sub>2</sub>. Subsequently, cells were fixed and washed as described in chapter 4.2.1.3. ROS accumulation was assessed either by fluorescence intensity measurement using the Envision plate reader or by image acquisition at 10 x magnification with a high-content imaging system with FITC and DAPI filter sets. Images were analyzed via the MetaXpress software to quantify the CM-H<sub>2</sub>DCFDA fluorescence per cell. Percentage of positively stained cells ('Imaging positive' read-out) was determined. Data were normalized as described in chapter 4.2.1.3.

#### **4.2.2.2 Counter-screens for fluorescent and dye-reactive compounds**

As compounds with fluorescent properties similar to dichlorofluorescein (DCF), cannot be discriminated from those that actually induce cellular ROS accumulation, all hit compounds were subjected to a counter-screen. This assay was performed as described in chapter 4.2.2.1 without the addition of CM-H<sub>2</sub>DCFDA to the staining medium. If a green fluorescence signal was detected by the Envision plate reader, the respective compound was excluded from the screening procedure.

Reactive compounds may oxidize CM-H<sub>2</sub>DCFDA directly, without inducing ROS in cells. Thus, all compounds were subjected to a counter-screen to test their reactivity with CM-H<sub>2</sub>DCFDA. The assay was performed as described in chapter 4.2.2.1, however in the absence of cells. Compounds with respective fluorescence properties were excluded from the screening procedure.

#### **4.2.2.3 Counter-screen for cellular glutathione depletion**

Small molecules might induce cellular ROS accumulation by directly reacting with cellular glutathione (GSH), thereby decreasing the cellular antioxidant pool. To exclude GSH-reactive compounds, all screening hits were subjected to a counter-screen that monitors total cellular GSH levels, using the GSH/GSSG-Glo assay kit. For this assay, 2 x 10<sup>3</sup> U-2 OS cells were plated into white 384-well cell culture plates and incubated at 37 °C and 5 % CO<sub>2</sub> for 24 h. Compounds were added using an acoustic dispenser and cells were incubated for 2 h at 37 °C and 5 % CO<sub>2</sub>. The total glutathione content was determined according to the manufacturer's protocol. For this, Luciferin-NT and passive lysis buffer were mixed and added to the cells. To facilitate cell lysis, plates were shaken for 5 min using a plate shaker. Afterwards, the 'Luciferin Generation Reagent' containing DTT, Glutathione-S-Transferase and a reaction buffer were mixed and added to the cells, followed by a 30-minute incubation step at ambient

temperature. After addition of the 'Luciferin Detection Reagent', the lysates were incubated for another 20 min at ambient temperature and subsequently the luminescence of each sample was measured using a Envision plate reader. The data obtained were normalized to the value for control cells treated with DMSO (= 100 %). Compounds decreasing the amount of total cellular glutathione by  $\geq 8.5$  % were excluded from the screening procedure.

#### 4.2.2.4 Screen for cell membrane-rupturing compounds

*Real-time live-cell analysis was performed at the MPI Dortmund.*

Immediate cytotoxic effects of compounds, which e.g. can be caused by cell-membrane rupture, were detected by using propidium iodide, a membrane-impermeable DNA intercalator. 1000 U-2 OS cells per well were seeded in 20  $\mu$ L growth medium into black 384-well plates with clear bottom and incubated overnight at 37 °C and 5 % CO<sub>2</sub>. Compounds were added by means of an acoustic dispenser and 5  $\mu$ L growth medium containing propidium iodide was added, yielding a final concentration of 25  $\mu$ M propidium iodide. Cells were monitored using the IncuCyte ZOOM device with a two-hour interval, acquiring both phase contrast and red fluorescent images, as described in chapter 4.2.1.6.

### 4.2.3 Target identification methods

#### 4.2.3.1 Affinity enrichment via photocrosslinked small-molecule affinity matrix

*Compound immobilization was performed by Yasumitsu Kondoh, co-worker of Prof. Hiroyuki Osada, RIKEN CSRS, Japan.*

For immobilization of a compound on photo-crosslinking beads, 1 mM compound solution in MeOH was prepared, mixed with beads and subsequently dried in a vacuum concentrator. Subsequently, the beads were irradiated at 365 nm (4 J/cm<sup>2</sup>) and washed once each with 50 % MeOH in H<sub>2</sub>O (v/v), MeOH, DMSO and thrice with MeOH. Beads were dried, resuspended in PBS and stored at 4 °C until further usage. To identify protein targets of a small molecule, active and inactive derivatives were immobilized to obtain beads carrying either a bioactive small molecule ('active beads') or a biologically inactive chemical analog ('inactive beads').

For lysate preparation, HeLa cells were grown in 15-cm cell culture dishes until 80-90 % confluence, washed with PBS and harvested using a cell scraper. Cells were collected at 350 x g for 3 min, supernatant was removed and cells were resuspended in 1 mL of PBS and transferred into a 1.5 mL

low-binding micro reaction tube. Cells were centrifuged at 1,000 x g for 5 min, supernatant was removed and cells were resuspended in 1 mL of affinity enrichment lysis buffer, followed by two 10-second ultrasonication treatments on ice. The lysate was centrifuged for 20 min at 12,000 x g at 4 °C and the supernatant was transferred into a fresh low-binding tube. Protein concentration was determined via the Bradford method, as described in chapter 4.2.5.1. Lysates were diluted with lysis buffer to a final concentration of 5 mg/mL, snap-frozen and stored at -80 °C until further usage.

For the binding reaction, 30 µL of bead slurry was transferred into a low-binding micro reaction tube, shortly centrifuged and the supernatant was discarded. Beads were washed twice with PBS before the addition of 200 µL of lysate (1 mg protein per sample). Binding reactions were performed at 4 °C for 2 h in a sample rotator. Beads were washed twice with affinity enrichment wash buffer and twice with PBS for 10 min each at 4 °C. After removal of the supernatant, an on-bead digestion was performed as described in chapter 4.2.3.2.

#### **4.2.3.2 On-bead digestion**

Proteins enriched on beads were denatured and disulfide bonds were reduced by addition of 8 M urea in 50 mM Tris-HCl, pH 7.5 containing 1 mM 1,4-dithiothreitol and incubation at ambient temperature for 30 min. To alkylate cysteine residues, chloroacetamide was added to a final concentration of 5 mM followed by 30 min of incubation at ambient temperature in the dark. Afterwards, 1 µg of endoproteinase Lys-C was added and samples were incubated for 1 h at 37 °C and 350 rpm. The supernatants of each sample were transferred into fresh low-binding micro reaction tubes. Beads were incubated with 1 µg of trypsin in 50 mM Tris-HCl (pH 7.5) per sample for 1 h at 37 °C and 350 rpm. Both Lys-C- and trypsin-containing supernatants of each sample were pooled, thereby lowering the urea concentration below 2 M. Another 2 µg of trypsin were added and samples were incubated at 37 °C overnight. The digestion was terminated by addition of 2 µL of TFA, prior to the Stage-tip purification and Nano-HPLC-MS/MS analysis.

#### **4.2.3.3 Stage-tip purification and proteomics analysis**

Approximately 1 mm discs of C18 chromatography matrix were placed into 200 µL pipette tips. The matrix was rinsed consecutively with 100 µL each of MeOH, stage-tip buffer B and stage-tip buffer A (twice), followed by centrifugation in a tip centrifuge after each addition. The first half of the peptide

samples were added into the tips, allowing the C18 matrix to be soaked, followed 1 min of incubation at ambient temperature. The tips were centrifuged and the flow-through was discarded. This procedure was repeated for the second half of the sample. The peptide-loaded matrix was washed once with 100  $\mu$ L of stage-tip buffer A. Peptides were eluted twice with 20  $\mu$ L of stage-tip buffer B, the eluate was collected in low-binding micro reaction tubes and dried in a vacuum concentrator.

*The following sample preparation, HPLC-MS/MS measurements and data analysis were performed by co-workers of the HRMS facility of the MPI Dortmund.*

For further analysis, the dried peptides were dissolved in aqueous 0.1 % (v/v) trifluoroacetic acid and applied onto a nano-HPLC-MS/MS. After chromatographic separation with a C18 PepMap 100 column, the peptides were subjected to mass spectrometry to acquire full mass spectra ( $m/z$  300 to 1650), and subsequent data-dependent high energy dissociation (HCD) MS/MS scans.

Proteins were identified and quantified via database matching of a human reference proteome (Uniprot database) and a contaminant database, which is part of the MaxQuant software.<sup>176</sup> Subsequent data mining was performed using the Perseus software.<sup>177</sup> This analysis was performed separately for each independent experiment. Proteins that were significantly enriched by 'active beads' over 'inactive beads' in both independent experiments were regarded as putative binding partners of the bioactive small molecule probe.

#### **4.2.3.4 Affinity enrichment via alkyne agarose beads**

For immobilization of azide-containing probes on alkyne agarose beads, alkyne beads with a total binding capacity of approximately 3.5  $\mu$ mol (175  $\mu$ L of slurry) were washed thrice with PBS and subsequently incubated in phosphate buffer containing 175 nmol chemical probe (approximately 5 % of the bead capacity), 0.1 mM  $\text{CuSO}_4$ , 0.5 mM Tris((1-hydroxy-propyl-1H-1,2,3-triazol-4-yl)methyl)amine (THPTA), 5 mM of aminoguanidine and 5 mM of sodium ascorbate for 1 h at ambient temperature in a sample rotator. Afterwards, the beads were washed thrice with PBS, resuspended in PBS and stored at 4 °C.

HeLa cell lysates were prepared by growing cells in four T175 cell culture flasks until 80-90 % confluence. Cells were washed with PBS and incubated in cell dissociation solution for 30 min at 37 °C and 5 %  $\text{CO}_2$ . Cell suspensions were collected in 50 mL falcon tubes and centrifuged at 350 x g for 5 min to collect the cells. After removing the supernatant, cells were resuspended in 1 mL PBS and

transferred into two 1.5 mL low-binding micro reaction tubes. Cells were collected via centrifugation at 1,000 x g for 5 min, followed by removal of the supernatant. Cells were resuspended in 500  $\mu$ L of lysis buffer. In case of detergent-containing lysis buffer, the cells were incubated on ice for 20 min. If detergent-free buffer was used, the cell suspension was subjected to three freeze-thaw cycles. Afterwards cellular debris was removed via centrifugation at 12,000 x g at 4 °C for 20 min. Supernatants were transferred into a 1.5 mL low-binding micro reaction tube and subjected to a protein concentration determination, as described in chapter 4.2.5.1. Lysates were diluted to 2 mg/mL, frozen in liquid nitrogen and stored at -80 °C until further use.

Binding reactions were set up by combining 500  $\mu$ L of lysate (1 mg protein per sample) with 30  $\mu$ L of the respective bead slurry, followed by a 2-hour incubation at 4 °C using a sample rotator. After removal of the supernatant, beads were washed twice with 1 mL of lysis buffer for 10 min at ambient temperature and thrice with PBS. The supernatant was removed and an on-bead digestion was performed as described in chapter 4.2.3.2. Experiments were conducted with three technical replicates in two independent experiments.

#### **4.2.3.5 Affinity enrichment via DBCO agarose beads**

As an alternative to the method described in chapter 4.2.3.4, azide-containing probes were immobilized on dibenzocyclooctyne (DBCO) agarose beads. For this, DBCO agarose beads with a binding capacity of approximately 3.5  $\mu$ mol (175  $\mu$ L of slurry) were washed thrice with PBS and subsequently incubated with 175 nmol azide-containing probe in PBS for 1 h at ambient temperature in a sample rotator. Beads were subsequently washed thrice with PBS, resuspended in PBS and stored at 4 °C. The subsequent affinity enrichment was performed as described in chapter 4.2.3.4.

#### **4.2.3.6 Affinity enrichment via NHS beads**

Chemical probes with a free amine were immobilized on NHS beads. For this, approximately 100  $\mu$ L slurry of Pierce NHS magnetic beads was washed once in cold 1 mM HCl. Beads were subsequently incubated in PBS containing 100 nmol of small molecule probe containing a free amine for 2 h rotating at ambient temperature. Beads were washed twice with 0.1 M glycine (pH 2.0), then once with ddH<sub>2</sub>O. Beads were incubated in 3 M ethanolamine (pH 9.0) for 2 h rotating at ambient temperature, washed four times with PBS and stored in 100  $\mu$ L of PBS at 4 °C.

Alternatively, approximately 100  $\mu$ L slurry of GE NHS magnetic beads was washed once in cold 1 mM HCl and incubated rotating in NHS coupling buffer containing 100 nmol of small molecule probe for 2 h at ambient temperature. Beads were rinsed in NHS blocking buffer A, then NHS blocking buffer B and then incubated in NHS blocking buffer A for 15 min at ambient temperature while rotating. Beads were sequentially rinsed in NHS blocking buffers B, A and B, finally washed thrice in PBS and stored in 100  $\mu$ L of PBS at 4 °C. The subsequent affinity enrichment was performed as described in chapter 4.2.3.4. To separate magnetic beads from its supernatant, a magnetic rack was used.

#### 4.2.3.7 Preparation of SILAC lysates

As alternative quantification method to LFQ for affinity enrichment experiments, SILAC lysates were prepared. HeLa cells were grown in arginine- and lysine-free DMEM supplemented with either  $^{12}\text{C}_6,^{14}\text{N}_2$ -L-lysine and  $^{12}\text{C}_6,^{14}\text{N}_4$ -L-arginine ('light SILAC medium') or  $^{13}\text{C}_6,^{15}\text{N}_2$ -L-lysine and  $^{13}\text{C}_6,^{15}\text{N}_4$ -L-arginine ('heavy SILAC medium') and dialyzed FBS over 7 days allowing amino acid incorporation of > 95%. Cells were washed with PBS, harvested using cell dissociation solution and washed twice in PBS. In low-binding micro reaction tubes, cells were resuspended in lysis buffer, incubated on ice for 20 min and centrifuged for 20 min at 14,000 x g at 4 °C. The supernatant was transferred into a low-binding micro reaction tube and the protein concentration was determined, as described in chapter 4.2.5.1. Lysates were diluted in lysis buffer to 2 mg/mL, frozen in liquid nitrogen and stored at -80 °C until further usage.

Prior to usage, all SILAC lysates were tested for incorporation efficiency via in-gel digestion. 20  $\mu$ g protein sample of lysate originating from cells grown in either light or heavy SILAC medium ('light lysate' or 'heavy lysate', respectively) and a 1:1 mixture of both lysate types was prepared, together with a sample containing 0.5  $\mu$ g BSA. Samples were diluted in SDS-PAGE loading buffer, incubated at 95 °C for 5 min and subjected to SDS-PAGE at 80V for 15 min. Gel pieces containing the lysate samples were cut out and transferred into micro reaction tubes, covered with In-gel digestion fixation solution and incubated at ambient temperature overnight. Gel pieces were washed with In-gel digestion wash buffer 1 for 30 min at 37 °C and 600 rpm and subsequently with In-gel digestion wash buffer 2 for 15 min at 37 °C and 600 rpm. Afterwards, the gel pieces were incubated in In-gel digestion reducing buffer for 45 min at 37 °C and 600 rpm and subsequently with In-gel digestion washing buffer 1 for 30 min at 37 °C and 600 rpm. Next, gel pieces were incubated in In-gel digestion alkylating solution for

60 min at ambient temperature in the dark and subsequently washed twice for 15 min at 25 °C and 600 rpm with In-solution digestion wash buffer 2. Gel pieces were dehydrated by incubation in acetonitrile and subsequent air-drying. Samples were soaked in In-gel digestion digestion buffer for 15 min at ambient temperature and 600 rpm. Subsequently, an equal volume of 25 mM  $\text{NH}_4\text{HCO}_3$  solution was added and samples were incubated at 30 °C and 350 rpm. The digestion was terminated by addition of 10% TFA and samples were subjected to ultrasonication. The supernatant was collected, and the gel pieces were dried out with acetonitrile. The peptide solution extracted from the gel pieces was pooled with the supernatant and dried in a vacuum concentrator.

*Samples were subjected to nano-HPLC-MS/MS analysis performed by the HRMS facility of the MPI Dortmund.*

#### **4.2.3.8 Photoaffinity labeling and *in situ* affinity enrichment**

HeLa cells were seeded into six 10-cm cell culture dishes with a cell density of  $5 \times 10^6$  cells/dish and incubated overnight at 37 °C and 5 %  $\text{CO}_2$ . Seeding medium was exchanged for medium containing 25  $\mu\text{M}$  of the respective photoaffinity probe and cells were incubated at 37 °C for 10 min. Cells were rinsed twice with PBS upon final addition of PBS. Cells were UV irradiated at 350 nm for 20 min on a chilled metal plate (4°C). Cells were scraped, transferred into low-binding micro reaction tubes and centrifuged at 1000 x g for 5 min at 4 °C. After supernatant removal, cells were resuspended in 75  $\mu\text{L}$  PAL lysis buffer and subjected to four freeze-thaw cycles. Crude lysates were centrifuged at 20,000 x g for 20 min at 4 °C and the supernatant was transferred into low-binding micro reaction tubes. To each sample, 2 nmol of TAMRA-biotin-azide (photoaffinity labeling) or biotin-azide (*in situ* affinity enrichment), 10 nmol  $\text{CuSO}_4$ , 50 nmol THPTA, 500 nmol aminoguanidine and 500 nmol sodium ascorbate were added and samples were incubated at 20 °C, 350 rpm for 60 min.

For photoaffinity labeling experiments, lysates were applied to SDS-PAGE and in-gel TAMRA fluorescence was detected using a gel documentation system.

For affinity enrichment experiments, excess biotin was removed using Pierce Dye and Biotin Removal Spin Columns, according to the manufacturer's protocol. Columns were equilibrated with PBS containing 0.4 % NP-40 alternative. Flow-through was collected in low-binding micro reaction tubes. Subsequently, 30  $\mu\text{L}$  of Streptavidin bead slurry was transferred into low-binding micro reaction tubes. Beads were washed twice with PBS using a magnetic rack for separation of beads and supernatant.



Lysate samples were mixed with 350  $\mu\text{L}$  of PAL lysis buffer, added to the beads and incubated at 4  $^{\circ}\text{C}$  overnight. Beads were washed twice with PAL wash buffer for 10 min and again washed four times with PBS for 5 min, all steps were performed at ambient temperature. Subsequent on-bead digestion and Stage-tip purification was performed as described in chapters 4.2.3.2 and 4.2.3.3, respectively.

#### 4.2.3.9 Thermal proteome profiling

HeLa cells were grown in T175 cell culture flasks as described in chapter 4.2.1.1. After reaching 80-90 % confluence, growth medium was removed and cells were washed once with PBS, followed by a 30-minute incubation with cell dissociation solution at 37  $^{\circ}\text{C}$  and 5 %  $\text{CO}_2$ . After detachment, cells were collected in a 50 mL falcon tube, centrifuged at 290 x g and the supernatant was removed. Cells were resuspended in 10 mL PBS, again centrifuged and the supernatant was removed. The cells were resuspended in 1 mL PBS and transferred into a 2 mL low-binding micro reaction tube. Cells were centrifuged again at 290 x g and supernatant was removed. Cells were lysed by resuspending in 500  $\mu\text{L}$  of PBS containing 0.4 % (v/v) NP-40 alternative and performing three freeze-thaw cycles. The lysate was subsequently centrifuged at 100,000 x g at 4  $^{\circ}\text{C}$  for 20 min and the soluble fraction was transferred into a fresh low-binding micro reaction tube. The protein concentration of the lysate was determined via Bradford assay, as described in chapter 4.2.5.1. Lysates were diluted in PBS + 0.4 % (v/v) NP-40 alternative to a final concentration of 2 mg/mL, snap frozen in liquid nitrogen and stored at -80  $^{\circ}\text{C}$  until further usage.

For the shift assay, 1.4 mL cell lysates were incubated at ambient temperature for 10 min in the presence of a compound or a respective amount of DMSO. Lysates were split into ten 120  $\mu\text{L}$  fractions each, which were subjected to a heat treatment ranging from 36.9  $^{\circ}\text{C}$  to 67  $^{\circ}\text{C}$ , in which each fraction was treated with a different temperature for 3 min. Subsequently, the samples were cooled to 4  $^{\circ}\text{C}$  and quickly transferred into ultracentrifugation tubes. To remove aggregated proteins, samples were subjected to 20 min of ultracentrifugation at 100,000 x g at 4  $^{\circ}\text{C}$ . The soluble fraction was transferred into low-binding micro reaction tubes.

For Thermal Proteome Profiling (TPP) 75  $\mu\text{L}$  of each sample were mixed with an equal volume of 100 mM triethylammonium bicarbonate (TEAB) buffer. To reduce protein disulfide bridges, samples were incubated at 55  $^{\circ}\text{C}$  for 1 h after the addition of 7.5  $\mu\text{L}$  TPP reducing buffer. Subsequently, 7.5  $\mu\text{L}$  of TPP alkylating solution was added to the samples, followed by incubation for 30 min in the dark.

Afterwards, proteins were precipitated by addition of 900  $\mu\text{L}$  of acetone ( $-20\text{ }^{\circ}\text{C}$ ) and incubation at  $-20\text{ }^{\circ}\text{C}$  overnight. Samples were centrifuged at  $8,000 \times g$  and  $4\text{ }^{\circ}\text{C}$ , followed by removal of the supernatant and 30 min of sample drying at ambient temperature. Addition of  $107.5\text{ }\mu\text{L}$  of TPP tryptic digestion solution, vortexing and incubation at  $37\text{ }^{\circ}\text{C}$  and 350 rpm overnight facilitated solubilization and tryptic digestion of the precipitated proteins.

*The following sample preparation, HPLC-MS/MS measurements and data analysis were performed by co-workers of the HRMS facility of the MPI Dortmund.*

The sample sets were labeled with TMT10plex™ tandem mass tags according to the manufacturer's protocol but with just half of the label amount mentioned there, so that each label type corresponded to one heat treatment temperature. Samples of one sample set (treated either with DMSO or compound) were pooled and dried in a vacuum concentrator. Samples were prefractionated via high pH reversed phase HPLC and dried again. The fractionated samples were analyzed by means of nano-HPLC-MS/MS. Protein identification and quantification was performed using MaxQuant.<sup>176</sup> Melting temperature determination via Boltzmann fit and data visualization was performed with Microsoft Office Excel in combination with a macro programmed in-house.

For the lysate-based cellular thermal shift assay (CETSA), 25  $\mu\text{L}$  of each soluble fraction were subjected to SDS-PAGE and subsequent immunoblotting for the protein of interest, as described in chapter 4.2.5.2. Band intensities were determined using Fiji ImageJ and normalized to the sample with the treated with the lowest temperature (= 100 %). Melting temperatures for sample sets treated either with DMSO or compound were determined via non-linear regression with four parameters using GraphPad Prism 7.03.

#### **4.2.3.10 Cellular thermal shift assay (CETSA)**

Two T75 cell culture flask containing HeLa cells (80-90 % confluence, approximately  $5 \times 10^6$  cells) were treated with DMSO or compound in growth medium for 10 min or 1 h. Cells were once washed with 5 mL PBS and detached via addition of 1.5 mL trypsin/EDTA solution and subsequent incubation at  $37\text{ }^{\circ}\text{C}$  and 5 %  $\text{CO}_2$  for 5 min. After addition of 5 mL growth medium, cells were centrifuged at  $350 \times g$  for 5 min and supernatant was removed. Cells were resuspended in 1 mL PBS and transferred in to a micro reaction tube and centrifuged again at  $1000 \times g$  for 3 min. The supernatant was discarded, and cells were resuspended in 0.6 mL of PBS. Cell suspensions were split in 10 fractions of 50  $\mu\text{L}$  each,

which were subjected to a gradient heat treatment and subsequent cooling to 4 °C. After addition of NP-40 alternative with a final concentration of 0.4 % (v/v), cells were lysed by performing three freeze-thaw cycles. The soluble protein fraction was separated from aggregated proteins and cellular debris by ultracentrifugation at 100,000 x g, 4 °C for 20 min and transferred into new micro reaction tubes. 16 µL of the soluble protein fractions were subjected to SDS-PAGE and immunoblot analysis for the protein of interest, as described in chapter 4.2.5.2. Data analysis was performed in the same manner as for lysate-based CETSA, as described in chapter 4.2.3.9.

#### 4.2.3.11 Cell Painting assay

*This experiment was performed by co-workers of COMAS, Dortmund.*

For this morphological profiling approach, 1,600 U-2 OS cells were seeded into black 384-well plates with clear bottom and incubated for 4 h at 37 °C and 5 % CO<sub>2</sub>. Compounds were added to each well using an acoustic dispenser, followed by a 20-hour incubation at 37 °C and 5 % CO<sub>2</sub>. Cells were stained with 100 nM of MitoTracker Deep Red for 30 min at 37 °C and 5 % CO<sub>2</sub> protected from light. Cells were fixed with 3.7 % formaldehyde in PBS for 20 min at ambient temperature in the dark, followed by three washing steps with PBS. Cells were stained with 5 µg/mL Hoechst-33342, 1.5 µg/mL Wheat germ agglutinin/Alexa-555, 25 µg/mL concanavalin A/Alexa-488, 5 µL/mL phalloidin/Alexa-568 solution and 1.5 µM SYTO 14 in PBS with 1 % BSA for 30 min at ambient temperature protected from light. Cells were washed thrice with PBS and subsequently imaged using a high content screening system in five fluorescence channels (DAPI: Ex 375(25) / Em 445(35); FITC: Ex 485(15) / Em 525(15); Spectrum Gold: Ex 532.5(12.5) / Em 567.5(12.5); TexasRed: Ex 560(25) / Em 625(25); Cy5: Ex 627.5(22.5) / Em 692.5(22.5)) at 20x magnification with 9 sites per well.

Images were analyzed using the CellProfiler software, thereby 1716 cellular features were extracted, which were aggregated as medians per well and subsequently per set of technical replicates.<sup>175</sup> A set of 579 parameters with high reproducibility was used for the generation of morphological profiles. For each parameter the Median Absolute Deviation (MAD) of the cells treated with compound was compared to the MAD of control cells treated with DMSO and a Z-score was calculated by dividing the difference between the median of the cells treated with compound and the median of the control cells by the MAD of the control cell samples. A phenotypic profile consists of the Z-scores of all 579 parameters. A parameter with a Z-score  $\geq 3$  was regarded as significantly changed in comparison

to control cells treated with DMSO. The percentage of all significantly changed parameters of a profile is called 'induction rate'. The biological similarity of two profiles was determined by calculating their correlation distances.

#### 4.2.3.12 Proteome profiling

To determine the impact of a compound on the cellular proteome, a proteome profiling was performed.  $10^6$  HeLa cells were seeded into ten 10-cm cell culture dishes and incubated at 37 °C and 5 % CO<sub>2</sub> overnight. Five dishes each were treated with compounds (24-hour treatment) or were treated 23 h later (1-hour treatment) and incubated at 37 °C and 5 % CO<sub>2</sub>. Cells were washed with PBS, harvested with cell dissociation solution and collected and washed with PBS again. The cells were resuspended in PBS containing 0.4 % NP-40 alternative and protease inhibitor cocktail and three freeze-thaw cycles were performed. Samples were centrifuged at 14,000 x g at 4 °C for 20 min and supernatant was transferred into low-binding micro reaction tubes. The protein concentration of each lysate was determined as described in chapter 4.2.5.1. Samples were diluted in lysate buffer to 2 mg/mL, frozen in liquid nitrogen and stored at -80 °C until further usage. 150 µg of protein was transferred into a low-binding micro reaction tubes and samples were reduced, alkylated and subjected to a tryptic digest and tandem mass tag labeling as described in chapter 4.2.3.9.

#### 4.2.3.13 Phosphoproteome profiling

*This assay was performed together with Dr. Elena Rudashevskaya (MPI Dortmund).*

To assess the influence of a compound on the cellular phosphoproteome, this profiling approach was performed. HeLa cells were seeded into 15 cm cell culture dishes at a density of  $6.5 \times 10^6$  cells and incubated at 37 °C and 5 % CO<sub>2</sub> overnight. Seeding medium was exchanged for medium containing compounds and cells were incubated for 30 min at 37 °C and 5 % CO<sub>2</sub>. Cells were rinsed twice with PBS and once with TBS and 1 mL of boiling phosphoproteomics lysing buffer was added. Cells were scraped and collected in low-binding micro reaction tubes. Samples were incubated at 96 °C for 5 min, subsequently incubated on ice and ultrasonicated. Samples were centrifuged at 16,000 x g for 30 min and the supernatants were collected in micro reaction tubes.

Hydrophilic and hydrophobic Sera-Mag™ SpeedBead™ bead were mixed in a micro reaction tube. Using a magnetic rack, beads were rinsed with water thrice. Sample lysate (1 mg protein in total) was

mixed with GndHCl and water, yielding a final GndHCl concentration of 1 M. Prepared bead slurry was added to the mixture and acetonitrile was added to a final concentration of 70 % (v/v). After 10 min of incubation at ambient temperature, proteins aggregated on the beads. The supernatant was removed using a magnetic rack. Beads were rinsed with acetonitrile once, then with 70 % (v/v) EtOH. Beads were dried briefly for 5 min at ambient temperature. 270  $\mu$ L of phosphoproteomics digestion buffer containing 1  $\mu$ g/ $\mu$ L LysC were added, followed by 30 min of incubation at 37 °C and 1000 rpm. To each sample 20  $\mu$ g of trypsin were added, followed by an overnight incubation at 37 °C and 1000 rpm.

For the enrichment of phosphopeptides, 2 mg magnetic titanium dioxide (MagReSyn TiO<sub>2</sub>) particles were placed into low-binding micro reaction tubes and washed with EtOH and thrice with phosphoproteomics loading buffer. Next, 1 mg of protein digest was mixed with an equivalent volume of phosphoproteomics loading buffer and centrifuged at 10,000 x g for 5 min at 4 °C. The supernatant was mixed with the particles, vortexed and incubated for 20 min at ambient temperature while rotating. Using a magnetic rack, beads were washed with phosphoproteomics loading buffer, thrice with phosphoproteomics wash buffer 1 and twice with phosphoproteomics wash buffer 2. To elute phosphopeptides, particles were incubated in 1 % (v/v) aqueous ammonia solution for 10 min at ambient temperature. The supernatant was collected in a low-binding micro reaction tube containing TFA yielding a final concentration of 3 % (v/v). This step was repeated twice, all eluates of one sample were collected in one tube.

Two discs of SDB-RPS matrix were placed into 200  $\mu$ L pipette tips. The matrix was rinsed consecutively with acetonitrile, SDB-RPS equilibration buffer and SDB-RPS wash buffer. Subsequently, the sample was loaded onto the matrix and washed twice with SDB-RPS wash buffer. Phosphopeptides were eluted by addition of SDB-RPS elution buffer and dried in a vacuum concentrator.

*Subsequent sample preparation, HPLC-MS/MS measurements and data analysis were performed by co-workers of the HRMS facility of the MPI Dortmund.*

#### **4.2.4 Target validation methods**

##### **4.2.4.1 Determination of glutathione reactivity**

For the detection of glutathione adducts *in vitro*, compounds were diluted to 20  $\mu$ M in PBS in the presence or absence of 5 mM GSH and incubated at 37 °C for 1 h. The reaction mixtures were analyzed by UHPLC with a C18 1.8  $\mu$ m column in line with ESI-MS, m/z: 110-2000. The chromatography was

performed with a flow rate of 250  $\mu\text{L}/\text{min}$  at 30  $^{\circ}\text{C}$ , detecting the UV absorption at 210 nm (buffer A: 0.1 % formic acid in  $\text{H}_2\text{O}$ ; buffer B: acetonitrile and 0.1 % formic acid, gradient: 10-95 % in 5 min). Data were analyzed using the Xcalibur software.

#### 4.2.4.2 Cellular glutathione depletion assay

As an alternative to the method described in chapter 4.2.2.3, the total GSH content after compound treatment was determined using the Cayman Glutathione assay kit according to the manufacturer's protocol. Briefly,  $1.5 \times 10^5$  HeLa cells were plated in 6-well plates and incubated overnight at 37  $^{\circ}\text{C}$  and 5 %  $\text{CO}_2$ . Cells were treated with compounds for 1 h at 37  $^{\circ}\text{C}$  and 5 %  $\text{CO}_2$  and harvested in PBS using a cell scraper. Cells were collected via centrifugation at 2000 x g for 5 min, supernatant was discarded and cells were resuspended in 50  $\mu\text{L}$  of MES buffer, followed by three freeze-thaw cycles. The lysate was centrifuged at 14,000 x g, 4  $^{\circ}\text{C}$  for 20 min and the supernatant was transferred into a micro reaction tube. Test lysates and GSH standards were diluted 1:10 in MES buffer and mixed with assay solution containing 5-5'-dithiobis-(2-nitrobenzoic acid) (DTNB, also known as Ellman's reagent), cofactors and enzymes (glutathione reductase and glucose-6-phosphate dehydrogenase). Absorbance at 405 nm was measured in a 5-minute interval for 30 min. Protein concentration of each lysate was determined as described in chapter 4.2.5.1. A GSH standard curve was plotted, total GSH concentrations were determined for each sample and normalized to its protein concentration.

#### 4.2.4.3 Cathepsin D enzymatic activity assay

To identify Cathepsin D-inhibitory effects of compounds, this enzymatic activity assay was conducted. The assay was performed using the Cathepsin D Inhibitor Screening Kit according to the manufacturer's protocol. Recombinant Cathepsin D protein was incubated in the presence of compounds for 10 min at 37  $^{\circ}\text{C}$  in black, 384-well plates. A substrate solution, containing a fluorescently labeled substrate peptide, was added and the fluorescence (excitation 328 nm / emission 460 nm) was measured in a 10-minute interval for 2 h at 37  $^{\circ}\text{C}$  with the Tecan Infinite M200 plate reader. A background sample only containing the substrate in reaction buffer was included. The background value was subtracted from all measured values and data were normalized to the value of samples treated with DMSO (=100 %)

#### 4.2.4.4 Glyoxalase I enzymatic activity assay

To identify Glyoxalase I-inhibitory effects of compounds, this enzymatic activity assay was conducted. The assay was performed using the Glyoxalase I Activity Assay Kit according to the manufacturer's protocol. Recombinant glyoxalase I was incubated in the presence of compounds for 15 min at ambient temperature in UV-transparent 96-well plates. A substrate mixture was prepared and incubated for 10 min at ambient temperature protected from light. The substrate mixture was added to the protein samples and the absorption at 240 nm was monitored in 1-minute intervals over 60 min. A background sample only containing the substrate in reaction buffer was included. The background value was subtracted from all measured values and data were normalized to the value of samples treated with DMSO (=100 %).

#### 4.2.4.5 Recombinant expression of human $\sigma$ receptors

*Recombinant insect cell expression of human  $\sigma_1$  and  $\sigma_2$  receptor was performed by Dr. Alexandra Friese, Max Planck Institute Dortmund.*

Protein encoding genes were amplified via PCR using cDNA clones OHu23479 and OHu30008 (GenScript Biotech, USA) for  $\sigma_1$  and  $\sigma_2$  receptor, respectively, as templates. Obtained PCR products were cloned into pFL vectors with an N-terminal His<sub>6</sub>-tag, which was a gift from Imre Berger (University of Bristol). Plasmid identity was confirmed via DNA sequencing. Bacmids for  $\sigma$  receptor expression were generated via recombination for 5 h at 37 °C in DH10EMBacY cells, which were a gift from Imre Berger (University of Bristol). A blue/white screening was performed to pick positive clones. Isolated bacmids were transfected into *Spodoptera frugiperda* Sf9 cells (Invitrogen) in Sf-900 III serum-free medium (Invitrogen) at 27 °C for 4 days. The supernatant was transferred to  $2 \times 10^6$  Sf9 cells in 10 mL medium and incubated at 27 °C for 4 days.

For  $\sigma_1$  and  $\sigma_2$  receptor expression,  $1.5 \times 10^6$  cells/mL of BTI-*Tnao38* cells (*Trichoplusia ni*) were transfected with a virus ratio of 1:20 and incubated for 4 days at 27 °C.<sup>170</sup> Cells were collected at 500 x g for 20 min and stored at -80 °C until further usage. Cells were resuspended in protein expression lysis buffer 1, lysed via ultrasonication and centrifuged at 75,000 x g for 30 min at 4 °C. The obtained supernatant was centrifuged again as described. Cells were mixed with protein expression lysis buffer 2 and resuspended with a glass dounce tissue grinder.  $\sigma$  receptor proteins were extracted overnight at 4 °C with gentle rotation. Samples were centrifuged at 75,000 x g for 30 min at 4 °C and the filtered

supernatant was supplemented with 5 mM or 10 mM imidazole for  $\sigma_1$  and  $\sigma_2$  receptor, respectively, and applied onto a HisTrap affinity chromatography column. Columns were washed with 50 mL of protein expression wash buffer 1 and 30 mL of protein expression wash buffer 2. The latter buffer was supplemented with 60 mM or 30 mM imidazole for  $\sigma_1$  and  $\sigma_2$  receptor, respectively, and proteins were eluted with a linear gradient of up to 500 mM imidazole. Samples were applied onto a gel filtration column in protein expression size exclusion buffer. Eluted proteins were concentrated, frozen in liquid nitrogen and stored at  $-80\text{ }^\circ\text{C}$  until further usage.

#### 4.2.4.6 Fluorescence polarization assay

The respective TAMRA probe was diluted in fluorescence polarization buffer to a final concentration of  $2\text{ }\mu\text{M}$ . Test proteins were diluted in probe-containing buffer to  $80\text{ }\mu\text{M}$  and a 1:1 dilution series with eleven steps was prepared in black, non-binding 96-well plates. Background wells with probe-containing buffer were included. Samples were incubated for 4-6 h at ambient temperature and subsequently subjected to a fluorescence polarization (Ex/Em 540/590 nm) measurement using the Tecan Spark plate reader.

#### 4.2.4.7 Radioligand binding assays

*$\sigma_1$  and  $\sigma_2$  receptor radioligand binding assays were performed by Dr. Dirk Schepmann, in the group of Prof. Bernhard Wünsch, University of Münster.<sup>178</sup>*

To test compounds for their ability to bind to  $\sigma_1$  or  $\sigma_2$  receptors, radioligand binding assays were conducted. Filtermats were incubated for 2 h at ambient temperature in 0.5 % aqueous polyethylenimine. Membrane preparations from either guinea big brain ( $\sigma_1$ ) or rat liver ( $\sigma_2$ ) were treated with compounds and [ $^3\text{H}$ ]-(+)-pentazocine ( $\sigma_1$  ligand) or [ $^3\text{H}$ ]-di-*o*-tolylguanidine ( $\sigma_2$  ligand), respectively, for 2 h, 500-600 rpm. The incubation was terminated by rapid filtration, followed by five washing steps with water. The filtermats were dried at  $95\text{ }^\circ\text{C}$  and a solid scintillator was melted onto them. The amount of bound radioligand was quantified via radioactivity measurements. Data were analyzed using GraphPad Prism.  $\text{IC}_{50}$  values were calculated via non-linear regression analysis and subsequently transformed into  $K_i$  values using the Cheng-Prusoff equation.<sup>179</sup>



#### 4.2.4.8 Mechanical allodynia assay

*Mechanical allodynia assays were performed by Antonia Artacho-Cordón under the supervision of Prof. Francisco Nieto, University of Granada, Spain. Animal care was provided in accordance with institutional, regional and international standards, according to the research ethics committee of the University of Granada, Granada, Spain, the Junta de Adalucía, Spain and the European Communities Council Directive 2010/63, respectively. The experimental protocol was approved by the Junta de Adalucía, Spain (License number 16/07/2020/083).*

To test compounds for agonism or antagonism of the  $\sigma_1$  receptor, mechanical allodynia assays were conducted. Female CD-1 mice were treated with compounds via subcutaneous administration, 30 min prior to intraplantar administration of capsaicin. After 15 min an electronic *von Frey*-device was used to apply a mechanical punctate stimulation with 0.5 g force to an area of secondary mechanical hypersensitivity, which was located at least 5 mm away from the capsaicin injection site. At the same time the paw withdrawal latency time was recorded. Three trials at 30 s intervals with a cutoff time of 50 s were performed for each animal and mean values were calculated. For competition studies, 32 mg/kg PRE-084 was administered subcutaneously 5 min prior to the compound administration. To calculate the degree of effect on mechanical allodynia in percent, the difference between latency times recorded from mice treated with vehicle or compound was divided by the difference between the cutoff time and the latency times recorded from mice treated with vehicle, multiplied by 100. A one-way analysis of variance (ANOVA) and a Bonferroni test were performed to determine statistical significance.

#### 4.2.4.9 Kinase activity and binding assays

*Kinase activity assays were performed by external providers, namely Thermo Fisher SelectScreen Services, Eurofins Discovery and SignalChem Biotech Inc, using recombinant kinases and different assay techniques.*

##### 1) Adapta activity assay (Thermo Fisher SelectScreen):

The Adapta assay measures the ADP formation by means of fluorescence resonance energy transfer (FRET). All kinase components and compounds were incubated, typically for 60 min. The kinase reaction was terminated by addition of EDTA. A europium-tagged anti-ADP antibody and an ADP-tracer

linked to Alexa-647, which form a FRET pair, were added. In the presence of ADP, the tracer is displaced from the antibody, which is detected as a decrease in the FRET signal.

II) LanthaScreen binding assay (Thermo Fisher SelectScreen):

For this binding assay, an affinity-tagged kinase of interest was incubated with a europium-linked antibody, which binds to the affinity tag, in the presence of an ATP-competitive Alexa-674 tracer and the compound. Both antibody and tracer bind to the affinity-tagged kinase, resulting in a FRET signal. In case the compound displaces the tracer, the FRET signal would decrease.

III) Z'-LYTE activity assay (Thermo Fisher SelectScreen):

This assay employs a small substrate peptide, which is labeled with a FRET pair, consisting of a donor and acceptor fluorophore. The peptide contains a tyrosine, serine or threonine side-chain, which can be phosphorylated by the kinase of interest and is part of a protease cleavage site. Phosphorylation of the before-mentioned side chain interferes with the proteolytic cleavage of the substrate. After the kinase reaction, a site-specific protease is added and the FRET signal is measured. Decrease in the FRET signal indicates a suppression of the kinase activity.

IV) Radiometric activity assay (Eurofins Discovery):

The kinase reaction was performed using  $\gamma$ -<sup>33</sup>P-ATP. The reaction was stopped after 40 min using phosphoric acid. The reaction mixture is spotted on a filtermat and washed prior to drying and scintillation counting.

V) ELISA activity assay (Eurofins Discovery):

The kinase reaction was performed using a GST- and cMyc-tagged substrate protein. The reaction was stopped after 30 min via addition of EDTA-containing stop solution. Subsequently, a fluorophore-labelled anti-GST antibody and a europium-labelled antibody binding the phosphorylated substrate protein were added and FRET signals were measured.

VI) ADP-Glo activity assay (SignalChem Biotech Inc.):

After the kinase reaction, the amount of ADP within the reaction mixture was quantified using the luciferase-based ADP-Glo™ assay.

#### **4.2.4.10 Superoxide dismutase enzymatic activity assay**

To test compounds for superoxide dismutase-inhibitory activities, a respective enzymatic assay was performed, using the Superoxide Dismutase Activity assay kit (Cayman) according to the

manufacturer's instructions. For the cellular assay, HeLa cells were plated into clear 96-well plates with a density of  $1.5 \times 10^4$  cells/well and incubated overnight at 37 °C and 5 % CO<sub>2</sub>. Seeding medium was exchanged for compound containing medium and cells were incubated for 2 h at 37 °C and 5 % CO<sub>2</sub>. Cells were rinsed once with PBS, before addition of 20 µL of SOD lysis buffer, followed by 5 min of incubation on a plate shaker at ambient temperature. 20 µL of lysis buffer were added to empty wells. The radical detector solution was diluted 1:400 in 1x assay buffer and the xanthine oxidase solution was diluted 1:40 in 1x sample buffer, which were provided in the assay kit. 180 µL of diluted radical detector solution and 20 µL of diluted xanthine oxidase solution were added to each well. Using a Tecan Infinite M200 plate reader, the absorption at 450 nm was monitored in a 60-second interval for 90 min in total. Data obtained during the first 30 min were analyzed via linear regression and slope values were normalized to the value of the buffer control (= 100 %).

For testing the inhibition of SOD1, bovine SOD1, provided in the assay kit, was incubated in 200 µL diluted radical detector in the presence of the compounds for 60 min at ambient temperature. Afterwards, 20 µL of diluted xanthine oxidase was added and the assay was performed as described above.

#### **4.2.4.11 PP2A $\alpha$ /PPP2R1A phosphatase activity assay**

*This assay was performed by an external provider (SignalChem Biotech Inc., Canada).*

PP2A $\alpha$  and PPP2R1A protein (full-length, recombinantly expressed in Sf9 insect cells) complex were mixed with compounds and phosphatase activity was detected using the Biomol Green phosphatase detection kit.

### **4.2.5 Other methods**

#### **4.2.5.1 Determination of protein concentrations**

Protein concentrations of cell lysates were determined via the Bradford method.<sup>180</sup> Protein standards of known concentrations ranging from 0.2 to 1.0 mg/mL BSA were prepared in the respective lysis buffer used for lysate preparation. The test lysate was diluted 1:10 in the respective lysis buffer. 1 µL of protein standards, diluted test lysate and lysis buffer (for background subtraction) were transferred into a clear 96-well plate. 199 µL of Bradford assay working solution (20 % (v/v) aqueous Bradford assay solution) were added and the plate was shaken for 5 min using a plater shaker. Afterwards, the absorption at

595 nm was determined spectrophotometrically. Background-subtracted absorption values of the BSA standards were plotted against their respective concentration to obtain a standard curve. On this basis, test lysate concentrations were calculated.

#### 4.2.5.2 Immunoblotting

For the detection of a specific protein in a complex mixture, e.g. cell lysates, an SDS polyacrylamide gel electrophoresis (SDS-PAGE) with subsequent immunoblotting was performed. For this, protein samples were diluted in 5x SDS sample buffer, incubated at 95 °C for 5 min and stored on ice for 3 min prior to the SDS-PAGE. Proteins were separated in an SDS polyacrylamide gel in SDS running buffer by applying an 80V current for 10 min, followed by a 120V current until the running front reached the bottom of the gel. A pre-stained protein ladder served as size control.

For protein transfer, a polyvinylidene difluoride (PVDF) membrane was first soaked in methanol for 1 min, followed by a 5-minute incubation in cold transfer buffer together with the SDS gel and filter paper. The blotting sandwich was assembled within a device for semi-dry electrophoresis by stacking filter paper, PVDF membrane, SDS gel and another piece of filter paper on top of each other. Air bubbles between the layers were removed carefully before closing the apparatus and applying a 24V current for 40-65 min.

For quantitative immunoblot analysis, fluorescently labeled secondary antibodies were used. The membrane was incubated in PBS-based Odyssey® Blocking buffer or 5% non-fat dried milk powder in PBS for 1 h at ambient temperature. The primary antibody was diluted in the respective blocking buffer containing 0.2 % Tween-20 and incubation was performed overnight at 4 °C, followed by three 5-minute washing steps at ambient temperature with PBS-T. The secondary antibody was diluted in blocking buffer containing 0.2 % Tween-20 and 0.01 % SDS and incubation was performed for 1 h at ambient temperature in the dark. Blots were washed thrice for 5 min with PBS-T at ambient temperature protected from light and rinsed with PBS. Blots were imaged using a gel and blot documentation system. Band intensities were quantified using the Fiji ImageJ software.

A more sensitive method for immunoblot detection is the use of secondary antibodies coupled to horseradish peroxidase (HRP), which was used for qualitative analysis. For this, the immunoblotting protocol was altered as followed: After secondary antibody incubation, the membrane was washed twice with PBS-T and once with PBS. For detection, the blot was incubated in SuperSignal™ West Pico PLUS

Chemiluminescent Substrate solution for 5 min at ambient temperature in the dark. Chemiluminescent signals were detected with a gel and blot documentation system. In case of weak signals, a second detection step using SuperSignal™ West Femto Maximum Sensitivity Substrate was performed.

#### 4.2.5.3 Iron chelation assay

To test whether compounds chelate Fe<sup>2+</sup> ions, compounds were incubated in a black 96-well plate in presence of an aqueous FeSO<sub>4</sub> solution for 5 min at ambient temperature. Next, a HEPES-based Calcein solution was added and fluorescence intensity (excitation 486 nm / emission 517 nm) was measured using a Tecan Spark plate reader. Final assay concentrations were 50 μM FeSO<sub>4</sub>, 25 μM Calcein and 6.25 - 50 μM compound in 25 mM HEPES, 94 mM NaCl, pH 7.2.

#### 4.2.5.4 Copper chelation/reduction assay

To assess whether compounds chelate Cu<sup>+</sup> ions, a mixture of CuSO<sub>4</sub> and hydroxylamine was incubated in a HEPES buffer (pH 7.5) for 2 min in a clear 384-well plate. Next, the compound was added and incubated for 2 min, before bathocuproinedisulfonic acid (BCA) addition, followed by 5 min of incubation. The absorption at 484 nm was measured with a Tecan Infinite M200 plate reader.

For the Cu<sup>2+</sup> chelation assay, the compound was incubated with CuSO<sub>4</sub> in HEPES buffer for 2 min. Subsequently, hydroxylamine was added and the samples were incubated for 2 min, before BCA addition followed by a 5-minute incubation and an absorption measurement. To test whether compounds can reduce Cu<sup>2+</sup>, CuSO<sub>4</sub>, BCA and the compound were incubated in HEPES buffer for 2 min and absorption was measured. The final concentrations were 50 μM CuSO<sub>4</sub>, 2 mM hydroxylamine, 1 mM BCA and 15 mM HEPES. All incubation steps were performed at ambient temperature.

#### 4.2.5.5 Redox cycling assay

*This assay was performed by co-workers of the Lead Discovery Center (LDC) Dortmund under the supervision of Dr. Matthias Baumann.*

To identify whether ROS-inducing compounds have redox-cycling properties, compounds were subjected to an *in vitro* redox cycling assay. Compounds were incubated in the presence of 1 mM DTT in Hank's balanced salt solution (HBSS) in a clear 384-well plate for 15 min at ambient temperature,

before adding phenol red and horseradish peroxidase with final concentrations of 100 and 60  $\mu\text{g/mL}$ , respectively. After 5 min of incubation at ambient temperature, NaOH is added to terminate the reaction and absorbance at 610 nm is measured using a plate reader.

## 5 Results

### 5.1 Phenotypic screening for small molecule inducers of ROS accumulation

To identify novel small molecule inducers of cellular ROS accumulation, a phenotypic screen was conducted at the Compound Management and Screening Center (COMAS) in Dortmund, which was adapted from Adams *et al.*<sup>181</sup> The screen, which was performed in U-2 OS cells, utilized the general ROS indicator 5/6-chloromethyl-2',7'-dichlorodihydrofluorescein diacetate (CM-H<sub>2</sub>DCFDA), a membrane-permeable, non-fluorescent derivative of fluorescein (Figure 13a).

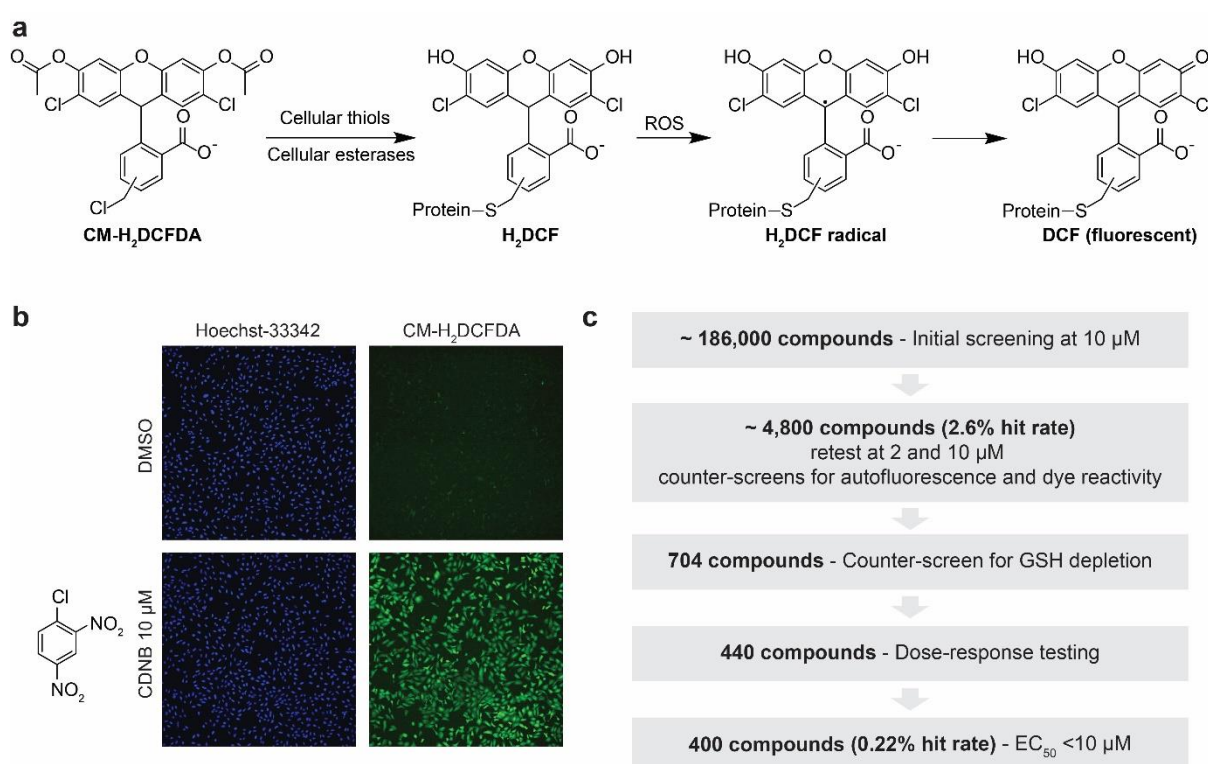


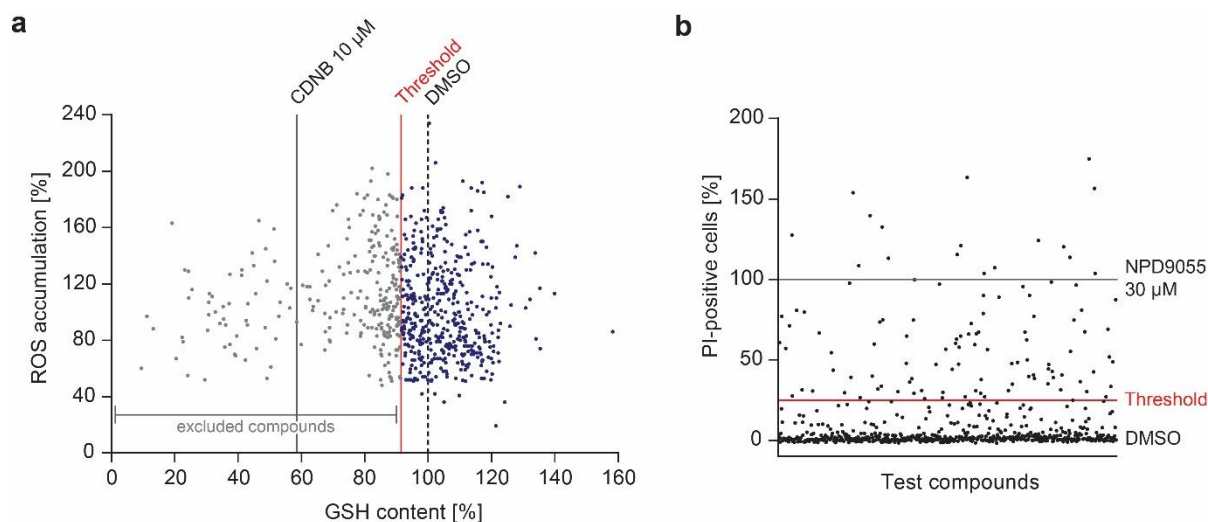
**Figure 13: Phenotypic screening for ROS-inducing small molecules.** (a) Chemical structure of the ROS indicator CM-H<sub>2</sub>DCFDA and its chemical modifications in cells. (b) Example images of U-2 OS cells treated with DMSO or 10  $\mu$ M CDNB (chemical structure shown). (c) Schematic overview of the ROS screening campaign, conducted by COMAS.

In cells, CM-H<sub>2</sub>DCFDA is de-esterified by cellular esterases and its chloromethyl moiety reacts with cellular thiols, yielding 2',7'-dichlorodihydrofluorescein (H<sub>2</sub>DCF). H<sub>2</sub>DCF is readily oxidized by various ROS, forming an H<sub>2</sub>DCF radical that further reacts to the fluorescent 2',7'-dichlorofluorescein (DCF) (Figure 13a).<sup>182</sup> Although CM-H<sub>2</sub>DCFDA is considered as a general ROS indicator, it displays different degrees of reactivity towards different reactive oxygen species. While hydroxyl radicals and

peroxynitrite evoke strong oxidation of H<sub>2</sub>DCF, the dye is less reactive with hydrogen peroxide or superoxide.<sup>183</sup> To identify small molecules that induce ROS via direct redox modulation, ROS levels were measured after 60 min of compound incubation. The DCF fluorescence response induced by compounds was detected by means of a plate-reader or fluorescence microscopy. As a positive control for ROS induction, cells were treated with 10  $\mu$ M of 1-chloro-2,4-dinitrobenzene (CDNB). CDNB is a GSH-depleting small molecule that induces fast ROS accumulation (Figure 13b).<sup>184</sup> Additionally, cells treated with DMSO were included as a negative control. Results obtained by compounds were normalized to the values of the DMSO (0 %) and CDNB (100 %) controls. In the primary screen, a compound library of approximately 186,000 compounds was screened at 10  $\mu$ M for cellular ROS induction (Figure 13c). Integrated DCF fluorescence intensity was detected using a plate reader. Approximately 4,800 compounds increased ROS levels > 50 %, which corresponds to an initial hit rate of 2.6 %. 4224 compounds with sufficient availability and purity were selected. These were subjected to counter-screens to identify and exclude fluorescent and CM-H<sub>2</sub>DCFDA-reactive compounds, as such properties lead to a false-positive read-out. Additionally, the compounds were tested again at concentrations of 2 and 10  $\mu$ M to confirm the activity of the initial screening hits. In total, 723 compounds elevated ROS levels either >55 % at 2  $\mu$ M or >75 % at 10  $\mu$ M and 704 were selected for further testing based on ROS activity and compound availability. Electrophilic compounds, like CDNB, can induce ROS accumulation by depletion of cellular glutathione, which is a well-known mode of action.<sup>184</sup> Therefore, compounds were tested for their influence on total cellular GSH levels using the GSH/GSSG-Glo™ assay after 1 h of incubation.

From the 704 compounds tested, 37.5 % were excluded, as they decreased cellular GSH levels by more than 8.5 % (Figure 14a). In the last step, dose-response ROS measurements for the remaining 440 compounds were performed. Of these, 400 compounds displayed a dose-dependent ROS induction with an EC<sub>50</sub> below 10  $\mu$ M, finally resulting in an overall hit rate of 0.22 %.

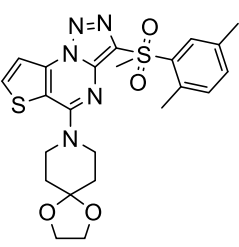
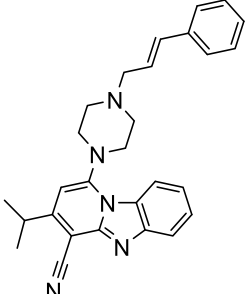
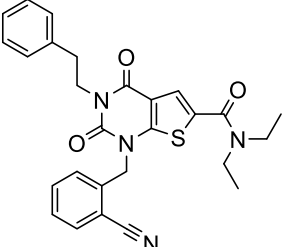
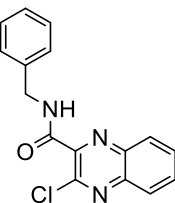
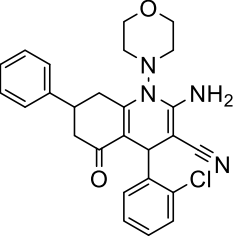
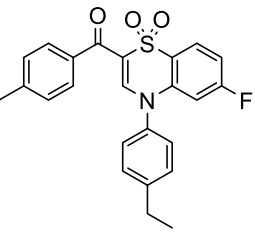
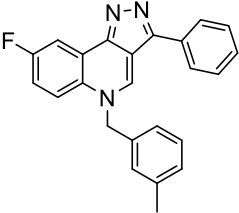
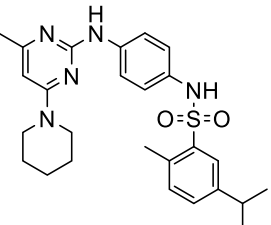
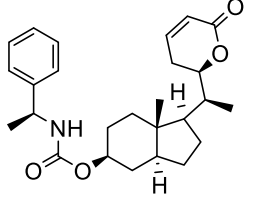




**Figure 14: GSH-depleting and cytotoxic effects of 704 preliminary ROS screening hits.** (a) ROS-inducing activity and influence of cellular GSH content of the 704 preliminary screening hits at 10  $\mu\text{M}$ . Dashed black line and gray line indicate the GSH content of cells treated with DMSO and 10  $\mu\text{M}$  CDNB, respectively. Red line indicates the exclusion threshold for GSH depleting-compounds. Data were obtained by COMAS, Dortmund. (b) Cytotoxic effects of the 704 preliminary screening hits determined via real-time live-cell analysis after propidium iodide (PI) staining after 24 h of compound incubation. Data were normalized to values of cells treated with DMSO (= 0 %) and 30  $\mu\text{M}$  of NPD9055 (= 100 %). Red line indicates 25 % threshold. Mean values,  $n = 3$ .

The compound subset tested for GSH depletion was in parallel subjected to a real-time live-cell analysis in U-2 OS cells. Cells were treated with compounds in the presence of propidium iodide (PI) and monitored over a 24-hour time course (Figure 14b). NPD9055 was used as positive control, as it evokes strong cytotoxic effects.<sup>185</sup> Compounds that induced a positive PI staining in  $\geq 25$  % of cells at 10  $\mu\text{M}$  after 24 h were regarded as cytotoxic. Interestingly, only 15.77 % of the compounds displayed such cytotoxic effects. This observation is in line with the results of Adams *et al.*, who reported that the majority of their ROS screening hits does not induce cytotoxicity.<sup>181</sup> This assay was not part of the general screening workflow and was solely intended to evaluate the cytotoxic effects of the preliminary hit compounds. Thus, none of the compounds was excluded from the screening based on their cytotoxic properties.

**Table 5: Chemical structures of selected ROS screening hits.** Compound IDs and ROS EC<sub>50</sub> values based on 'stained area' measurements in U-2 OS cells are shown. Mean values  $\pm$  SD, n = 3. Data were obtained by COMAS, Dortmund.

		
<b>201980</b> 0.5 $\pm$ 0.2 $\mu$ M	<b>179946</b> 0.7 $\pm$ 0.3 $\mu$ M	<b>228873</b> 0.8 $\pm$ 0.2 $\mu$ M
		
<b>240458</b> 0.9 $\pm$ 0.1 $\mu$ M	<b>176492</b> 1.3 $\pm$ 0.4 $\mu$ M	<b>217951</b> 1.4 $\pm$ 0.6 $\mu$ M
		
<b>243679</b> 1.8 $\pm$ 0.6 $\mu$ M	<b>226028 (DP01)</b> 2.3 $\pm$ 0.3 $\mu$ M	<b>344368</b> 3.1 $\pm$ 0.2 $\mu$ M

Chemical structures of selected potent screening hits are depicted in Table 5. Among all hit compounds, compound 201980 induced ROS accumulation most potently with an EC<sub>50</sub> of 0.5  $\pm$  0.2  $\mu$ M. Compound 179946, the second most potent hit, is chemically similar to BRD5459, one of the top hit molecules identified in the ROS screening performed by Adams *et al.*<sup>181</sup> Based on potency and chemical structure, the commercially available compounds 217951, 243679 and 226028 (DP01), as well as the withanolide-derived compound 344368, which was synthesized in-house, were selected for in-depth characterization.<sup>186</sup> For all four compound classes, additional derivatives were available in the screening library and were included for further studies. Due to solubility issues, studies of the compound classes comprising 217951 and 243679 were terminated after initial experiments. Studies of the withanolide-inspired compound class were stopped due to limited compound availability. The

biological investigation of the diaminopyrimidine-based class comprising the compound 226028 (DP01) is reported in chapter 5.3.

## 5.2 Identification of cytotoxic, GSH-reactive inducers of ROS accumulation

Glutathione is the most abundant antioxidant in cells with intracellular concentrations ranging from 1-10 mM.<sup>187</sup> In the course of the phenotypic screening campaign, the influence of hit compounds on cellular GSH levels was determined to exclude electrophilic compounds that induce ROS via direct reaction with GSH, thereby depleting the cellular GSH pool. In line with the literature, compounds containing a 5-chloro-2-((methylsulfonyl)pyrimidin-4-yl)methanone moiety, strongly decreased cellular GSH levels, thereby validating the assay.<sup>188</sup> Among the most potent GSH-depleting compounds, another two chemical moieties were found multiple times, namely 4,5-dihalo-2-methylpyridazin-3-one (DHMP) and 2,3,4,5(6)-tetrachloro-6(5)-methylpyridine (TCMP). DHMP and TCMP were mentioned previously in a study by Mervin *et al.* that investigated cytotoxic effects of selected fragments in screening compound libraries. Both displayed cytotoxic effects with unknown modes of action.<sup>189</sup>

The 30 most potent GSH-depleting small molecules that reduced cellular GSH content below 40 % included 16 DHMP and four TCMP compounds (

Supplementary Table 1). To investigate the link between GSH depletion, ROS induction and cytotoxicity, three compounds of each group were selected for in-depth studies (Figure 15a). With the exception of DHMP-3 and TCMP-3, all compounds induced cellular ROS accumulation (Figure 15b) and cytotoxicity in HeLa cells (Figure 15c). ROS induction and cytotoxicity of the compounds correlated, suggesting a mechanistic link between both processes. Interestingly, TCMP-2 displayed only moderate cytotoxic effects, despite inducing the strongest ROS accumulation among the six compounds.

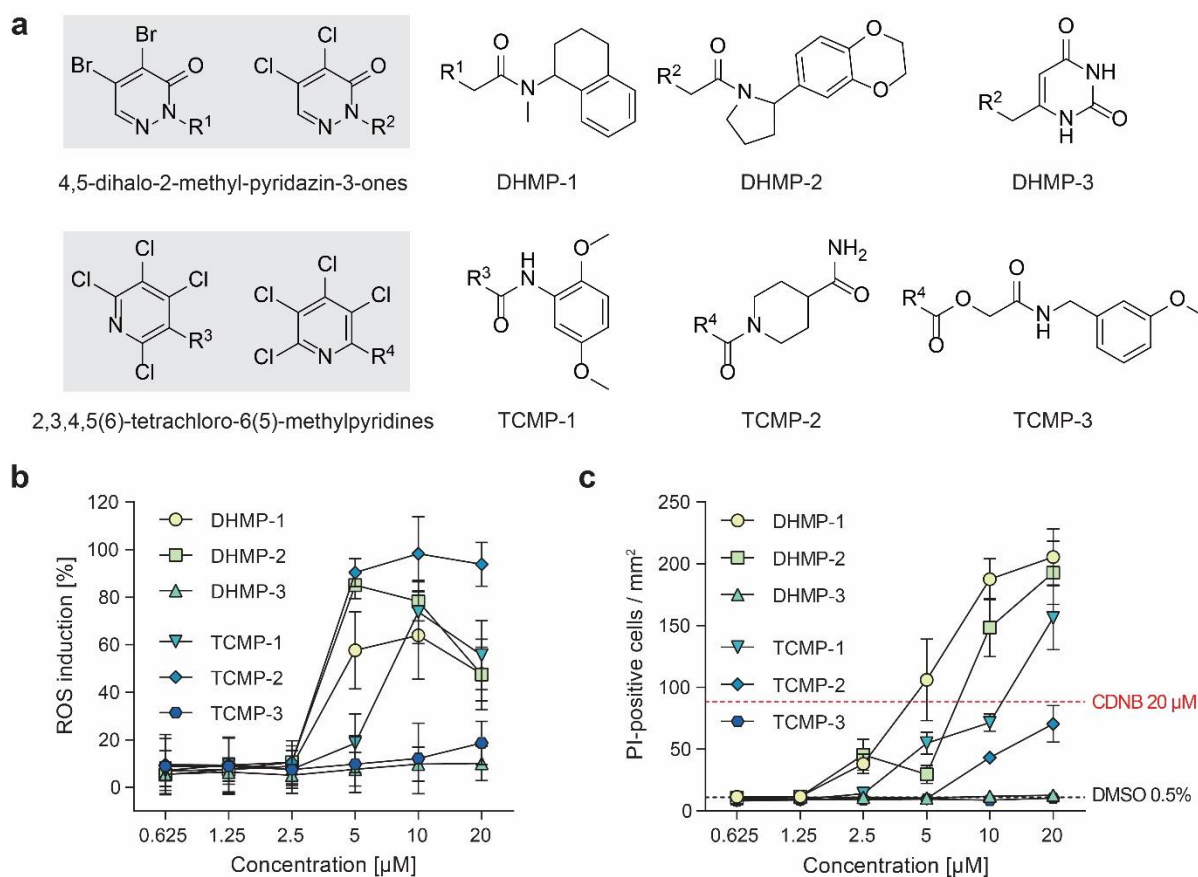


**Figure 15: Selected DHMP and TCMP compounds induce ROS accumulation and cytotoxicity. (a)** Chemical structures of three DHMP and three TCMP compounds that were selected for in-depth studies. **(b)** ROS induction measured by CM-H<sub>2</sub>DCFDA in HeLa cells after 60 min of compound treatment. Data were normalized to values of cells treated with 0.5 % DMSO (=0 %) or 10 µM CDNB (100 %). Mean values ± SD, N = 4, n = 3 **(c)** Cytotoxicity induction in HeLa cells determined via IncuCyte ZOOM-based real-time live-cell analysis combined with propidium iodide (PI) staining. Cells were treated with compounds in the presence of 25 µM PI and monitored over 24 h. Number of PI-positive cells after 24 h is shown. Mean values ± SD, N = 3, n = 3

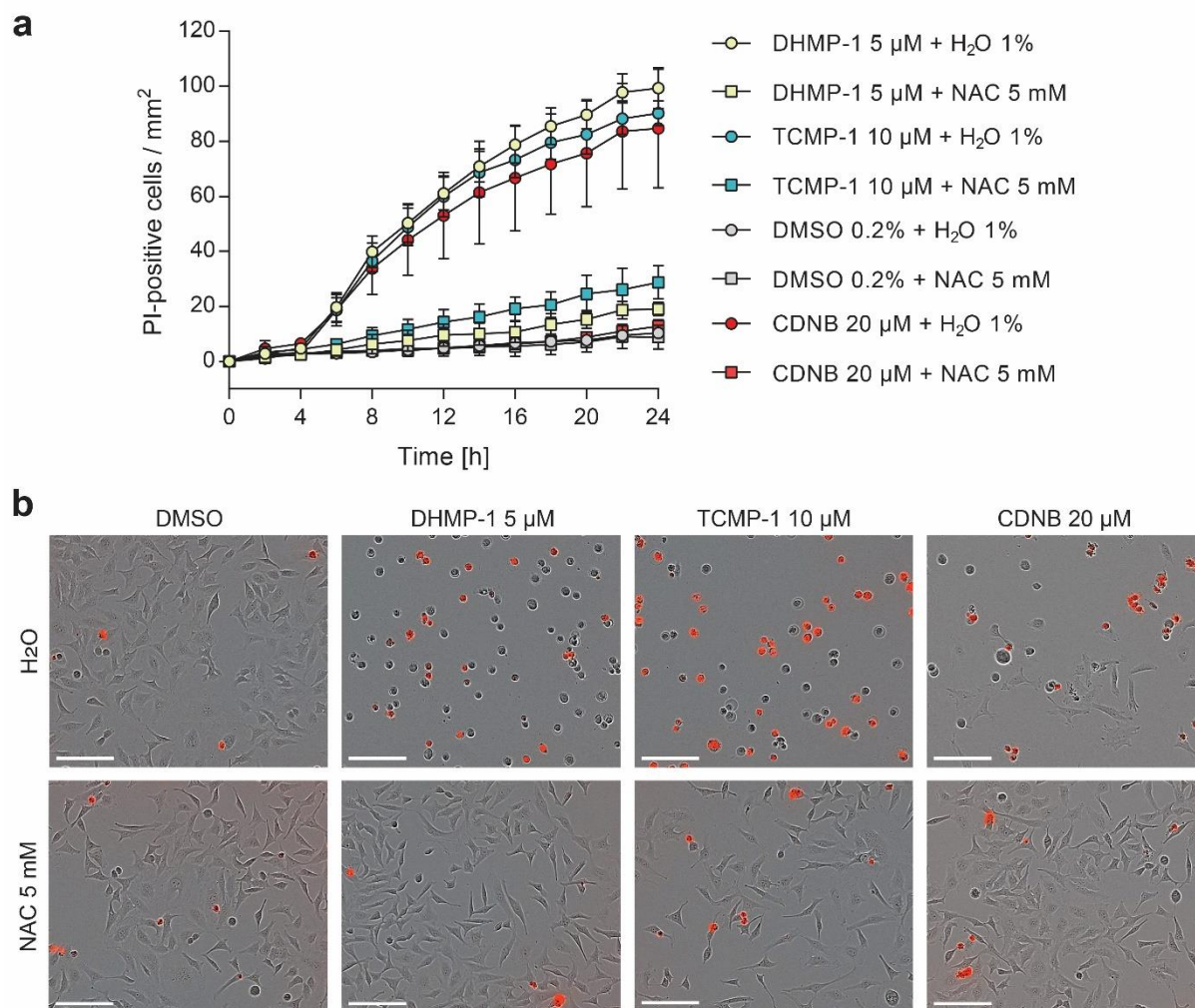


**Figure 16: Cytotoxic effects of DHMP-1 and TCMP-1 are prevented by antioxidant treatment.** HeLa cells were treated with 5 mM N-acetylcysteine (NAC) 1 h prior and during treatment with compounds in the presence of 25 µM propidium iodide (PI, red staining). Cytotoxic effects were monitored by means of IncuCyte ZOOM-based real-time live-cell analysis. **(a)** Quantification of a representative data set Mean values  $\pm$  SD, N = 3, n = 3. **(b)** Representative images after 24 h of compound treatment, scale bar = 150 µm.

To test this hypothesis, DHMP-1 and TCMP-1 were subjected to a co-treatment with the cell-permeable antioxidant N-acetylcysteine (NAC) (Figure 16). If the cytotoxicity was ROS-dependent, antioxidants should prevent it due to their ROS-scavenging property. NAC treatment partly suppressed cytotoxic effects of both compounds and of the known GSH-depleting compound CDNB, reflected in the low PI-count and unaffected cellular morphology.

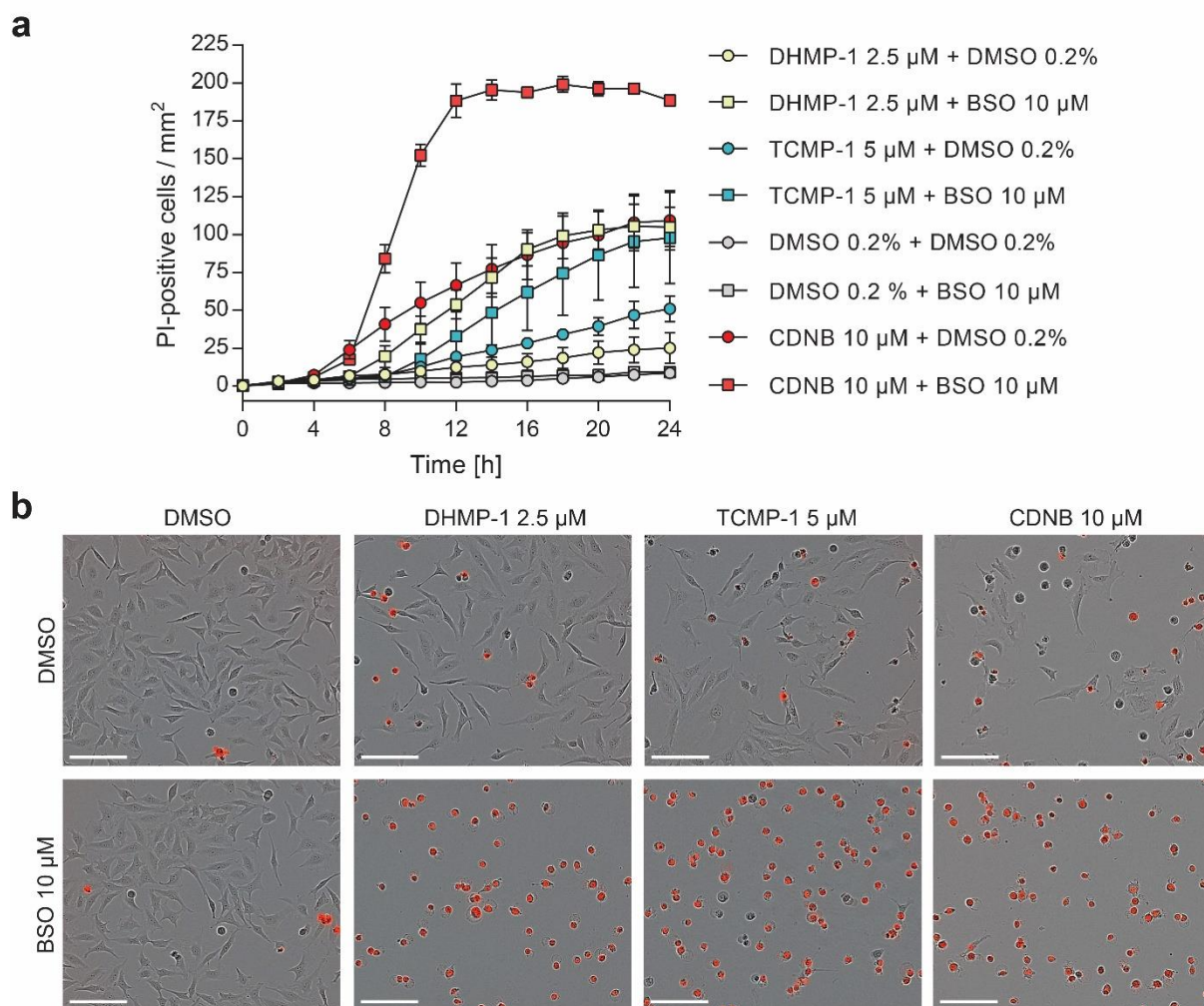


**Figure 17: Combinatorial DHMP-1 or TCMP-1 treatment with a GSH synthesis inhibitor induce synergistic cytotoxicity.** HeLa cells were co-treated with compounds and 10  $\mu\text{M}$  BSO at subtoxic concentrations in the presence of 25  $\mu\text{M}$  propidium iodide (PI, red staining). Cytotoxic effects were monitored by means of IncuCyte ZOOM-based real-time live-cell analysis. **(a)** Quantification of a representative data set. Mean values  $\pm$  SD,  $N = 3$ ,  $n = 3$ . **(b)** Representative images after 24 h of compound treatment, scale bar = 150  $\mu\text{m}$ .

Furthermore, GSH-depleting compounds should display synergistic effects with buthionine sulfoximinine (BSO), which decreases cellular GSH levels via inhibition of GSH synthesis.<sup>190</sup> Thus, cells were co-treated with non-toxic concentrations of DHMP-1 or TCMP-1 and the GSH synthesis inhibitor buthionine sulfoximinine (BSO), which induced cytotoxicity (Figure 17). Both anti- and prooxidative co-treatment modulates the cytotoxic properties of DHMP-1 and TCMP-1, which further supports the hypothesis that the cytotoxicity of these compounds is ROS-dependent.

Next, the influence of the compounds on cellular glutathione levels was confirmed (Figure 18). DHMP-1 and -2, as well as TCMP-2 displayed a strong depletion, comparable to CDNB, while

DHMP-3 and TCMP-3 hardly influenced GSH levels. Surprisingly, TCMP-1 did not alter the cellular GSH content, although it induced strong ROS accumulation and cytotoxicity.

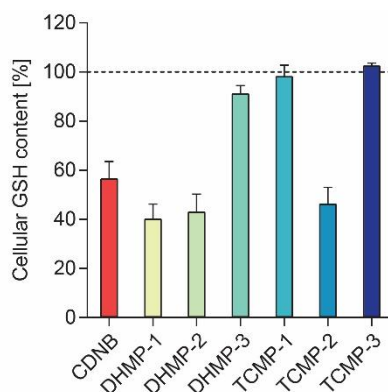


**Figure 18: DHMP and TCMP deplete GSH in cells.** GSH content of HeLa cells was determined after 1 h of compound treatment via Ellman's reagent. Data were normalized to values of cells treated with DMSO (100 %). Mean values  $\pm$  SD, N = 1, n = 3

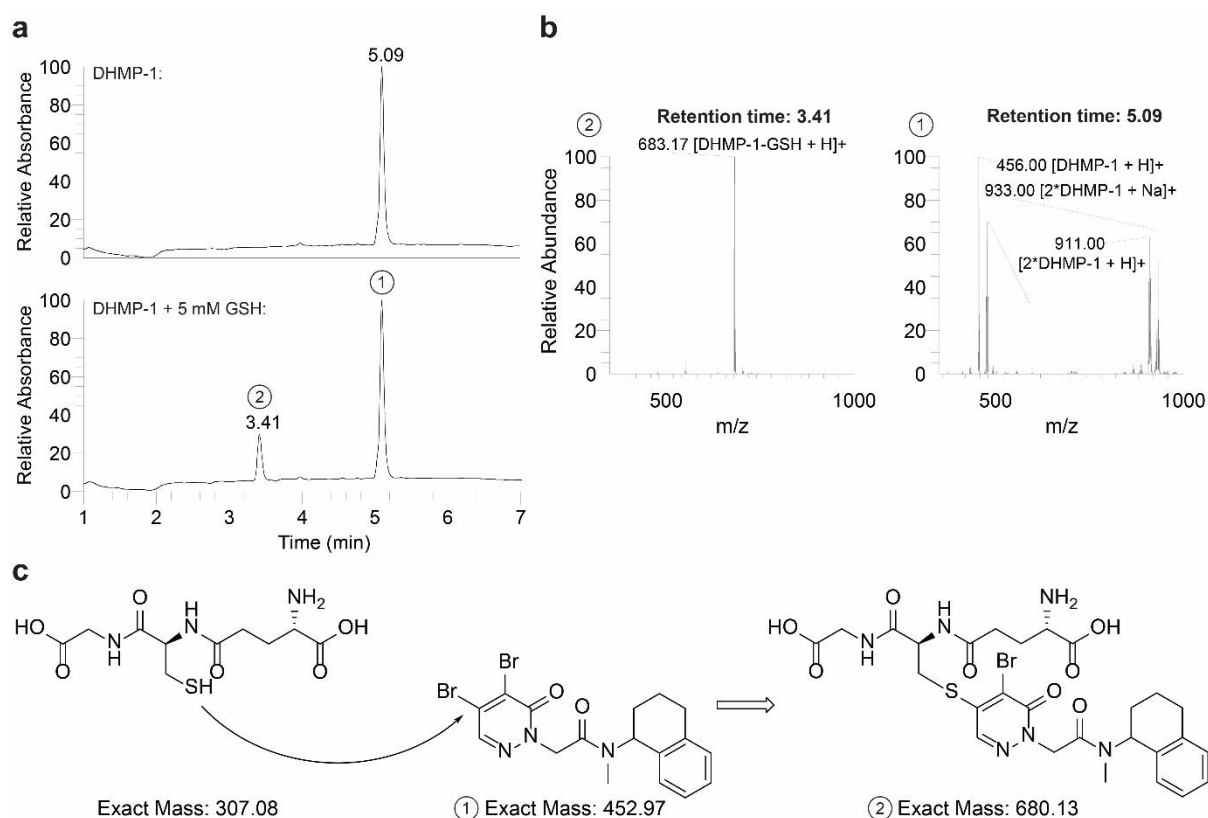


**Figure 19: DHMP-1 spontaneously reacts with GSH in solution.** DHMP-1 (100  $\mu$ M) was incubated in PBS for 1 h at 37  $^{\circ}$ C in the presence or absence of GSH (5 mM) and analyzed via UHPLC/ESI-MS. **(a)** Liquid chromatograms (C18 column; buffer A: H<sub>2</sub>O + 0.1 % formic acid; buffer B: acetonitrile + 0.1 % formic acid; 10-95 % gradient in 5 min) **(b)** Mass spectra of DHMP-1 and its putative GSH-conjugate. **(c)** Proposed reaction of DHMP-1 with GSH.

GSH-reactive compounds react with GSH spontaneously, however the reaction can be catalyzed by GST.<sup>191</sup> To test whether the depletion of GSH by DHMP- and THMP-containing compounds depends on the catalysis via glutathione-S-transferases, the reaction of the six DHMP and TCMP compounds with GSH in aqueous solutions was investigated. For this, compounds were incubated in PBS in the presence or absence of GSH for 1 h and subjected to a UHPLC/ESI-MS measurement. Results for DHMP-1 and TCMP-1 are shown in Figure 19 and Figure 20, respectively.

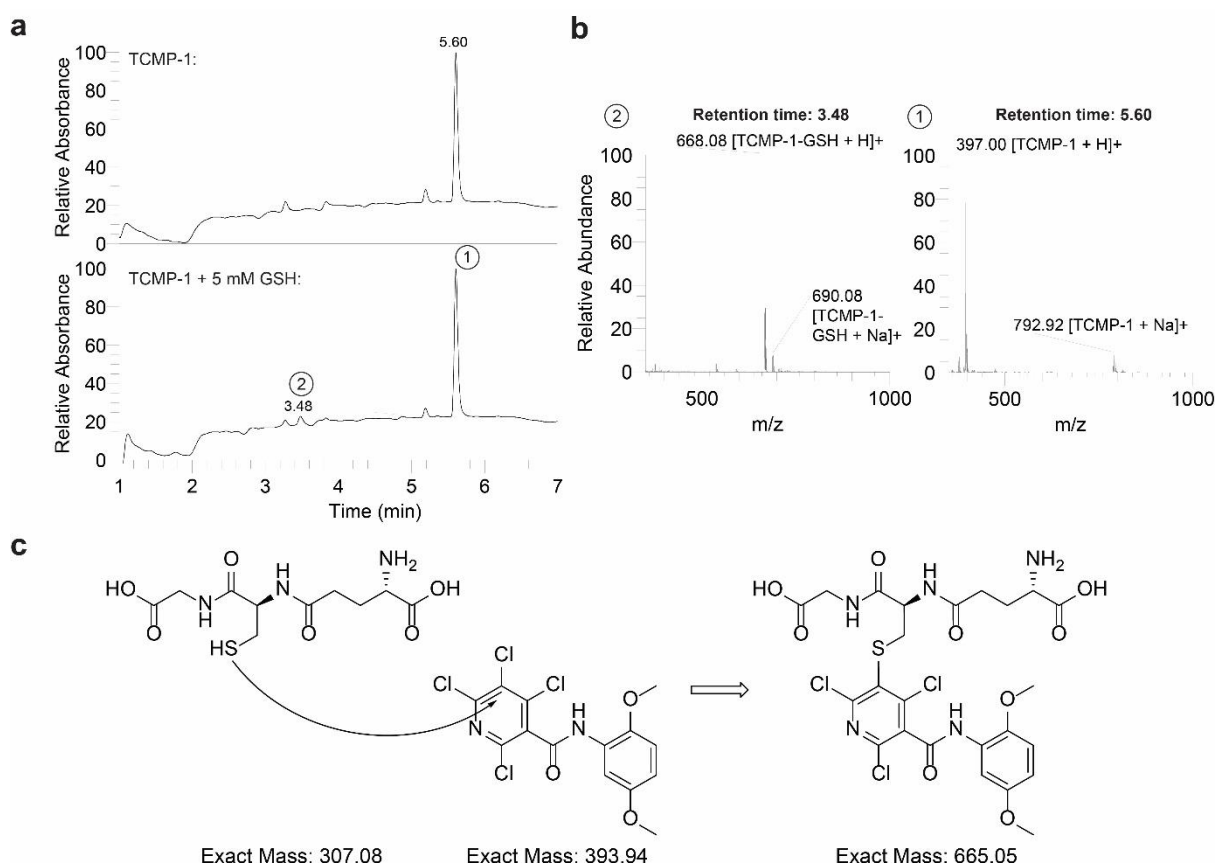


**Figure 20: TCMP-1 spontaneously reacts with GSH in solution.** TCMP-1 (100  $\mu$ M) was incubated in PBS for 1 h at 37  $^{\circ}$ C in the presence or absence of GSH (5 mM) and analyzed via UHPLC/ESI-MS. **(a)** Liquid chromatograms (C18 column; buffer A: H<sub>2</sub>O + 0.1 % formic acid; buffer B: acetonitrile + 0.1 % formic acid; 10-95 % gradient in 5 min) **(b)** Mass spectra of TCMP-1 and its putative GSH-conjugate. **(c)** Proposed reaction of TCMP-1 with GSH.

In both samples a strong peak with a retention time of 5.09 min (Figure 19a) was found, which corresponds to DHMP-1. In the presence of GSH, a second peak with a retention time of 3.41 was detected. Based on its mass and isotope pattern, this peak may correspond to a DHMP-1-GSH conjugate, formed by nucleophilic substitution of one of the bromides by the thiol group of GSH



(Figure 19b). One of the two possible reaction products is depicted in Figure 19c. TCMP-1 displayed a peak with a retention time of 5.60 min as well as an additional peak with a retention time of 3.48 after incubation with GSH (Figure 20a). Mass and isotope pattern of this reaction product suggest a conjugate formation by a nucleophilic substitution of one of the four chlorines by the thiol group of GSH (Figure 20b and 20c). Similar results were obtained for the other four compounds (Supplementary Figure 1-6). Interestingly, all six compounds form GSH conjugates in solution, although only half of them depleted GSH in cells.

Subsequently, the effects of the six compounds and additional derivatives on cellular GSH levels were studied at varying concentrations (Figure 21). Except for TCMP-3, all of the tested compounds showed a concentration-dependent, moderate to strong depletion of cellular GSH. TCMP-1, which did not affect cellular GSH levels measured by Ellman's reagent (Figure 18), also reduces GSH in HeLa cells dose-dependently.

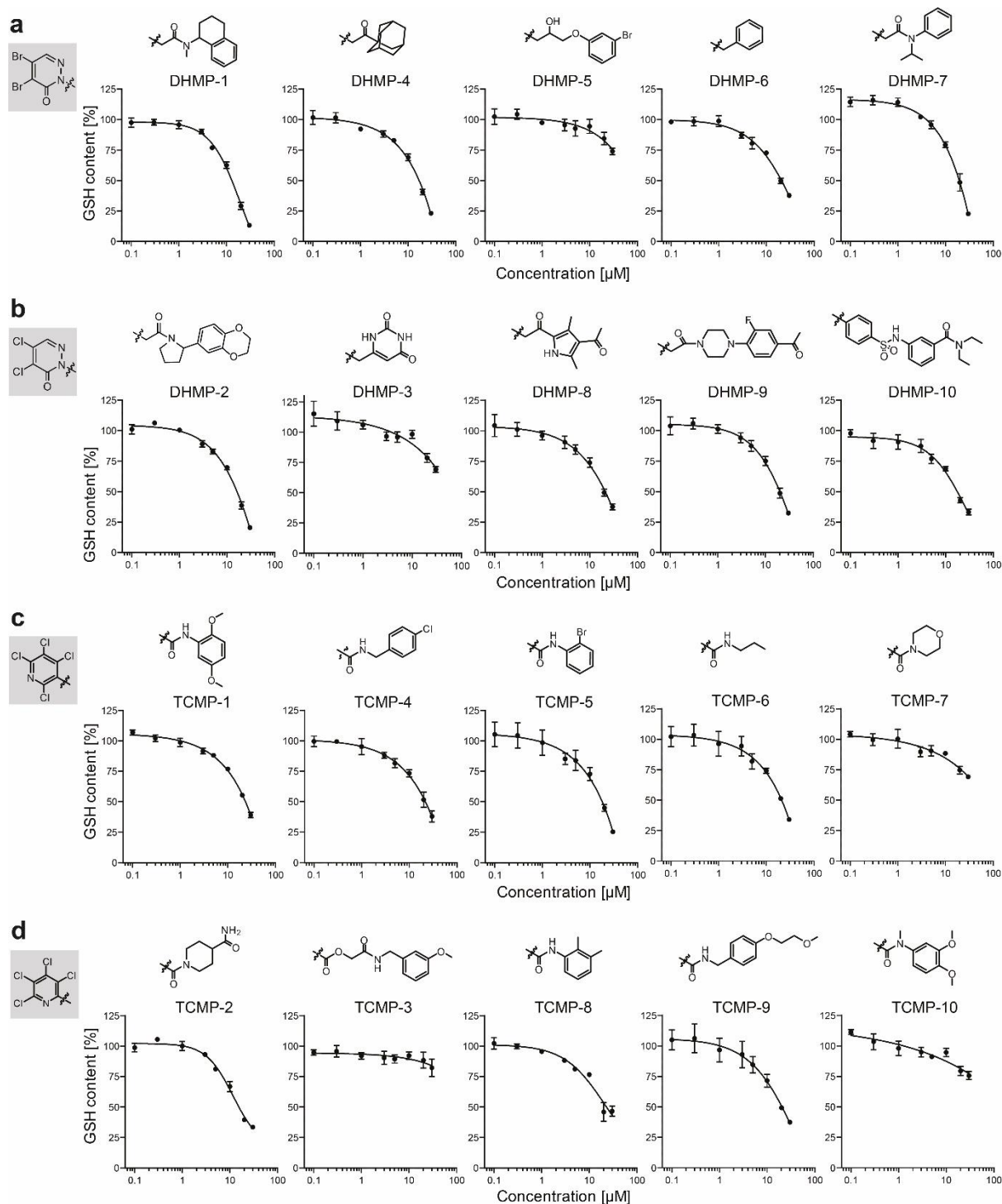


**Figure 21: DHMP and TCMP compounds deplete GSH in cells.** HeLa cells were treated with compounds for 1 h and total glutathione levels were determined via a luminescence-based assay. Data were normalized to values of cells treated with DMSO (100 %). Mean values  $\pm$  SD, N = 2, n = 3

Taken together, both DHMP- and TCMP-containing compounds were identified as strong depleters of cellular glutathione. Both moieties react with GSH spontaneously and their GSH-depleting property may cause cellular ROS induction and cytotoxicity.

### 5.3 Diaminopyrimidines as novel inducers of cellular ROS accumulation

In the course of the phenotypic screening, a group of diaminopyrimidine-based compounds was identified as potent inducers of ROS accumulation with low micromolar potency. The hit compound DP01 induced ROS accumulation not only in U-2 OS cells, which were used for screening, but also in HeLa cells with comparable potency. Further in-depth characterization was conducted in HeLa cells.

#### 5.3.1 Structure-activity relationship study

To improve the potency of the initial screening hit, a structure-activity relationship (SAR) study of the diaminopyrimidine-based compound class was explored based on 32 commercially available compounds. The initial screening hit DP01 was also found active in a phenotypic assay for inhibitors of rapamycin- and starvation-induced autophagy. To distinguish whether these activities are linked to ROS induction by DP01, all DP01 derivatives were also tested for inhibition of autophagy. In addition, its limited water solubility restricted the use of DP01 in cellular assays to a maximal concentration of 10  $\mu$ M. Both issues were addressed in the course of the SAR study.

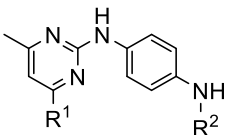
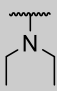
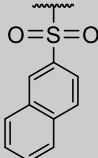
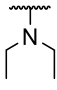
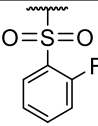
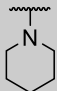
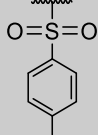
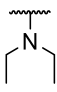
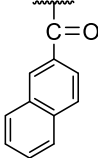
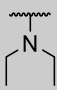
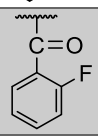
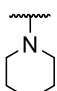
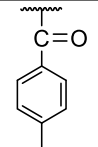
The piperidine group was the first moiety to be investigated by substitution for other amines (Table 6). A diethylamine substitution (DP02) did not influence the ROS-inducing activity, pyrrolidine (DP03) and morpholine (DP04) substitutions were tolerated with a moderate increase in the  $EC_{50}$ . The smaller dimethylamine (DP05) and ethylamine (DP06) substitutions caused a large decrease in activity and replacement for the bulkier (methoxy)phenylamine (DP07 / DP08) led to complete loss of activity. In terms of autophagy inhibition, different amines were tolerated. Ethylamine and morpholine substitutions (DP06 / DP04) displayed the strongest activities among these substituents.

**Table 6: SAR of the piperidine group.** ROS induction in HeLa cells and inhibition of rapamycin- and starvation-induced autophagy in eGFP-LC3-expressing MCF7 cells. Mean values  $\pm$  SD,  $n \geq 3$ , n.d. = not determined. Data were obtained by COMAS, Dortmund.

R <sup>1</sup>	ID	ROS EC <sub>50</sub> [μM]	Rapamycin-induced autophagy IC <sub>50</sub> [μM]	Starvation-induced autophagy IC <sub>50</sub> [μM]
	DP02	2.4 $\pm$ 0.8	n.d.	1.8 $\pm$ 0.4
	DP01	2.7 $\pm$ 0.9	3.8 $\pm$ 4.1	8.9 $\pm$ 0.4
	DP03	6.1 $\pm$ 1.9	4.7 $\pm$ 2.2	1.8 $\pm$ 0.7
	DP04	7.6 $\pm$ 0.2	0.5 $\pm$ 0.1	0.1 $\pm$ 0.0
	DP06	14.4 $\pm$ 2	0.8 $\pm$ 0.3	0.1 $\pm$ 0.0
	DP05	25.4 $\pm$ 4	>30	n.d.
	DP07	>30	1.5 $\pm$ 0.2	0.5 $\pm$ 0.2
	DP08	>30	2.3 $\pm$ 0.9	0.8 $\pm$ 0.3

The influence of the sulfonamide group was evaluated by comparing three compounds with their respective analogs that contain an amide group instead (Table 7). All of these were lacking ROS-inducing activity, thereby demonstrating the necessity of the sulfonamide group for this activity. No clear trend was observable for inhibition of autophagy.

**Table 7: SAR of the sulfonamide group.** ROS induction in HeLa cells and inhibition of rapamycin- and starvation-induced autophagy in eGFP-LC3-expressing MCF7 cells. Mean values  $\pm$  SD,  $n \geq 3$ . Data were obtained by COMAS, Dortmund.

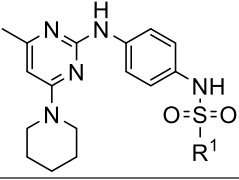
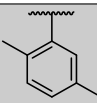
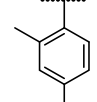
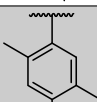
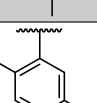
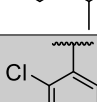
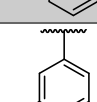
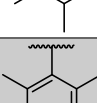
					
R <sup>1</sup>	R <sup>2</sup>	ID	ROS EC <sub>50</sub> [μM]	Rapamycin- induced autophagy IC <sub>50</sub> [μM]	Starvation- induced autophagy IC <sub>50</sub> [μM]
		<b>DP19</b>	6.2 $\pm$ 1.1	>30	>30
		<b>DP16</b>	7.5 $\pm$ 0.7	1.1 $\pm$ 0.2	1.1 $\pm$ 0.1
		<b>DP23</b>	8.5 $\pm$ 0.0	1.4 $\pm$ 0.7	0.5 $\pm$ 0.1
		<b>DP41</b>	>30	3.1 $\pm$ 2.1	2.8 $\pm$ 1.6
		<b>DP39</b>	>30	>30	>30
		<b>DP37</b>	>30	0.5 $\pm$ 0.1	0.1 $\pm$ 0.1

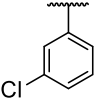
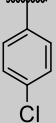
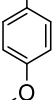
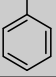
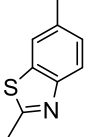
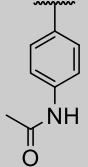
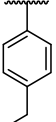
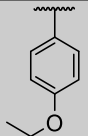
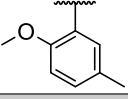
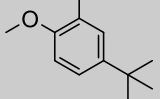
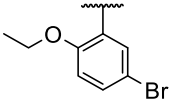
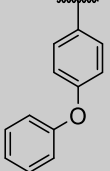
Various substitution patterns of the sulfonylphenyl group were tested (Table 8). Removal of the methyl and isopropyl groups from DP01 (DP43) led to an approximately three-fold decrease in ROS-induction. Single substitution with chloride was tolerated in the 2-position (DP29), however decreased activity in the 3- and 4-position (DP42 / DP33). All tested substitutions in the 4-position led to decrease or complete loss of activity (DP44 / DP21 / DP46 / DP48 / DP31). A 2,5-dimethyl substitution (DP55) increased activity three-fold, however combinations of bulkier substituents in these positions strongly decreased the activity (DP10 / DP26 / DP38). Other di- and also trimethyl substitution patterns were

tolerated, with moderate to high biological activity (DP14 / DP24 / DP40 / DP17). Replacement of the phenyl group by a methylbenzothiazole is tolerated with moderate activity.

The substitution pattern of the sulfonylphenyl group hardly influenced autophagy inhibition. All of the before-mentioned derivatives were active with low micromolar potency, with a few exceptions that were inactive in the assay for inhibition of rapamycin-induced autophagy (DP48 / DP31 / DP17 / DP40). DP55, which was the most potent ROS-inducing compound with an EC<sub>50</sub> of 0.9 μM, also inhibited starvation-induced autophagy with an IC<sub>50</sub> of 0.2 μM.

**Table 8: SAR of the sulfonylphenyl group substitution.** ROS induction in HeLa cells and inhibition of rapamycin- and starvation-induced autophagy in eGFP-LC3-expressing MCF7 cells. Mean values ± SD, n ≥ 3, n.d. = not determined. Data were obtained by COMAS, Dortmund.

				
R <sup>1</sup>	ID	ROS EC <sub>50</sub> [μM]	Rapamycin- induced autophagy IC <sub>50</sub> [μM]	Starvation- induced autophagy IC <sub>50</sub> [μM]
	DP55	0.9 ± 0.2	3.1 ± 1.7	0.2 ± 0.1
	DP14	1.2 ± 0.2	5.2 ± 2.6	0.4 ± 0.1
	DP17	2.1 ± 0.2	>30	2.3 ± 0.5
	DP01	2.7 ± 0.9	3.8 ± 4.1	8.9 ± 0.4
	DP29	2.7 ± 0.5	1.5 ± 0.3	0.4 ± 0.1
	DP24	5.0 ± 0.9	4.9 ± 2.4	0.9 ± 0.2
	DP40	7.6 ± 0.6	>30	5.9 ± 1.1

	<b>DP42</b>	7.7 ± 0.2	1.5 ± 0.4	0.2 ± 0.1
	<b>DP33</b>	9.2 ± 0.3	3.4 ± 0.3	0.6 ± 0.2
	<b>DP21</b>	9.7 ± 0.9	3.7 ± 1.1	1.3 ± 0.3
	<b>DP43</b>	10.2 ± 0.0	0.7 ± 0.1	0.4 ± 0.1
	<b>DP34</b>	12.1 ± 1	4.6 ± 1.9	0.6 ± 0.0
	<b>DP31</b>	13.2 ± 1	>30	6.7 ± 0.2
	<b>DP44</b>	14.9 ± 2.0	4.2 ± 1.5	0.5 ± 0.1
	<b>DP46</b>	21.3 ± 2.0	4.8 ± 1.1	1.5 ± 0.2
	<b>DP10</b>	>30	6.0 ± 3.1	2.0 ± 0.5
	<b>DP26</b>	>30	n.d.	2.1 ± 0.8
	<b>DP38</b>	>30	9.6 ± 0.3	5.9 ± 0.6
	<b>DP48</b>	>30	>30	4.4 ± 0.3

To further explore the SAR, additional compounds were synthesized by Dr. Hao Xu and Dr. Houhua Li. As aumitin, a chemically related diaminopyrimidine, inhibits autophagy via inhibition of mitochondrial respiration, selected compounds were subjected to a *Mito Stress Test* to assess their influence on this

process.<sup>192</sup> In this assay, the oxygen consumption rate (OCR) of living cells is monitored as a measure of oxidative phosphorylation. At first, test compounds are injected followed by a continuous measurement over one hour, followed by sequential injections of different mitochondrial inhibitors. At first, Oligomycin was added, which inhibits the ATP synthase.<sup>193</sup> As a result, cells switch from oxidative phosphorylation to glycolysis, which is reflected in a decrease in the OCR. Next the uncoupling agent FCCP was injected, which disrupts the mitochondrial proton gradient.<sup>194</sup> Cells counteract this effect by increasing the activity of the ETC complexes, which transport protons from the mitochondrial matrix to the intermembrane space, thereby increasing the OCR to its maximum.<sup>195</sup> In the last step, rotenone and antimycin A, which inhibit ETC complex I and III, respectively, are added to inhibit mitochondrial respiration completely.<sup>196,197</sup> DP01 and DP55 potently inhibited mitochondrial respiration with  $IC_{50}$  values of  $1.7 \pm 0.2 \mu\text{M}$  and  $0.7 \pm 0.2 \mu\text{M}$ , respectively (Figure 22).

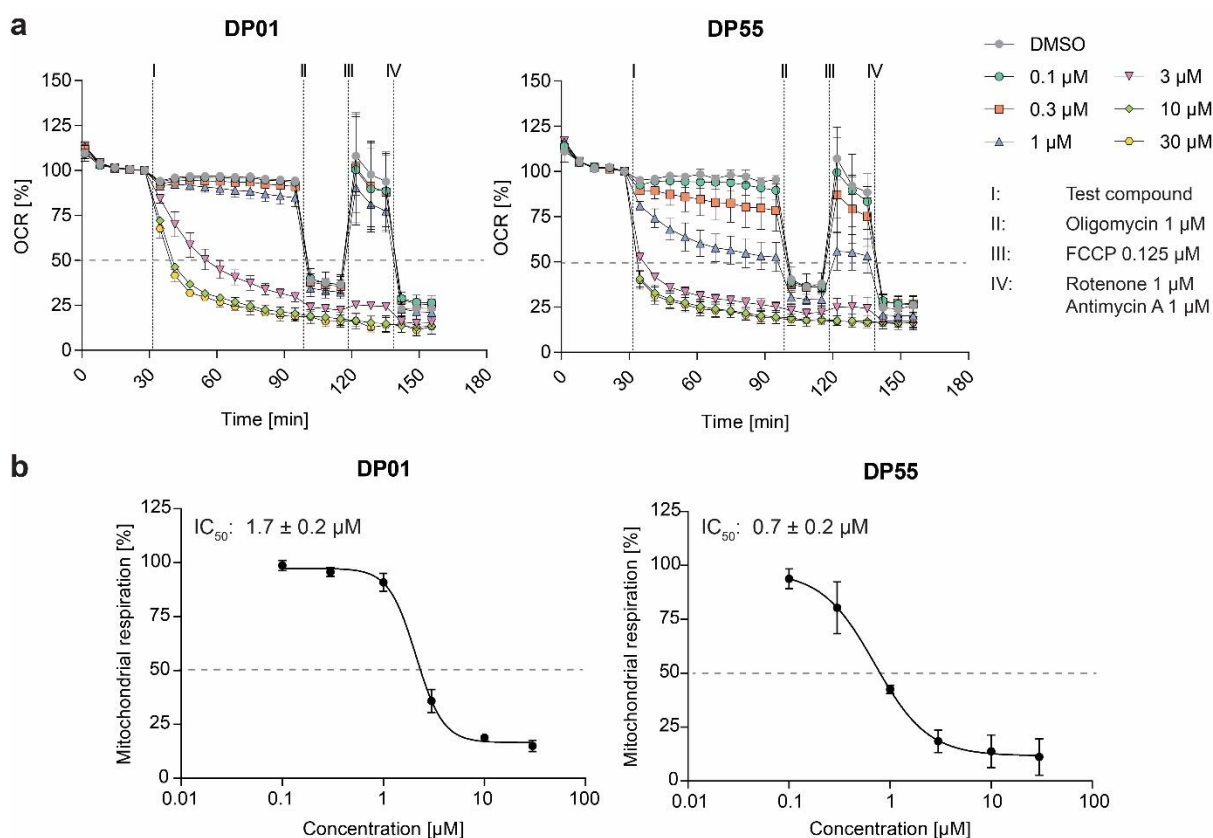


**Figure 22: DP01 and DP55 inhibit mitochondrial respiration.** The oxygen consumption rate (OCR) of HeLa cells was measured in the course of a ‘Mito Stress Test’. **(a)** Test compounds, 1  $\mu\text{M}$  oligomycin, 125 nm FCCP and 1  $\mu\text{M}$  rotenone and antimycin A were injected at the indicated time points. **(b)**  $IC_{50}$  values were calculated based on the last measurement before the injection of oligomycin. Mean values  $\pm$  SD,  $N \geq 2$ ,  $n = 3$ . Data were obtained by Dr. Yushi Futamura, co-worker of Prof. Hiroyuki Osada, RIKEN CSRS, Japan.



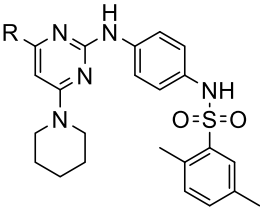
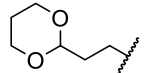
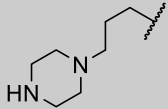
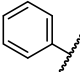
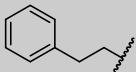
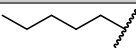
The influence of an altered pyrimidine ring orientation on ROS induction was evaluated by comparing DP55 with DP56 and DP61 with DP63, respectively (Table 9). Such alteration was well tolerated, with a minor decrease in ROS-inducing activity. However, the altered ring orientation strongly decreased the inhibitory activities on autophagy and mitochondrial respiration (DP63).

**Table 9: SAR of the pyrimidine ring orientation.** ROS induction in HeLa cells and inhibition of rapamycin- and starvation-induced autophagy in eGFP-LC3-expressing MCF7 cells. Mean values  $\pm$  SD,  $n \geq 3$ . Data on ROS induction and autophagy inhibition were obtained by COMAS, Dortmund. Data on mitochondrial respiration inhibition (except for DP63) were obtained by Dr. Yushi Futamura, co-worker of Prof. Hiroyuki Osada, RIKEN CSRS, Japan.

R <sup>1</sup>	R <sup>2</sup>	R <sup>3</sup>	ID	ROS EC <sub>50</sub> [μM]	Rapamycin- induced autophagy IC <sub>50</sub> [μM]	Starvation- induced autophagy IC <sub>50</sub> [μM]	Mitochondrial respiration IC <sub>50</sub> [μM]
N	CH	Me	<b>DP55</b>	0.9 $\pm$ 0.2	3.1 $\pm$ 1.7	0.2 $\pm$ 0.1	0.7 $\pm$ 0.2
CH	N		<b>DP56</b>	1.2 $\pm$ 0.3	>30	5.9 $\pm$ 0.5	5.7 $\pm$ 1.0
N	CH	Et	<b>DP61</b>	1.3 $\pm$ 0.3	>30	2.5 $\pm$ 1.1	2.5 $\pm$ 0.4
CH	N		<b>DP63</b>	2.6 $\pm$ 1.0	>30	>30	>30

The 4-position of the pyrimidine ring was explored for its influence on ROS induction (Table 10). While a phenyl (DP64) or phenethyl (DP66) substitution displayed moderate activity, a pentyl substitution (DP66) showed a complete loss of ROS-inducing activity, potentially caused due to decreased water solubility. The addition of more polar substituents of comparable size, like 1,3-dioxan-2-yl ethyl (DP69), 4-piperazin-1-ylpropyl (DP70) or 3-morpholinopropyl (DP68), led to a potency comparable to DP55. Together with DP69, DP68 is the most potent ROS inducer of the collection with an EC<sub>50</sub> of 0.5 μM. Interestingly, substituents exceeding the size of an ethyl group completely diminished both autophagy- and mitochondrial respiration-inhibiting activities, as it is the case for DP68 (Figure 23). DP69, however, is an exception, as it still inhibited starvation induced autophagy. Furthermore, the piperazinylpropyl derivative (DP70) was found to increase the number of eGFP-LC3 punctae.

**Table 10: SAR of the 4-substituent of the pyrimidine ring.** ROS induction in HeLa cells and inhibition of rapamycin- and starvation-induced autophagy in eGFP-LC3-expressing MCF7 cells. Mean values  $\pm$  SD,  $n \geq 3$ . Data on ROS induction and autophagy inhibition were obtained by COMAS, Dortmund. Data on mitochondrial respiration inhibition (except for DP68 and DP70) were obtained by Dr. Yushi Futamura, co-worker of Prof. Hiroyuki Osada, RIKEN CSRS, Japan.

R	ID	ROS EC <sub>50</sub> [ $\mu$ M]	Rapamycin-induced autophagy IC <sub>50</sub> [ $\mu$ M]	Starvation-induced autophagy IC <sub>50</sub> [ $\mu$ M]	Mitochondrial respiration IC <sub>50</sub> [ $\mu$ M]
	DP68	0.5 $\pm$ 0.1	>30	>30	>30
	DP69	0.5 $\pm$ 0.1	>30	4.5 $\pm$ 0.3	n.d.
Me	DP55	0.9 $\pm$ 0.2	3.1 $\pm$ 1.7	0.2 $\pm$ 0.1	0.7 $\pm$ 0.2
Et	DP61	1.3 $\pm$ 0.3	>30	2.5 $\pm$ 1.1	2.5 $\pm$ 0.4
	DP70	1.5 $\pm$ 0.4	potential co-activator	potential co-activator	>30
	DP64	6.5 $\pm$ 2.0	>30	>30	>30
	DP65	8.4 $\pm$ 1.1	>30	>30	>30
	DP66	>30	>30	>30	n.d.

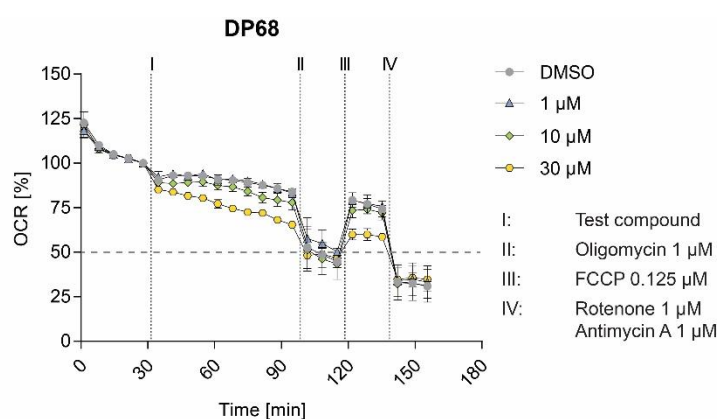
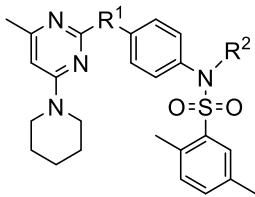


**Figure 23: DP68 does not inhibit mitochondrial respiration.** The oxygen consumption rate (OCR) of HeLa cells was measured in the course of a 'Mito Stress Test'. Compounds, (II) 1  $\mu$ M oligomycin, (III) 125 nm FCCP and (IV) 1  $\mu$ M rotenone and antimycin A were injected at the indicated time points. IC<sub>50</sub> values were calculated based on the last measurement before the injection of oligomycin. Mean values  $\pm$  SD, N = 2, n = 3

The substitution of the amine group between the pyrimidine and benzene ring for an ether group (DP67) led to a strong decrease of activity in all four assays (Table 11). Methylation of the sulfonamide group strongly decreased the ROS-inducing activity (DP60), however hardly affected the inhibition of autophagy or mitochondrial respiration.

**Table 11: SAR of the p-amino-aniline.** ROS induction in HeLa cells and inhibition of rapamycin- and starvation-induced autophagy in eGFP-LC3-expressing MCF7 cells. Mean values  $\pm$  SD,  $n \geq 3$ . Data on ROS induction and autophagy inhibition were obtained by COMAS, Dortmund. Data on mitochondrial respiration inhibition were obtained by Dr. Yushi Futamura, co-worker of Prof. Hiroyuki Osada, RIKEN CSRS, Japan.



R <sup>1</sup>	R <sup>2</sup>	ID	ROS EC <sub>50</sub> [μM]	Rapamycin- induced autophagy IC <sub>50</sub> [μM]	Starvation- induced autophagy IC <sub>50</sub> [μM]	Mitochondrial respiration IC <sub>50</sub> [μM]
NH	H	<b>DP55</b>	0.9 $\pm$ 0.2	3.1 $\pm$ 1.7	0.2 $\pm$ 0.1	0.7 $\pm$ 0.2
O	H	<b>DP67</b>	10.0 $\pm$ 1	>30	4.2 $\pm$ 0.3	11.0 $\pm$ 1.7
NH	CH <sub>3</sub>	<b>DP60</b>	19.6 $\pm$ 5	3.7 $\pm$ 1.1	0.5 $\pm$ 0.2	1.8 $\pm$ 0.3

The removal of the 2,5-dimethylbenzenesulfonyl moiety (DP59 / DP71 / DP72) led to complete loss of ROS induction, but only slightly decreased the autophagy- and mitochondrial respiration-inhibitory activity of DP59 (Table 12). With few exceptions, all compounds showed a similar trend in the rapamycin- and starvation- induced autophagy inhibition assays. The majority of the active compounds displayed a greater potency in the latter assay, which was also observed for aumitin.<sup>192</sup> The IC<sub>50</sub> values for inhibition of starvation-induced autophagy and mitochondrial respiration strongly correlated for each compound tested, which may indicate a mechanistic link between those two activities. In contrast, the structure-activity relationships for ROS induction and autophagy inhibition were strongly divergent, which suggests the independence of both biological activities. Thus, autophagy inhibition was considered to be an off-target effect of the hit compound DP01. In the course of the SAR study, DP01 was optimized in different ways. Relative to DP01, DP68 has an > 5-fold increased potency for ROS induction in HeLa cells. The 4-position of the pyrimidine ring tolerated the attachment of larger moieties

without compromising the ROS activity, enabling the synthesis of affinity probes for target identification. The substitution of the methyl group for a morpholinopropyl moiety not only increased the compound's water solubility, allowing its use up to 50  $\mu\text{M}$  in cell-based assays, but also diminished off-target effects, namely the inhibition of mitochondrial respiration and autophagy.

**Table 12: SAR of the 2,5-dimethylbenzenesulfonyl moiety.** ROS induction in HeLa cells and inhibition of rapamycin- and starvation-induced autophagy in eGFP-LC3-expressing MCF7 cells. Mean values  $\pm$  SD,  $n \geq 3$ . Data on ROS induction and autophagy inhibition were obtained by COMAS, Dortmund. Data on mitochondrial respiration inhibition (except for DP68 and DP70) were obtained by Dr. Yushi Futamura, co-worker of Prof. Hiroyuki Osada, RIKEN CSRS, Japan.

R <sup>1</sup>	R <sup>2</sup>	ID	ROS EC <sub>50</sub> [ $\mu\text{M}$ ]	Rapamycin-induced autophagy IC <sub>50</sub> [ $\mu\text{M}$ ]	Starvation-induced autophagy IC <sub>50</sub> [ $\mu\text{M}$ ]	Mitochondrial respiration IC <sub>50</sub> [ $\mu\text{M}$ ]
		DP68	0.5 $\pm$ 0.1	>30	>30	>30
Me		DP55	0.9 $\pm$ 0.2	3.1 $\pm$ 1.7	0.2 $\pm$ 0.1	0.7 $\pm$ 0.2
		DP70	1.5 $\pm$ 0.4	co-activator	co-activator	>30
		DP72	>30	>30	>30	n.d.
Me	H	DP59	>30	4.2 $\pm$ 4.3	1.8 $\pm$ 0.2	3.1 $\pm$ 0.9
		DP71	>30	>30	>30	n.d.

### 5.3.2 Biological characterization

The screening hit DP01 and the two highly potent derivatives DP55 and DP68 were tested in a manually conducted ROS assay in HeLa cells to confirm the data obtained during the SAR investigation (Figure 24a). For the three compounds the determined potency was comparable between both assays. The optimized compound DP68 was selected for further characterization. Time-dependent ROS measurements revealed that DP68-induced ROS accumulation is detectable in cells approximately 30 min after compound treatment (Figure 24b) and is constant over a time period of at least three days (Figure 24c).

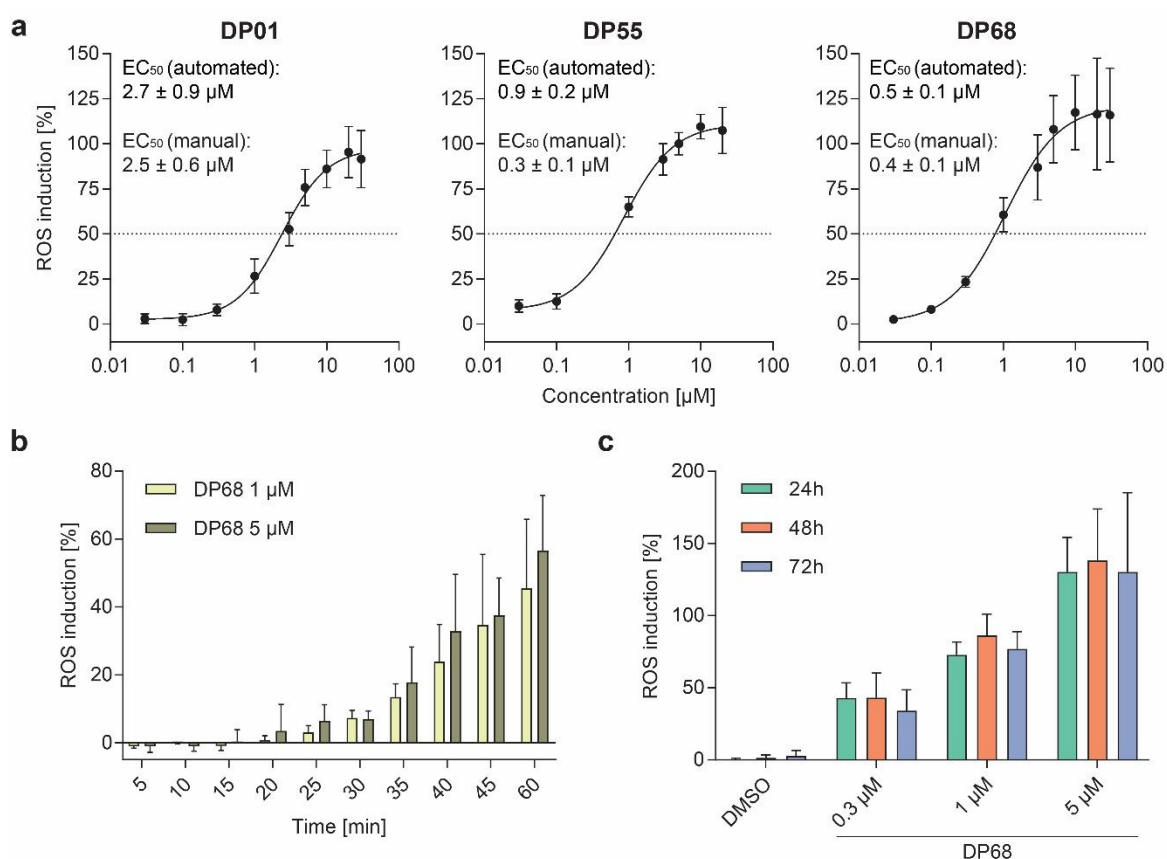


**Figure 24: DP68 induces a rapid and long-lasting induction of cellular ROS accumulation in HeLa cells.** (a) ROS-inducing activities of DP01, DP55 and DP68 obtained via manual assays. EC<sub>50</sub> values obtained from automated and manual assays shown. (b and c) Time-dependent ROS induction by DP68 over 60 min (b) or 72 h (c). ROS levels were measured via CM-H<sub>2</sub>DCFDA in HeLa cells. Mean values ± SD, N ≥ 3, n = 3. Data displayed in (b) and (c) were obtained by Daya Agne, MPI Dortmund.

It is known that ROS-inducing small molecules can exert their respective bioactivity in various ways, which not always include the modulation of a protein target. For instance, the natural product

salinomycin and the autophagy-inhibiting small molecule autoquin, both sequester and accumulate  $\text{Fe}^{2+}$  in lysosomes, thereby inducing lysosomal ROS elevation.<sup>198,185</sup> Thus, DP55, DP68 and their inactive analogs were tested for lysosomal accumulation, a process termed lysosomotropy, and for iron-chelation (Figure 25).

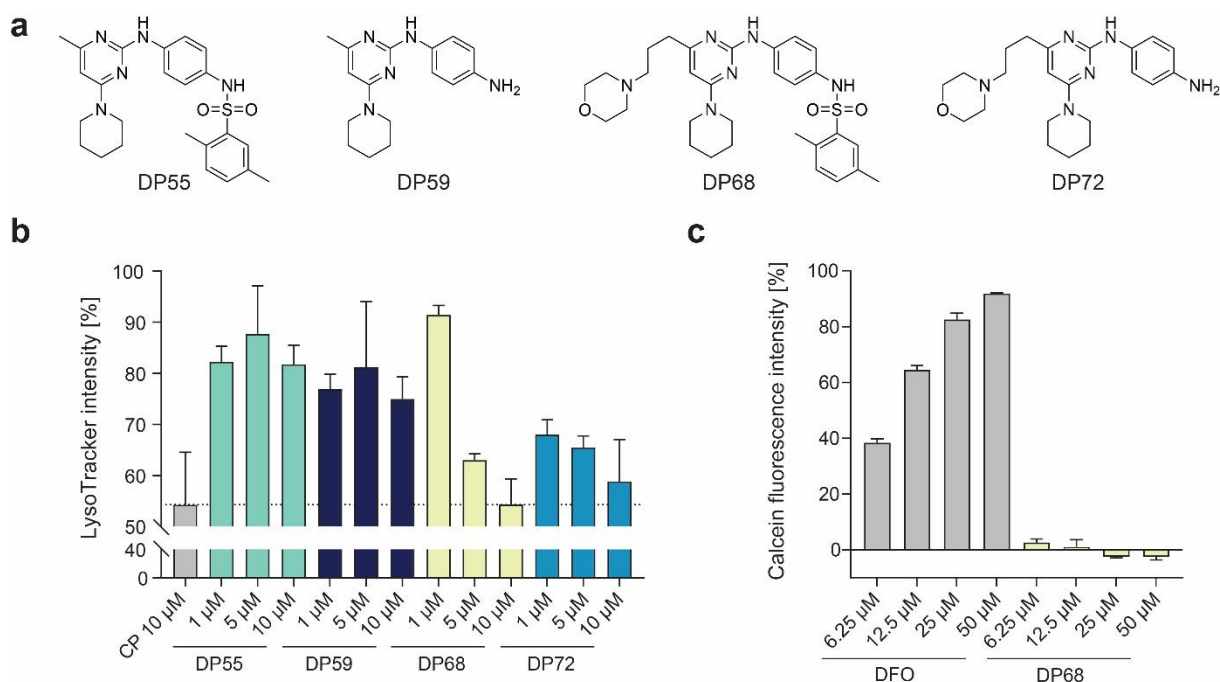


**Figure 25: DP68 accumulates in lysosomes, but does not induce ROS via iron chelation. (a)** Chemical structures of selected diaminopyrimidines. **(b)** Lysosomotropy assay. HeLa cells were treated with compounds for 60 min. Subsequently, LysoTracker Red DND-99 was added for 30 min, cells were washed, fixed and imaged. CP = Chlorpromazine. Data were normalized to values of cells treated with DMSO (100 %). Mean values  $\pm$  SD, N = 3, n = 3. **(c)** Fe<sup>2+</sup> chelation assay. Compounds were incubated in the presence of 12.5  $\mu\text{M}$  FeSO<sub>4</sub> and 25  $\mu\text{M}$  calcein at ambient temperature for 5 min prior to measuring calcein fluorescence. DFO = Deferoxamine. Data were normalized to values of vehicle samples (0 %) and calcein without FeSO<sub>4</sub> (100 %). Mean values  $\pm$  SD, N = 1, n = 3

For this, cells were incubated with the compounds prior to the addition of LysoTracker Red DND-99, which is a lysosomotropic fluorophore. Lysosomotropic compounds, which often are lipophilic and contain basic amines, diffuse into lysosomes, get protonated and thereby increase the pH within this acidic organelle. Therefore, lysosomotropic compounds like chlorpromazine (CP), interfere with the lysosomal accumulation of the LysoTracker dye.<sup>199</sup> DP55 and DP59 only slightly interfered with the dye accumulation, while 3-morpholinopropyl analogs showed lysosomotropic effects comparable to chlorpromazine at 5 and 10  $\mu\text{M}$  (Figure 25b). Interestingly, unlike DP72, DP68 displays lysosomotropic

effects only at concentrations  $\geq 5 \mu\text{M}$ . Since both DP68 and its inactive analog DP72 display lysosomotropic effects, while DP55 does not, lysosomotropic properties alone may not be sufficient to cause ROS induction. To assess whether DP68 induces ROS via iron sequestering, a calcein-based iron chelation assay was performed. In the presence of  $\text{Fe}^{2+}$ , the fluorescence of calcein is quenched and can thus be used as a sensor for unbound  $\text{Fe}^{2+}$ . Compounds were incubated in a  $\text{FeSO}_4$  solution prior to calcein addition and subsequent fluorescence intensity measurement. Iron-chelators like deferoxamine (DFO) lead to an increase in calcein fluorescence (Figure 25c). DP68 showed no iron-chelating effects, suggesting that lysosomal iron accumulation is not the cause of the ROS accumulation induced by DP68.

To confirm the ROS-inducing activity of DP68 and gain insights into the reactive oxygen species identity, additional ROS indicator dyes were applied. As mitochondria are one of the main sources of cellular ROS, we tested DP68 and DP72 for their ability to induce mitochondrial superoxide, by means of the indicator dye MitoSOX Red.<sup>60</sup> MitoSOX Red is a derivative of the superoxide indicator dihydroethidium, whose triphenylphosphonium cation moiety facilitates preferential accumulation in mitochondria.<sup>200</sup> In line with the results obtained in the CM- $\text{H}_2\text{DCFDA}$ -based ROS measurements, DP68 induced mitochondrial superoxide with comparable potency, while DP72 did not (Figure 26a and b). To test whether superoxide induction is restricted to the mitochondria, DP68 and analogs were tested using a set of compartment-specific superoxide probes, namely HK-SOX1r (cytosol), HK-SOX1m (mitochondria) and HK-SOX-2L (lysosomes) (Figure 26c).<sup>171</sup> In accordance with previous ROS measurements, DP68 and DP55 induced superoxide in the cytosol, mitochondria and lysosomes, while DP72 and DP59 were inactive. Interestingly, in lysosomes, the lysosomotropic DP68 led to a stronger superoxide accumulation relative to DP55. The use of these orthogonal methods confirmed the ROS-inducing activity of DP68 and suggests that DP68 is a general inducer of cellular superoxide accumulation.

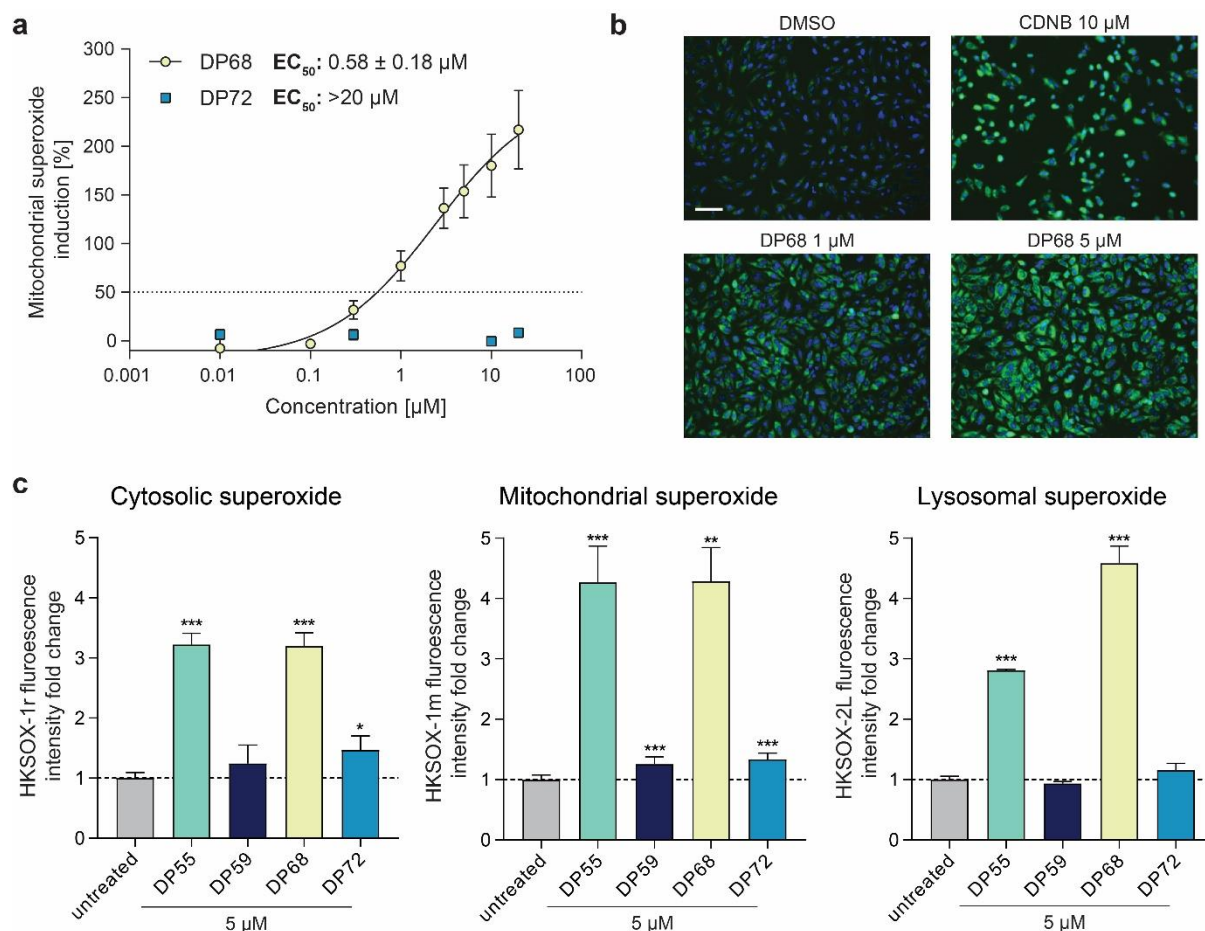


**Figure 26: DP68 induces superoxide accumulation in mitochondria, cytosol and lysosomes.** (a) Detection of mitochondrial superoxide in HeLa cells using MitoSOX Red assay. Data were normalized to values of cells treated with DMSO (0 %) and  $10 \mu\text{M}$  CDNB (100 %). Mean values  $\pm$  SD,  $N = 4$ ,  $n = 3$  (b) Representative images, Hoechst-33342 (blue), MitoSOX Red (green), scale bar =  $100 \mu\text{m}$  (c) Compartment-specific superoxide detection using HK-SOX-1r (cytosol), HK-SOX-1m (mitochondria) and HKSOX-2L (lysosomes). Mean values  $\pm$  SEM.,  $n = 3$ , \* $p < 0.05$ , \*\* $p < 0.01$ , \*\*\* $p < 0.001$ , all groups were compared to untreated group. Data displayed in (c) were obtained by Mingyang Lu, co-worker of Prof. Dan Yang, University of Hong Kong.

To further investigate the superoxide-inducing properties of DP68, cytosolic superoxide levels were measured at different concentrations by means of HK-SOX-1r (Figure 27a). The compound showed a dose-dependent increase in cytosolic superoxide levels. An  $\text{EC}_{50}$  value of  $0.3 \pm 0.5 \mu\text{M}$  was determined, which was calculated based on 50% of the superoxide-inducing effect of  $10 \mu\text{M}$  CDNB, analogous to the CM-H<sub>2</sub>DCFDA- and MitoSOX Red-based assays (Figure 24a and Figure 26a). However, at  $50 \mu\text{M}$ , the maximal level of superoxide induction by DP68 was not reached. Furthermore,  $10 \mu\text{M}$  of CDNB hardly increased cytosolic superoxide levels (Figure 27b). The calculated  $\text{EC}_{50}$  value therefore does not reflect the actual superoxide-inducing potency of DP68. Ideally, the  $\text{EC}_{50}$  value should be calculated based on the inflection point of the dose-response curve. As the upper plateau of the curve is not



reached at 50  $\mu\text{M}$  and DP68 could not be tested at higher concentrations due to limited solubility, an actual  $\text{EC}_{50}$  value cannot be calculated.

Interestingly, the superoxide-inducing effects of both DP55 and DP68 could be dampened by co-incubation with their respective analogs DP59 and DP72, which both do not induce ROS accumulation (Figure 27c). These findings suggest that DP55 and DP68 may induce ROS accumulation by modulation of a protein. DP59 and DP72 may bind to the same binding site within such target protein, however, without modulating its activity. Thus, DP59 and DP72 would compete with DP55 and DP68 for such binding sites and prevent ROS induction.

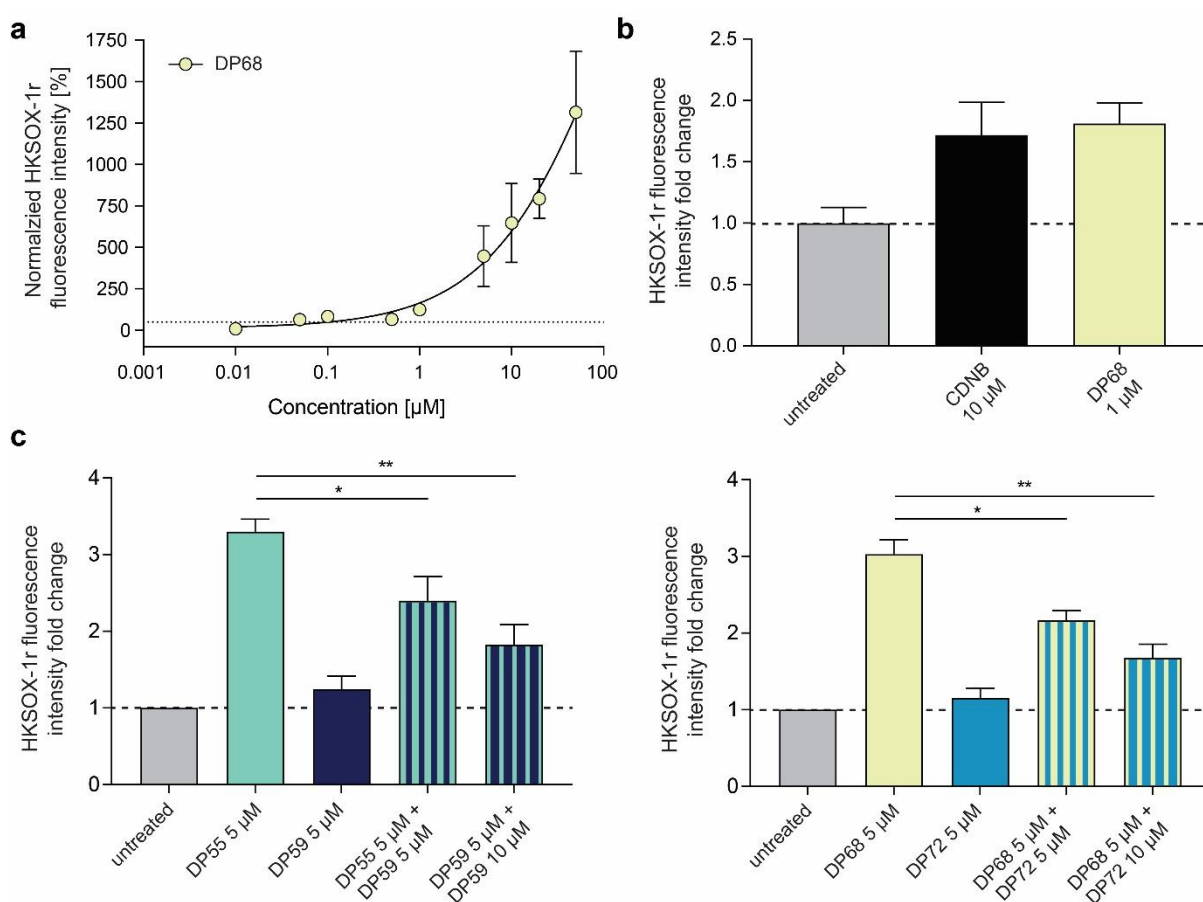


**Figure 27: Cytosolic superoxide induction by DP68 is dose-dependent and can be scavenged by DP72.**

(a) Dose-response curve of DP68 for increase in cytosolic superoxide determined using HK-SOX-1r. Data were normalized to values of untreated cells (0 %) and cells treated with 10  $\mu\text{M}$  CDNB (100 %). The dotted line indicates the 50% level. (b) Cytosolic superoxide levels after 1 h treatment with 1  $\mu\text{M}$  DP68 or 10  $\mu\text{M}$  CDNB (c) Influence of DP59 and DP72 on cytosolic superoxide induction by DP55 and DP68, respectively. Mean values  $\pm$  SEM,  $n = 3$ , \* $p < 0.05$ , \*\* $p < 0.01$ , \*\*\* $p < 0.001$ , all groups were compared to untreated group. Data were obtained by Mingyang Lu, co-worker of Prof. Dan Yang, University of Hong Kong.

In theory, small molecules can increase cellular superoxide levels by various mechanisms, one example being redox cycling. Redox-cycling compounds facilitate the formation of superoxide in the reducing environment of the cytoplasm.<sup>201,202</sup> To detect redox cycling in a cell-free system, compounds were incubated in the presence of DTT. Subsequently, hydrogen peroxide production is determined via horseradish peroxidase-catalyzed oxidation of phenol red, which can be monitored via absorbance measurement. Redox-cycling compounds, like phenanthrenequinone (PAQ) strongly increase the absorbance.<sup>203</sup> However, none of the diaminopyrimidine-based compounds were active for redox cycling (Figure 28).

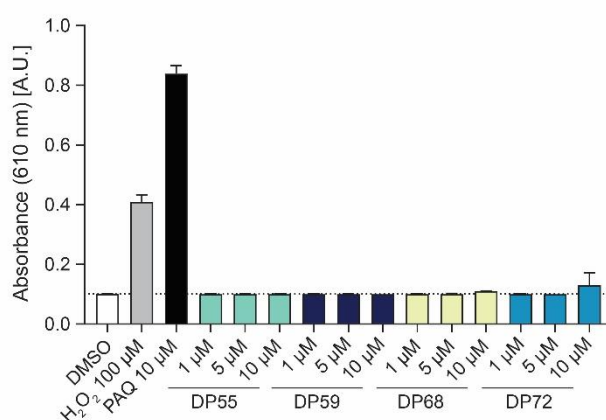


**Figure 28: Diaminopyrimidine-based ROS inducers are not redox cycling compounds.** Compounds were incubated in the presence of DTT for 20 min, prior to the addition of horseradish peroxidase and phenol red and incubation for 5 min. After NaOH addition, absorbance at 610 nm was measured. Mean values  $\pm$  SD, n = 3; PAQ = Phenanthrenequinone. Data were obtained by Dr. Matthias Baumann, Lead Discovery Center, Dortmund.

Mitochondria are regarded as a major cellular source of superoxide. Within this organelle, at least eleven sites are known to produce superoxide, especially the electron transport chain (ETC) complexes.<sup>204</sup> Reverse electron transport (RET) at complex I, which is caused by strong reduction of the coenzyme Q pool in combination with a high proton gradient, causes superoxide formation that is inhibited by the proton ionophore FCCP.<sup>205</sup> Furthermore, electron leakage at the ubiquinone-binding sites of complex I and III leads to the formation of superoxide that can be suppressed by the site-specific superoxide-scavengers S1QEL1.1 and S3QEL2.<sup>206</sup> To assess, whether ROS induced by DP68 originates from the ETC complexes, cells were incubated with FCCP, S1QEL1.1 or S3QEL2 prior to treatment with DP68 and subsequent CM-H<sub>2</sub>DCFDA-based ROS measurement (Figure 29). None of the three compounds suppressed DP68-induced ROS accumulation. Furthermore, inhibition of the

ETC, e.g. of complex III via Antimycin A can increase superoxide levels, however, DP68 did not inhibit mitochondrial respiration (Figure 23).<sup>197,207</sup> Thus, superoxide induced by DP68 most likely does not originate from the ETC.

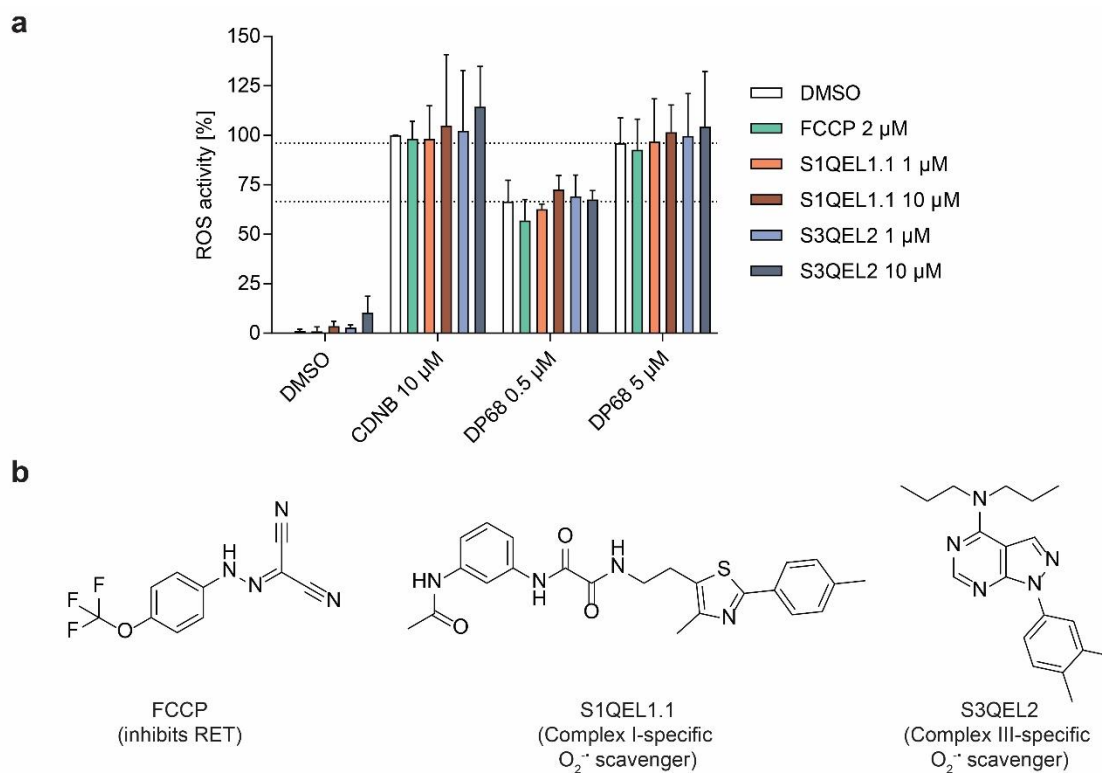


**Figure 29: Superoxide induced by DP68 may not originate from the electron transport chain.**

**(a)** CM-H<sub>2</sub>DCFDA-based ROS detection in HeLa cells. Cells were treated for 30 min with the uncoupling agent FCCP, the complex I electron leak inhibitor S1QEL1.1 or the inhibitor of complex III-mediated superoxide production S3QEL2, prior to incubation with DP68 for 60 min. Mean values  $\pm$  SD, N = 4, n = 3 **(b)** Chemical structures of FCCP, S1QEL1.1 and S3QEL2.

Another prominent source of superoxide is the group of NADPH oxidases (NOX).<sup>74</sup> NOX complexes are prominent targets in drug discovery, which led to the development of various inhibitors targeting different members of the NOX family.<sup>207</sup> A preincubation with four different NOX inhibitors did not suppress the ROS formation of DP68 (Figure 30). Thus, DP68 induces superoxide accumulation in a NOX-independent manner.

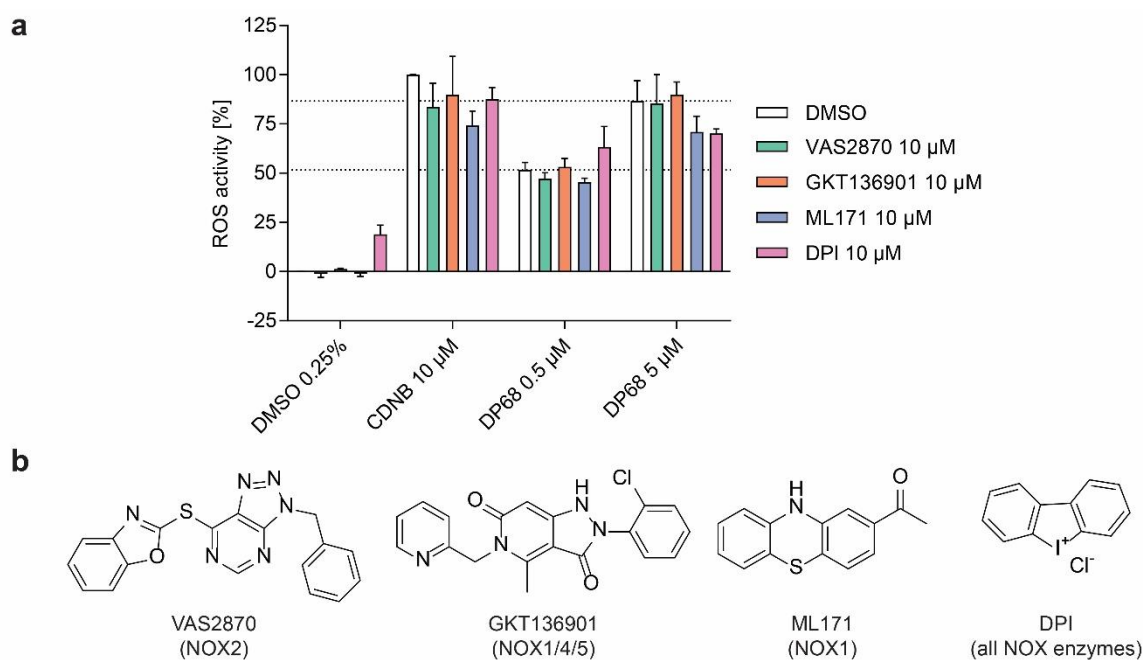


**Figure 30: DP68-induced superoxide does not originate from NADPH oxidases. (a)** CM-H<sub>2</sub>DCFDA-based ROS detection in HeLa cells. Cells were treated for 30 min with different inhibitors of NADPH oxidases (VAS2870, GKT136901, ML171 and DPI) prior to a 60 min treatment with compounds. Mean values  $\pm$  SD, N = 4, n = 3 **(b)** Chemical structures and molecular targets of the four NOX inhibitors. DPI = diphenyliodonium chloride

In cells, superoxide is readily converted into other reactive oxygen species, mainly via SOD-catalyzed dismutation into hydrogen peroxide or via reaction with nitric oxide to form peroxynitrite (Figure 6). As detection of such secondary reactive oxygen species may provide insights whether ROS accumulation is a consequence of increased ROS production or decreased ROS scavenging, peroxynitrite and hydrogen peroxide levels were determined in HeLa cells after treatment with DP68 (Figure 31). For this, the reactive oxygen species-selective probes HKPerox-1 and HKGreen-4 were used, which detect hydrogen peroxide and peroxynitrite, respectively.<sup>173,174</sup> Interestingly, despite the strong induction of superoxide by DP68, both hydrogen peroxide and peroxynitrite levels remained constant. Due to the action of superoxide dismutases, an increase in superoxide production should result in elevated hydrogen peroxide levels. The absence of such increase is thus indicative of inhibition of superoxide dismutases as this should cause an accumulation of superoxide without increase in hydrogen peroxide levels. The formation of peroxynitrite is limited by the availability of nitric oxide. Peroxynitrite levels were not elevated by DP68 despite the increase in superoxide levels, indicating low nitric oxide availability in HeLa cells.

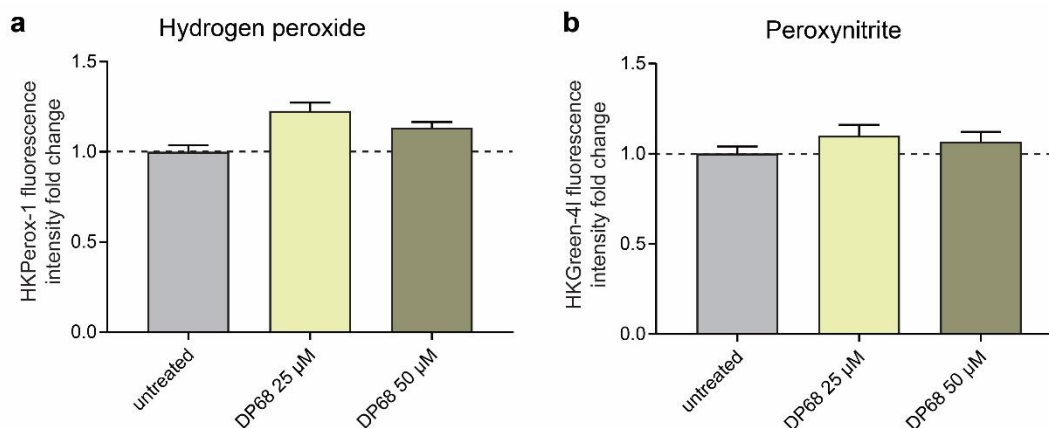


**Figure 31: DP68 does not increase hydrogen peroxide and peroxynitrite levels.** Peroxynitrite (a) and hydrogen peroxide (b) measurements in HeLa cells using HKGreen-4 and HKPerox-1, respectively, after 1 h of treatment with DP68. Mean values  $\pm$  SEM,  $n = 3$ . Data were obtained by Mingyang Lu, co-worker of Prof. Dan Yang, University of Hong Kong.

As mentioned in chapter 2.2.3, cells react to oxidative stress via an NRF2-mediated antioxidant response. Thus, an NRF2 reporter gene assay was performed in HeLa cells to test DP68 for induction of this response (Figure 32). Cells were treated with compounds for 24 h prior to monitoring NRF2-mediated reporter gene expression, i.e. firefly luciferase. The control compound tert-butylhydroquinone (t-BHQ) induced a concentration-dependent increase in reporter gene activity up to four-fold relative to cells treated with DMSO. This relatively weak response could be explained by the comparably high basal NRF2 activity of HeLa cells.<sup>208</sup> Neither DP68 nor DP72 induced an antioxidant response.

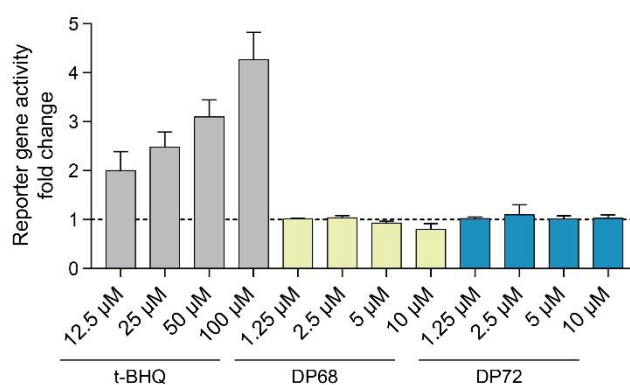


**Figure 32: DP68 does not induce an NRF2-dependent antioxidant response.** NRF2-dependent reporter gene assay in HeLa cells transiently transfected with two plasmids encoding either firefly luciferase (FLuc) under the control of antioxidant response elements (ARE) or Nano luciferase (NanoLuc) under the control of a constitutive promoter. Cells were treated with compounds for 24 h and NRF2 activity was determined via luminescence measurement. FLuc to NanoLuc ratios were calculated per well. Data were normalized to values of cells treated with DMSO. Mean values  $\pm$  SD,  $N = 3$ ,  $n = 3$ . t-BHQ = tert-butylhydroquinone

### 5.3.3 Target identification via photo-crosslinking beads

In the course of the investigations for this thesis, different proteomics techniques were applied to identify the molecular target mediating the ROS-inducing activity of DP55 and DP68. In the first approach, DP55 and its analog DP59, which lacks ROS-inducing activity, were immobilized on photo-crosslinking beads (chapter 2.1.2) and used for affinity-based chemical proteomics experiments using HeLa cell lysates (Table 13). Proteins enriched on the beads were subjected to on-bead digestion and subsequent HPLC-MS/MS analysis with label-free quantification. In both biological replicates, 22 proteins were selectively enriched by DP55 over DP59, however only ten proteins displayed LFQ ratios >5 in both replicates.

**Table 13: Proteins enriched by DP55 over DP59 using photo-crosslinking beads.** Affinity beads were incubated with HeLa cell lysates for 2 h and washed to remove loosely bound proteins. Bound proteins were subjected to a tryptic digestion and identification and label-free quantification (LFQ) via HPLC-MS/MS. Mean LFQ ratios of proteins significantly enriched by DP55, false discovery rate (FDR) = 0.05, N = 3, n = 2. Bead preparation was performed by Yasumitsu Kondoh, co-worker of Prof. Hiroyuki Osada, RIKEN CSRS, Japan.

Protein name	Gene	LFQ ratio DP55/DP59	
		n = 1	n = 2
Deoxycytidine kinase	DCK	specific	specific
Cell division control protein 45 homolog	CDC45	specific	specific
Cathepsin D	CTSD	13.05	8.3
Ketosamine-3-kinase	FN3KRP	5.17	11.21
WD repeat-containing protein 61, N-terminally processed	WDR61	4.34	11.04
Lactoylglutathione lyase	GLO1	9.07	5.75
Rap1 GTPase-GDP dissociation stimulator 1	RAP1GDS1	7.37	specific
Retinoid-inducible serine carboxypeptidase	SCPEP1	6.43	4.82
Serine/threonine-protein kinase 26	STK26	5.32	specific
COMM domain-containing protein 3	COMMD3	specific	5.05
COMM domain-containing protein 2	COMMD2	4.73	specific
Tyrosine--tRNA ligase, cytoplasmic, N-terminally processed	YARS	3.35	5.62
Isocitrate dehydrogenase [NAD] subunit alpha, mitochondrial	IDH3A	2.79	5.88
2,4-dienoyl-CoA reductase, mitochondrial	DECR2	4.32	specific
Ribose-phosphate pyrophosphokinase 2	PRPS2	4.26	4.31
Dimethyladenosine transferase 2, mitochondrial	TFB2M	4.26	specific
Neutral alpha-glucosidase AB	GANAB	3.92	4.14
Catechol O-methyltransferase	COMT	3.9	specific
Protein NipSnap homolog 1	NIPSNAP1	2.53	3.44
Phosphatidylinositol transfer protein alpha isoform	PITPNA	2.27	2.6
Phosphatidylinositol transfer protein beta isoform	PITPNB	2.17	2.42
Pyruvate dehydrogenase E1 component subunit alpha, mitochondrial	PDHA1	2.19	2.19

The lysosomal protease cathepsin D (CTSD) and the methylglyoxal-converting enzyme lactoylglutathione lyase (GLO1) were described in the literature to influence cellular ROS levels. Su *et al.* examined the effects of *CTSD* knock-down in HeLa cells and observed increased lysosomal membrane permeability and ROS accumulation.<sup>209</sup> GLO1 participates in the detoxification of methylglyoxal, an oxidative stress-promoting metabolite and ROS precursor, by conjugating it with glutathione forming S-D-lactoylglutathione (SLG).<sup>210</sup> As the inhibition of these enzymes might elevate cellular ROS levels, the influence of DP55 on their enzymatic activity was tested.

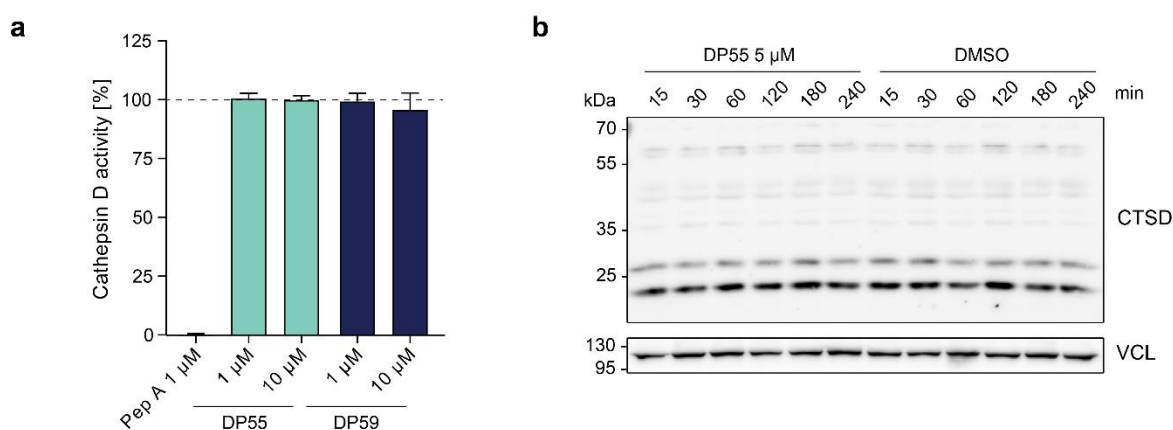


**Figure 33: DP55 does not inhibit the enzymatic activity and the proteolytic processing of cathepsin D.** (a) Recombinant CTSD protein was incubated with compounds for 10 min at 37 °C prior to the addition a non-fluorescent substrate peptide-conjugate. Proteolytic cleavage of the conjugate results in increased fluorescence. The protease inhibitor pepstatin A (Pep A) was used as positive control. Mean values  $\pm$  SD, N = 3, n = 3 (b) HeLa cells were treated with DP55 or DMSO for 15-240 min, lysed and analyzed via immunoblotting to detect CTSD or vinculin (VCL) as loading control. Representative blot, N = 1, n = 3.

In contrast to the known CTSD inhibitor pepstatin A, DP55 and DP59 did not inhibit the enzymatic activity of CTSD (Figure 33a). In cells, CTSD is expressed as pre-pro-enzyme that undergoes proteolytic cleavage and glycosylation.<sup>211</sup> To test, whether DP55 interferes with this maturation process, HeLa cells were treated with DP55 for 15 min to 4 h, lysed and subjected to immunoblotting to detect CTSD (Figure 33b). The different cleavage and glycosylation products originating from the pre-pro-enzyme display differences in their electrophoretic mobility, reflected in a respective band pattern. Inhibition of cleavage or glycosylation steps would result in the accumulation of respective precursors. As this was not observed, DP55 did not influence the CTSD band pattern and, thus, did not interfere with CTSD processing.

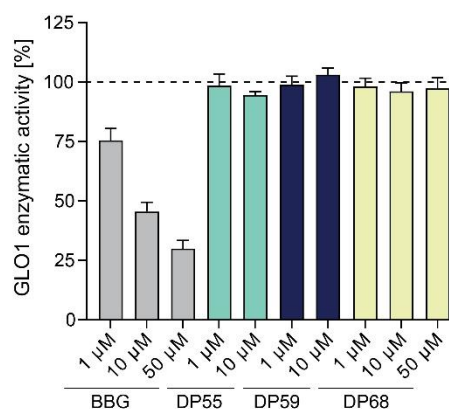


**Figure 34: DP55 and DP68 do not inhibit the enzymatic activity of GLO1.** Recombinant GLO1 protein was incubated with compounds for 10 min at ambient temperature prior to the addition of a substrate mix. The formation of S-D-lactoylglutathione was monitored via UV absorbance measurement. S-p-bromobenzylglutathione (BBG) was used as positive control of GLO1 inhibition. Mean values  $\pm$  SD, N = 1, n = 3

DP55, DP59 and DP68 were tested for their influence on the enzymatic activity of GLO1 (Figure 34). Unlike the known GLO1 inhibitor S-p-bromobenzylglutathione (BBG), none of the three diaminopyrimidines inhibited the GLO1-catalyzed formation of SLG. Since these target validation experiments did not indicate an influence of DP55 on CTSD and GLO1, both proteins were not considered for further validation studies.

### 5.3.4 Target identification via thermal proteome profiling and Cell Painting assay

The target identification approach using photo-crosslinking beads identified several putative targets. Two targets, CTSD and GLO1, which are known to influence cellular ROS levels, could not be confirmed as targets of DP55. As target validation of all other proteins in the list would be a laborious endeavor, alternative target identification approaches were applied. This allows prioritization of those target candidates that were identified via two independent target identification techniques. Therefore, the optimized compound DP68 was subjected to two profiling approaches, the Cell Painting assay (CPA), a high-content morphological profiling approach and thermal proteome profiling (TPP), an adaptation of the cellular thermal shift assay (CETSA) with a mass spectrometry-based read-out.

The CPA monitors the effect of compounds on cellular morphology by application of six fluorescent dyes that stain different cellular compartments.<sup>31</sup> Subsequent high-content imaging and automated image analysis recorded 579 morphological parameters, which were compared to those of cells treated with DMSO to create morphological fingerprints. Comparisons to fingerprints of over 3000 compounds



with an annotated target or mode of action were used for target prediction.<sup>32</sup> The similarity of two profiles was calculated from the correlation distances, which is given as biosimilarity in percent. Furthermore, the percentage of significantly changed parameters ('induction rate') indicates the strength of the morphological effect.<sup>33</sup> Compounds with an induction rate  $\geq 5\%$  were regarded as active in the CPA. In the CPA, DP68 induced strong morphological changes at 1  $\mu\text{M}$ , significantly altering 35 % of the 579 morphological features (Figure 35a). Increasing concentrations of DP68 further elevated the number of significantly changed morphological features, while all profiles showed a high fingerprint similarity ( $\geq 85\%$ ) to the profile of the lowest concentration of DP68. Thus, the morphological changes induced by DP68 are dose-dependent. At 10  $\mu\text{M}$  DP72, which lacks the ROS-inducing activity, displayed an induction value comparable to 1  $\mu\text{M}$  of DP68 and profile similarity of 82 %. Fingerprint comparison of 1  $\mu\text{M}$  of DP68 with 3,900 reference compounds with annotated targets or modes of action revealed a high biological similarity ( $\geq 85\%$ ) to 265 references (Supplementary Table 2), which were clustered with regard to their annotated main target class (Figure 35b). Interestingly, the majority of reference compounds targets G-protein coupled receptors (GPCR), mainly serotonin and dopamine receptors. However, not all members of these receptor families are expressed in U-2 OS and HeLa cells (Supplementary Table 3).

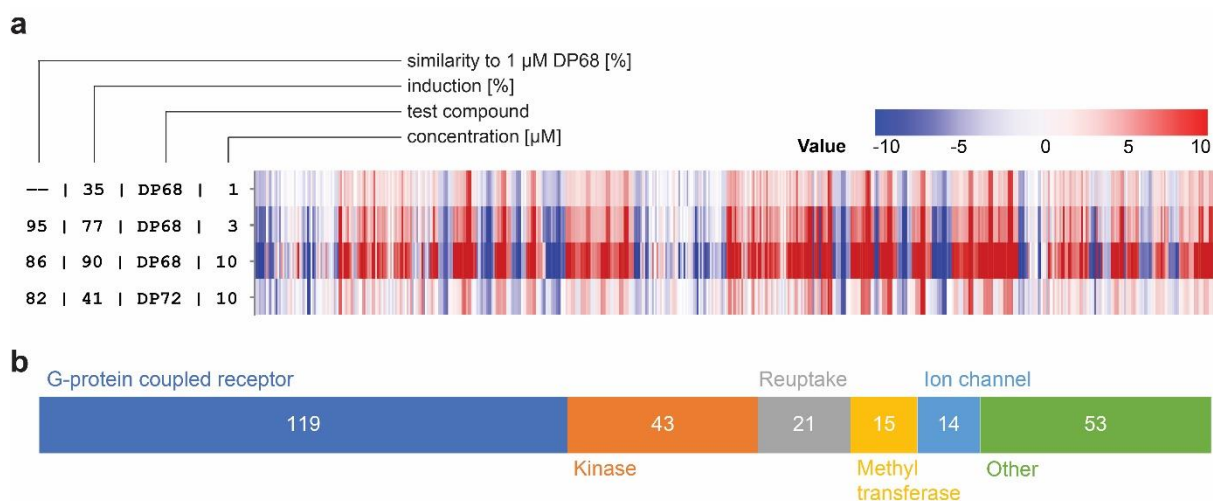


**Figure 35: DP68 induces morphological changes in the Cell Painting assay in a dose-dependent manner.**

**(a)** CPA fingerprint comparison for DP68 and DP72. DP68 displays a dose-dependent induction increase with high profile similarity among the different test concentrations. 1  $\mu\text{M}$  DP68 and 10  $\mu\text{M}$  DP72 trigger morphological changes with similar induction range and high biological similarity. **(b)** Target class annotation of 265 reference compounds sharing a high biological similarity ( $\geq 85\%$ ) to 1  $\mu\text{M}$  DP68. Data were obtained by COMAS, Dortmund.

The thermal stability of a protein can be altered upon binding of a small-molecule interaction partner, e.g. by inducing an alteration in its conformation. Based on this phenomenon, a small molecule-protein interaction can be detected via the cellular thermal shift assay.<sup>22</sup> For this, cell lysates are treated with a compound or vehicle control and split into fractions, which are subjected to a heat treatment at different temperatures within a temperature gradient. Aggregated protein is removed via centrifugation and the soluble fraction is subjected to immunoblotting to detect alterations in the thermal stability of the protein of interest. Alternatively, soluble fractions can be subjected to tandem mass tag labeling and subsequent MS/MS analysis to measure the thermal stability of various proteins in parallel. This method is called thermal proteome profiling, which can identify small molecule-protein interactions in an unbiased manner.<sup>23,24</sup>

**Table 14: List of proteins with altered melting behavior upon DP68 treatment.** Thermal proteome profiling was performed in HeLa cell lysates using 50  $\mu$ M DP68. Proteins displaying an average  $\Delta T_m \geq 2$  °C or  $\leq -2$  °C were regarded as hits. Mean values  $\pm$  SD, N = 1, n = 3

Protein name	Gene	$\Delta T_m$ [°C]
Trypsin-3	PRSS3	5.3 $\pm$ 2.4
Tetraspanin-4	TSPAN4	3.3 $\pm$ 1.0
Cysteine-rich with EGF-like domain protein 1	CRELD1	3.2 $\pm$ 1.4
MORF4 family-associated protein 1	MRFAP1	2.4 $\pm$ 0.5
Gamma-interferon-inducible lysosomal thiol reductase	IFI30	2.2 $\pm$ 0.6
SRE-binding protein cleavage-activating protein	SCAP	-2.1 $\pm$ 0.4
Sushi domain-containing protein 5	SUSD5	-2.3 $\pm$ 0.7
Insulin-like growth factor 1 receptor	IGF1R	-2.4 $\pm$ 0.6
Histone acetyltransferase p300	EP300	-3.0 $\pm$ 1.2
Putative hydroxypyruvate isomerase	HYI	-3.0 $\pm$ 0.9
ADP-ribosylation factor-like protein 6-interacting protein 4	ARL6IP4	-3.1 $\pm$ 1.5
O-phosphoserine-tRNA(Sec) selenium transferase	SEPSECS	-3.3 $\pm$ 0.9
Bis(5-adenosyl)-triphosphatase	FHIT	-3.4 $\pm$ 0.7
Genetic suppressor element 1	GSE1	-3.9 $\pm$ 1.7
Sigma non-opioid intracellular receptor 1	SIGMAR1	-4.6 $\pm$ 0.5

In TPP, 15 proteins displayed a significant alteration in their melting behavior after treatment with DP68 (Table 14). One of these is the sigma non-opioid intracellular receptor 1 ( $\sigma_1$  receptor), one of two members of the  $\sigma$  receptor family. This receptor is located in the mitochondria-associated membrane (MAM) of the endoplasmic reticulum (ER) and used to be falsely classified as opioid receptor.<sup>212–214</sup>

The  $\sigma_1$  receptor has a chaperone function and may be involved in the ER stress response.<sup>215</sup> It is found in many different tissues and is overexpressed in a variety of cancer cell lines.<sup>216</sup> Furthermore, it is known to bind many psychoactive substances.<sup>215</sup> Interestingly, the list of the CPA reference compounds that display high profile similarity to DP68 contains five known ligands of the  $\sigma_1$  receptor, namely opipramol, L-687,384, perphenazine, siramesine and carbetapentane.

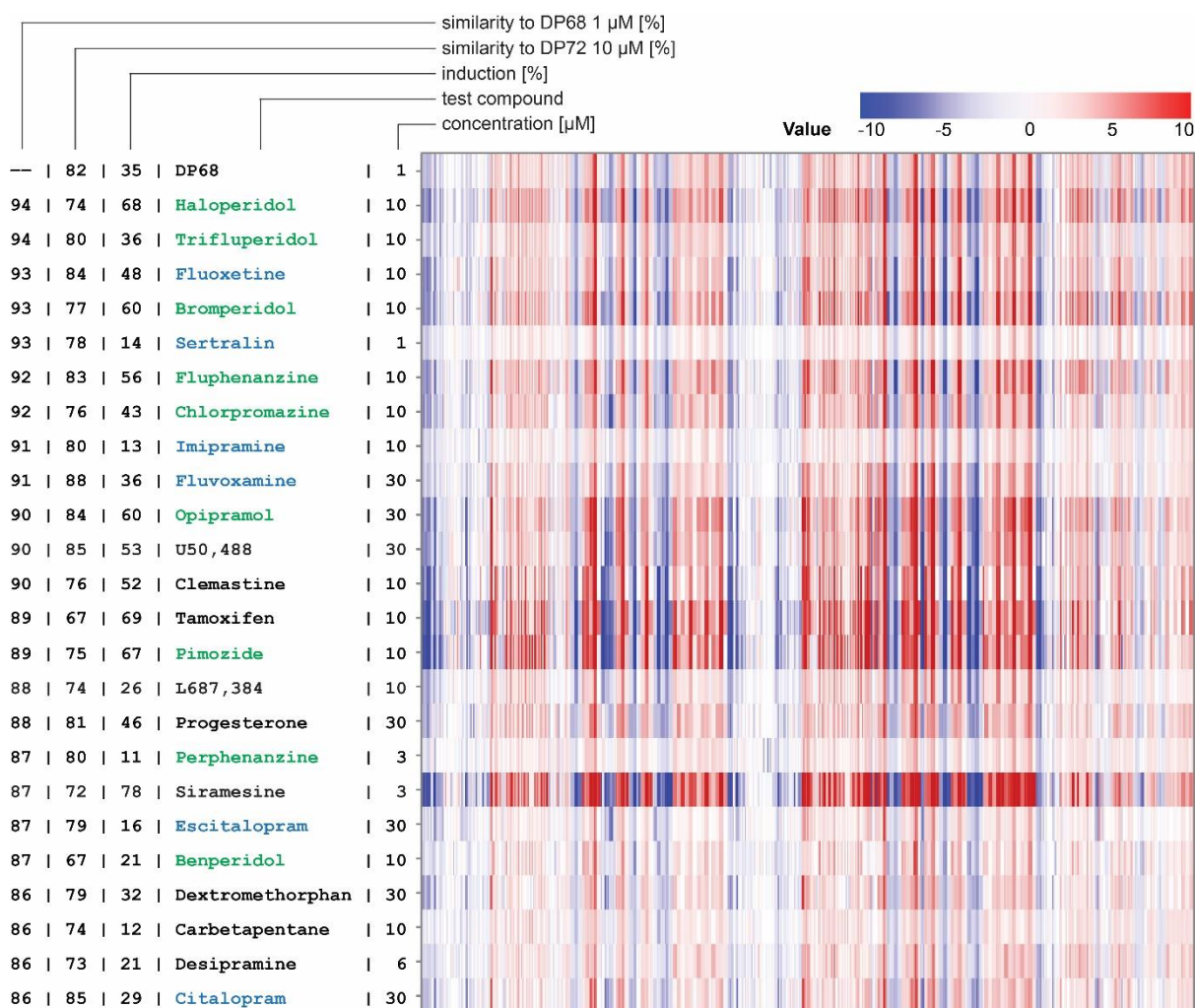


**Figure 36: Cell Painting assay indicates high biological similarity of DP68 to  $\sigma_1$  ligands.** Comparison of CPA fingerprints of DP68 and 24 known ligands of  $\sigma_1$ . Fingerprint similarity to 1  $\mu$ M DP68 and 10  $\mu$ M DP72 is given. Only reference compounds within an induction range of 5-85 % and with a cell count >80 % were considered. For each compound, the profile most similar to 1  $\mu$ M DP68 was selected. The list contains 9 dopamine receptor antagonists (green) and 6 serotonin reuptake inhibitors (blue). Data were obtained by COMAS, Dortmund.

A manual in-depth target annotation of the CPA reference compounds revealed that DP68 displays a high biological similarity to an additional 19  $\sigma$  receptor ligands (Figure 36).<sup>215,217-226</sup> With the exception

of Fluvoxamine, U50,488 and Citalopram, DP72 only shows moderate fingerprint similarity ( $\leq 78\%$ ) to these  $\sigma$  receptor ligands. The CPA reference set additionally contained another 7 known  $\sigma$  receptor ligands displaying lower or no biological similarity to DP68, including the allosteric modulator phenytoin (Figure 37).<sup>227</sup> While Fluspidine and Spiperone show a fingerprint similarity to DP68 of 84 % and 83 %, respectively, high affinity  $\sigma_1$  receptor ligands, like SKF-10047, PRE-084 and 3-PPP, were not affecting the cellular morphology in the assay.<sup>217,221,228</sup> Despite these findings, the  $\sigma_1$  receptor was considered as target candidate of DP68 and was chosen for further studies due to its involvement in the regulation of oxidative stress.<sup>229,230</sup>

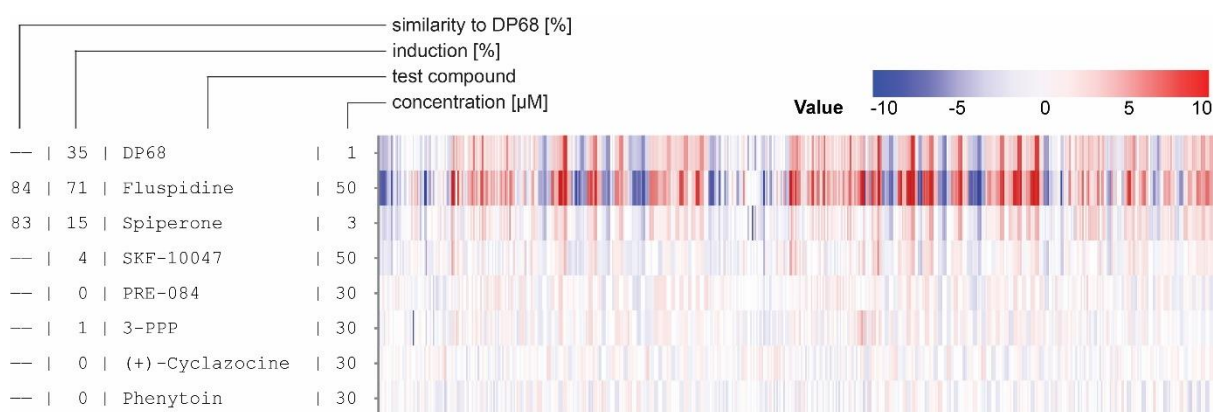


**Figure 37: Cell Painting assay fingerprint comparison of DP68 with additional  $\sigma_1$  receptor ligands.** Comparison of CPA profiles of DP68 and 7 known ligands of S1R displaying fingerprint similarity < 85 %. Only reference compounds within an induction range of 5-85 % and with a cell count >80 % were considered. For each compound, the profile most similar to 1  $\mu$ M DP68 was selected. Data were obtained by COMAS, Dortmund.

#### 5.3.4.1 Validation of the $\sigma_1$ receptor as target of DP68

To investigate the  $\sigma_1$  receptor as potential target of DP68, the interaction with both members of the  $\sigma$  receptor family was investigated. In the TPP, DP68 altered the thermal stability of the  $\sigma_1$ , but not the  $\sigma_2$  receptor (Figure 38a), suggesting that DP68 is a selective ligand of the  $\sigma_1$  receptor. To confirm this finding, a radioligand binding assay in membrane preparations was performed, in which the displacement of  $\sigma_1$ - or  $\sigma_2$ -specific radioligands, [ $^3$ H]-(+)-pentazocine and [ $^3$ H]1,3-di-(2-tolyl)-guanidine, respectively, by DP68 and its inactive analog DP72 was measured (Figure 38b and 38c).

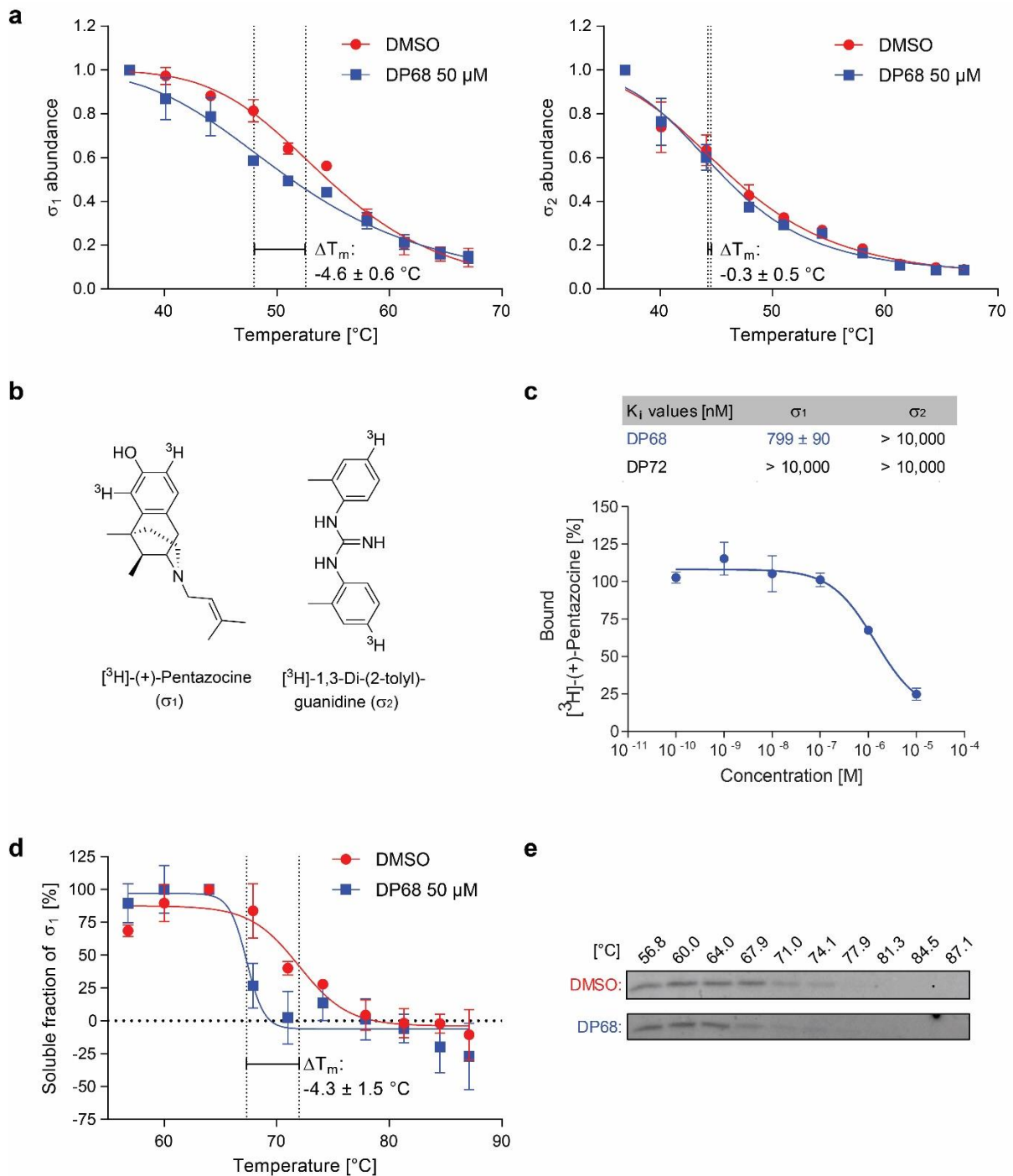


**Figure 38: DP68 selectively binds to  $\sigma_1$  over  $\sigma_2$  receptor and engages the  $\sigma_1$  receptor in cells. (a)** TPP melting curves of the  $\sigma_1$  and  $\sigma_2$  receptor. Mean values  $\pm$  SD, N = 1, n = 3 **(b and c)** Radioligand binding assay for  $\sigma$  receptors. Chemical structures of [ $^3$ H]-(+)-Pentazocine ( $\sigma_1$ -specific radioligand) and [ $^3$ H]-DTG ( $\sigma_2$ -specific radioligand) (b) and assay results (c) with S1R-binding curve for DP68. Mean values  $\pm$  SD, n = 3 **(d)** CETSA in intact HeLa cells for the  $\sigma_1$  receptor. Mean values  $\pm$  SD, N = 1, n = 3, representative blots **(e)** shown. Data displayed in (c) were obtained by Dr. Dirk Schepmann, co-worker of Prof. Bernhard Wünsch, University of Münster. Data displayed in (d) and (e) were obtained by Alexandra Brause, MPI Dortmund.

In line with the TPP results, DP68 showed a concentration-dependent displacement of the  $\sigma_1$  radioligand [ $^3\text{H}$ ]-(+)-pentazocine, with a  $K_i$  of  $799 \pm 90$  nM (Figure 38c). A displacement of [ $^3\text{H}$ ]-1,3-di-(2-tolyl)-guanidine ( $\sigma_2$ ) by DP68 was not observed. DP72 did not show activity in these assays. Next, a CETSA experiment in HeLa cells was conducted to investigate whether DP68 engages the  $\sigma_1$  receptor in cells. Analogous to the TPP results, DP68 caused a thermal destabilization with a  $\Delta T_m$  of  $-4.3 \pm 1.5$  °C, indicating that DP68 engages the  $\sigma_1$  receptor in cells (Figure 38d and 38e).

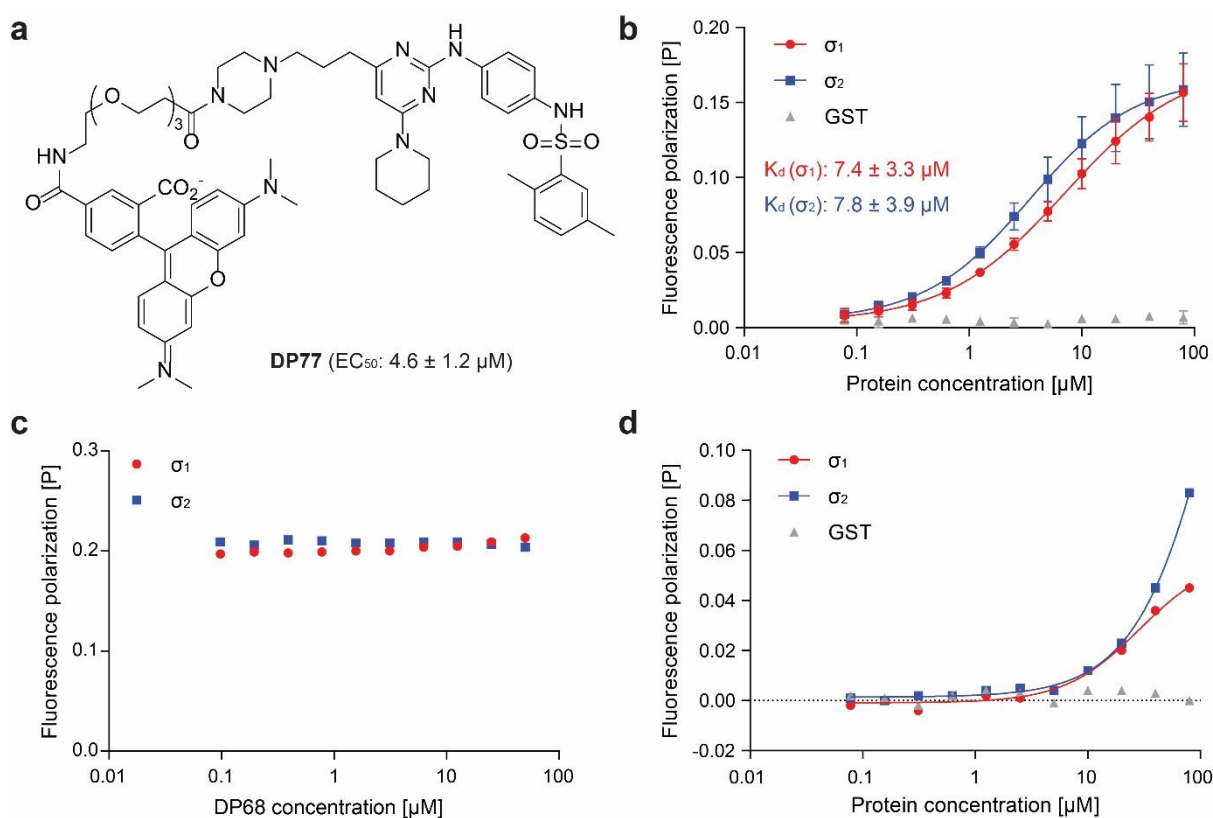


**Figure 39: DP68- $\sigma$  receptor protein interaction via fluorescence polarization measurements could not be confirmed due to TAMRA binding.** (a) Chemical structure and ROS-inducing activity of the TAMRA probe DP77. ROS activity was determined in HeLa cells using CM-H<sub>2</sub>DCFDA. Mean values  $\pm$  SD, N = 4, n = 3. (b)  $K_d$  determination of DP77 for  $\sigma_1$  and  $\sigma_2$  receptors using recombinantly expressed proteins. 2  $\mu\text{M}$  of DP77 was incubated with varying concentrations of  $\sigma$  receptor proteins and binding was determined by means of fluorescence polarization measurement. Glutathione S-transferase (GST) was used as control. Mean  $\pm$  SD, N = 1, n = 3 (c) Competition FP measurement.  $\sigma_1$  receptor (20  $\mu\text{M}$ ) and  $\sigma_2$  receptor (10  $\mu\text{M}$ ) were incubated with 2  $\mu\text{M}$  DP77 in the presence of DP68. N = 1, n = 1 (d) FP measurement as described in (b) using 2  $\mu\text{M}$  5-TAMRA. N = 1, n = 1.  $\sigma$  receptor protein expression was performed by Dr. Alexandra Friese, MPI Dortmund.

To confirm this interaction *in vitro*, fluorescence polarization studies were performed using recombinantly expressed  $\sigma_1$  and  $\sigma_2$  receptor protein and the DP68-based TAMRA probe DP77, which

displayed moderate ROS-inducing activity in HeLa cells (Figure 39a). Both  $\sigma$  receptor proteins induced a dose-dependent increase in DP77 fluorescence polarization, with  $K_d$  values of  $7.4 \mu\text{M} \pm 3.3$  and  $7.8 \mu\text{M} \pm 3.9$  for the  $\sigma_1$  and  $\sigma_2$  receptor, respectively (Figure 39b), indicating interaction between DP77 and those two proteins. In contrast, the control protein GST did not influence the polarization of the probe. However, in the presence of DP68, the fluorescence polarization of DP77 for both  $\sigma$  receptor proteins (Figure 39c) did not decrease, indicating that the proteins may not interact with the DP68-derived portion of the DP77 molecule. To test this hypothesis, both receptors were incubated with 5-TAMRA instead of DP77 and fluorescence polarization was measured. Both proteins increased the fluorescence polarization (Figure 39d) of 5-TAMRA, indicating binding of the receptor to the fluorophore. Due to the TAMRA-binding properties of both proteins, DP77 is unsuitable to investigate the interaction of DP68 with the recombinantly expressed  $\sigma$  receptor proteins.

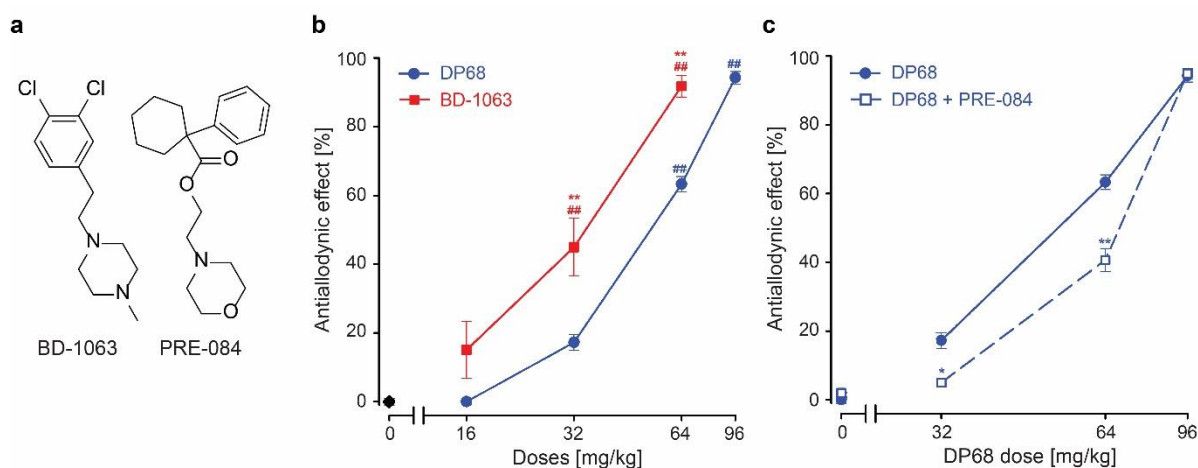


**Figure 40: DP68 acts as weak antagonist of the  $\sigma_1$  receptor.** (a) Chemical structures of BD-1063 and PRE-084 (b/c) mechanical allodynia assay in female CD-1 mice after subcutaneous administration of DP68 or BD-1063 (b) or administration of DP68 after pretreatment with 32 mg/kg PRE-084 (c). Mean  $\pm$  SEM values obtained from 6-8 mice per condition. ## =  $p < 0.01$  in comparison to animals treated with vehicle (black symbol), \* =  $p < 0.05$  / \*\* =  $p < 0.01$  in comparison between animals treated with equal doses of either DP68 or BD-1063 (b) or between animals treated with or without PRE-084 pretreatment (c). Data were obtained by Antonia Artacho-Cordón, co-worker of Prof. Francisco R. Nieto, University of Granada.

$\sigma_1$  receptor agonists, like PRE-084, are known to promote mechanical allodynia, while antagonists, e.g. BD-1063 or haloperidol, dampen it.<sup>231,232</sup> The term ‘mechanical allodynia’ refers to a pain sensation as response to a mechanical stimulus, which under normal conditions is painless, however after sensitization causes pain.<sup>233</sup> To assess whether the interaction with the  $\sigma_1$  receptor influences its

physiological function, DP68 was subjected to a mouse model of mechanical allodynia (Figure 40). In this assay, capsaicin was injected intraplantarly to sensitize the paws of female CD-1 mice. Paw withdrawal time in response to a mechanical punctae stimulation was measured after subcutaneous administration of compounds. DP68 displayed an antiallodynic effect, which was partially reversed by PRE-084. Therefore, DP68 behaves like an antagonist of the  $\sigma_1$  receptor. However, in comparison to the high affinity  $\sigma_1$  receptor antagonist BD-1063, DP68 is not very potent. These observations are in line with the radioligand displacement assays, in which a  $K_i$  of  $799 \pm 90$  nM was determined for DP68, which is approximately two orders of magnitude higher than the reported  $K_i$  of BD-1063.<sup>234</sup>

To elucidate whether the  $\sigma_1$  receptor-antagonistic effect is mechanistically linked to the ROS accumulation induced by DP68, chemical and genetic validation studies were conducted.  $\sigma_1$  receptor ligands that displayed high biological similarity to DP68 in the CPA were tested for ROS induction in HeLa cells (Table 15). The majority of  $\sigma_1$  receptor ligands did not induce ROS accumulation, with the exception of pimozone with an  $EC_{50}$  value of  $4.4 \mu\text{M}$  and sertraline, fluphenazine, perphenazine and chlorpromazine, which displayed only weak activity in the assay.

**Table 15: ROS-inducing activities of different  $\sigma$  receptor ligands.** 19 different ligands of  $\sigma$  receptors have been tested for ROS induction in a CM-H<sub>2</sub>DCFDA-based assay after 1 h compound incubation in HeLa cells. Mean values  $\pm$  SD, N = 3, n = 3. Data were obtained by COMAS, Dortmund.

Compound	ROS $EC_{50}$ [ $\mu\text{M}$ ]	Compound	ROS $EC_{50}$ [ $\mu\text{M}$ ]
Pimozone	$4.4 \pm 3.3$	Imipramine	>30 $\mu\text{M}$
Sertraline	$23.8 \pm 3.0$	Fluvoxamine	>30 $\mu\text{M}$
Fluphenazine	$25.3 \pm 0.0$	Opipramol	>30 $\mu\text{M}$
Perphenazine	$25.3 \pm 2.0$	Tamoxifen	>30 $\mu\text{M}$
Chlorpromazine	$25.6 \pm 1.0$	L-687,384	>30 $\mu\text{M}$
Clemastine	>30 $\mu\text{M}$	Siramesine	>30 $\mu\text{M}$
Haloperidol	>30 $\mu\text{M}$	Benperidol	>30 $\mu\text{M}$
Flutexine	>30 $\mu\text{M}$	Carbetapentane	>30 $\mu\text{M}$
Bromperidol	>30 $\mu\text{M}$	Spiperone	>30 $\mu\text{M}$
SKF-10047	>30 $\mu\text{M}$		

DP68 and the ROS-inducing  $\sigma_1$  receptor ligand pimozone were tested for ROS induction in wild-type and  $\sigma_1$  receptor-deficient HAP1 cells (Figure 41). DP68 induced ROS accumulation in both cell types with comparable potency (Figure 41a), a similar observation was made for pimozone (Figure 41b).



Taken together, DP68 was identified as a novel antagonist of the  $\sigma_1$  receptor by means of TPP and the CPA, however the  $\sigma_1$  receptor is not the target that mediates the ROS-inducing activity of the compound.

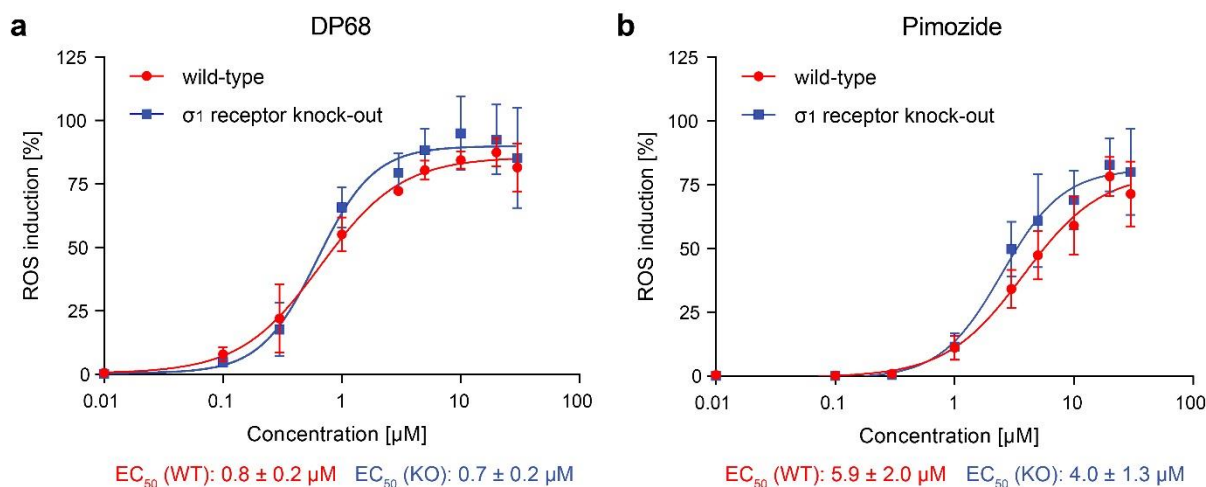


**Figure 41: The  $\sigma_1$  receptor interaction of DP68 is not necessary for its ROS-inducing activity.** ROS assay for (a) DP68 and (b) pimoizide, performed in HAP1 wild-type (WT) and  $\sigma_1$  knock-out cells ( $\sigma_1$  receptor KO).  $\text{EC}_{50}$  values were interpolated from non-linear regression curve. Mean  $\pm$  SD, N = 4, n = 3. Data were obtained by Daya Agne, MPI Dortmund.

#### 5.3.4.2 Validation of selected kinases as targets of DP68

Apart from the  $\sigma_1$  receptor, another 14 proteins were identified as putative binding partners of DP68, but none of these were identified in the affinity enrichment experiments using photo-crosslinking beads. However, the list of 14 proteins identified via TPP includes one kinase, namely the insulin-like growth factor 1 receptor (IGF1R). 43 kinase inhibitors displayed high profile similarity to DP68 in the CPA and compounds with a 2,4-diaminopyrimidine scaffold have been described as inhibitors of kinases.<sup>235,236</sup> Thus, the IGF1R and other kinases were investigated as potential target responsible for the ROS-inducing activity of DP68. For this, ten IGF1R inhibitors were tested for their ability to induce ROS accumulation in HeLa cells (Figure 42).<sup>237–245</sup> Out of ten inhibitors, only BMS-536924, which inhibits the enzymatic activity of the IGF1R *in vitro* with an  $\text{IC}_{50}$  of 100 nM, displayed ROS activity above 50 % at 10  $\mu\text{M}$ .<sup>245</sup> Due to the large gap in potency, it is unlikely that the inhibition of IGF1R by BMS-536924 is responsible for the ROS induction. Furthermore, DP68 was tested for modulation of kinases, including IGF1R, kinases located downstream of IGF1R, and for other growth factor receptor kinases (Table 16). None of the tested kinases were inhibited at 10  $\mu\text{M}$  test concentration.

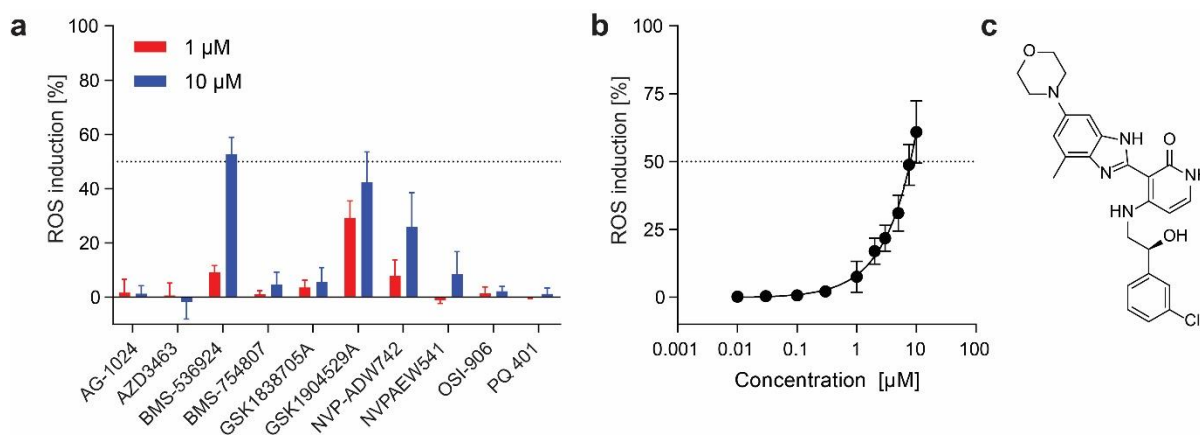


**Figure 42: Influence of IGF1R inhibitors on cellular ROS levels.** ROS assay in HeLa cells after 60 min of incubation with (a) ten small molecule IGF1R inhibitors at 1 and 10 μM and (b) BMS-536924 at varying concentrations. Mean values ± SD, N = 4, n = 3. (c) Chemical structure of BMS-536924. Data were obtained by Daya Agne, MPI Dortmund.

**Table 16: *In vitro* activity assays of DP68 for kinases involved in IGF1R signaling or growth factor receptor kinases.** Assay was performed at SelectScreen (Thermo Fisher), n = 2; N = 2

Kinase assay	Technology	ATP [μM]	Inhibition / Displacement [%]		
			Mean	St.Dev	
IGF1R	Z'LYTE	Km app	12.1	0.6	Kinases involved in IGF1R signaling
AKT1 (PKB alpha)	Z'LYTE	Km app	2.1	1.8	
AKT2 (PKB beta)	Z'LYTE	Km app	-3.8	0.6	
AKT3 (PKB gamma)	Z'LYTE	Km app	4.8	0.3	
BRAF	Z'LYTE	100	11.0	1.6	
CHUK (IKK alpha)	Adapta	Km app	7.1	2.0	
FRAP1 (mTOR)	Z'LYTE	Km app	0.2	2.3	
GSK3A (GSK3 alpha)	Z'LYTE	Km app	-7.2	1.0	
GSK3B (GSK3 beta)	Z'LYTE	Km app	-4.2	0.2	
IKKB (IKK beta)	Z'LYTE	Km app	-1.0	2.7	
MAPK10 (JNK3)	Z'LYTE	100	-7.2	5.9	
MAPK8 (JNK1)	Z'LYTE	100	-11.5	10.0	
MAPK9 (JNK2)	Z'LYTE	100	-4.5	10.0	
RAF1 (cRAF) Y340D Y341D	Z'LYTE	100	-2.1	7.1	
EGFR (ErbB1)	Z'LYTE	Km app	-5.6	1.5	Growth factor receptor kinases
EPHA1	Z'LYTE	Km app	6.3	2.2	
EPHA2	Z'LYTE	Km app	-0.7	0.2	
EPHA3	Lantha		16.3	5.8	
EPHA4	Z'LYTE	Km app	5.7	0.2	
EPHA5	Z'LYTE	Km app	-2.7	0.0	
EPHA7	Lantha		10.7	1.5	
EPHA8	Z'LYTE	Km app	-1.1	0.4	
EPHB1	Z'LYTE	Km app	7.5	1.1	
EPHB2	Z'LYTE	Km app	1.6	3.8	
EPHB3	Z'LYTE	Km app	0.6	0.1	
EPHB4	Z'LYTE	Km app	4.6	3.3	
ERBB2 (HER2)	Z'LYTE	Km app	-1.6	1.8	
FGFR1	Z'LYTE	Km app	56.3	0.2	
FGFR2	Z'LYTE	Km app	6.4	0.5	
FGFR3	Z'LYTE	Km app	23.5	6.1	
FGFR4	Z'LYTE	Km app	-8.8	0.8	
FLT1 (VEGFR1)	Z'LYTE	Km app	-6.9	1.7	
FLT3	Z'LYTE	Km app	5.8	0.5	
FLT4 (VEGFR3)	Z'LYTE	Km app	-23.0	1.6	
INSR	Z'LYTE	Km app	6.4	1.2	

Kinase assay	Technology	ATP [ $\mu$ M]	Inhibition / Displacement [%]	
			Mean	St.Dev
KDR (VEGFR2)	Z'LYTE	Km app	4.5	0.4
NTRK1 (TRKA)	Z'LYTE	Km app	12.6	2.2
NTRK2 (TRKB)	Z'LYTE	Km app	8.8	3.8
NTRK3 (TRKC)	Z'LYTE	Km app	6.6	0.1
NUAK1 (ARK5)	Adapta	Km app	2.5	0.9
PDGFRA (PDGFR alpha)	Z'LYTE	Km app	-1.3	0.6
PDGFRB (PDGFR beta)	Z'LYTE	Km app	0.6	1.4

In addition, the influence of DP68 on the activity of kinases, that were annotated as targets for the 43 kinase inhibitors that displayed high fingerprint similarity in the CPA), was tested (Table 17). None of the tested kinases were inhibited by DP68.

**Table 17: *In vitro* activity assays of DP68 for kinases annotated in the CPA reference compound set for DP68.** Assay was performed at SelectScreen (Thermo Fisher), n = 2, N = 2

Kinase	Technology	ATP [ $\mu$ M]	Inhibition / Displacement [%]	
			Mean	St.Dev
PI4K2A (PI4K2 alpha)	Adapta	10	-6.1	1.8
PI4K2B (PI4K2 beta)	Adapta	10	-16.1	1.4
PI4KA (PI4K alpha)	Adapta	10	-1.4	6.1
PI4KB (PI4K beta)	Adapta	Km app	-12.7	5.4
PIK3C2A (PI3K-C2 alpha)	Adapta	Km app	1.9	7.7
PIK3C2B (PI3K-C2 beta)	Adapta	10	17.5	12.8
PIK3C2G (PI3K-C2 gamma)	Adapta	10	-9.4	3.1
PIK3C3 (hVPS34)	Adapta	Km app	-35.7	7.2
PIK3CA/PIK3R1 (p110 alpha/p85 alpha)	Adapta	Km app	13.7	4.5
PIK3CA/PIK3R3 (p110 alpha/p55 gamma)	Adapta	10	3.4	3.5
PIK3CB/PIK3R1 (p110 beta/p85 alpha)	Adapta	Km app	-10.2	5.3
PIK3CB/PIK3R2 (p110 beta/p85 beta)	Adapta	10	3.4	10.4
PIK3CD/PIK3R1 (p110 delta/p85 alpha)	Adapta	Km app	-3.6	1.1
PIK3CG (p110 gamma)	Adapta	Km app	8.7	4.6
PIP4K2A	Adapta	10	-31.2	3.6
PIP5K1A	Adapta	10	-22.8	1.0
PIP5K1B	Adapta	10	-5.3	5.2
PIP5K1C	Adapta	10	-24.6	6.0
ABL1	Z'LYTE	Km app	-0.7	0.7
AURKA (Aurora A)	Z'LYTE	Km app	-5.5	2.0
AXL	Z'LYTE	Km app	4.6	1.7
CAMK2A (CaMKII alpha)	Z'LYTE	Km app	12.9	0.7
CAMK2B (CaMKII beta)	Z'LYTE	Km app	36.5	6.0
CAMK2D (CaMKII delta)	Z'LYTE	Km app	26.3	0.3
CAMK2G (CaMKII gamma)	Lantha		5.2	4.6
CDK1/cyclin B	Z'LYTE	Km app	3.2	1.1
CDK2/cyclin A	Z'LYTE	Km app	-1.3	0.3
CSF1R (FMS)	Z'LYTE	Km app	1.8	0.9
DDR1	Lantha		9.9	1.0
DDR2	Lantha		7.0	0.3
DNA-PK	Z'LYTE	Km app	7.8	0.3
JAK2	Z'LYTE	Km app	1.7	1.2
KIT	Z'LYTE	Km app	-2.8	6.6
LTK (TYK1)	Z'LYTE	Km app	3.8	0.3
MAPK14 (p38 alpha) Direct	Z'LYTE	Km app	-15.2	1.0

Kinase	Technology	Inhibition / Displacement [%]		
		ATP [ $\mu\text{M}$ ]	Mean	St.Dev
MET (cMet)	Z'LYTE	Km app	8.5	4.6
NUAK2	Lantha		-12.0	2.7
PIM1	Z'LYTE	Km app	-1.6	2.3
PIM2	Z'LYTE	Km app	-6.1	4.0
PIM3	Z'LYTE	Km app	6.1	5.1
PLK1	Z'LYTE	Km app	3.8	0.7
RET	Z'LYTE	Km app	6.2	0.9
ROS1	Z'LYTE	Km app	-3.7	0.5
RPS6KA4 (MSK2)	Z'LYTE	Km app	-0.4	0.2
SRC	Z'LYTE	Km app	-1.7	7.2
TEK (Tie2)	Z'LYTE	Km app	-4.0	0.9
YES1	Z'LYTE	Km app	2.6	0.6

In MitoSOX Red- and HK-SOX-1m-based assays, DP68 induced mitochondrial superoxide accumulation. Interestingly, the compound does not influence mitochondrial respiration and complex I- and III-specific scavengers of superoxide did not interfere with the ROS induction by DP68. Besides the ETC, there are other sites within the mitochondria that contribute to the organelle's overall superoxide production, e.g. the pyruvate dehydrogenase complex.<sup>246</sup> This multienzyme complex catalyzes the conversion of pyruvate into acetyl-CoA and is negatively regulated by a set of four kinases, namely the pyruvate dehydrogenase kinases (PDHK) 1-4. These kinases phosphorylate and thereby inactivate the pyruvate dehydrogenases (PDH), which catalyze the first step of the reaction. Interestingly, small molecule-mediated inhibition of PDHKs as well as siRNA-mediated suppression of PDHK2 were found to increase mitochondrial ROS levels.<sup>247</sup> Therefore, the ROS-inducing activity of two inhibitors of PDHK2, AZD7545 and PS10, were measured in HeLa cells. Both inhibitors failed to increase cellular ROS levels (Figure 43a).<sup>248,249</sup> Additionally, DP68 was tested in an *in vitro* activity assay for PDHK1-4, but was found not to inhibit these kinases (Figure 43b). Therefore, an involvement of PDHKs in the superoxide accumulation induced by DP68 was ruled out.

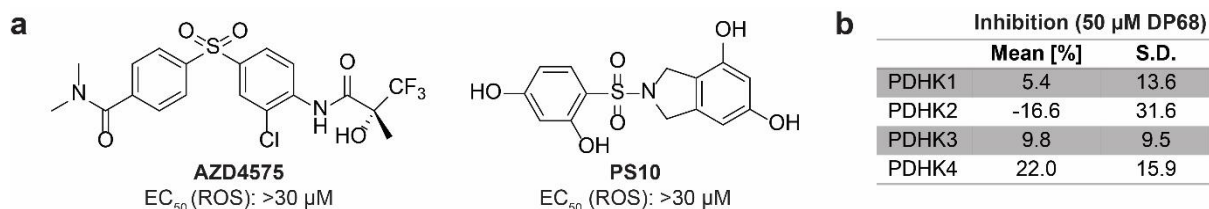


**Figure 43: Mitochondrial superoxide induction by DP68 is not mediated by pyruvate dehydrogenase kinases.** (a) Chemical structures and ROS-inducing activity of PDHK2 inhibitors AZD4575 and PS10 in HeLa cells. Mean values  $\pm$  SD, N = 4, n = 3. (b) *In vitro* activity assays for PDHKs (SignalChem Biotech Inc., Canada) using 50  $\mu\text{M}$  DP68. Mean values  $\pm$  SD, N = 1, n  $\geq$  3.

### 5.3.5 Target identification via affinity-based chemical proteomics

In the course of this project, different affinity-based chemical proteomics experiments were carried out. Apart from the approach described in chapter 4.2.3.1, different compound immobilization strategies were tested, which are described below.

#### 5.3.5.1 Compound immobilization via click chemistry

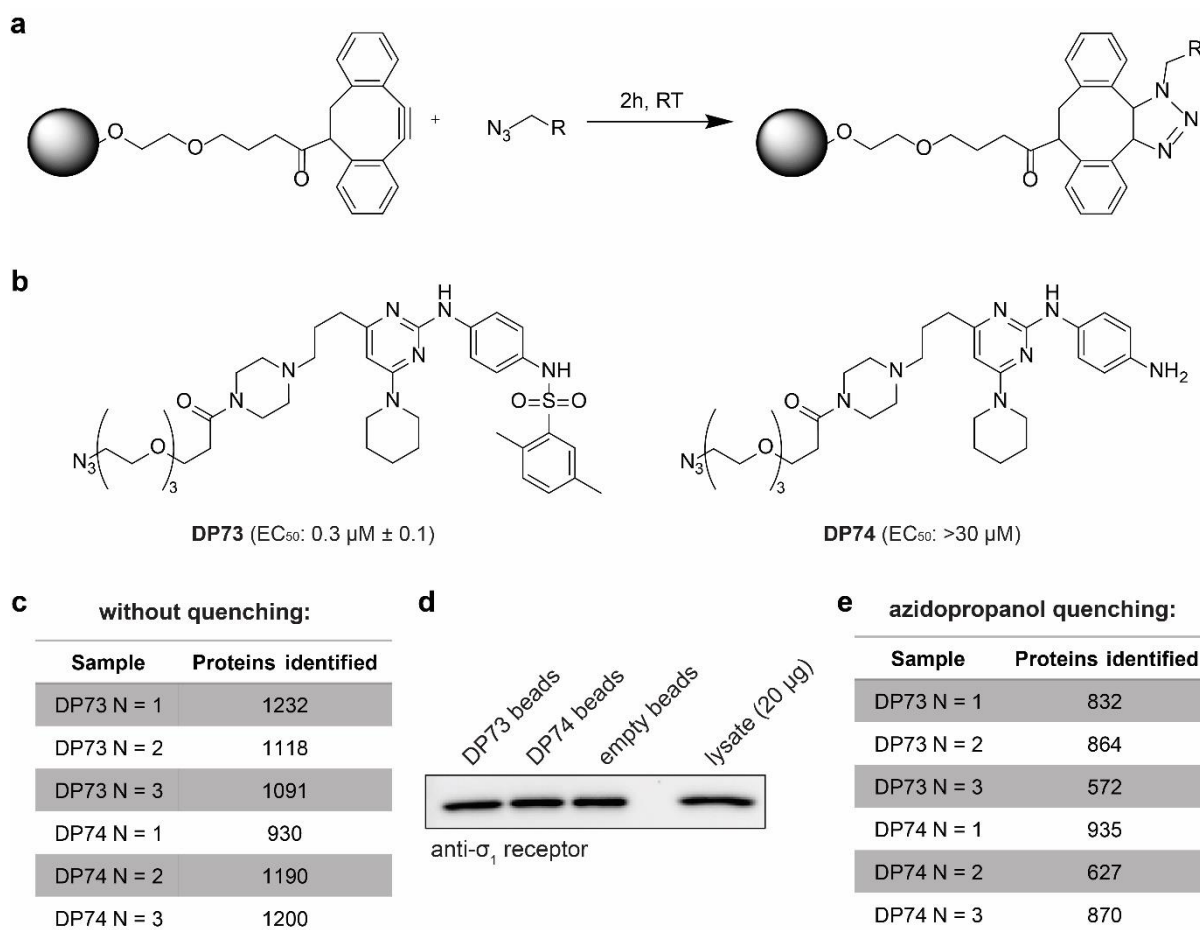


**Figure 44: Affinity enrichment via DBCO beads is unsuitable for target identification due to strong protein background.** (a) Compound immobilization via copper-free click chemistry using DBCO agarose beads. (b) Chemical structures and  $EC_{50}$  values for ROS induction of DP73 and DP74. Mean values  $\pm$  SD,  $N = 4$ ,  $n = 3$ . (c) Affinity-based chemical proteomics in HeLa cell lysates using DBCO agarose beads. Number of proteins identified in each technical replicate are listed. FDR = 0.05,  $N = 3$ ,  $n = 1$ . (d) Affinity enrichment of the  $\sigma_1$  receptor by DP73, DP74 and empty DBCO beads. Detection via immunoblotting. 100  $\mu\text{g}$  HeLa cell lysate input.  $N = 1$ ,  $n = 1$ . (e) Proteomics-based affinity enrichment in HeLa cell lysates using DBCO agarose beads, which were quenched with 3-azido-1-propanol after the compound immobilization step. Protein numbers identified in each technical replicate are listed.  $N = 3$ ,  $n = 1$ .

Using the insights obtained from the SAR study (chapter 5.3.1), a set of affinity probes based on DP68 and DP72 were synthesized by Dr. Houhua Li, containing a triethylene glycol linker with a terminal azide moiety. These affinity probes allowed the immobilization on a resin via click chemistry (Figure 44a).

The DP68 analog DP73 showed comparable potency in the CM-H<sub>2</sub>DCFDA-based ROS assay, while DP74, analogous to DP72, did not display ROS-inducing activity (Figure 44b). Both probes were immobilized in a copper-free reaction on agarose beads decorated with dibenzocyclooctyne (DBCO) moieties and subjected to affinity-based chemical proteomics with LFQ in HeLa cell lysates. Although the number of enriched proteins was high (Figure 44c), ranging from 930 to 1232 proteins, only 14 proteins were found to be significantly enriched on DP73 beads (Table 18).

**Table 18: Proteins enriched by DP73 over DP74 using DBCO beads.** Affinity beads were incubated with HeLa cell lysates for 2 h and washed to remove loosely bound proteins. Bound proteins were subjected to a tryptic digestion and identification and LFQ via HPLC-MS/MS. Mean LFQ ratios of proteins significantly enriched by DP73, FDR = 0.05, N = 3, n = 1

Protein name	Gene	LFQ ratio DP73/DP74
Cleavage stimulation factor subunit 2	CSTF2	3.38
Cathepsin B	CTSB	2.86
Fibulin-1	FBLN1	4.42
Glutathione S-transferase P	GSTP1	7.90
Lipoma HMGIC fusion partner-like 2 protein	LHFPL2	6.59
Methylcrotonoyl-CoA carboxylase beta chain, mitochondrial	MCCC2	4.58
Male-enhanced antigen 1	MEA1	3.48
S-methyl-5-thioadenosine phosphorylase	MTAP	4.34
Myosin-9	MYH9	6.83
Proteasome subunit alpha type-7	PSMA7	5.01
Rap1 GTPase-GDP dissociation stimulator 1	RAP1GDS1	23.91
40S ribosomal protein S5	RPS5	2.85
Multifunctional methyltransferase subunit TRM112-like protein	TRMT112	5.38
UbiA prenyltransferase domain-containing protein 1	UBIAD1	7.50

Furthermore, the previously validated target  $\sigma_1$  receptor was not among these potential hits, as it was found in all technical replicates of both samples. Most likely, unreacted DBCO moieties might strongly enrich various proteins due to their rather hydrophobic nature. Thus, an affinity enrichment experiment with DP73, DP74 and untreated (empty) beads was performed and the eluted proteins were subjected

to immunoblotting for S1R (Figure 44d). All three bead samples enriched the  $\sigma_1$  receptor in comparable amounts, suggesting that the rather hydrophobic DBCO groups may bind the  $\sigma_1$  receptor directly.

**Table 19: Proteins enriched by DP73 over DP74 using DBCO beads after 3-azido-1-propanol quenching.**

Affinity beads were incubated with HeLa cell lysates for 2 h and washed to remove loosely bound proteins. Bound proteins were subjected to a tryptic digestion and identification and label-free quantification (LFQ) via HPLC-MS/MS. Mean LFQ ratios of proteins significantly enriched by D735, FDR = 0.05, N = 3, n = 1

Protein name	Gene	LFQ ratio DP73/DP74
ADP-ribosylation factor-like protein 6-interacting protein 1	ARL6IP1	6.03
Clathrin light chain A	CLTA	2.52
Myosin-9	MYH9	3.20
Myosin regulatory light chain 12A	MYL12A	3.25
Phosphatidylinositol transfer protein beta isoform	PITPNB	2.75

To reduce this non-specific protein binding, an additional quenching step was implemented after the compound immobilization step by incubation with an excess of 3-azido-1-propanol to decrease the hydrophobicity of the bead surface. This indeed lowered the number of identified proteins (Figure 44e), however, this additional quenching step increased the sample variation among technical replicates, which was also reflected in a very short list of potential hits (Table 19). Taken together, this affinity enrichment approach failed due to the high protein background of the DBCO beads.

In an alternative approach, the azide-containing probes were immobilized on alkyne agarose beads by means of a copper-catalyzed click reaction (Figure 45a). Despite their high chemical similarity, DP73 enriched notably less proteins compared to DP74 (Figure 45b). Since the wash buffer used for the affinity enrichment experiments contains a 15-times higher  $MgCl_2$  concentration compared to the lysis buffer, proteins bound by DP73 may not withstand washing with such high  $MgCl_2$  concentrations. However, in an approach using wash buffer with 25 mM  $MgCl_2$ , comparable protein numbers were obtained. The HPLC traces of the respective peptide samples displayed a strong contamination with polymers, presumably detergents, exclusively in the samples obtained with DP73 beads (Figure 45c). Such contaminations can interfere with the identification of proteins, explaining the large difference in the number of identified proteins between DP73 and DP74. To circumvent this issue, affinity enrichment experiments with detergent-free lysis and wash buffer were performed (Figure 45d). This time, the number of proteins was comparable in all samples, with the exception of the first technical replicate of DP74 of the first experiment, which can be regarded as outlier. This approach however identified

106 potential DP73-binding proteins with an FDR = 0.01 (Supplementary Table 4). Again, the  $\sigma_1$  receptor was not enriched by DP73-decorated beads. As the  $\sigma_1$  receptor is a membrane protein, it may not have been solubilized during the lysis preparation in the absence of detergents.

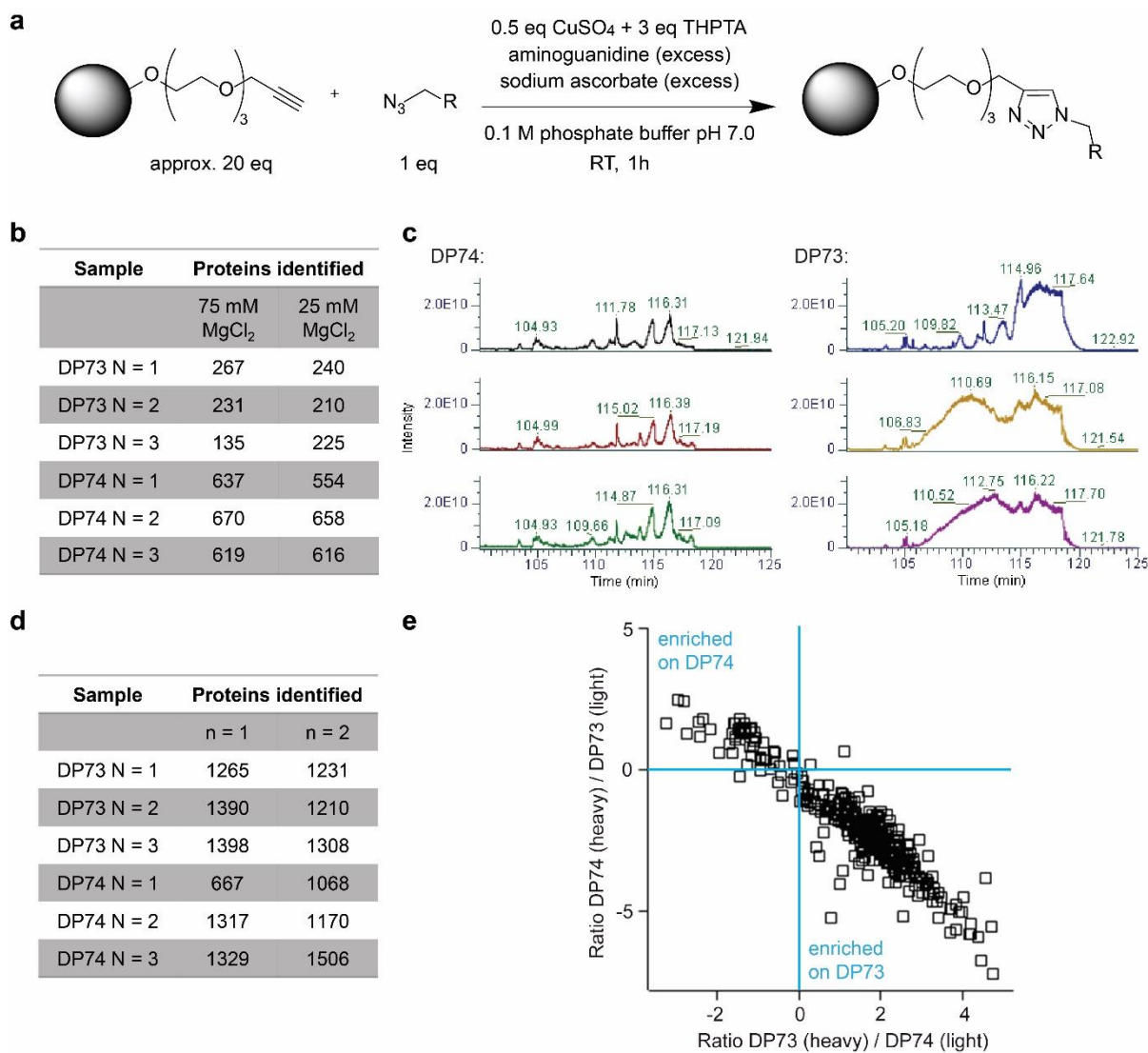


**Figure 45: Affinity enrichment using alkyne agarose beads reveals a substantial difference in the protein binding properties between DP73 and DP74. (a)** Compound immobilization via copper-catalyzed click chemistry, THPTA = Tris(3-hydroxypropyltriazolylmethyl)amine **(b)** Affinity-based chemical proteomics in HeLa cell lysates using detergent-containing lysis and washing buffer with either 75 or 25 mM MgCl<sub>2</sub>. Protein numbers identified in each technical replicate are listed. N = 3, n = 1. **(c)** HPLC traces of the affinity enrichment experiment using wash buffer with 25 mM MgCl<sub>2</sub>. **(d)** Affinity-based chemical proteomics in HeLa cell lysates using lysis and washing buffer without detergents containing 25 mM MgCl<sub>2</sub>. Protein numbers identified in each technical replicate are listed. N = 3, n = 2. **(e)** Proteomics-based affinity enrichment in HeLa cell SILAC lysates using washing buffer without detergents. Representative scatter plot of SILAC ratios (forward against reverse experiment), N = 4, n = 2.



Apart from LFQ, other MS quantification methods are available, e.g. SILAC. For this method, two cell cultures were grown in parallel using growth medium supplemented with amino acids, in this case arginine and lysine, that differ in their isotopic composition. As cells incorporate these 'light' or 'heavy' amino acids into their proteins, samples originating from two cultures can be pooled, but still distinguished from another in MS/MS. In affinity-based proteomics, proteins enriched by different bead types and originating from different cultures can be pooled after elution from the beads, which lowers the technical variability within these sample pairs and allows a more precise quantification.

The approach using detergent-free lysates and buffers was repeated using SILAC lysates (Figure 45e). The SILAC ratio scatter plot shows that the majority of proteins is strongly enriched by DP73 beads. Ideally, most proteins in the samples should bind to the solid phase itself and are therefore enriched by both bead types in comparable amounts. Only few proteins, those that interact with the immobilized small molecule directly, would be enriched on only one bead type. Here however, the SILAC-based quantification revealed that although the numbers of different proteins identified via LFQ on the two bead types are similar, DP73 beads enrich an overall higher total protein amount. Due to this substantially different protein enrichment behavior of the two bead types, it is impossible to draw any conclusions in regard to putative binding proteins of DP73.

At first glance, the comparably small differences in the chemical structures of DP73 and DP74 could not explain these observations. However, since copper was present during the immobilization step, copper-chelating qualities of one of the probes may account for these large differences between the two probes with regard to their protein binding properties. Therefore, a chelation assay for  $\text{Cu}^+$  was performed using bathocuproinedisulfonic acid (BCA) that forms a complex with  $\text{Cu}^+$ , which can be quantified photospectrometrically. None of the diaminopyrimidine-based compounds tested displayed any  $\text{Cu}^+$ -chelating properties (Figure 46a) in aqueous buffer under reducing conditions. To test compounds for  $\text{Cu}^{2+}$  chelation, compounds were incubated in the absence of a reducing agent first, which then was added later together with BCA. Interestingly, if BCA is added without addition of a reducing agent, a color change was observed for all samples containing diaminopyrimidine compounds to a certain extent (Figure 46b). This finding indicates  $\text{Cu}^{2+}$ -reducing activities of these compounds. Thus, DP73 and DP74 may not be chemically stable in the presence of copper and chemical alteration of the probes may occur during the copper-catalyzed compound immobilization on alkyne beads.

Therefore, this immobilization method is unsuitable to identify the target identification of these diaminopyrimidine-based compounds.

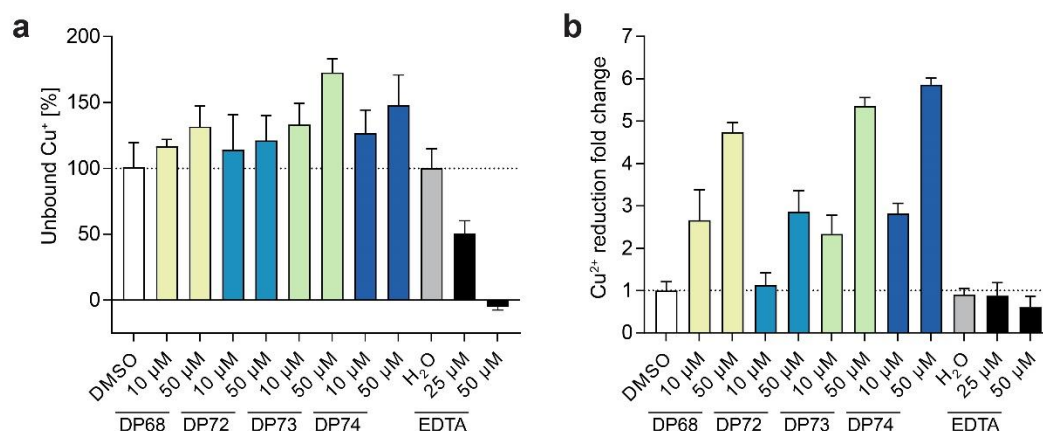


**Figure 46: Selected diaminopyrimidine-based compounds do not chelate Cu<sup>+</sup> but reduce Cu<sup>2+</sup> in aqueous solution.** (a) Cu<sup>+</sup> chelation assay. Briefly, compounds were incubated in a reducing buffer containing 50 μM CuSO<sub>4</sub>. Unbound Cu<sup>+</sup> was quantified via absorbance measurement at 484 nm after addition of BCA. Ethylenediaminetetraacetic acid (EDTA) was used as control. (b) Cu<sup>2+</sup> reduction assay with the same procedure described in (a), however using an assay buffer without reducing agent. Both methods adapted from Campos et al.<sup>250</sup>. Mean values ± SD, N = 3, n = 3.

### 5.3.5.2 Compound immobilization on NHS beads

As the click chemistry-based affinity enrichment approaches failed, a different compound immobilization strategy was pursued using N-hydroxysuccinimide (NHS) beads as solid support. These beads are decorated with NHS carboxylic acid. Since NHS is a good leaving group, NHS esters readily react with free amines to form an amide bond. For this immobilization strategy, a new set of probes was synthesized containing a triethylene glycol linker with a primary amine as reaction partner for the NHS ester. (Figure 47a). In contrast to the azide analog DP73, DP79 displayed a lower potency in the CM-H<sub>2</sub>DCFDA-based ROS assay, presumably due to a reduced membrane permeability caused by the primary amine. DP80 did not show ROS-inducing activity and was thus used as inactive control. For this approach, two types of NHS beads were used, *GE NHS Mag Sepharose* ('GE NHS beads') and *Pierce™ NHS Magnetic Beads* ('Pierce NHS beads'), which mainly differ in the length of the linker connecting the NHS ester to the solid support (Figure 47b and 47c).

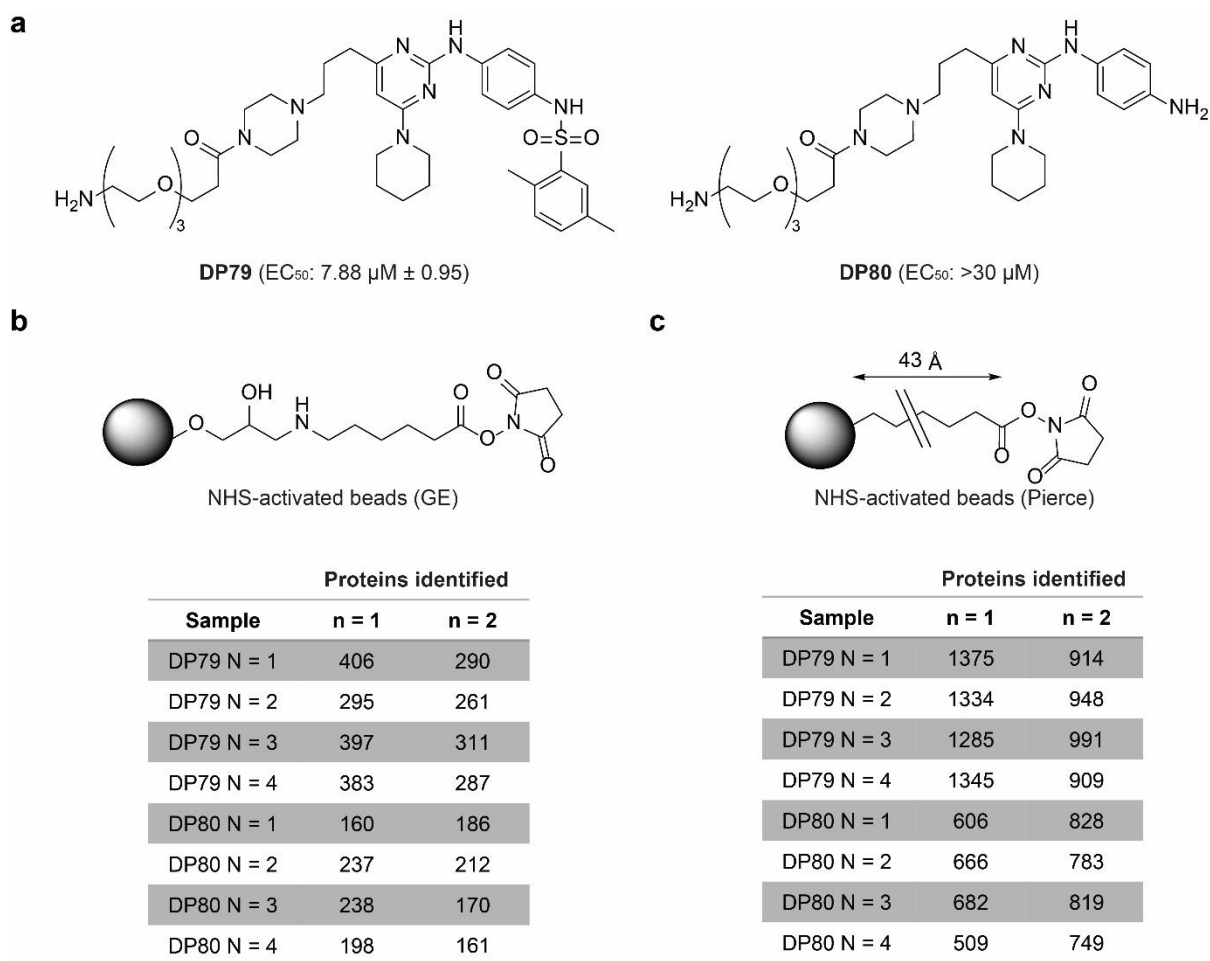


**Figure 47: Affinity enrichment using NHS beads.** (a) Chemical structures and ROS-inducing activities of DP79 and DP80. Mean values  $\pm$  SD, N = 4, n = 3. (b and c) Affinity-based chemical proteomics in HeLa cell lysates using NHS beads from GE (b) or Pierce (c). Number of proteins identified in each technical replicate are listed.

After the compound immobilization step, unreacted NHS esters were quenched via incubation with ethanolamine. For each approach, two independent experiments were conducted. Interestingly, GE NHS beads enriched fewer proteins than Pierce NHS beads. As the probes immobilized on the GE NHS beads are in closer proximity to the solid phase, protein binding may be more sterically hindered compared to a similar approach with Pierce NHS beads. Independent of the bead type used, DP79 beads enriched a higher number of different proteins compared to DP80 throughout all experiments. Thus, the subsequent data analysis protocol for the label-free quantification was adjusted: Instead of normalizing all samples to one common protein background value, each set of technical replicates was normalized separately, taking the varying protein amounts enriched by the different bead types into account.

For the GE NHS bead-based approach, 75 proteins were significantly enriched by DP79 (Supplementary Table 5), while in the Pierce NHS bead-based approach, 428 proteins were identified with DP79 (Supplementary Table 6). As the majority of proteins that were most strongly enriched in the respective experiments was overlapping between both approaches, combined results are shown in Table 20.

**Table 20: Proteins significantly enriched during affinity enrichment experiments using NHS beads.**

60 proteins were found enriched on DP79 beads in experiments using both types of NHS beads, including 4 phosphatidylinositol 3-kinase-related kinases (blue), 15 nuclear pore complex proteins (red) and 17 proteins that contain HEAT repeats (according to UniProt) (underlined). FDR = 0.0001, LFQ ratios (DP79/DP80) of technical replicates are listed, N = 4, n = 2. GE = GE NHS beads, Pierce = Pierce NHS beads.

Protein names	Gene	GE n = 1	GE n = 2	Pierce n = 1	Pierce n = 2
<u>Translational activator GCN1</u>	GCN1L1	1,475.8	1,462.4	3,315.8	919.4
<u>Serine/threonine-protein kinase mTOR</u>	MTOR	109.1	1,718.3	3,309.7	618.1
<u>Exportin-1</u>	XPO1	334.7	898.8	2,744.9	1,747.4
Fanconi anemia group I protein	FANCI	45.1	30.2	1,511.5	979.2
<u>Exportin-2</u>	CSE1L	1,094.5	301.0	767.2	238.3
<u>E3 ubiquitin-protein ligase listerin</u>	LTN1	12.8	25.9	1,366.7	129.7
<u>Serine/threonine-protein kinase ATR</u>	ATR	94.6	32.3	1,093.5	158.4
<u>Exportin-5</u>	XPO5	211.4	194.3	388.9	504.0
Fatty aldehyde dehydrogenase	ALDH3A2	46.8	20.1	985.9	168.3
Target of rapamycin complex subunit LST8	MLST8	40.6	17.2	889.2	210.6
<u>DNA-dependent protein kinase catalytic subunit</u>	PRKDC	129.2	556.9	407.0	27.0
<u>Serine-protein kinase ATM</u>	ATM	17.6	5.8	548.0	294.9
<u>Importin-11</u>	IPO11	190.7	402.1	96.3	99.5
Fatty acid desaturase 2	FADS2	5.9	6.8	338.9	281.8
<b>Sigma non-opioid intracellular receptor 1</b>	<b>SIGMAR1</b>	<b>33.8</b>	<b>79.7</b>	<b>282.8</b>	<b>171.5</b>
<u>Exportin-6</u>	XPO6	39.4	42.2	245.1	150.4
<u>Importin-7</u>	IPO7	42.7	280.5	97.2	49.0
7-dehydrocholesterol reductase	DHCR7	34.5	43.4	161.0	204.6
Brefeldin A-inhibited guanine nucleotide-exchange protein 2	ARFGEF2	10.5	22.6	260.2	149.7
<u>Exportin-7</u>	XPO7	107.2	102.5	135.9	79.0
Prohibitin	PHB	24.5	271.3	10.4	109.7
Surfeit locus protein 4	SURF4	36.6	34.6	215.3	108.1
Signal transducer and activator of transcription 3	STAT3	67.1	20.5	151.4	134.5
<u>Transportin-1</u>	TNPO1	114.8	110.5	68.8	63.6
<u>Importin-8</u>	IPO8	36.7	64.6	93.8	129.7
Voltage-dependent anion-selective channel protein 1	VDAC1	3.7	15.7	67.5	233.8
<u>Importin-5</u>	IPO5	72.2	162.8	37.3	44.1
Probable methyltransferase TARBP1	TARBP1	5.6	10.8	152.9	140.5

Protein names	Gene	GE n = 1	GE n = 2	Pierce n = 1	Pierce n = 2
Probable arginine--tRNA ligase, mitochondrial	RARS2	5.8	8.0	124.5	169.5
Voltage-dependent anion-selective channel protein 2	VDAC2	8.3	33.0	53.0	197.9
<b>Importin-4</b>	IPO4	43.4	35.1	100.5	77.1
<b>Transportin-3</b>	TNPO3	65.0	116.8	40.7	25.3
D-3-phosphoglycerate dehydrogenase	PHGDH	49.6	50.3	9.9	130.5
Gem-associated protein 4	GEMIN4	33.0	17.6	127.4	41.6
Protein MON2 homolog	MON2	4.9	6.7	113.2	75.6
Basic leucine zipper and W2 domain-containing protein 1	BZW1	53.0	23.3	93.4	24.3
Probable ATP-dependent RNA helicase DDX20	DDX20	8.5	14.4	80.9	85.0
Prohibitin-2	PHB2	14.8	89.7	10.3	70.3
Thyroid adenoma-associated protein	THADA	39.9	72.4	35.9	32.9
Very-long-chain enoyl-CoA reductase	TECR	32.1	29.2	92.5	24.6
<b>Importin-9</b>	IPO9	42.7	47.3	51.3	35.4
Conserved oligomeric Golgi complex subunit 7	COG7	36.5	48.8	12.4	77.6
Conserved oligomeric Golgi complex subunit 5	COG5	12.4	82.5	8.3	60.7
Tubulin beta-6 chain	TUBB6	48.4	54.5	15.4	6.7
Sterol O-acyltransferase 1	SOAT1	13.3	63.7	12.1	5.7
<b>Exportin-4</b>	XPO4	14.1	55.1	16.5	4.7
Pachytene checkpoint protein 2 homolog	TRIP13	19.7	7.2	34.2	29.2
Conserved oligomeric Golgi complex subunit 2	COG2	5.1	38.4	7.0	31.2
Dolichyl-diphosphooligosaccharide--protein glycosyltransferase subunit 1	RPN1	17.6	6.0	38.0	7.7
<b>Importin subunit beta-1</b>	KPNB1	18.0	36.6	5.6	6.2
4F2 cell-surface antigen heavy chain	SLC3A2	4.4	6.7	16.9	30.1
<b>Dynein assembly factor 5, axonemal</b>	DNAAF5	16.9	10.7	16.6	6.0
Alkyldihydroxyacetonephosphate synthase, peroxisomal	AGPS	24.7	6.5	7.5	3.8
Tubulin alpha-4A chain	TUBA4A	16.4	10.0	8.2	5.8
Long-chain-fatty-acid--CoA ligase 3	ACSL3	8.5	11.4	6.1	7.5
Tubulin alpha-1C chain	TUBA1C	11.5	8.4	6.7	4.0
Tubulin alpha-1B chain	TUBA1B	8.7	8.1	7.1	4.2
Tubulin beta-4B chain	TUBB4B	6.1	6.4	8.1	5.7
Tubulin beta chain	TUBB	6.2	5.8	7.7	5.7

In all four experiments, the  $\sigma_1$  receptor (highlighted in bold) was significantly enriched on DP79 beads, thereby validating this affinity enrichment approach. Furthermore, two prominent protein groups were found: phosphatidylinositol 3-kinase related kinases (PIKK, highlighted in blue) and nuclear pore complex (NPC) proteins (highlighted in red). PIKKs are a family of large (280-470 kDa) serine/threonine kinases, comprising the *mammalian target of rapamycin* (mTOR), a key regulator of cellular growth, the *DNA-dependent protein kinase* (DNA-PK), which is involved in DNA repair via non-homologous end-joining, as well as *Ataxia Telangiectasia Mutated* (ATM) and *Ataxia telangiectasia and Rad3-*

*related protein* (ATR), both involved DNA damage sensing and SMG1, which regulates nonsense-mediated decay. In addition the transcriptional co-activator TRRAP is part of the PIKK family despite the lack of kinase activity.<sup>251</sup> Apart from the latter two, all PIKK family members are significantly enriched by DP79. Additionally, LST8, a subunit of the mTOR complex was also identified. The PIKK family and many NPC proteins share HEAT repeats as common structural feature (underlined proteins).<sup>252,253</sup> HEAT (Huntingtin, Elongation factor 3, protein phosphatase 2A subunit A and IOR1) repeat domains consist of short motifs containing two  $\alpha$ -helices, have a rather amphiphilic character and may facilitate protein-protein interactions.<sup>253</sup> The translational activator GCN1 and the E3 ligase listerin, which both are also strongly enriched, contain HEAT repeat domains as well, according to the UniProt database (UniProt-IDs: Q92616; O94822).<sup>254</sup> Since 10 of 15 most strongly enriched proteins in the combined hit list contain HEAT repeats, DP79 may be a direct binder of this structural motif.

### 5.3.5.3 Validation of mTOR as target of DP68

As described in the previous chapter, PIKKs have been identified as putative target proteins of ROS-inducing diaminopyrimidines by means affinity enrichment experiments using NHS beads. DP68 induces a strong cytosolic accumulation of superoxide, which may be facilitated by interfering with superoxide dismutases. Interestingly, mTOR has been described to influence the activity of SOD1. Tsang *et al.* reported that under fed conditions, the mTOR complex 1 (mTORC1) phosphorylates SOD1 at T40 and thereby inhibits its catalytic activity, a process that is suppressed upon starvation.<sup>255</sup> Inactivation of enzymatic activity of SOD1 by mTOR may trigger an increase in cytosolic superoxide. Thus, mTOR was explored as a target for DP68-induced superoxide induction.

For this, 28 known mTOR inhibitors were evaluated for their activity in the CM-H<sub>2</sub>DCFDA-based ROS assay in HeLa cells (Table 21). 75 % of these inhibitors did not increase cellular ROS levels. Some inhibitors, e.g. Rapamycin and Torin 2, induced ROS with EC<sub>50</sub> values ranging from 4 to 8  $\mu$ M. However, it is questionable whether this activity is actually linked to their mTOR-inhibiting properties, as these compounds display nanomolar potency in cellular assays for mTOR inhibition.<sup>256,257</sup>

**Table 21: ROS-inducing activities of different mTOR inhibitors.** 28 different mTOR inhibitors were tested for ROS induction in a CM-H<sub>2</sub>DCFDA-based assay after 1 h compound incubation in HeLa cells. Mean values  $\pm$  SD, N = 3, n = 3. Data were obtained by COMAS, Dortmund.

Compound	ROS EC <sub>50</sub> [ $\mu$ M]	Compound	ROS EC <sub>50</sub> [ $\mu$ M]
CC-223	4.6 $\pm$ 1.2	VS-5584	>10
Torin 2	4.9 $\pm$ 1.3	Ridaforolimus	>10
Rapamycin	5.1 $\pm$ 2.6	KU-0063794	>10
Everolimus	6.1 $\pm$ 1.2	WYE-132	>10
WAY-600	6.9 $\pm$ 0.7	GSK2126458	>10
Temsirolimus	7.9 $\pm$ 1.3	BGT226	>10
WYE-354	8.3 $\pm$ 1.1	AZD8055	>10
SAR245409	>10	PP242	>10
Palomid 529	>10	OSI-027	>10
GSK1059615	>10	PP121	>10
INK 128	>10	GDC-0980	>10
PI-103	>10	AZ20	>10
AZD2014	>10	eCF309	>10
PF-04691502	>10	CC-223	>10

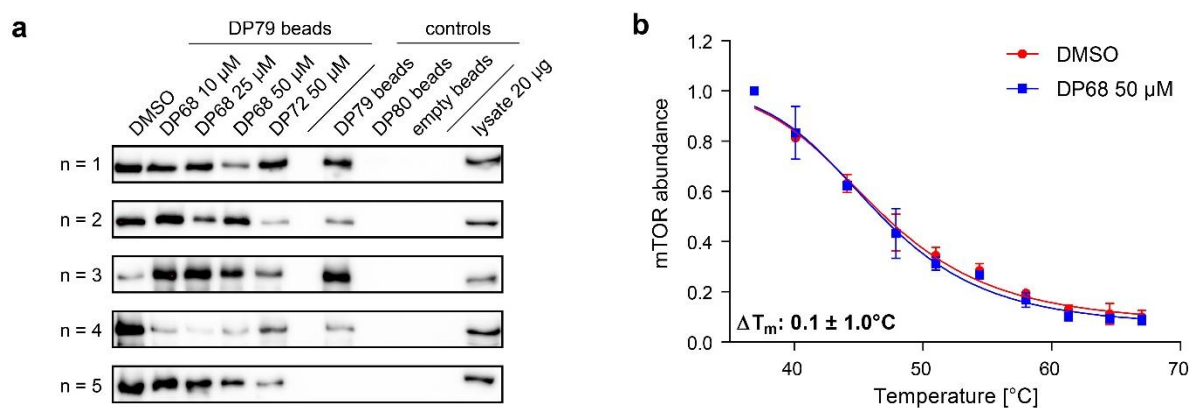


**Figure 48: Validation of mTOR as binding partner of DP68.** (a) Competition pull-down using Pierce NHS beads. Briefly, HeLa cell lysates were preincubated with DMSO, DP68 or DP72 for 1 h prior to 2 h of incubation with DP79 beads. Bound proteins were eluted and subjected to SDS-PAGE and subsequent immunoblotting for mTOR detection. In parallel, untreated lysates were incubated with DP79, DP80 or empty beads. n = 5. (b) TPP melting curves of mTOR in presence or absence of DP68. Mean values  $\pm$  SD, N = 1, n = 3

To investigate the potential interaction of mTOR and DP68, competition pull-downs using Pierce NHS beads were performed (Figure 48a). For this, HeLa cell lysates were preincubated with increasing concentrations of DP68, 50  $\mu$ M of DP72 or DMSO for 1 h on ice prior to an incubation with DP79 beads. Beads were washed and bound proteins were eluted by heating. Enrichment of mTOR

was detected via immunoblotting. As controls, DP79, DP80 or empty beads were incubated with untreated lysates. In four out of five experiments, mTOR was exclusively enriched by beads decorated with DP79, but not by DP80 or empty beads. In the first biological replicate, mTOR was enriched by DP79 in all conditions in a comparable degree, except for the sample incubated with lysate containing 50  $\mu$ M DP68, indicating that DP68 interferes with the enrichment of mTOR. However, this observation could not be reproduced over the course of five independent experiments. Furthermore, in TPP DP68 did not influence the melting behavior of mTOR (Figure 48b).

If the superoxide-inducing activity was actually caused by an mTOR-mediated phosphorylation of SOD1, as described by Tsang *et al.*, inhibition of the kinase activity of mTOR should interfere with the accumulation of ROS caused by DP68. Thus, DP68-induced ROS levels were evaluated after a preincubation with four different mTOR inhibitors (Figure 49). None of the inhibitors induced ROS or acted as general antioxidant, since ROS levels of cells treated with CDNB and the respective inhibitor, did not significantly deviate from the levels in cells treated with CDNB. The ROS-inducing activity of DP68 was not dampened by any of the four mTOR inhibitors, suggesting that superoxide induction by DP68 is independent of mTOR kinase activity.

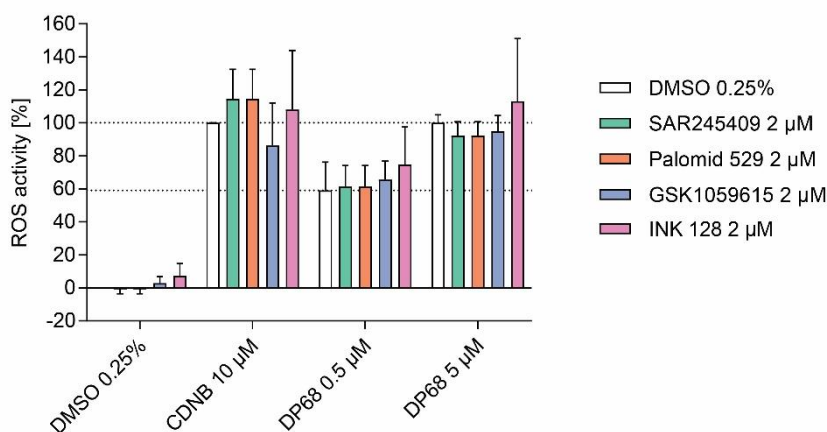


**Figure 49: Influence of mTOR inhibitors on DP68-induced ROS induction.** HeLa cells were preincubated with mTOR inhibitors that lack ROS-inducing activity (Table 21) prior to the addition of DP68, followed by 60 min of incubation. Afterwards, ROS levels were determined by means of CM-H<sub>2</sub>DCFDA. Mean values  $\pm$  SD, N = 4, n = 3.

To test the influence of DP68 on the catalytic activity of PIKKs, *in vitro* kinase activity assays were performed for mTOR, alone and in combination with FKBP12, as well as for DNA-PK, ATM, ATR in



combination of with the ATR-interacting protein (ATRIP) (Table 22). At 50  $\mu$ M, DP68 did not influence the activity of any of the tested kinases.

**Table 22: Influence of DP68 on the kinase activity of different PIKKs.** *In vitro* kinase activity assays of DP68 (50  $\mu$ M) using full-length protein, performed by Eurofins Discovery Services. Mean values  $\pm$  SD, N = 2, n = 3.

Assay	Residual activity [%]	
	mean	SD
mTOR	91.7	14.6
mTOR/FKBP12	88.0	9.5
ATM	84.5	24.8
ATR/ATRIP	85.1	10.4
DNA-PK	100.2	6.8

Although mTOR was strongly enriched in the affinity enrichment experiments using NHS beads, validation experiments could not confirm this target hypothesis. The majority of mTOR inhibitors do not induce ROS, selected mTOR inhibitors do not interfere with ROS accumulation induced by DP68 and the kinase activity was not influenced by DP68 in an *in vitro* assay. Furthermore, the enrichment of mTOR via DP79 beads could not be reproducibly competed by DP68 and DP68 did not influence the thermal stability of mTOR. Taken together, mTOR could not be confirmed as target responsible for DP68-induced ROS induction.

#### 5.3.5.4 Validation of superoxide-dismutating enzymes as targets of DP68

DP68 induced a strong increase in cytosolic superoxide levels (Figure 26), however without affecting hydrogen peroxide levels (Figure 31). These findings indicate that DP68 may interfere with superoxide dismutation. Therefore, superoxide dismutases were investigated as putative targets of DP68. Apart from SOD enzymes, the cytosolic NAD(P)H dehydrogenase (quinone 1) (NQO1) was reported to possess superoxide-dismutating properties and was thus considered as a possible target of DP68.<sup>258</sup> In the affinity enrichment experiments using NHS beads, none of the three SOD family members were identified in any of the samples. In contrast, NQO1 was found in all four experiments, however, it was not significantly enriched on DP79 over DP80 (Table 23). In experiments using Pierce NHS beads, NQO1 was found more frequently on DP79 beads compared to DP80 beads.

Table 23: LFQ intensities for NQO1 in affinity enrichment experiments using NHS beads.

	DP79 beads				DP80 beads			
	N = 1	N = 2	N = 3	N = 4	N = 1	N = 2	N = 3	N = 4
GE n = 1	0	0	0	2.4	1.6	2.0	2.0	0
GE n = 2	2.2	1.0	1.9	1.4	1.6	2.5	1.5	1.7
Pierce n = 1	9.3	8.7	9.6	11.6	0	0	9.9	0
Pierce n = 2	2.2	2.3	0	2.2	0	0	0	0

However, this enrichment could not be detected via immunoblotting against NQO1 (Figure 50a). Additionally, in TPP no influence of DP68 on the NQO1 thermal stability was detected (Figure 50b). Furthermore, SOD1 and SOD2 were detected in TPP, however DP68 did not influence their thermal stability (Figure 50c).

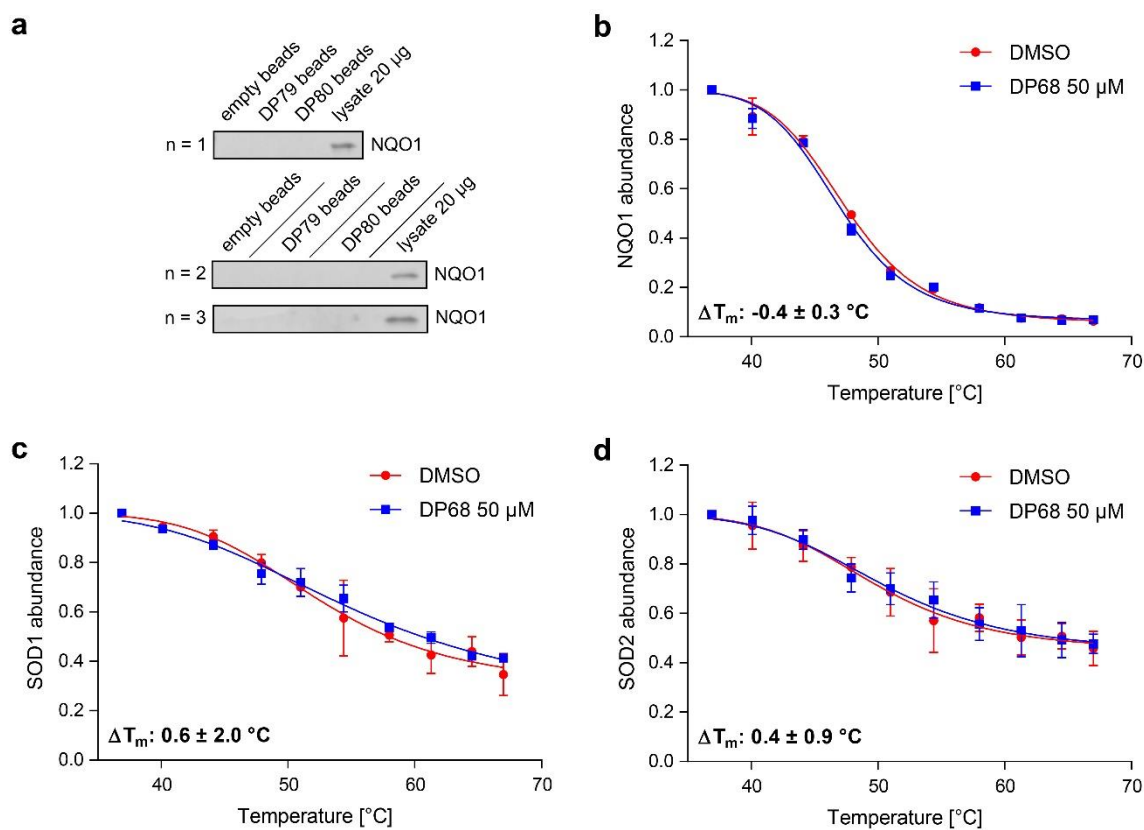


**Figure 50: Validation of superoxide-dismutating enzymes as binding partners of DP68.** (a) Affinity enrichment using Pierce NHS beads. Briefly, DP79, DP80 or empty beads were incubated with HeLa cell lysates for 2 h. Bound proteins were eluted and subjected to SDS-PAGE and subsequent immunoblotting for NQO1. n = 3. (b-d) TPP melting curves of NQO1, SOD1 and SOD2, respectively. Mean values  $\pm$  SD, N = 1, n = 3. Data displayed in (a) were obtained by Alexandra Brause, MPI Dortmund.

To test whether DP68 might influence the enzymatic activity of superoxide dismutases, a respective activity assay was performed (Figure 51). The assay detects the superoxide-scavenging properties of a biological sample, using a tetrazolium salt that forms a yellow formazan dye upon reaction with superoxide. Xanthine oxidase is used as superoxide source in this assay. The direct influence of diaminopyrimidine compounds on a recombinant bovine SOD1 was tested (Figure 51a), which shares a high sequence similarity to its human ortholog (Supplementary Figure 7). The copper-chelating compound ATN-224, which is a potent inhibitor of SOD1, was used as a control.<sup>259</sup> While ATN-224 inhibited SOD1 in a dose-dependent manner, none of the tested diaminopyrimidines displayed activity in this assay. HeLa cells were treated with compounds for 2 h prior to measuring their superoxide-scavenging properties (Figure 51b). Again, ATN-224 showed concentration-dependent inhibition. However, it reduced the cellular superoxide-scavenging capacities to lesser extent compared to recombinant SOD1, since ATN-224 inhibits SOD1, but not SOD2 or NQO1, which are also present in cells. Again, none of the tested diaminopyrimidines were found active. In conclusion, DP68 neither targets superoxide-dismutating enzymes directly, nor inhibits their enzymatic activity.

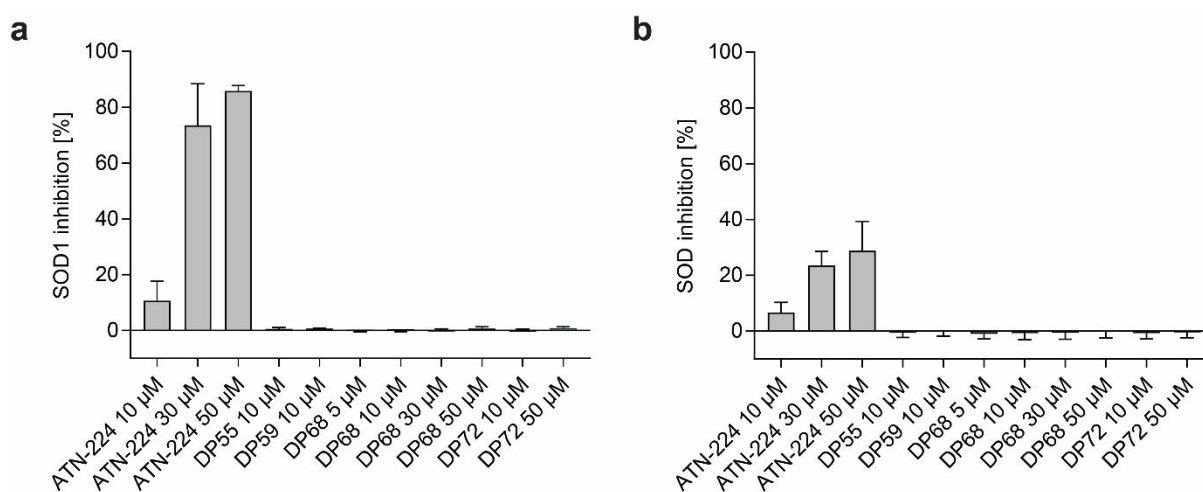


**Figure 51: Influence of diaminopyrimidines on the catalytic activity of superoxide dismutases. (a)** Bovine SOD1 was incubated with compounds for 60 min prior to the assessment of its superoxide-scavenging properties. Mean values  $\pm$  SD, N = 2, n = 3. **(b)** HeLa cells were treated with compounds for 2 h, chemically lysed and tested for superoxide-scavenging. Mean values  $\pm$  SD, N = 2, n = 3.

### 5.3.6 Target identification via *in situ* pulldown

With the exception of the Cell Painting assay, all target identification approaches were performed using cell lysates. As described in chapter 2.1.2, lysates do not completely reflect the cellular environment

due to lack of compartmentalization and absence of certain proteins, which are not extracted from cellular debris during lysis preparation. To circumvent these limitations, a PAL-based *in situ* pulldown can be performed instead.<sup>14</sup> For this, cells are treated with probes containing a photoaffinity group. These probes can engage their target proteins in cells and get covalently linked to proteins in close proximity upon UV irradiation. For the target identification of DP68, PAL probes containing a diazirine 'minimalist' linker with a terminal alkyne developed by *Li et al.* were synthesized by Dr. Matthias Bischoff (Figure 52a).<sup>15</sup>

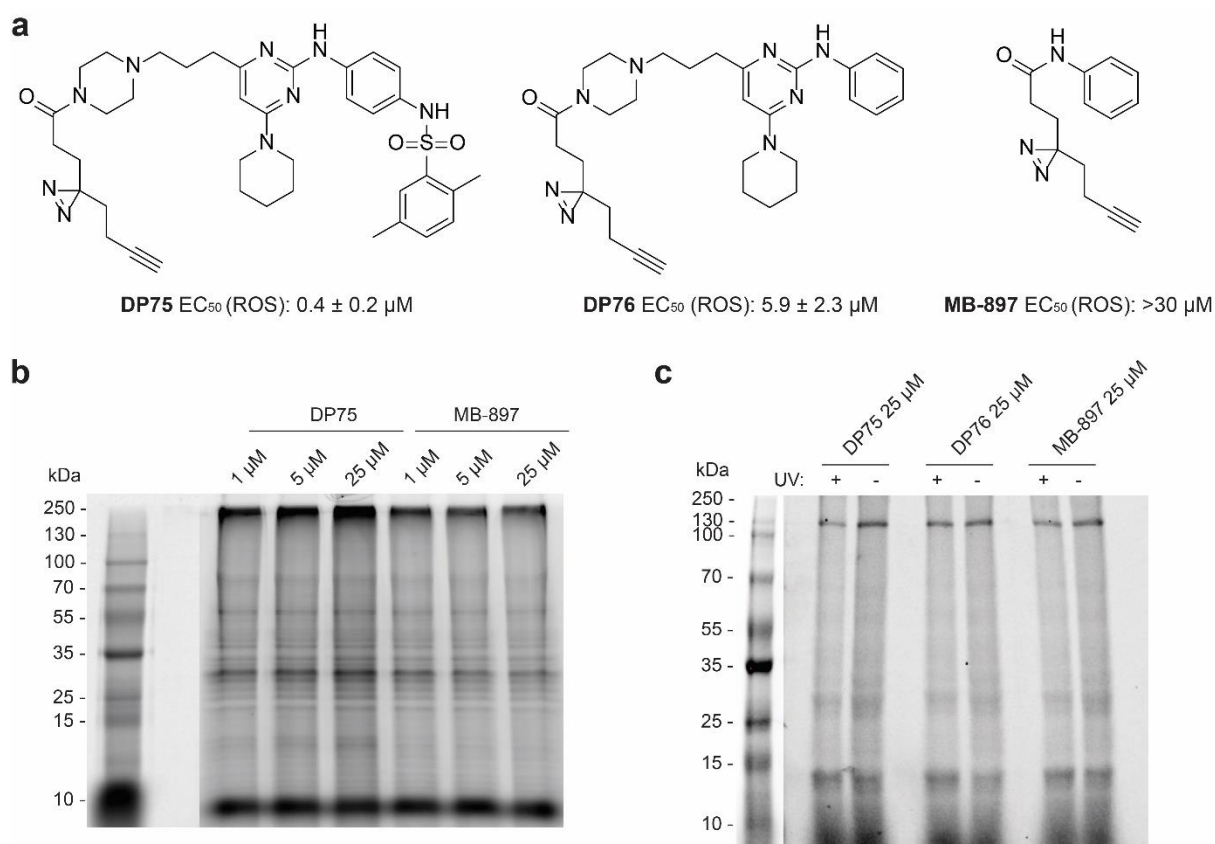


**Figure 52: Photoaffinity labeling in HeLa cells. (a)** Chemical structures of diaminopyrimidine-based PAL probes (DP75 and DP76) and a simple control probe (MB-897). ROS-inducing activities were determined in HeLa cells using CM-H<sub>2</sub>-DCFDA. Mean values ± SD, N = 4, n = 3 **(b and c)** Photoaffinity labeling in HeLa cells using DP75 and MB-897. Cells were treated with PAL probes, UV irradiated and lysed. Cell lysates were reacted with TAMRA-biotin-azide to label alkyne-tagged proteins and subjected to SDS-PAGE. Enriched proteins were visualized via in-gel TAMRA fluorescence. Labeling with different probe concentrations (b) and with or without UV crosslinking (c).

The DP68-based probe DP75 displayed comparable ROS-inducing activity in HeLa cells. DP76 was originally designed to be used as negative control. In contrast to DP72, DP74 and DP80, DP76 is lacking

the para-amino group on the phenyl ring. Despite its comparably low potency with an EC<sub>50</sub> value of 5.86  $\mu$ M, it is still not suitable as a negative probe due to its residual ROS-inducing activity. Therefore, MB-897, a simplified negative PAL probe also used by Li *et al.*, was employed as a negative control instead, as it was inactive for ROS accumulation in HeLa cells.<sup>15</sup>

To evaluate the specificity of DP75 and MB-897, a photoaffinity labeling experiment in HeLa cells was performed (Figure 52b and 52c). For this, cells were treated with the respective probe for 10 min, washed to remove excess probe and irradiated with UV light. After cell lysis, the soluble supernatant was subjected to a copper-catalyzed click-reaction to label alkyne tagged proteins with a TAMRA-biotin-azide conjugate and subjected to SDS-PAGE. Labeled proteins were visualized by means of in-gel fluorescence. Based on the band pattern, DP75 interacts with a variety of proteins, however a very similar band pattern was observed for samples originating from cells treated with the simplified negative probe MB-897, questioning the specificity of DP75 in terms of its PAL properties. The PAL minimalist linkers used in this approach were described by Horning *et al.* to label the majority of proteins in a UV-radiation-independent manner. Thus, all three available probes were tested for protein labeling in the presence or absence of UV irradiation (Figure 52c).<sup>260</sup> For all three probes, the band patterns and intensities were comparable among all samples, indicating a high degree of non-specific, UV-independent labeling. Such high degree of protein background rendered this approach unsuitable to detect significantly enriched probes via in-gel fluorescence.

Alternatively, an *in situ* pulldown with subsequent on-bead digestion and mass spectrometry analysis was performed. After compound treatment, washing, UV irradiation and lysis of cells, proteins were reacted with an excess of biotin azide to label all photoaffinity-tagged proteins. After performing a gel filtration to remove unreacted biotin azide, lysates were incubated with Streptavidin-coated beads to enrich biotin-tagged proteins, followed by stringent washing with wash buffer containing 4 M urea and subsequent on-bead digestion, stage-tip purification and mass spectrometry analysis. The number of proteins identified in this approach (Figure 53a) was lower compared to the lysate-based affinity enrichment experiments using NHS beads (Figure 47b and 47c). This may be due to a lower protein background caused by the denaturing washing steps, which should remove proteins that are not bound to the affinity matrix via biotin-streptavidin interaction. The photoaffinity labeling experiment (Figure 52b) did not reveal differences in the protein band patterns between DP75 and MB-897. In line with this observation, in the *in situ* pulldown no proteins were found significantly enriched in the samples derived

from cells treated with DP75 compared to the control cells (FDR = 0.05). The low LFQ intensity correlations of the identified proteins indicate an insufficient technical reproducibility, which again questions the selectivity of the respective probes. In conclusion, the usage of affinity probes for target identification was not successful due to lack of probe specificity.

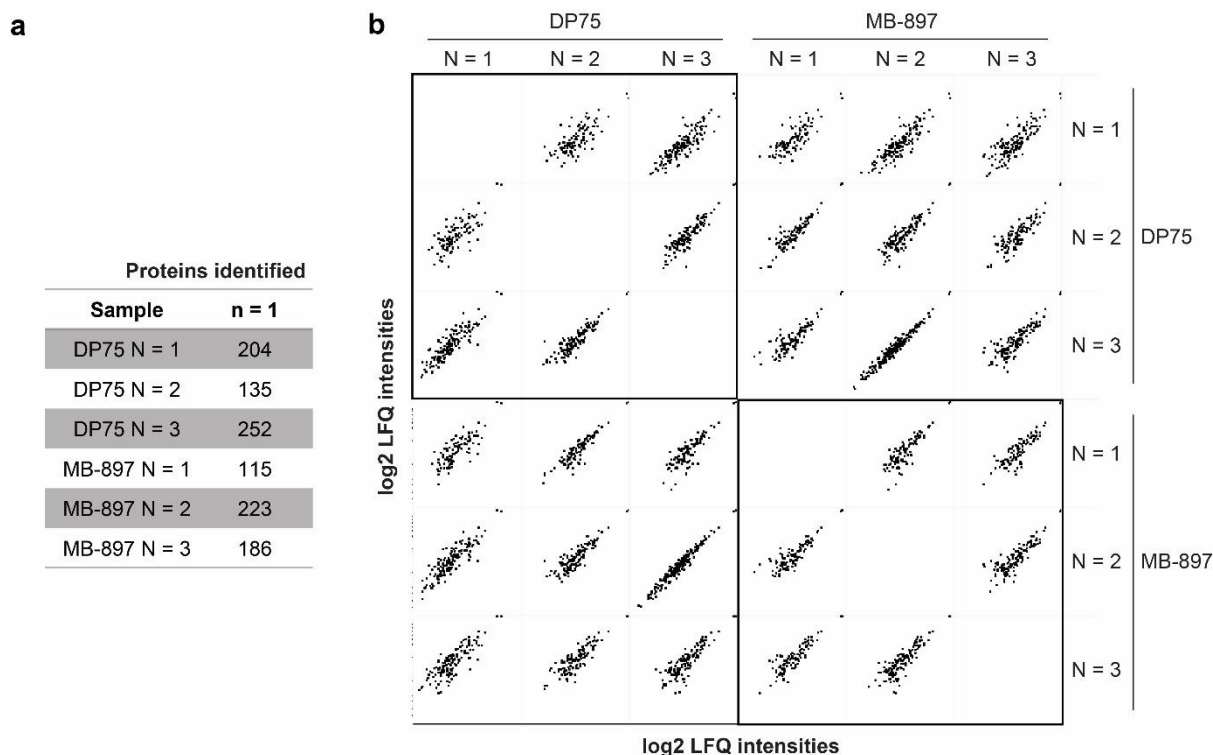


**Figure 53: *In situ* pulldown with on-bead digestion. (a)** Number of proteins identified per sample. **(b)** Scatter plot of the LFQ intensities of proteins identified. N = 3, n = 1

### 5.3.7 Target identification via proteome profiling

All target identification techniques presented in the previous chapters did not lead to the identification of the target protein of DP68 responsible for its ROS-inducing activity. As DP68 is a fast-acting inducer of ROS accumulation, a mode of action involving alterations in gene expression could be ruled out. However, in theory, DP68 might influence protein levels, e.g. by triggering degradation of a protein. To investigate this, a proteome profiling was performed. For this, HeLa cells were treated with 1 or 5  $\mu$ M of DP68 or DP72 for either 1 h, allowing to observe immediate effects or for 24 h to detect cellular responses on the proteome level. After compound treatment, changes in the proteome in TMT-labeled samples were analyzed by MS/MS. Proteins that were significantly up- or downregulated by DP68, but not by DP72, compared to the respective control treated with DMSO in all three biological replicates

were regarded for further analysis (Table 24). As TMT-based quantification of protein ratios is known to underestimate the actual protein abundance, quantitative results are not shown.<sup>261</sup> All proteins whose abundance was significantly altered by DP68, were upregulated.

**Table 24: Proteome profiling of DP68 and DP72 in HeLa cells.** Cells were treated with DP68, DP72 or DMSO for 1 or 24 h, lysed and subjected to a tryptic digest. Obtained peptides were TMT-labeled, pooled and subjected to MS/MS-based proteome analysis for relative protein quantification. Protein intensities from sample cells treated with compound were normalized to values of the respective DMSO control samples. Proteins that were changed significantly ( $p < 0.05$ ) by DP68, but not by DP72, over all three biological replicates are listed. All proteins listed were upregulated. N = 1, n = 3

Protein name	Gene	p-values		
		n = 1	n = 2	n = 3
<b>5 <math>\mu</math>M DP68 / DMSO, 1 h treatment</b>				
Protein CYR61	CYR61	$6 \times 10^{-9}$	$1 \times 10^{-7}$	$1 \times 10^{-3}$
<b>5 <math>\mu</math>M DP68 / DMSO, 24 h treatment</b>				
Acetyl-coenzyme A synthetase, cytoplasmic	ACSS2	$2 \times 10^{-55}$	$1 \times 10^{-29}$	$3 \times 10^{-142}$
Fatty acid-binding protein, heart	FABP3	$8 \times 10^{-57}$	$2 \times 10^{-11}$	$1 \times 10^{-75}$
Hydroxymethylglutaryl-CoA synthase, cytoplasmic	HMGCS1	$2 \times 10^{-58}$	$8 \times 10^{-11}$	$2 \times 10^{-68}$
Lanosterol 14- $\alpha$ demethylase	CYP51A1	$7 \times 10^{-42}$	$7 \times 10^{-12}$	$5 \times 10^{-57}$
Fatty acid desaturase 2	FADS2	$2 \times 10^{-31}$	$3 \times 10^{-10}$	$7 \times 10^{-55}$
Isopentenyl-diphosphate Delta-isomerase 1	IDI1	$3 \times 10^{-42}$	$5 \times 10^{-8}$	$5 \times 10^{-48}$
Acyl-CoA desaturase	SCD	$2 \times 10^{-44}$	$2 \times 10^{-10}$	$2 \times 10^{-21}$
7-dehydrocholesterol reductase	DHCR7	$7 \times 10^{-20}$	$5 \times 10^{-9}$	$6 \times 10^{-20}$
Transmembrane protein 97	TMEM97	$1 \times 10^{-10}$	$6 \times 10^{-13}$	$2 \times 10^{-14}$
Proprotein convertase subtilisin/kexin type 9	PCSK9	$6 \times 10^{-18}$	$4 \times 10^{-9}$	$1 \times 10^{-16}$
Low-density lipoprotein receptor	LDLR	$1 \times 10^{-23}$	$2 \times 10^{-4}$	$6 \times 10^{-24}$
WW domain-binding protein 2	WBP2	$3 \times 10^{-11}$	$6 \times 10^{-6}$	$2 \times 10^{-15}$
Farnesyl pyrophosphate synthase	FDPS	$5 \times 10^{-17}$	$1 \times 10^{-3}$	$5 \times 10^{-16}$
Sterol-4- $\alpha$ -carboxylate 3-dehydrogenase	NSDHL	$3 \times 10^{-9}$	$5 \times 10^{-4}$	$1 \times 10^{-13}$
Diphosphomevalonate decarboxylase	MVD	$1 \times 10^{-12}$	$5 \times 10^{-4}$	$1 \times 10^{-9}$

DP68 hardly influenced protein levels after 1 h of incubation, except for CYR61, which was upregulated after treatment with 5  $\mu$ M of DP68. CYR61 is a extracellular matrix protein, which promotes cellular proliferation, cell survival and angiogenesis.<sup>262</sup> A literature search did not reveal a mechanistic link of this protein to redox regulation. A stronger change in the proteome was detected after 24 h of treatment with 5  $\mu$ M DP68, as 15 proteins were significantly upregulated, including many proteins involved in lipid metabolism. A major pathway regulating the expression of such proteins is the sterol-responsive element binding protein (SREBP) pathway. With the exception of the WW domain-binding protein 2, the

expression of all these proteins is regulated by the SREBP pathway, suggesting that DP68 may activate this pathway.<sup>263–276</sup> However, as lysosomotropic compounds can interfere with the intracellular transport of cholesterol and thereby activate this pathway, it is unclear, whether this observation is linked to ROS induction.<sup>277</sup> Furthermore, the activation of the SREBP pathway was only observed after 24 h incubation and may therefore be a consequence of the cellular accumulation of ROS or may be an unrelated bioactivity. Therefore, investigations of this pathway were not continued.

### 5.3.8 Target identification via phosphoproteome profiling

Since DP68 induces ROS accumulation within approximately 30 min, only cellular mechanisms with a comparably short response time could mediate this bioactivity. Since changes in the phosphorylation state of a protein can occur within few minutes, DP68-induced superoxide induction might be a result of alterations in the phosphoproteome of the cell.<sup>278</sup> Therefore, a phosphoproteome profiling for DP68 was performed (Figure 54). For this, cells were treated with compounds, briefly washed and lysed. Proteins were precipitated on beads and subjected to tryptic digestion. Subsequently, phosphopeptides were enriched on titanium dioxide beads, and analyzed via HPLC-MS/MS.

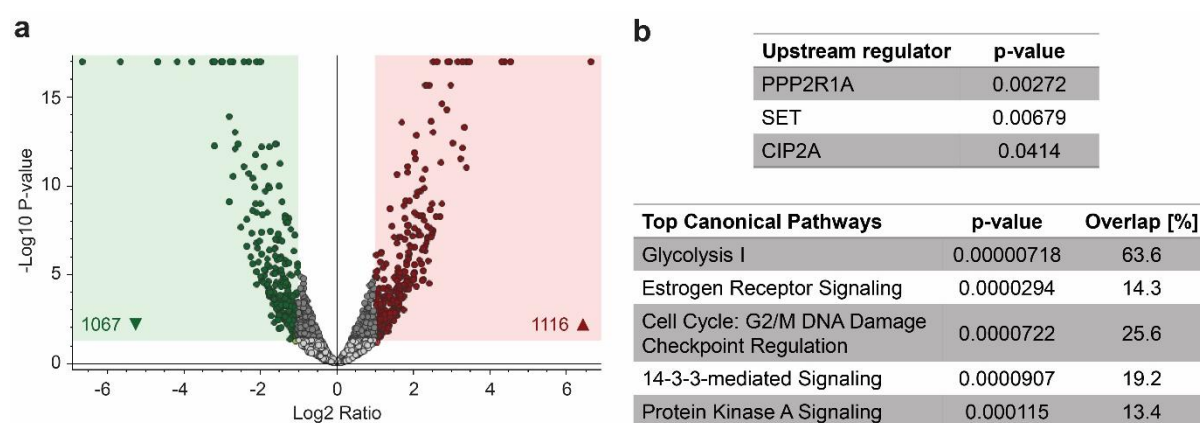


**Figure 54: Phosphoproteome analysis upon DP68 treatment.** HeLa cells were treated with 10  $\mu$ M DP68, DP72 or DMSO for 30 min prior to a phosphoproteome analysis. **(a)** Volcano plot of phosphopeptide ratios of samples of cells treated with DP68- vs. cells treated with DMSO. The DP68 treatment led to downregulation of 1067 and an upregulation of 1116 phosphopeptides.  $p < 0.05$ ,  $N = 1$ ,  $n = 3$  **(b)** Data analysis via *Ingenuity Pathway Analysis (IPA)* software. A list of significantly up- or downregulated phosphopeptides (DP68/DMSO) was created and all phosphopeptides, which were significantly altered by DP72 in the same direction, were removed. The protein IDs, abundance log2 ratios and the respective p-values of the remaining 958 phosphopeptides were analyzed using a phosphopeptide analysis based on p-values. Predicted upstream regulators and top five canonical pathways are shown. Data were obtained in collaboration with Dr. Elena Rudashevskaya, MPI Dortmund.



A treatment of HeLa cells for 30 min with 10  $\mu$ M DP68 led to significant differences in the abundance of 2183 phosphopeptides compared to cells treated with DMSO. To distinguish, which of these alterations may be related to the ROS-inducing property of DP68, the same analysis was performed for 10  $\mu$ M DP72. All phosphopeptides whose abundance was significantly changed in the same direction by both DP68 and DP72 (relative to DMSO) were excluded from the analysis.

Three upstream regulators have been predicted based on the analysis using the IPA software: The 'serine/threonine-protein phosphatase 2A 65 kDa regulatory subunit A alpha isoform' (PPP2R1A), which is part of the protein phosphatase 2a (PP2A), as well as SET and CIP2A, which both are negative regulators of PP2A.<sup>279,280</sup> Furthermore, the top 5 enriched pathways are either regulated by PP2A, or, in the case of Protein Kinase A, regulate this phosphatase.<sup>281–285</sup> Interestingly, PPP2R1A contains a HEAT repeat domain comprising of 15 repeats, which is important for the correct assembly of the enzyme.<sup>286</sup> In affinity-based proteomics using NHS beads, DP79 strongly enriched proteins with HEAT repeat domains, but no protein phosphatases were found on the combined hitlist (Table 20). However, some members of the serine/threonine-protein phosphatase family were enriched by DP79 immobilized on Pierce NHS beads, including regulatory subunits of the protein phosphatases 1 and 2A and all known subunits of protein phosphatase 6 (PP6) (Table 25).<sup>287</sup>

**Table 25: Protein phosphatases significantly enriched by DP79.** List of all members of the serine/threonine-protein phosphatase family that were significantly enriched by DP79 (relative to DP80) in both biological replicates of the affinity enrichment experiments using Pierce NHS beads. LFQ ratios, N = 4, n = 2

Protein names	Gene	LFQ ratio DP79/DP80		
		n = 1	n = 2	mean
Protein phosphatase 1 regulatory subunit 15B	PPP1R15B	11.2	6.8	9.0
Protein phosphatase 1 regulatory subunit 35	PPP1R35	11.3	3.6	7.4
Serine/threonine-protein phosphatase 2A 56 kDa regulatory subunit delta isoform	PPP2R5D	146.7	208.3	177.5
Serine/threonine-protein phosphatase 6 catalytic subunit	PPP6C	86.3	128.8	107.6
Serine/threonine-protein phosphatase 6 regulatory ankyrin repeat subunit A	ANKRD28	63.4	93.5	78.4
Serine/threonine-protein phosphatase 6 regulatory ankyrin repeat subunit B	ANKRD44	35.7	76.5	56.1
Serine/threonine-protein phosphatase 6 regulatory ankyrin repeat subunit C	ANKRD52	6.2	9.7	8.0
Serine/threonine-protein phosphatase 6 regulatory subunit 1	PPP6R1	92.6	107.5	100.1
Serine/threonine-protein phosphatase 6 regulatory subunit 2	PPP6R2	10.0	9.9	9.9
Serine/threonine-protein phosphatase 6 regulatory subunit 3	PPP6R3	175.0	196.0	185.5

DP68 induced cellular superoxide accumulation without increasing hydrogen peroxide levels (Figure 26 and Figure 31), which led to the hypothesis that the compound may interfere with superoxide dismutation. However, DP68 did not inhibit the enzymatic activity of superoxide dismutases in cells (Figure 51). The phosphoproteome analysis additionally revealed that DP68, but not DP72, induced a phosphorylation of S99 in SOD1 (Figure 55). Interestingly, apart from the mTOR-mediated phosphorylation of T40, SOD1 can get phosphorylated at S60 and S99 by Chk2, triggering the nuclear localization of SOD1.<sup>255,288,289</sup> Nuclear accumulation of SOD1 may lower the superoxide-dismutating capacity of the cytosol, potentially leading to an increase in cytosolic superoxide levels. In addition, Chk2 can be directly inhibited through dephosphorylation via PP2A.<sup>290</sup> Thus, an inhibition of PP2A by DP68 may lead to an activation of Chk2, which would explain the phosphorylation of SOD1 at S99. On the basis of this data, PPP2R1A was selected for further target validation.

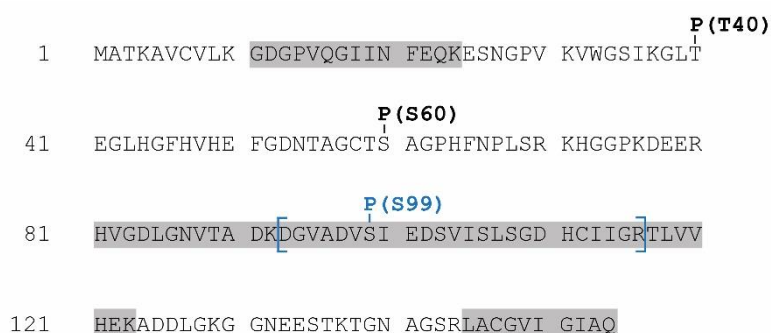


**Figure 55: Phosphorylation status of superoxide dismutase 1.** Amino acid sequence of human SOD1. Sequence coverage in the phosphoproteome analysis is highlighted in gray. A phosphopeptide spanning from D92 to R115 (indicated with blue brackets) including a phosphorylation at S99 was found specifically enriched in all samples originating from cells treated with DP68 ( $p < 10^{-17}$ ).

### 5.3.8.1 Validation of PPP2R1A as target of DP68

To investigate PPP2R1A as potential target of DP68, affinity enrichment experiments using Pierce NHS beads were performed and PPP2R1A levels were detected via immunoblotting (Figure 56a). In all three experiments, PPP2R1A was not enriched by DP79 and DP80. Furthermore, the thermal stability of PPP2R1A by was not altered by DP68 in TPP (Figure 56b). In addition, the influence of DP55 and DP68 and their respective inactive analogs were tested in an *in vitro* assay for PP2A activity, using PPP2R1A in combination with the catalytic subunit  $\alpha$  of PP2A (PPP2CA) (Table 26).

None of the tested compounds inhibited the enzymatic activity. In conclusion, PPP2R1A could not be confirmed as target of DP68.

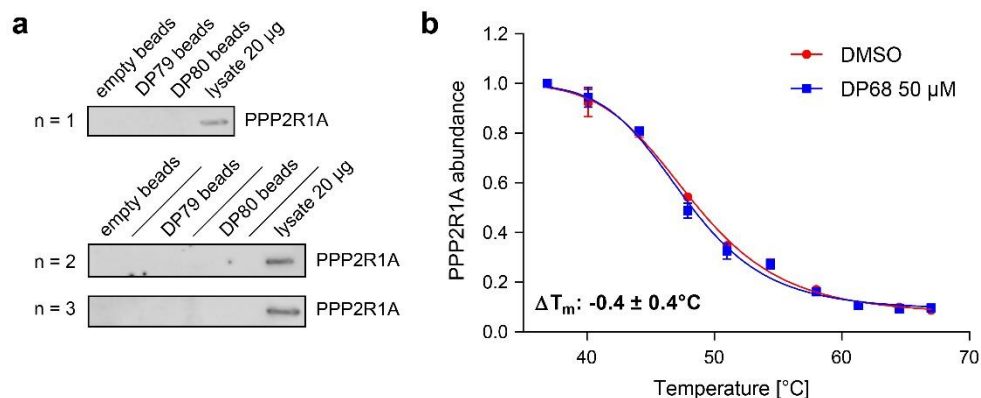


**Figure 56: Validation of PPP2R1A as binding partner of DP68.** (a) Affinity enrichment using Pierce NHS beads. Briefly, DP79, DP80 or empty beads were incubated with HeLa cell lysates for 2 h. After two 10-minute washing steps with wash buffer, bound proteins were eluted and subjected to SDS-PAGE and subsequent immunoblotting for PPP2R1A. n = 3. (b) TPP melting curves of PPP2R1A. Mean values  $\pm$  SD, N = 1, n = 3 Data displayed in (a) were obtained by Alexandra Brause, MPI Dortmund.

**Table 26: PPP2CA/PPP2R1A phosphatase activity assay.** *In vitro* activity assays for PPP2CA/PPP2R1A complex (full-length proteins) (SignalChem Biotech Inc., Canada). Mean  $\pm$  SD, N = 1, n = 3

Compound	Inhibition [%] at 10 µM	Inhibition [%] at 50 µM
DP55	4.9 $\pm$ 4.3	14.0 $\pm$ 3.0
DP59	3.9 $\pm$ 6.5	3.5 $\pm$ 8.8
DP68	-8.8 $\pm$ 11.0	-3.9 $\pm$ 8.5
DP72	-1.5 $\pm$ 5.6	-0.7 $\pm$ 10.8

### 5.3.9 Influence on cell viability

One aim of this thesis was to investigate the potential of ROS-inducing small molecules to induce cancer-selective cytotoxicity. For this, the influence of DP55 and DP68 on cell viability was examined by means of real-time live-cell analysis. Cytotoxicity studies of DP55 were performed in six different cancer cell lines, namely A549, HCT 116, HeLa, MCF7, U-2 OS and PANC-1 (Figure 57).

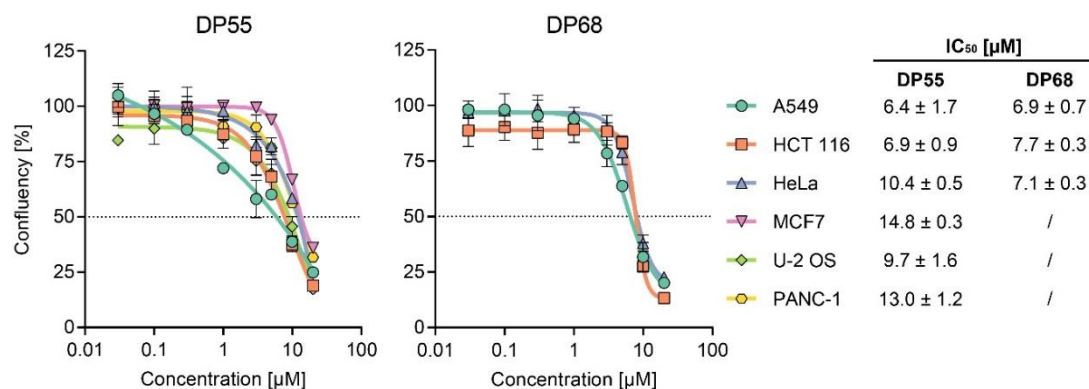


**Figure 57: ROS-inducing diaminopyrimidines display cytotoxic effects in different cancer cell lines.** Cells were treated with compounds and incubated over 48 h. Changes in cell confluency were monitored via IncuCyte-based real-time live-cell analysis. End-point confluency values were normalized to values of cells treated with DMSO (100 %) and IC<sub>50</sub> values were calculated via non-linear regression. Mean ± SD, N = 3, n = 3. Data were obtained by Naomi Hönisch Gravel, MPI Dortmund.

Surprisingly, DP55 showed rather weak cytotoxic effects with IC<sub>50</sub> values ranging from 6 to 15 µM, which is ≥10-fold higher than its effective concentration for general ROS induction in HeLa cells. The lung carcinoma cell line A549 and the colorectal carcinoma cell line HCT 116 were most sensitive to DP55 with IC<sub>50</sub> values of approximately 7 µM. DP68 displayed cytotoxic effects with IC<sub>50</sub> values of approximately 7 µM in all three cell types. Interestingly, in HeLa cells, the DP72, which lacks ROS-inducing activity, did not cause cytotoxicity, indicating that the cytotoxic properties of DP68 may be ROS-dependent (Figure 58).

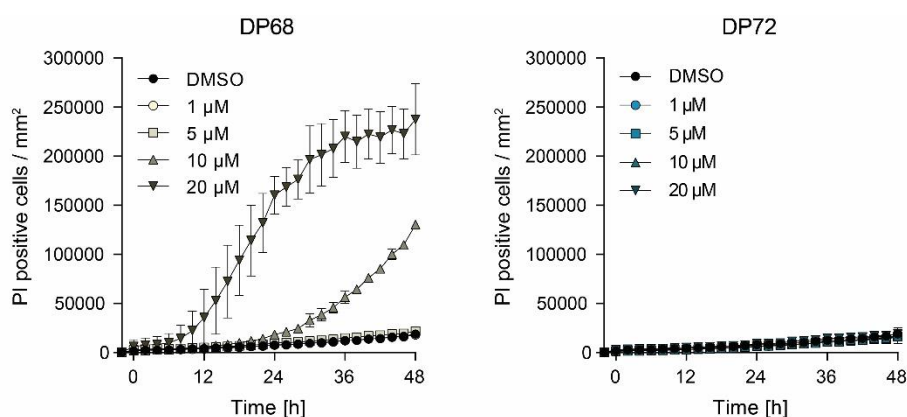


**Figure 58: DP68, but not DP72 induces cytotoxicity in HeLa cells.** Cells were treated with compounds and incubated over 48 h. Cytotoxic effects were detected via propidium iodide staining monitored via IncuCyte-based real-time live-cell analysis. Mean values ± SD, N = 3, n = 3.

Cytotoxicity of DP68 was investigated in HCT 116 spheroids (Figure 59). Due to the heterogeneous distribution of nutrients and oxygen, large spheroids (>500  $\mu\text{m}$  in diameter) possess a necrotic core, which is also found in tumors.<sup>291</sup> Thus, this three-dimensional cell culture model mimics certain tumor properties better compared to its monolayer counterpart. DP68 induced cytotoxicity only at comparably high concentrations: At 10  $\mu\text{M}$  the PI intensity increased slightly, while 20  $\mu\text{M}$  induced strong cytotoxicity after 24 h of treatment, reflected in a drastic PI intensity elevation (Figure 59a) and spheroid disintegration after 30 h of compound treatment (Figure 59b).

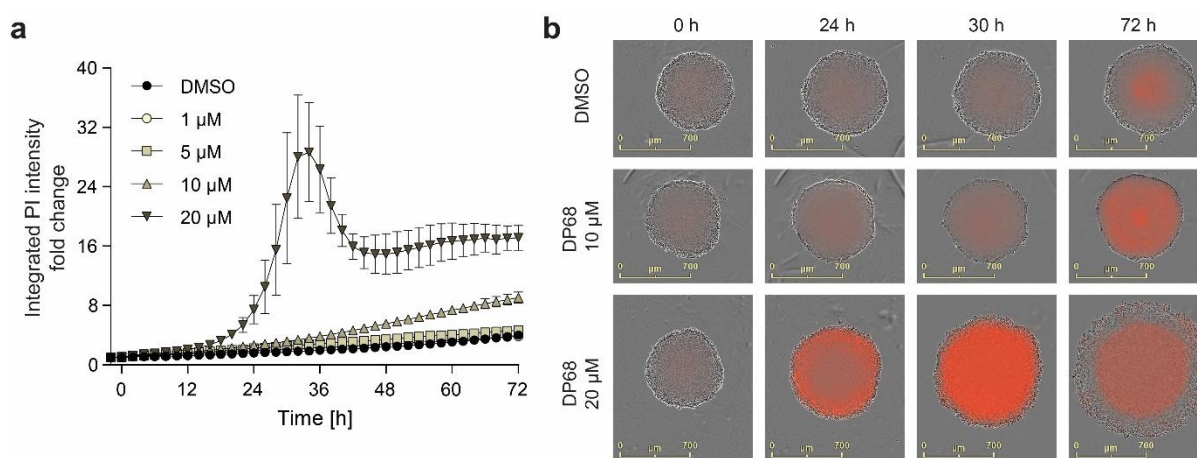


**Figure 59: High concentrations of DP68 induce cytotoxicity in HCT 116 spheroids.** (a) HCT 116 spheroids were treated with compounds and subjected to real-time live-cell analysis for 72 h in the presence of PI. Data were normalized to values obtained 2h prior to compound treatment. (b) Example images of selected spheroids. Mean values  $\pm$  SD, N = 4, n = 3. Data were obtained by Naomi Hönisch Gravel, MPI Dortmund.

To investigate whether the cytotoxicity of DP68 is a consequence of its ROS-inducing activity, the influence of different antioxidants on DP68-induced cytotoxicity was tested (Figure 60). For this, HCT 116 cells were preincubated with the general thiol antioxidant N-acetylcysteine (NAC), the lipophilic antioxidant  $\alpha$ -tocopherol or the iron chelator DFO that suppresses hydroxyl radicals formation and ferroptosis.<sup>71</sup>

In two-dimensional culture, NAC and DFO did not mitigate DP68-induced cytotoxicity, while  $\alpha$ -tocopherol completely suppressed it (Figure 60a and 60c). In spheroids,  $\alpha$ -tocopherol only partially decreased DP68-induced cytotoxicity (Figure 60b and 60d). DFO did not influence the cytotoxic effects, while NAC slightly attenuated them. The strong influence of  $\alpha$ -tocopherol suggests that DP68 might

induce lipid peroxidation, however, without inducing ferroptosis, as DFO failed to prevent cell death in both models.

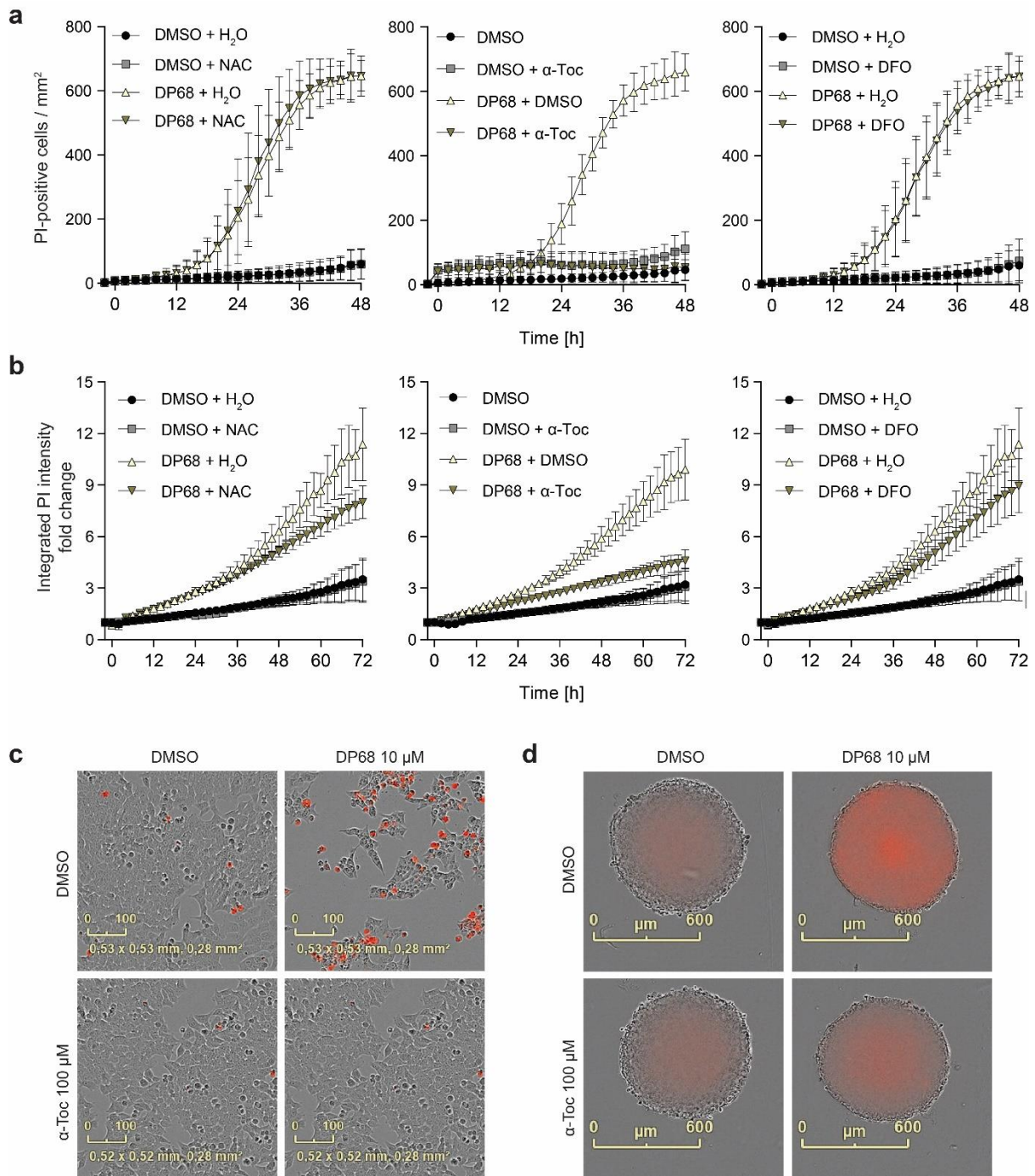


**Figure 60: α-tocopherol mitigates DP68-induced cytotoxicity in HCT 116 cells and spheroids.** HCT 116 cells cultured in 2D (**a**) and 3D (**b**) were treated with 5 mM N-acetylcysteine (NAC), 100 μM α-tocopherol (α-Toc) or 100 μM Deferoxamine (DFO) for 1 h (2D) or 5 h (3D) prior to addition of 10 μM DP68 in the presence of 25 μM propidium iodide (PI, red staining). Cytotoxic effects were quantified via PI staining. Representative images for α-tocopherol treatment were obtained after 48 h for 2D (**c**) and after 72 h for 3D (**d**). Mean values ± SD, N = 3 (2D) N = 4 (3D), n = 3. Data were obtained by Naomi Hönisch Gravel, MPI Dortmund.

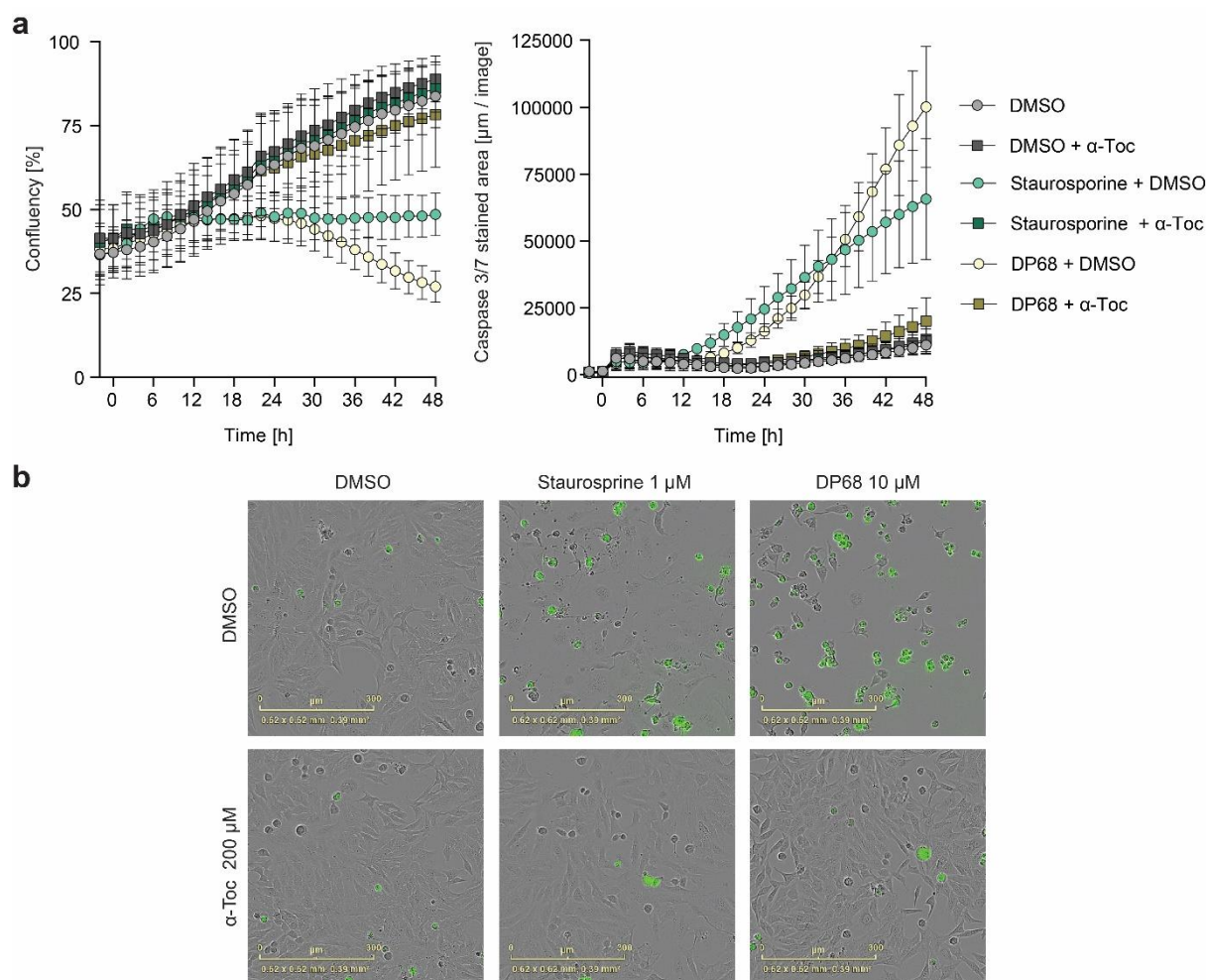


**Figure 61: DP68 induces apoptosis in HeLa cells, which is suppressed by  $\alpha$ -tocopherol.** HeLa cells were treated with 200  $\mu\text{M}$   $\alpha$ -tocopherol ( $\alpha$ -Toc) or DMSO 2 h prior to addition of 10  $\mu\text{M}$  DP68 or 1  $\mu\text{M}$  staurosporine in the presence of 5  $\mu\text{M}$  InCuCyte Caspase-3/7 Green Apoptosis Assay Reagent. Confluency and green fluorescence were monitored over 48 h via real-time live-cell analysis (a), representative images 48 h after treatment are shown (b). Mean values  $\pm$  SD, N = 3, n = 3.

To further characterize the underlying cell death mechanism of DP68, the activity of caspase-3/7 activity was detected as a measure of apoptosis using InCuCyte Caspase-3/7 Green Apoptosis Assay Reagent. As positive control, staurosporine, an unselective kinase inhibitor and known inducer of apoptosis, was used.<sup>292</sup> Both 10  $\mu\text{M}$  DP68 and 1  $\mu\text{M}$  staurosporine strongly decreased the cell confluency compared to cells treated with DMSO, and induced caspase-3/7 activity after approximately 12 h (Figure 61). A co-treatment with  $\alpha$ -tocopherol completely suppressed caspase 3/7 activation induced by staurosporine and DP68. Staurosporine displayed only weak activity in the phenotypic screen for ROS inducers (29.5 %  $\pm$  12.0 ROS induction in U2-OS cells, N = 1, n = 2). As  $\alpha$ -tocopherol suppressed cytotoxicity and caspase 3/7 activation of both compounds, it is uncertain whether those effects actually

depend on its antioxidant properties. To assess whether DP68 is less cytotoxic in non-malignant cells, the compound was subjected to a real-time live-cell analysis in human peripheral blood mononuclear cells (PBMC), using PI to quantify cytotoxicity (Figure 62). DP68 induced cytotoxicity at 10 and 20  $\mu\text{M}$ , with the exception of cells obtained from donor 1, which were not sensitive to DP68 concentrations below 20  $\mu\text{M}$ . In line with the activity in HeLa cells, DP72 did not display cytotoxic effects.

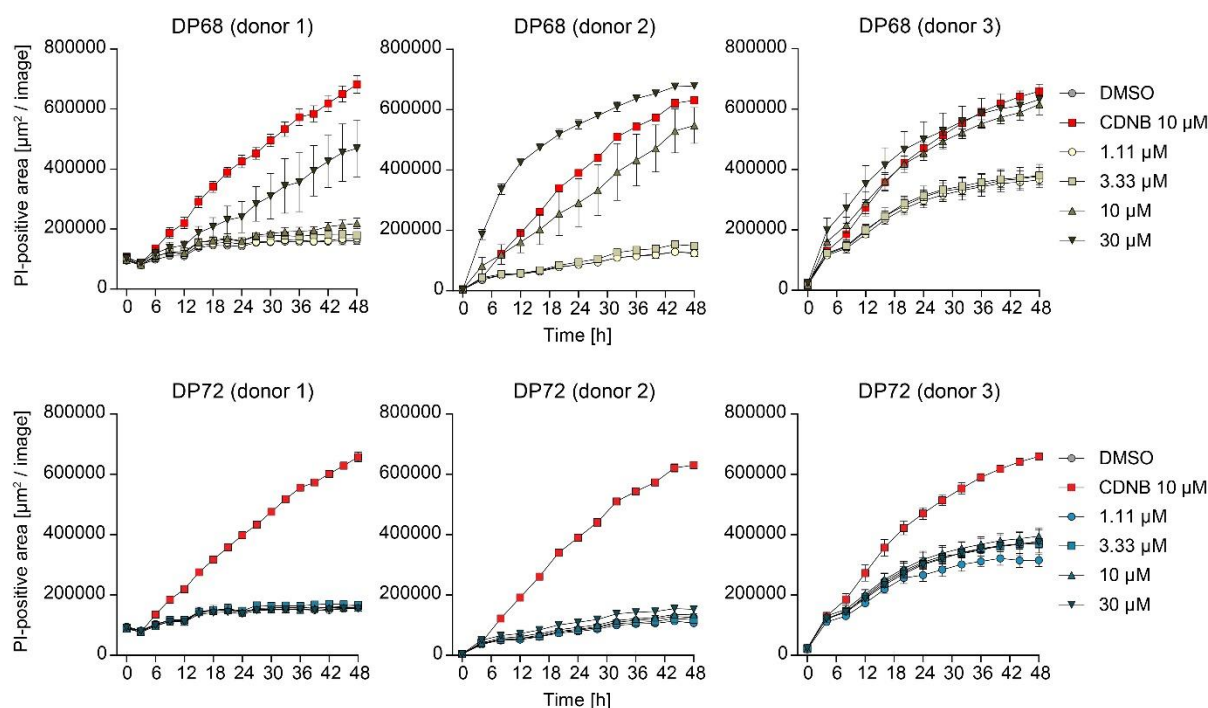


**Figure 62: PBMCs are comparably sensitive to DP68-induced cytotoxicity as malignant cell lines.** Human PBMCs from three different donors were treated with compounds in the presence of 25  $\mu\text{M}$  PI and subjected to IncuCyte-based real-time live-cell analysis for 48 h. Mean values  $\pm$  SD, N = 3 Data were obtained by Elisabeth Hennes, MPI Dortmund.

In summary, DP68 induced cytotoxicity at concentrations of approx. 10  $\mu\text{M}$ . None of the cancer cell lines tested was particularly sensitive towards a treatment with DP55 or DP68. Furthermore, DP68 display cytotoxicity in HCT 166 spheroids and in non-malignant cells (PBMCs) at concentrations comparable to those of the tested cancer cell lines. Based on this data, cancer-selective cytotoxic effects of DP68 were not observed. In addition, it remains to be elucidated, whether the cytotoxic effects of DP68 are ROS-dependent, as it is uncertain whether suppression of its cytotoxicity by  $\alpha$ -tocopherol was mediated by its antioxidant properties. The observation that DP72, which does not induce ROS, was not cytotoxic, indicates that DP68 might facilitate cytotoxicity in a ROS-dependent manner.



## 6 Discussion

### 6.1 DHMP and TCMP compounds as novel GSH-depleting ROS inducers

In the phenotypic screening, compounds containing 4,5-dihalo-2-methylpyridazin-3-one and 2,3,4,5(6)-tetrachloropyridine moieties were identified as potent inducers of ROS accumulation and strong depleters of cellular glutathione. In a previously reported high-throughput screen for cytotoxic compounds by Mervin *et al.*, sixteen 4,5-dichloro-2-methylpyridazin-3-one- and four 2,3,4,5-tetrachloropyridine-containing compounds were identified in a subset of 5784 cytotoxic and cytostatic compounds, however the underlying mode of action was not elucidated.<sup>189</sup>

The discovery of DHMP- and TCMP-containing small molecules (Figure 63) as inducers of cellular ROS accumulation and strong GSH depletion in U-2 OS cells suggested that these properties might cause the observed cytotoxicity. As the compounds displayed spontaneous GSH reactivity in solution, an involvement of cellular enzymes, such as glutathione-S-transferases, may not be necessary to lower cellular GSH levels. Although a correlation between ROS induction and cytotoxicity was observed for the six compounds, it is yet to be elucidated whether these two activities are mechanistically linked. The strong NAC-mediated reduction of cytotoxic effects may not be exclusively attributed to its antioxidant properties, as its thiol group might also react with the compounds analogous to GSH. Treatment of cells with subtoxic concentrations of DHMP/TCMP compounds and BSO, an inhibitor of GSH synthesis, induced cytotoxic effects.<sup>190</sup> This finding could also indicate that the compound mediates cytotoxicity via depletion of GSH. However, DHMP and TCMP compounds may also induce cytotoxicity by reacting with other cellular thiols, e.g. cysteine residues, potentially leading to an alteration in the function of the respective protein. In this case, the GSH level-lowering effect of BSO would increase the probability for such reactions, as it would increase the amount of DHMP and TCMP compounds available.

Although all DHMP compounds share the same reactive moiety, some compounds, e.g. DHMP-1 and -3, strongly differ in the severity of the cellular GSH depletion they induce. This may be explained by different reactivities towards GSH or could be caused by the cellular environment. Some compounds may be less cell membrane-permeable or, in case of an enzymatically catalyzed GSH conjugation, might have varying affinities towards the respective enzyme.

Furthermore, a comparable degree of GSH depletion does not always translate into ROS induction and cytotoxicity. Treatment with 5  $\mu\text{M}$  of DHMP-1 or 20  $\mu\text{M}$  of DHMP-3 both decreased cellular GSH levels by approximately 20 %, however only DHMP-1 caused ROS induction and cytotoxicity, implying a

difference in the GSH reaction rate of both compounds. In such case, DHMP-1 would induce a quick drop in GSH levels, thereby provoking a fast, strong and non-compensable ROS accumulation, ultimately leading to cell death. In contrast, DHMP-3 might react with GSH at a lower rate, thereby provoking a weaker, more prolonged ROS accumulation, which may be counterbalanced by antioxidative measures.

TCMP-3 lacks cellular activity for GSH depletion and ROS induction, which might be attributed to its ester bond, which could be hydrolyzed by cellular esterases. However, this reaction would not affect the TCMP moiety itself. If the reaction of TCMP-3 with GSH was catalyzed by a GST, hydrolyzed TCMP-3 may not be part of the substrate scope of the respective GST. The lack of bioactivity of TCMP-3 could alternatively be caused by low membrane permeability.

Two independent methods were employed to determine the influence of compounds on cellular GSH levels, one based on Ellman's reagent and one using a luminescence-based read-out. For TCMP-1, contradictory results were obtained, as GSH levels were not affected in the Ellman's reagent-based assay. The dose-dependent effect in the luciferase-based assay in combination with its ROS-inducing and cytotoxic effects, suggests that TCMP-1 depletes GSH in cells. The discrepancy in the assay results can be attributed to differences in the cell number and supernatant volume during compound treatment. Although HeLa cells contain low millimolar GSH concentrations, 10  $\mu$ M of DHMP-1 induced a 38 % reduction of GSH levels, despite the equimolar compound ratio, which is assumed based on the proposed conjugation reaction.<sup>293</sup> Such disproportion can be explained by a strong enrichment of DHMP-1 in cells, an occurrence that is also reported for other GSH-depleting small molecules.<sup>191,294</sup>

DHMP moieties are found in a variety of bioactive molecules, e.g. in the herbicide Norflurazon or in the SOD1 inhibitor, LCS-1, which was originally discovered as inducer of cytotoxicity in lung adenocarcinoma cell lines (Figure 63).<sup>295-297</sup> Furthermore, 4,5-dichloro-2-methylpyridazin-3-one compounds were described as covalent inhibitors of disulfide-forming enzymes in *E. Coli.*, indicating that these moieties can also react with protein thiols.<sup>298</sup> These compounds also inhibited *E. coli* growth. A study by Ma *et al.* identified LGH00168 as activator of C/BEP homologous protein (CHOP)-mediated gene expression.<sup>299</sup> Interestingly, the compound induced ROS formation and cytotoxicity in A549 cells, which was prevented by an NAC co-treatment. Four other studies identified cytotoxic DHMP-containing compounds in HCT 116 spheroids, murine colon cancer cell lines, as well as in the parasitic microorganisms *Plasmodium falciparum* and *Giardia intestinalis*.<sup>300-303</sup> All of these compounds induce

cytotoxicity in the respective cell culture model or organism studied. Whether these cytotoxic effects are also mediated by depletion of glutathione remains to be elucidated, as none of the studies report glutathione reactivity. Apart from skin-sensitizing properties of tetrachloropicolinic acid, hardly any biological activities of 2,3,4,5(6)-tetrachloropyridines are reported.<sup>304</sup>

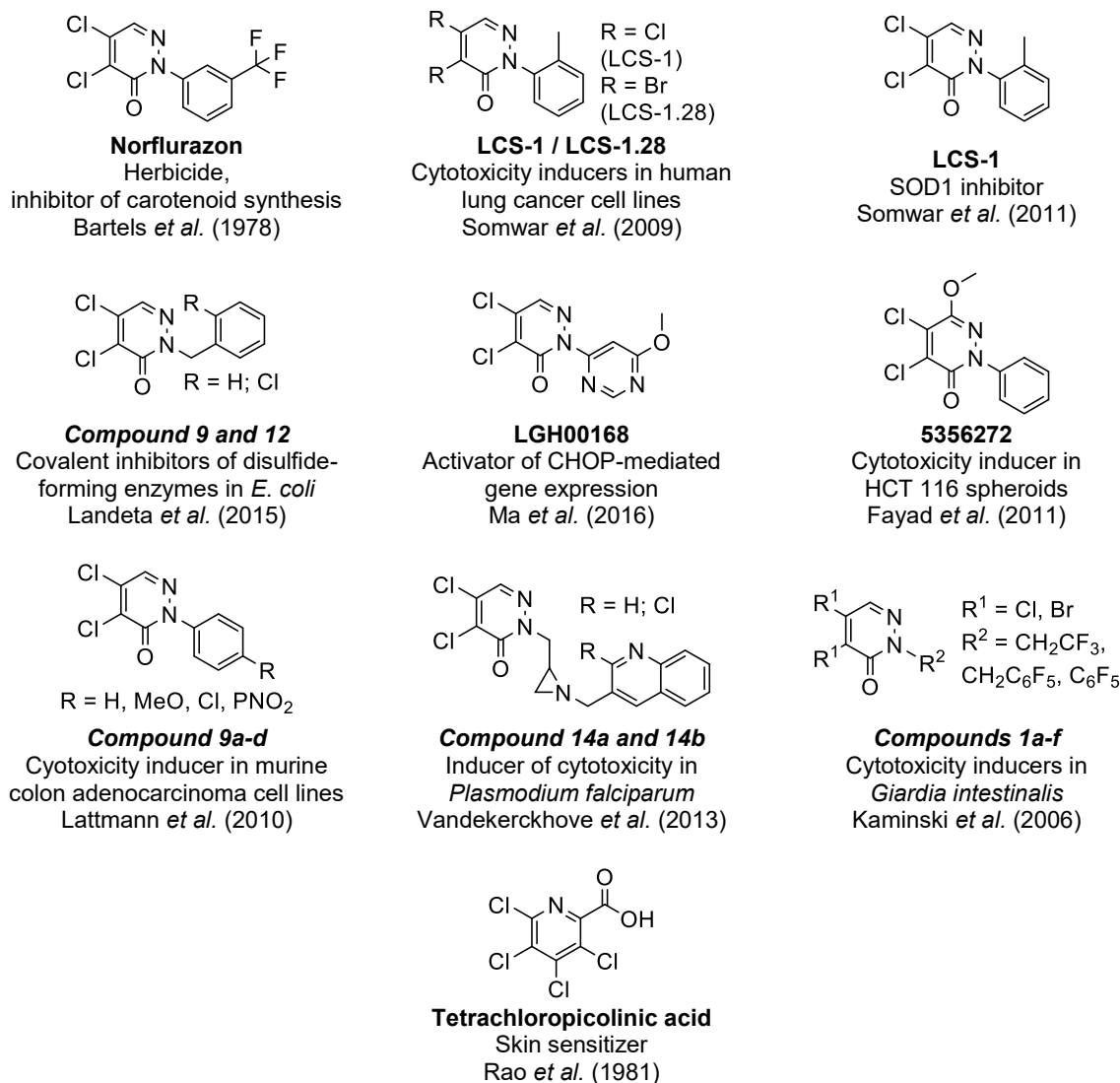
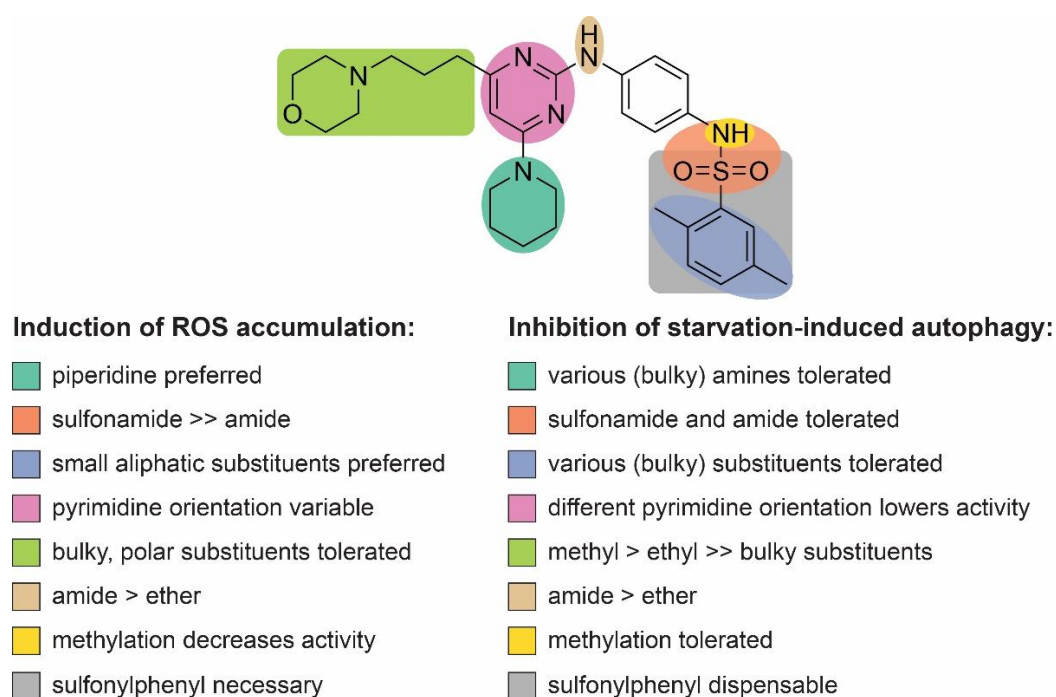


**Figure 63: Biological activities of different DHMP- and TCMP-containing small molecules.**<sup>295–304</sup>

Taken together, small molecules containing DHMP and TCMP moieties can react with glutathione, most likely via nucleophilic halide substitution by the thiol group of GSH. Reactivity towards other cellular thiols and its possible involvement in cytotoxic effects was not explored. A non-specific thiol reactivity of these compounds might render them unsuitable as starting points for drug discovery. Thus, such chemotypes should be carefully considered for the development of novel bioactive compounds.

## 6.2 Chemical optimization of diaminopyrimidine-based ROS inducers

The phenotypic screen based on the general ROS indicator CM-H<sub>2</sub>DCFDA identified a class of diaminopyrimidines as novel, fast-acting inducers of cellular ROS accumulation. The commercially available screening hit DP01 induces ROS with low micromolar potency in both U-2 OS and HeLa cells, and does not affect the total cellular glutathione levels within 1 h of compound incubation. Thus, the compound does not induce ROS accumulation via depletion of the cell's most abundant antioxidant. In addition, DP01 also inhibited autophagy and mitochondrial respiration.

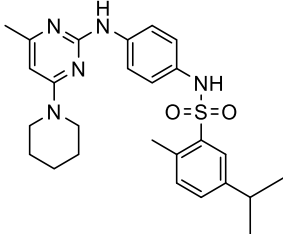
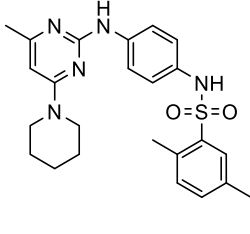
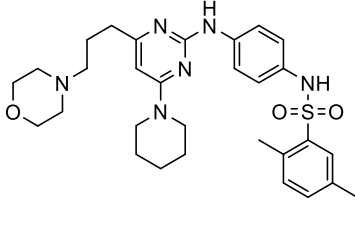


**Figure 64: Overview on the SAR of the diaminopyrimidine-based compound class for ROS-inducing and autophagy-inhibitory activities.** The chemical structure of DP68 is shown. In terms of ROS-inducing activity, hardly any portion of the molecule was susceptible to alteration without loss of activity. The only exceptions are the 4-position of the pyrimidine ring (light green), which allowed the addition of larger moieties, and the orientation of the pyrimidine ring (pink). Regarding the autophagy-inhibitory activity, various parts of the molecule allow modification, with the exception of the diaminopyrimidine moiety, which is not susceptible to variations of the pyrimidine orientation and the substituents of the 4- and 6-position.

In the course of a structure-activity relationship study, further derivatives of DP01, originating from both commercial sources and in-house synthesis, were evaluated for their ROS-inducing and autophagy-inhibiting properties. Since the structurally related compound aumitin inhibits autophagy via inhibition of the mitochondrial complex I, selected diaminopyrimidines were also tested for their influence on mitochondrial respiration.<sup>192</sup> In regard to the ROS-inducing activity, only few alterations in the chemical

structure of DP01 were tolerated. Only the substitution of the methyl group at the 4-position of the pyrimidine ring for larger, more hydrophilic substituents and a different orientation of this ring did not affect the ROS-inducing activity. Small alterations, like methylation of the sulfonamide or exchange of the piperidine ring for smaller secondary amines led to a large drop in activity. This may indicate that these diaminopyrimidines potentially interact with a distinct binding pocket, thereby modulating the activity of the respective protein, which could trigger ROS accumulation. In contrast to ROS induction, the majority of the structural variations hardly influenced autophagy inhibition by this compound class, with the exception of alterations at the pyrimidine ring. As shown in Figure 64, the structure-activity relationships regarding ROS accumulation and starvation-induced autophagy strongly diverge suggesting that these two activities are independent of another. The fact that inhibition of autophagy and mitochondrial respiration by the diaminopyrimidines strongly correlate, could be indicative that DP01 may inhibit autophagy via inhibition of the mitochondrial complex I, as it is the case for the diaminopyrimidine aumitin.

**Table 27: Compound optimization of the diaminopyrimidine-based class of ROS inducers.** ROS induction measured via CM-H<sub>2</sub>DCFDA based on ‘imaging positive’ read-out; inhibition of starvation-induced autophagy; inhibition of mitochondrial respiration measured via Mito Stress Test. Mean values  $\pm$  SD,  $n \geq 3$ . Water solubility was estimated upon monitoring of crystal formations in cell culture medium under a light microscope.

			
	<b>DP01</b>	<b>DP55</b>	<b>DP68</b>
<b>EC<sub>50</sub> (ROS)</b>	2.7 $\pm$ 0.9 $\mu$ M	0.9 $\pm$ 0.2 $\mu$ M	0.5 $\pm$ 0.1 $\mu$ M
<b>IC<sub>50</sub> (autophagy inhibition)</b>	8.9 $\pm$ 0.4 $\mu$ M	0.2 $\pm$ 0.1 $\mu$ M	inactive
<b>IC<sub>50</sub> (mitochondrial respiration)</b>	1.7 $\pm$ 0.2 $\mu$ M	0.7 $\pm$ 0.2 $\mu$ M	inactive
<b>Water solubility</b>	up to 10 $\mu$ M	up to 10 $\mu$ M	up to 50 $\mu$ M

The screening hit DP01 differs from the optimized compound DP68 in two positions: Its isopropyl moiety was changed to a methyl group, and the substituent at the 4-position of the pyrimidine ring was exchanged for a 4-propylmorpholine moiety. The latter alteration did not only lead to the loss of

autophagy and mitochondrial respiration inhibition, but also increased the compound's potency and water solubility (Table 27). Furthermore, it allowed the design of probes, i.e. fluorescent probes or affinity probes, without interfering with ROS induction. In addition, compounds lacking the 2,5-dimethylphenylsulfonyl moiety (DP59 and DP72) were identified as inactive analogs and were thus used as control compounds throughout the project.

### 6.3 DP68 interferes with superoxide dismutation

The ROS-inducing properties of DP68 were investigated in detail to narrow down putative targets or modes of action. ROS elevation by DP68 is detectable already after approximately 30 min and remains constant over the course of 72 h. As CM-H<sub>2</sub>DCFDA reacts with a broad range of reactive oxygen species, different reactive oxygen species-selective probes were applied as well. Both DP55 and DP68 induced cytosolic, mitochondrial and lysosomal superoxide. As superoxide is considered to be a primary reactive oxygen species, which can be converted into other ROS, these diaminopyrimidines may be regarded as general inducers of superoxide accumulation.<sup>65</sup> While levels of cytosolic and mitochondrial superoxide induced by DP55 and DP68 were comparable, DP68 triggered stronger lysosomal superoxide accumulation compared to DP55. DP68 differs from DP55 by an additional 4-ethylmorpholine group, which is a lysosomotropic motif as it is aliphatic and contains a basic amine. Indeed, DP68 interfered with the lysosomal accumulation of LysoTracker DND-99 more potently compared to DP55. Thus, the fact that DP68 provoked a stronger lysosomal superoxide response may be a consequence of its increased accumulation in lysosomes relative to DP55. Unlike hydrogen peroxide, superoxide cannot freely diffuse through biological membranes, apart from superoxide flux via certain ion channels.<sup>305,306</sup> Thus, superoxide must be predominantly formed within the respective organelle. As a consequence, the target of the diaminopyrimidine responsible for the superoxide accumulation is presumably present in the cytosol, mitochondria and lysosome.

However, this consideration does not take into account, that compartment-specific indicator dyes, like MitoSOX Red, HKSOX-1m and -2L, only preferentially accumulate in their respective target organelle. Due to the fact that these indicator dyes are oxidized by superoxide in an irreversible manner, these dyes do not necessarily indicate that superoxide is present within their target organelle. For example, a non-oxidized MitoSOX Red molecule may by chance diffuse out of the mitochondria into the cytosol. If superoxide is present in the cytosol, the molecule might get oxidized and subsequently diffuse back

into the mitochondria. Such event would be more likely in case of high levels of cytosolic superoxide. Thus, one should carefully evaluate findings obtained by such organelle-specific indicators.

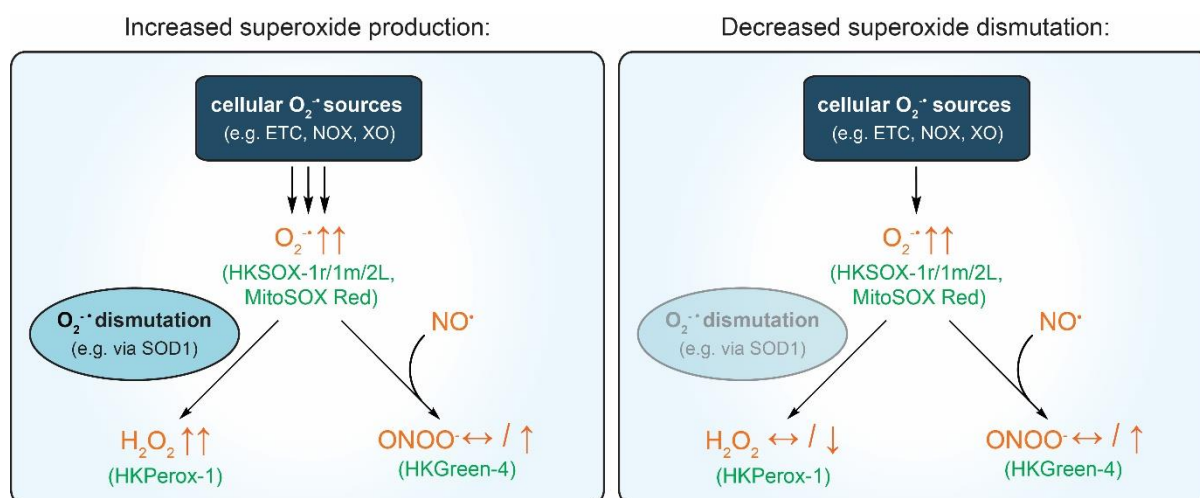


**Figure 65: Superoxide accumulation may be caused via two distinct mechanism.** Increased superoxide production may lead to increased levels of superoxide, hydrogen peroxide and peroxynitrite, while an interference with superoxide dismutation may not alter hydrogen peroxide levels. Reactive oxygen species and their respective indicator dyes are highlighted in orange and green, respectively. ETC = electron transport chain; NOX = NADPH oxidase; SOD = superoxide dismutase; XO = xanthine oxidase

In cells, superoxide undergoes two main reactions. It either reacts with nitric oxide to form peroxynitrite or is converted into hydrogen peroxide by SODs. Interestingly, while DP68 triggered a strong superoxide accumulation, levels of hydrogen peroxide and peroxynitrite were hardly affected. While the peroxynitrite formation might be limited by the availability of nitric oxide, the absence of increased hydrogen peroxide levels is unusual. If DP68 triggered an increase in superoxide production, e.g. via activation of NOX enzymes, hydrogen peroxide levels would increase immediately, due to the rapid action of superoxide dismutases. The absence of elevated hydrogen peroxide levels therefore rules out that DP68 increases the production of superoxide. Alternatively, superoxide accumulation could be triggered by alleviating its clearance rate (Figure 65). Consequently, this should lead to a decrease in hydrogen peroxide levels, which was not detected after treatment with DP68. However, catalase and glutathione peroxidase, which both facilitate hydrogen peroxide detoxification, are inhibited by superoxide.<sup>307,308</sup> If the activity of both SODs and hydrogen peroxide scavenging enzymes is inhibited, hydrogen peroxide levels may remain rather constant.

The reactive oxygen species-selective detection thus indicates that DP68 interferes with superoxide dismutation. Superoxide scavenging is predominantly performed by superoxide dismutases, namely the cytosolic SOD1, the mitochondrial SOD2 and the extracellular SOD3. Additionally, the cytosolic NAD(P)H dehydrogenase (quinone 1) (NQO1) also acts as a superoxide-dismutating enzyme, however catalyzing the reaction less efficiently compared to SODs.<sup>258,309</sup> Interestingly, treatment of HeLa cells with DP68 did not influence SOD activity. As the employed assay is not specific towards any superoxide-dismutating enzyme, an inhibition of any of the SOD enzymes or NQO1 should have been detected. Furthermore, no SOD family member was enriched by DP79 in the respective affinity enrichment experiments. The enrichment of NQO1 in the affinity-based chemical proteomics experiments could not be confirmed via immunoblotting. Additionally, DP68 did not alter the thermal stability of SOD1, SOD2 or NQO1, while the extracellular superoxide dismutase SOD3 was not detected in TPP. If DP68 induces superoxide predominantly in the cytosol, alterations in the localization of SOD1 or NQO1, e.g. via accumulation in a different organelle, could account for the induction of superoxide, without alteration of the enzymatic activity of these proteins. Taken together, DP68 may interfere with superoxide dismutation, however it does not directly interact with superoxide-dismutating enzymes. Surprisingly, despite the strong and prolonged ROS accumulation induced by DP68, it did not trigger an NRF2-mediated antioxidant response. The hypothesis that DP68 may not increase ROS production but instead interferes with the conversion of superoxide into hydrogen peroxide might explain the lack of an antioxidant response. An NRF2-mediated response is caused by the oxidation of certain cysteine residues in KEAP1 (Figure 8).<sup>94</sup> In comparison to hydrogen peroxide, superoxide hardly oxidizes biomolecules, with few exceptions, like cytochrome c or ascorbate.<sup>310</sup> Therefore, DP68 does not trigger an NRF2-mediated antioxidant response despite its strong ROS induction, because KEAP1 may simply not be oxidized by superoxide.

#### 6.4 ROS-inducing potency of DP68

For the screening of novel ROS inducers via CM-H<sub>2</sub>DFCDA, all data obtained were normalized to values of cells treated with DMSO (= 0 %) and cells treated with 10  $\mu$ M CDNB (= 100 %). EC<sub>50</sub> values were defined as the compound concentration causing 50 % of the ROS levels induced by 10  $\mu$ M of CDNB. Alternatively, one could determine the EC<sub>50</sub> as the concentration of the half-maximal ROS level induced by the respective test compound, i.e. based on the inflection point of the dose-response curve. Different



chemotypes may induce ROS via various mechanisms. In consequence, the maximal ROS levels caused by different compounds may vary, as depicted for three hypothetical ROS inducing-compounds in Figure 66. In this example, the maximal ROS level induced by compound A is the same as for 10  $\mu\text{M}$  CDNB (100%). In this case,  $\text{EC}_{50}$  values calculated by the two methods are comparable.

Normalization to a reference compound is necessary to compare the potency between the three compound classes. In this example, compound B induces the strongest ROS response. However, if  $\text{EC}_{50}$  values were determined based on inflection points of the respective dose-response curves, compound C would be the most potent compound, despite its comparably low maximal ROS level. This method to determine compound potency is thus misleading, as it does not take the maximal ROS level of each compound class into account.

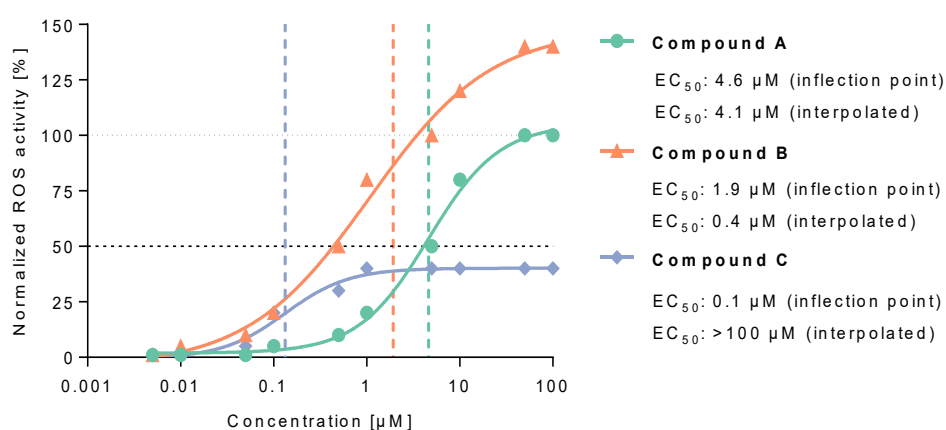


**Figure 66: Differences in normalization-dependent and -independent  $\text{EC}_{50}$  determination.** Dose-response curves of three hypothetical ROS-inducing compounds, based on data normalized to values obtained from cells treated with DMSO (= 0%) and 10  $\mu\text{M}$  CDNB (= 100 %).  $\text{EC}_{50}$  values were calculated either on the basis of the curve inflection point (normalization-independent) or by interpolating the compound concentration at the half-maximal concentration of 10  $\mu\text{M}$  CDNB (50%) (dependent on normalization). Vertical dashed lines indicate the inflection points of the respective curves. Horizontal lines indicate the (half)-maximal effect of 10  $\mu\text{M}$  CDNB.

However, an  $\text{EC}_{50}$  value determined on the basis of normalized data may also not fully reflect the actual potency of a small molecule, as such values strongly depend on the potency of the reference compound used for normalization. In the CM- $\text{H}_2\text{DCFDA}$ -based assay, the maximal ROS level induced by DP68 was in the same range as for 10  $\mu\text{M}$  CDNB. Therefore, comparable values were obtained with both  $\text{EC}_{50}$  determination methods, similar to the hypothetical Compound A (Figure 66).

However, this is not the case for the superoxide measurement based on HKSOX-1r, as 10  $\mu\text{M}$  CDNB induces comparably low levels of cytosolic superoxide. Therefore, data normalization to CDNB is misleading as the compound would appear more potent as it actually is. In addition, one also needs to take the dynamic range of the respective assays into account. The maximal superoxide level induced by DP68 in the HKSOX-1r-based assay is not reached, even at 50  $\mu\text{M}$ . In contrast, DP68 induces the maximal ROS level (upper plateau of the dose-response curve) detected by CM-H<sub>2</sub>DCFDA at approximately 10  $\mu\text{M}$ . As the DP68-induced superoxide levels further increase above 10  $\mu\text{M}$ , the dynamic range of the CM-H<sub>2</sub>DCFDA-based assay may not suffice to detect the compound's full ROS-inducing potential. Therefore, the actual potency of DP68 may be reflected better by an EC<sub>50</sub> value based on HKSOX-1r. However, as the upper plateau of the dose-response curve was not reached at 50  $\mu\text{M}$  and higher compound concentrations exceed its maximal water solubility, an EC<sub>50</sub> value of DP68 could not be determined in this assay. As the percentual superoxide induction at 10  $\mu\text{M}$  is approximately half of the superoxide level at 50  $\mu\text{M}$ , the EC<sub>50</sub> value is presumably >10  $\mu\text{M}$  and not 0.4  $\mu\text{M}$  as determined in the CM-H<sub>2</sub>DCFDA-based assay.

The half-maximal effective concentration of a compound is a valuable information for the identification and validation of targets. If a compound induced ROS e.g. via inhibition of an antioxidative enzyme, the compound would presumably inhibit 50% of the activity of the respective enzyme in cells at its half-maximal effective concentration for ROS induction. Thus, the EC<sub>50</sub> allows to estimate a suitable concentration range for target validation experiments, meaning that less potent compounds need to be tested at higher concentrations to properly validate a target candidate.

## 6.5 DP68 as antagonist of the $\sigma_1$ receptor

During the search for the molecular target mediating the ROS induction by DP68, the compound was subjected to two unbiased profiling approaches, namely the CPA and TPP, ultimately leading to the discovery of DP68 as novel antagonist of the  $\sigma_1$  receptor. Despite the fact that the  $\sigma_1$ -antagonistic property of DP68 is not responsible for triggering cellular ROS accumulation, this finding demonstrates the potential of these two techniques for the identification of bioactive small molecules and their molecular targets. DP68 induced strong morphological alterations in the CPA in a concentration-dependent manner, thereby detecting its general bioactivity. However, the large amount of reference compounds displaying high fingerprint similarity to DP68, which together covered a plethora of

annotated targets, did not allow to derive a target hypothesis based solely on the CPA data. In contrast, TPP revealed a list of 15 putative interaction partners of DP68 based on alterations in their thermal stability in the presence of the compound. However, not all of these interactions may also occur in the cellular environment and may not all translate into an actual phenotype. A comparison of the putative interaction partners identified in the TPP with the annotated targets of the 265 CPA reference compounds with high fingerprint similarity to DP68, revealed fingerprint similarity to five  $\sigma_1$  receptor ligands. Based on a focused literature search, another 19 ligands of this receptor were identified in the list of the 265 reference compounds. As both techniques indicated that DP68 could target the  $\sigma_1$  receptor, it was chosen for in-depth studies.

Both 10  $\mu$ M DP72 and 1  $\mu$ M DP68 induced morphological changes within a similar induction range. Despite the differences in potency, both compounds display a fingerprint similarity of 82 %. As DP72 does not induce ROS accumulation, it is questionable, whether these phenotypic changes actually reflect ROS-inducing properties. A subset of the 265 CPA references comprising 181 compounds was included in the phenotypic screening for ROS inducers. Interestingly, only three compounds displayed elevated cellular ROS levels above 50 % in the U-2 OS-based screen, again indicating that the phenotypic fingerprint of DP68 may not represent ROS induction. Additionally, one should consider the great differences in compound treatment time between these two assays. ROS induction was measured after 1 h, while morphological changes were investigated after 20 h of compound treatment. Therefore, the respective morphological profile of a ROS-inducing small molecule might rather reflect the cellular response to the redox alterations induced.

Furthermore, it is questionable whether the CPA fingerprint of DP68 actually reflects its  $\sigma_1$ -antagonistic properties. The majority of the CPA references are not described as  $\sigma$  receptor ligands. Neither potent  $\sigma_1$  agonists like SKF-10047 nor the allosteric modulator phenytoin induced morphological alterations. Among the 24  $\sigma$  receptor ligands that display high fingerprint similarity to DP68, both  $\sigma_1$  agonists (fluoxetine, imipramine) and antagonists (haloperidol, progesterone) were found.<sup>227,228</sup> Thus, another common feature among DP68 and its reference compounds may cause their shared morphological phenotype. A large portion of the 265 reference compounds were developed to target the central nervous system (CNS), e.g. dopamine receptor antagonists and serotonin reuptake inhibitors. As those compounds need to cross the blood-brain barrier in order to reach their respective target tissue, a certain degree of lipophilicity is prerequisite. A common structural motif is the combination of a basic

amine with a lipophilic stretch, providing both adequate water solubility and sufficient lipophilicity to enter the CNS.<sup>311</sup> However, on a cellular level such motif may also trigger lysosomal accumulation.<sup>312</sup> The comparison of the lysosomotropic properties of DP55 and DP68 suggests that the 4-propylmorpholine moiety of DP68, which consist of a basic amine and a lipophilic stretch, may cause its lysosomotropic properties. A cluster of potentially lysosomotropic CNS-targeting compounds, comprising fluphenazine, metoclopramide and procaine was previously described in the first report on the CPA.<sup>313</sup> Therefore, lysosomotropic effects may at least partially contribute to the morphological profile of DP68. Interestingly, the beforementioned structural motif overlaps with a pharmacophore model for  $\sigma_1$  receptor ligands, comprising two hydrophobic moieties surrounding a basic amine.<sup>313</sup> Thus, the biological similarity between DP68 and 24  $\sigma$  receptor ligands may predominantly be caused by their physicochemical properties. Nevertheless, on the basis of the CPA analysis, the  $\sigma_1$  receptor was prioritized for validation studies over all other putative binding proteins identified in TPP, which ultimately led to the discovery of a novel antagonist of this receptor.

The  $\sigma_1$ -antagonistic property of DP68 is however not necessary for mediating its ROS-inducing properties, as the majority of  $\sigma_1$  ligands did not trigger ROS elevation. Furthermore, DP68 induced a dose-dependent ROS increase in both wildtype and  $\sigma_1$  knock-out HAP1 cells. Still, the discovery of DP68 as a novel  $\sigma_1$  antagonist highlights the power of the combined application of the CPA and TPP for target identification.

## 6.6 Target identification using affinity-based chemical proteomics

In the course of the investigations for this thesis, various approaches were applied to identify the molecular target responsible for the ROS-inducing activity of the diaminopyrimidine class, comprising both affinity-based chemical proteomics approaches, as well as multiparametric profiling. All chemical probes used throughout the project were summarized in Figure 67. With the exception of the Cell Painting assay, all techniques applied were proteomics-based, assuming that its ROS-inducing activity is mediated by a protein target.

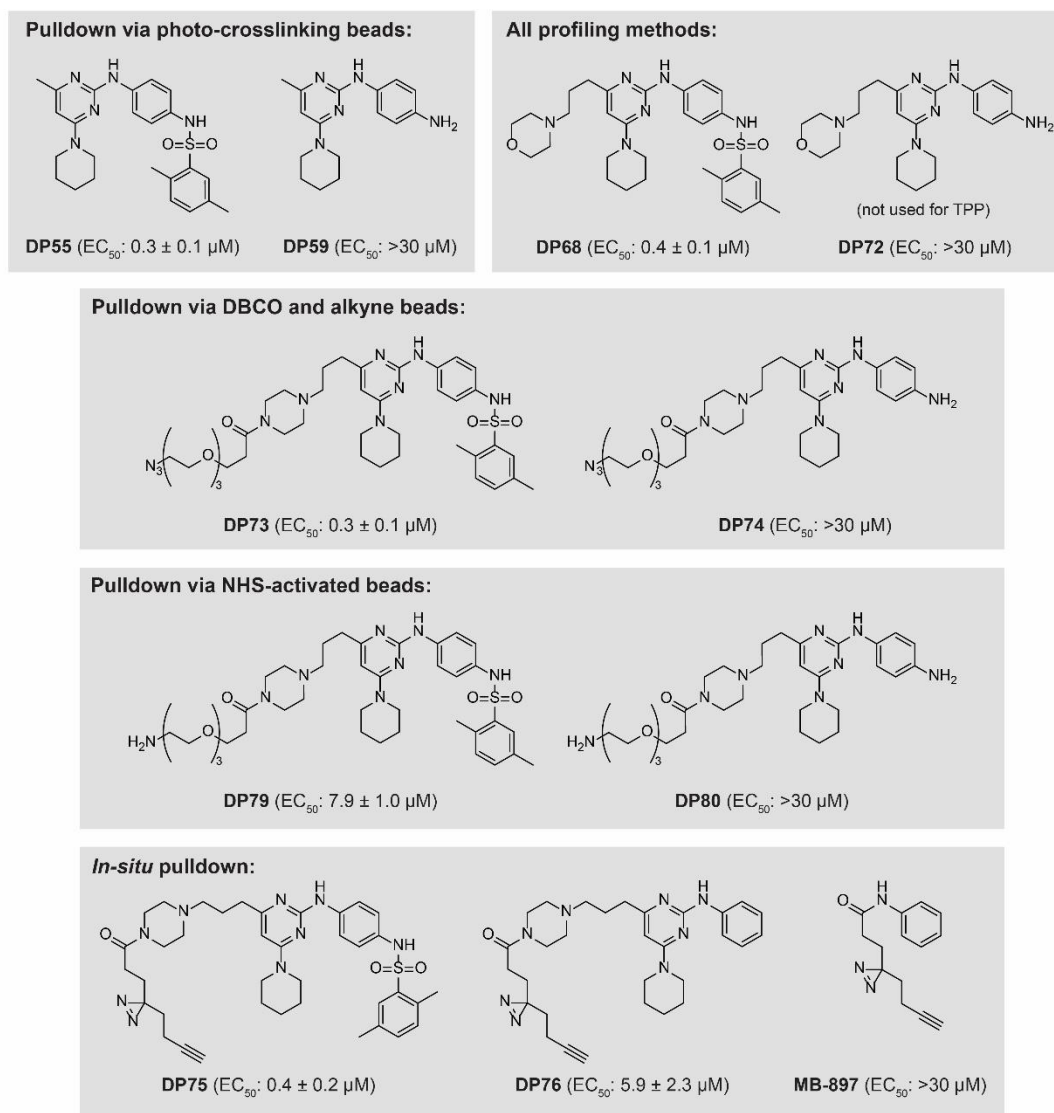


**Figure 67: Overview of all probes used for target identification of ROS-inducing diaminopyrimidines.** ROS-inducing activities were determined in HeLa cells using CM-H<sub>2</sub>DCFDA. Mean values  $\pm$  SD, N = 4, n = 3

For affinity enrichment via photo-crosslinking beads, DP55 and its inactive analog DP59 were immobilized onto beads decorated with photoactivatable groups by UV irradiation. This technique enables compound immobilization without prior SAR knowledge, which is appealing especially for target identification of natural products, for which chemical derivatization may not be accessible. However, its biggest drawback is the immobilization of the compound in a randomized orientation. As small molecules in most cases address a certain binding pocket within their respective target protein, the compound orientation on the affinity resin is a critical factor for the successful identification of the target. Ideally, all surfaces of the small molecule involved in the interaction with the target protein need to be freely accessible to enrich the respective protein. Furthermore, the small molecules need to be

appropriately distanced from the resin as steric hindrance may interfere with the compound-protein interaction, especially in the case of large target proteins. The success of an affinity enrichment experiment using photo-crosslinking beads depends on the amount of molecules that by chance are immobilized in a suitable orientation. In case of DP55, which contains only few positions susceptible to chemical alterations without loss of bioactivity, the vast majority of molecules may have been immobilized in an orientation that did not allow interaction with the target protein of interest.

Out of 22 proteins that were reproducibly and significantly enriched by DP55, two proteins, namely CTSD and GLO1, were selected for validation studies as they were described to influence cellular ROS levels.<sup>209,210</sup> Interestingly, GLO1 was identified previously as molecular target of an osteoclastogenesis inhibitor using photo-crosslinking beads.<sup>13</sup> For both enzymes, modulation of their enzymatic activity by DP55 was not detected and DP55 did not influence the proteolytic maturation of CTSD. Due to the beforementioned limitations of this technique and the fact that DP55 also inhibits autophagy and mitochondrial respiration, further efforts were invested in the target identification of DP68 instead, also taking the available SAR knowledge into account for immobilization of the compound.

In the second affinity enrichment approach, affinity probes containing a PEG<sub>3</sub>-linker with a terminal azide were synthesized on the basis of DP68 and DP72. Both probes displayed the desired bioactivity, as the positive probe DP73 induced cellular ROS accumulation with comparable potency as DP68, while DP74 was completely inactive. These probes were immobilized onto DBCO agarose beads via strain-promoted click reaction. Due to the spontaneous reaction of DBCO with azides, this Huisgen cycloaddition does not require any additional catalyst.<sup>314</sup> However, it turned out that this approach was unsuitable for target identification due to the high degree of protein binding by DBCO. The non-specific binding of proteins to affinity matrices is a general issue for all affinity enrichment experiments. Inclusion of control beads, decorated with either a biologically inactive analog or a chemical linker, allows to distinguish proteins that specifically interact with the probe from those that bind to the affinity matrix itself.<sup>3</sup> However, the number of proteins interacting with the affinity matrix, also termed 'bead proteome', is a critical determinant for the success of such target identification approaches.<sup>315</sup> If the protein of interest is part of the respective bead proteome, its identification becomes impossible. For example, the  $\sigma_1$  receptor, which was validated as a target of DP68 in the course of the investigations for this thesis, was strongly enriched on DBCO beads. The amount of azide probe added to the reaction mixture during the bead preparation corresponds to approximately 5 % of the DBCO moieties on the beads. Even if all

of the probe molecules were immobilized, unreacted DBCO moieties were present on the beads in an approximately 20-fold excess relative to the probe. The  $\sigma_1$  receptor was equally enriched on beads decorated with the active and inactive probe and could therefore not be identified as target in this approach.

Due to the high protein background of DBCO beads, a copper-catalyzed click reaction was employed to immobilize DP73 and DP74 on alkyne agarose beads instead. Surprisingly, the amount of proteins enriched by DP74 was significantly higher relative to DP73. However, the DP73 samples were reproducibly found to be strongly contaminated, presumably by detergents. As such contaminants suppress weaker MS signals, including those corresponding to peptides, less proteins were identified in the respective samples. DP73 differs from DP74 only by its 2,5-dimethylphenyl-sulphonyl moiety. As this should not result in strong differences in the physicochemical properties of both probes, e.g. in their lipophilicity, it is incomprehensible why DP73 but not DP74 enriched these contaminants. To circumvent this issue, affinity enrichment experiments were repeated in the absence of detergents. Although the number of proteins identified on beads decorated with DP73 or DP74 were comparable, quantification via SILAC revealed that DP73 enriched proteins in much higher amounts relative to DP74. Such immense differences in protein binding of these two probes consequently interfered with the identification of a protein target. Again, the differences in the chemical structures of the two probe molecules are not indicative for such unequal protein binding behavior. Since these observations were not made in the affinity enrichment experiments using the DBCO agarose resin, the differences in the protein binding abilities may not originate from the probe molecules per se, but may rather be attributed to the combination of the probes and their immobilization on the alkyne agarose beads. The presence of copper during the immobilization reaction may play a role in this regard, as certain arylsulfonamides are known to chelate copper.<sup>316,317</sup> Copper-chelating properties of DP73 may account for the comparably strong protein binding properties relative to DP74. Both probes did not chelate  $\text{Cu}^+$ , but displayed  $\text{Cu}^{2+}$ -reducing activity. It is however questionable, whether this property is a prerequisite for the cellular superoxide accumulation, as DP74, which lacks the ROS-inducing activity, reduced  $\text{Cu}^{2+}$  as well. DP68 and DP72 were also both found to reduce  $\text{Cu}^{2+}$ . The majority of copper in cells is bound by proteins and the concentration of free copper in cells is estimated to be attomolar.<sup>318,319</sup> However, diaminopyrimidines might also reduce protein-bound  $\text{Cu}^{2+}$ . In such scenario, only DP68 but not DP72 might be able to bind the respective pocket. In such case, only DP68 may modulate the activity of the

respective copper-binding protein, although both DP68 and DP72 may be able to reduce  $\text{Cu}^{2+}$ . A prominent copper-binding protein involved in superoxide scavenging is the cytosolic protein SOD1, however DP68 did not influence its enzymatic activity neither *in vitro* nor in cells. Independent of its putative role for ROS induction, the copper-reducing activity of DP73 and DP74 rendered compound immobilization via copper-catalyzed click reaction unsuitable, as it is unclear whether the probes are chemically stable in the presence of copper.

As the usage of azide-containing probes turned out to be unsuitable for target identification, a set of probes containing a PEG<sub>3</sub>-linker with a terminal amine was synthesized for immobilization on NHS beads. DP79, which was designed analogous to DP73, displayed ROS-inducing activities, however with an approximately 13-fold higher  $\text{EC}_{50}$  value compared to DP68. The primary amine may lower the membrane permeability of the compound, presumably causing the drop in cellular activity. Nonetheless, DP79 was used together with the inactive probe DP80 for affinity enrichment experiments with two different types of NHS beads, which varied in linker length. Surprisingly, a higher number of proteins was found strongly enriched on DP79 beads, relative to DP80 beads throughout all experiments. However, this time, the  $\sigma_1$  receptor was found among the enriched proteins, thereby validating this approach.

The majority of the top protein hits was identified using both types of NHS beads. At first glance, two protein groups were strongly enriched by DP79, namely PIKKs (mTOR, DNA-PK, ATM, ATR) and various NPC proteins. As the 2,4-diaminopyrimidine scaffold is part of various ATP-competitive kinase inhibitors, DP68 may inhibit kinases.<sup>235,236</sup> However, DP68 did not influence the *in vitro* activity of any of the four PIKKs identified in the affinity-based chemical proteomics experiments. Interestingly, both PIKKs and certain NPC proteins contain a common structural motif, namely HEAT repeat domains.<sup>253</sup> In addition, two other top hit proteins, the translational activator GCN1 and the E3 ligase listerin, also contain HEAT repeat domains.<sup>252,320</sup> Taken together, this finding indicates that DP68 may bind to HEAT repeats. This may also explain why the kinase activity of the PIKKs is not inhibited despite their strong enrichment, as DP68, unlike ATP-competitive kinase inhibitors, may not address the ATP-binding domain of PIKKs. However, it is unclear whether binding to HEAT repeat domains mediates the ROS-inducing activity of DP68. As HEAT repeat domains are common among many proteins, but do not share a consensus amino acid sequence, their validation as targets responsible for the ROS-inducing activity may be very challenging. Despite the relatively strict statistical



analysis with an FDR of 0.0001, the combined hit list of both approaches using NHS beads contained 59 putative target proteins, of which 17 proteins contain HEAT repeat domains. A literature search did not reveal an obvious mechanistic link between superoxide accumulation and one of the putative target proteins identified in this affinity enrichment approach, with the exception for PIKKs. Apart from the  $\sigma_1$  receptor, none of the proteins identified in the TPP was found among these 59 protein hits.

An important factor for the success of target identification approaches via affinity-based chemical proteomics are suitable controls. Ideally, an analog of the bioactive compound, which completely lacks the respective bioactivity, should be used as control.<sup>3</sup> Thereby, proteins interacting specifically with the immobilized bioactive compound can be distinguished from proteins binding to the resin. The inactivity of such analog should be indicative of its inability to bind the target protein that facilitates the biological effect of the bioactive compound. The biologically inactive analog may still exert binding affinity towards the target protein, however may not modulate its activity. For the target identification of DP68, control probes based on DP72 were used, which is chemically similar to DP68 however lacks ROS-inducing activity. Interestingly, DP72 was able to dampen the cytosolic superoxide induction by DP68 in a co-incubation experiment. Assuming that DP68 addresses an intracellular target, this finding could indicate that DP72 is cell-membrane permeable and may also bind to the same binding pocket of the target protein as DP68. However, in contrast to DP68, binding of DP72 to this pocket may not result in a functional modulation of the target protein. Thus, DP72 may simply block the respective binding pocket, thereby interfering with binding of DP68, which could cause the reduction in superoxide levels upon co-treatment with DP72. This however does not render DP72 and all affinity enrichment probes derived from it unsuitable as negative control compounds for target identification experiments. Since 10  $\mu$ M of DP72 did not fully suppress the superoxide-inducing effects of 5  $\mu$ M DP68, DP72 may bind the target protein with lower affinity compared to DP68. Thus, it is likely that the ROS-inducing probe DP79 may enrich the target protein more strongly compared to its inactive analog DP80. As all affinity-based chemical proteomics experiments were analyzed quantitatively, it would have been possible to identify the target protein, even though the biologically inactive control probe may also bind to it.

## 6.7 Target identification via photoaffinity probes

All of the affinity-based chemical proteomics approaches discussed above were performed in lysates, which do not fully reflect the cellular environment, as they lack e.g. some membrane proteins that were not solubilized by detergents in the lysis buffer. A physiologically more relevant approach is to perform the binding reaction directly in cells. For this, an *in situ* pull-down was performed, using probes containing minimalist photoaffinity linkers developed by Li *et al.*<sup>15</sup> These linkers contain a diazirine-group, allowing to covalently bind proteins in close proximity, and an alkyne handle for subsequent enrichment. Analogous to DP68 and DP72, two related PAL probes, DP75 and DP76, were synthesized. DP75 displayed ROS-inducing activity with a potency comparable to DP68. DP76, which was synthesized as a negative control, differs from other control probes of the diaminopyrimidine class (e.g. DP72, DP80) by its lack of the para-amino moiety. Because of its moderate ROS-inducing activity, it was not suitable for its use as negative control. Thus, MB-897, a simplified control compound that was also included in the studies by Li *et al.*, was employed instead, as it displayed no ROS-inducing activity.

In an SDS-PAGE-based *in situ* labeling approach, very similar band patterns were observed for both probes. Interestingly, for this type of minimalist linker, Horning *et al.* reported a strong degree of irradiation-independent protein labeling, which was also confirmed for the three probes used in the course of the investigations for this thesis.<sup>260</sup> Due to the high degree of unspecific binding, an in-gel fluorescence read-out was unsuitable to identify the target due to its lack of sensitivity. Thus, an *in situ* pull-down was performed and enriched proteins were subjected to on-bead digestion and MS analysis. None of the proteins identified was found significantly enriched by DP75 relative to MB-897. In general, a high variability among the technical replicates was observed and the previously validated target of DP68, the  $\sigma_1$  receptor, was not identified.

In the respective case study, Li *et al.* identified c-Src as target of Dasatinib, using a minimalist linker probe. Interestingly, despite Dasatinib's low nanomolar potency in terms of c-Src inhibition, the respective PAL probe was used at 10  $\mu\text{M}$ .<sup>322</sup> Based on the measurements using HKSOX-1r, DP68 induces superoxide accumulation presumably with an  $\text{EC}_{50} > 10 \mu\text{M}$  and the respective PAL probe was used at 25  $\mu\text{M}$ . Furthermore, lysate-based affinity enrichment experiments indicated that DP68 may interact with a high number of proteins. In conclusion, DP68 and the respective PAL probe DP75 may not display sufficient potency and selectivity for the molecular target of interest. Additionally, the high

degree of irradiation-independent protein labeling by this type of photoaffinity linkers render this approach unsuitable for the target identification of the diaminopyrimidine compound class.

## 6.8 Biological profiling of DP68 for target identification

Apart from the affinity-based chemical proteomics experiments, different profiling approaches were applied to predict putative targets and the mode of action of DP68. Thereby, compound-induced changes in the thermal stability, abundance and phosphorylation status of proteins, as well as alterations of the cellular morphology were investigated. As it typically takes several hours until changes in gene expression affect the respective protein level, alterations in gene expression were ruled out as possible effector mechanism, since DP68 induces ROS accumulation already after approximately 30 min.<sup>323</sup> A comprehensive overview of all methods applied for the target identification of ROS-inducing diaminopyrimidines is provided in Table 28.

**Table 28: Overview of methods applied for target identification of ROS-inducing diaminopyrimidines.**

Target identification approach	Proposed targets / mode of action
Pulldown via photo-crosslinking beads	cathepsin D; glyoxalase 1
Pulldown via DBCO beads	none (high protein background)
Pulldown via alkyne beads	none (copper-reactivity of pulldown probes)
Pulldown via NHS beads	HEAT repeat domain-containing proteins (PIKKs, NPC proteins)
<i>In situ</i> pulldown	none (high protein background)
Thermal proteome profiling	$\sigma_1$ receptor (validated); IFG-1 receptor; SCAP (SREBP pathway)
Cell Painting assay	$\sigma_1$ receptor (validated); kinases
Proteome profiling	activation of the SREBP pathway
Phosphoproteome profiling	PP2A as upstream regulator; phosphorylation of SOD1 (S99)

Besides the  $\sigma_1$  receptor, whose discovery was discussed in chapter 6.5, another 14 proteins were identified as putative binding partners of DP68 in TPP. The IGF1R was the only kinase among these. DP68 may target kinases based on its diaminopyrimidine scaffold.<sup>235,236</sup> As IMC-A12, an IGF1R-specific antibody, which blocks the interaction with its endogenous ligand IGF-1, was described to induce a strong ROS accumulation in MCF7 cells after 60 min of treatment, the receptor was investigated as target candidate.<sup>324</sup> However, the majority of IGF1R inhibitors did not increase cellular ROS levels and

the IGF1R, along with 28 other growth factor receptor kinases, as well as 13 kinases involved in IGF1R signaling were not inhibited by DP68 *in vitro*.

Another group of kinases directly influencing ROS levels are pyruvate dehydrogenase kinases that negatively regulate the pyruvate dehydrogenase complex, a major contributor to mitochondrial superoxide production.<sup>246</sup> However, known inhibitors of these kinases were found inactive for ROS induction and DP68 did not influence the activity of the respective kinases. In addition, kinases that were annotated as targets of the 43 kinase inhibitors that displayed high fingerprint similarity to DP68 in the CPA were also not inhibited by DP68 *in vitro*.

A proteome profiling was performed to investigate immediate and long-term effects of DP68 on the cellular proteome. Small molecules can affect their target proteins in several ways, e.g. by inhibiting enzymatic activities or blocking the binding to an interaction partner. Apart from this, small molecules may also facilitate the degradation of a target protein in a short time frame.<sup>325</sup> However, DP68 did not significantly decrease the abundance of any proteins detected in this approach. In contrast, a 24-hour incubation with DP68 significantly increased the abundance of 14 proteins, whose expression is controlled by the SREBP pathway. Therefore, DP68 may activate this pathway, which controls the synthesis of sterols. The SREBP protein, which resides in the ER membrane is bound to the *SREBP cleavage-activating protein* (SCAP). In case of sufficient cellular sterol abundance, SCAP is inhibited by the ER membrane protein INSIG. At low cholesterol levels, INSIG does not interact with SCAP, leading to its activation and both, SREBP and SCAP, are translocated to the Golgi apparatus. Subsequently, SREBP is proteolytically cleaved by the site-1 and site-2 proteases (S1P and S2P). The cytosolic N-terminal portion of SREBP is thereby liberated and translocates into the nucleus, where it acts as transcription factor for the expression of various genes, including those involved in cholesterol synthesis.<sup>326</sup>

It is known that lysosomotropic small molecules can activate the SREBP pathway by triggering sterol accumulation in lysosomal membranes due to their cholesterol-binding properties.<sup>277</sup> Additionally, accumulation of lysosomotropic compounds in lysosomal membranes can inhibit mTORC1.<sup>327</sup> Inactivation of mTORC1 leads to a decreased inhibition of the phosphatase Lipin 1, which activates the SREBP pathway.<sup>328</sup> Interestingly, although both DP68 and DP72 display strong lysosomotropic effects, an upregulation of SREBP target proteins was exclusively observed for DP68. Furthermore, DP68 caused a thermal destabilization of SCAP and the histone acetyltransferase p300, which both are

known interaction partners of SREBP, indicating that DP68 might directly interact with critical members of this pathway.<sup>326,329</sup> However, as the activation of the SREBP pathways takes several hours, it was unlikely that this biological activity was linked to the ROS induction by DP68. Thus, the investigation of this pathway was not further prioritized.

In contrast, alterations in posttranslational modifications, e.g. phosphorylation, can occur within a few minutes after a respective stimulus.<sup>278</sup> Phosphoproteome profiling suggested that DP68 may alter the activity of the *65 kDa regulatory subunit A alpha isoform of the protein phosphatase 2A* (PPP2R1A), which is one of two scaffolding subunits for the family of heterotrimeric holoenzymes of protein phosphatases 2A (PP2A). Interestingly, this protein nearly exclusively consists of 15 HEAT repeats.<sup>330</sup> Despite the strong enrichment of HEAT repeat domain-containing proteins in the affinity-based chemical proteomics experiments using NHS beads, PPP2R1A was not identified as hit protein, neither by means of mass spectrometry, nor via immunoblotting. In addition, DP68 did not influence the enzymatic activity of the PPP2CA/PPP2R1A complex *in vitro*. Thus, it is questionable, if PPP2R1A is actually involved in the mechanism causing the superoxide accumulation induced by DP68. As the software used for this phosphoproteome analysis cannot distinguish different phosphorylation sites within a protein, an alternative analysis approach might predict other pathways modulated by DP68. Such alternative analyses are currently established by the HRMS facility of the MPI Dortmund.

## **6.9 Perspectives on the target identification of diaminopyrimidine-based ROS inducers**

As discussed in chapter 6.3, DP68 may interfere with superoxide dismutation, as it increases superoxide levels without hydrogen peroxide elevation. However, none of the three superoxide dismutase family members was identified as interaction partners, neither by affinity enrichment experiments, nor via TPP. Although the superoxide-dismutating enzyme NQO1 was identified in affinity-based chemical proteomics experiments, its interaction with DP68 could not be confirmed. Furthermore, DP68 did not interfere with cellular superoxide dismutation in an enzymatic activity assay.

Phosphoproteome profiling revealed that DP68, but not DP72, induced the phosphorylation of SOD1 at S99. Based on the current literature, phosphorylation at S60 and S99, presumably mediated by the kinase Chk2, triggers the nuclear localization of SOD1.<sup>288,289</sup> Due to incomplete sequence coverage of SOD1 in the phosphoproteome profiling, the phosphorylation status of S60 could not be determined.

Alteration of the subcellular localization of SOD1 may decrease the superoxide-dismutating capacities of the cytoplasm. This may cause the observed superoxide accumulation without influencing the enzymatic activity of SOD1.

Chk2 is activated mainly by ATM, but ATR and DNA-PK are also known activators of the kinase.<sup>290,331,332</sup> Although all three PIKKs were found strongly enriched in affinity-based chemical proteomics experiments, their enzymatic activity was not influenced by DP68 *in vitro*. However, HEAT repeats can facilitate protein-protein interactions.<sup>253</sup> If DP68 indeed binds to HEAT repeats, it may influence the activity of either ATM, ATR or DNA-PK by blocking certain protein-protein interactions. For example, DP68 may inhibit the binding of a negative regulator, which could lead to an activation of the respective kinase. To test this hypothesis, the influence on the subcellular localization of SOD1 by DP68 needs to be investigated, e.g. via expression of a fusion protein comprising SOD1 and a fluorescent protein to track its localization by means of fluorescence microscopy. If DP68 indeed triggered nuclear localization of SOD1, chemical and genetic validation of ATM, ATR or DNA-PK should be considered. This hypothetical mode of action is depicted in Figure 68.

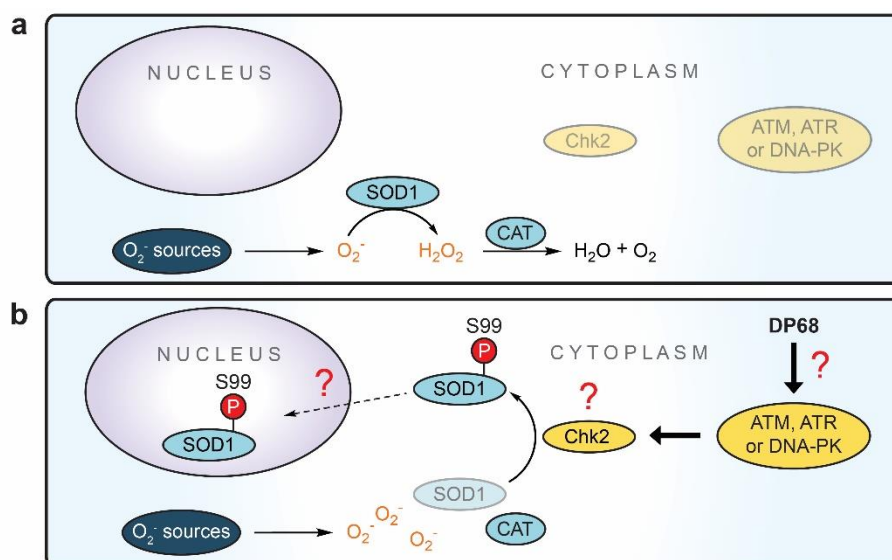


**Figure 68: Hypothetical mode of action for DP68-induced superoxide accumulation.** (a) During redox homeostasis, cytosolic superoxide is converted into hydrogen peroxide by SOD1. Subsequently catalase (and GPX1) scavenge hydrogen peroxide. (b) Treatment with DP68 induces a phosphorylation of SOD1 at S99, potentially caused by the kinase Chk2. Chk2 can be activated by ATM, ATR or DNA-PK, whose activity may be influenced by DP68. Phosphorylation of SOD1 may induce its nuclear localization, which could lead to an accumulation of superoxide in the cytoplasm. ATM = *Ataxia Telangiectasia Mutated*; ATR = *Ataxia telangiectasia* and Rad3-related protein; CAT = catalase; Chk2 = Checkpoint kinase 2; DNA-PK = DNA-dependent protein kinase; SOD = Superoxide dismutase

Despite the application of various target identification techniques, the target responsible for superoxide accumulation induced by DP68 could not yet be identified. The large number of putative interaction partners found in the affinity-based chemical proteomics experiments using NHS beads, indicates that DP68 may bind proteins in a rather promiscuous manner, which would hamper the identification of the protein mediating the ROS-inducing activity. Another explanation for the failure in the identification of the target protein may be, that the applied target identification methods were unsuitable. All proteome-based approaches used can only detect protein targets. However, DP68 may also address non-protein targets, e.g. carbohydrates, lipids or (deoxy)ribonucleic acids (DNA/RNA). In addition, proteins with very low abundance or proteins that are not solubilized in their native conformation during cell lysis, e.g. GPCRs, may also not be identified.<sup>321</sup>

## 6.10 Cancer-selective cytotoxic effects of ROS-inducing compounds

An additional aspect of this thesis was to investigate whether ROS-inducing compounds are able to induce cancer-selective cytotoxicity. As cancer cells usually display higher ROS levels, these cells should be more sensitive towards further ROS elevation.<sup>43</sup> However, in line with the current literature, the majority of hit compounds identified in this phenotypic screen, only showed moderate to low cytotoxic effects.<sup>181</sup>

In an isogenic cell line model, cells overexpressing H-Ras<sup>G12V</sup> were more sensitive to the GSH depletor PEITC, indicating that GSH-depleting small molecules might induce cancer-selective cytotoxicity.<sup>147</sup> Like PEITC, ROS-inducing compounds containing DHMP and TCMP moieties were found to strongly deplete cellular glutathione within 1 h. However, it is unclear, whether these compounds could also trigger cancer-selective cytotoxicity. In general, GSH-depleting compounds may only induce cancer-selective cytotoxicity, if the respective oncogenic transformation actually leads to a decrease in the cellular GSH levels, as it was shown for H-Ras<sup>G12V</sup>-transformed cells in the study on PEITC. Another critical factor for the use of GSH-depleting compounds for cancer therapy is the involvement of glutathione-S-transferases. For different GSH-depleting compounds including PEITC it was shown that their conjugation with GSH is catalyzed by GSTs.<sup>184,191,333</sup> Thus, the anti-cancer effect of PEITC and other glutathione-depleting isothiocyanates, depends on the activity of the respective GST, as GST polymorphisms strongly influenced cytotoxicity.<sup>334</sup> Therefore, an investigation of the potential

involvement of GSTs in the GSH adduct formation of DHMP and THMP compounds should be considered.

Another important consideration is the general thiol reactivity of GSH-depleting compounds. Such compounds may not exclusively react with glutathione, but also with protein thiols, thereby potentially modulating the activity of the respective protein.<sup>335</sup> Depending on the target, such interaction might also mediate cytotoxic effects independently of GSH and ROS levels. However, to achieve such protein-modulating activity, the thiol-reactive compound needs to react preferentially with thiol groups of the respective target. In the course of this thesis, potential protein targets of DHMP and TCMP compounds were not investigated. To do so, affinity enrichment experiments, either *in vitro* or *in situ*, could be applied to examine whether these thiol-reactive compounds may have protein targets in addition to GSH. A compound with a high degree of glutathione-selective reactivity could be a valuable tool to investigate GSH depletion as anti-cancer strategy.

In the course of this thesis, the cytotoxic activities of DP68 were broadly studied. Among three different human cancer cell lines, DP68 displayed cytotoxic effects with IC<sub>50</sub> values of approximately 7  $\mu$ M. In both, cancer cell spheroids and human PBMCs, cytotoxic effects were observed only at 10  $\mu$ M or higher concentrations. Taken together, none of the tested cell culture models displayed a pronounced sensitivity towards DP68. In addition, DP68 activated caspase-3/-7 in HeLa cells, indicating that the compound induces apoptosis.

As mentioned before, in order to investigate the potential of ROS-elevating compounds to induce cancer-selective cytotoxicity, it is important to examine, whether cytotoxic effects are actually ROS-mediated. For this, the influence of antioxidants on the cytotoxicity of DP68 was investigated. While the thiol-containing antioxidant NAC did not dampen its cytotoxicity,  $\alpha$ -tocopherol displayed a strong suppression. Considering that DP68 induces an accumulation of superoxide without elevation of hydrogen peroxide or peroxynitrite, it is not surprising that NAC did not interfere with its cytotoxicity, as it is hardly reactive towards superoxide.<sup>336</sup>  $\alpha$ -tocopherol is an important lipophilic antioxidant and able to suppress lipid peroxidation. However, lipid peroxidation is caused by the reaction of lipids with hydroxyl radicals, which originate from hydrogen peroxide or peroxynitrite.<sup>337,338</sup> As the abundance of the latter two is not increased by DP68, it is unlikely that DP68 triggers hydroxyl radical formation and subsequent lipid peroxidation. In addition, the iron chelator deferoxamine, which suppresses the formation of hydroxyl radicals by inhibiting the Fenton reaction, did not affect the cytotoxicity of DP68.<sup>339</sup>



However,  $\alpha$ -tocopherol is known to inhibit apoptosis independently from its antioxidant properties.<sup>340</sup> Thus, the strong suppression of DP68-induced cytotoxicity by  $\alpha$ -tocopherol could be a consequence of inhibiting apoptosis. Preincubation studies with superoxide-specific antioxidants, e.g. chemical mimetics of SOD, could provide insights into the ROS-dependency of the cytotoxic effects of DP68. Surprisingly, despite its high potency in regard to ROS induction, with an  $EC_{50}$  of  $0.4 \pm 0.1 \mu\text{M}$  in the CM-H<sub>2</sub>DCFDA-based assay, DP68 induces cytotoxic effects in HeLa cells with an  $IC_{50}$  of  $7.1 \pm 0.3 \mu\text{M}$ . Such potency difference could indicate, that the cytotoxic effects of DP68 may be independent of its ROS-inducing activity. However, as discussed in chapter 6.4, cytosolic superoxide measurements indicate that the CM-H<sub>2</sub>DCFDA-based ROS assay may not suffice to cover the full activity range of DP68. Thus, the half-maximal concentration of DP68 in terms of cytosolic superoxide induction is  $>10 \mu\text{M}$ . Therefore, DP68 displays a lower potency in terms of cytotoxicity compared to its superoxide-inducing properties. In addition, DP72, which was found inactive for induction of both ROS and superoxide, did not display cytotoxic effects in HeLa cells and PBMCs. Taken together, the superoxide-inducing activity of DP68 may account for its cytotoxic effects, however further investigations are necessary to confirm this.

A critical parameter whether an increase in cellular ROS levels induces cytotoxic effects is the identity of the reactive oxygen species induced, as different ROS display different degree of reactivity towards different biomolecules. Small molecule elevation of cellular superoxide levels, e.g. by redox-cycling compounds, can trigger cytotoxic effects.<sup>201</sup> However, unlike DP68, such compounds would also cause elevated hydrogen peroxide levels, as SODs readily metabolize superoxide induced by redox cycling. The cytotoxic effects of DP68 may thus be best compared to those of a SOD1 inhibitor, like the copper-chelating compound ATN-224. ATN-224 was reported to induce cytotoxicity in different lymphoma cell lines in a peroxynitrite-dependent manner.<sup>341</sup> Interestingly, peroxynitrite levels in HeLa cells remained unaffected by DP68, indicating a restricted availability of nitric oxide in these cells. Thus, in HeLa cells DP68 may induce cell death via a different mechanism as in cells with higher nitric oxide levels. LD100 is another SOD1 inhibitor that does not chelate copper but instead inhibits the enzyme by blocking its active site. LD100 thereby elevated superoxide concentrations and decreased hydrogen peroxide levels after 24 h in HeLa cells.<sup>342</sup> Interestingly, analogous to DP68, LD100 induced caspase-dependent apoptosis in HeLa cells.<sup>343</sup> Furthermore, in a human prostate cell line model, LD100 selectively induced cytotoxicity in a malignant cell line, while hardly affecting the viability of the

non-malignant counterpart, indicating that interference with superoxide dismutation could be an interesting strategy to selectively target cancer cells.<sup>343</sup> A similar observation was made for ATN-224, which induced cytotoxicity in A549 cells in a SOD1-dependent manner. In contrast, ATN-224 did not display cytotoxic effects in normal bronchial epithelial cells.<sup>344</sup> Surprisingly, despite SOD1 inhibition, ATN-224 increased hydrogen peroxide levels in A549 cells after 24 h, which was caused by a superoxide-mediated inhibition of GPX1, which, together with catalase, detoxifies hydrogen peroxide. The authors found that the cytotoxic effects of ATN-224 were dependent on hydrogen peroxide-mediated activation of p38 MAP kinases.<sup>344</sup> As hydrogen peroxide is an important signaling molecule, the cytotoxic effect of superoxide dismutation-interfering compounds might depend on their influence on hydrogen peroxide levels. LD100 was found to lower hydrogen peroxide levels in HeLa cells, while ATN-224 lead to an increase in A549 cells, both after 24 h. In contrast, DP68 did not affect hydrogen peroxide levels, but these were determined after 1 h of compound treatment. It is questionable, whether DP68 may increase hydrogen peroxide levels after 24 h of compound incubation, as this should also trigger the oxidation of KEAP1, leading to an NRF2-mediated antioxidant response. Such response was however not observed after 24h of treatment with DP68.

In general, the effect on hydrogen peroxide levels could influence tumor cell growth, as hydrogen peroxide oxidizes and thereby inhibits different phosphatases. Lower hydrogen peroxide levels would decrease the inhibition of MAPK phosphatases, which would in turn reduce ERK phosphorylation. In addition, decreased hydrogen peroxide levels may attenuate the inhibition of protein tyrosine phosphatases, consequentially lowering the phosphorylation and activity of growth factor receptors. The latter effect was demonstrated for ATN-224, which reduced ERK1/2 phosphorylation in A431 cells stimulated with EGF.<sup>345</sup>

In addition, ATN-224 was also found to suppress angiogenesis in a mouse model and to attenuate FGF-2- and VEGF2-induced ERK1/2 phosphorylation in human umbilical vein endothelial cells (HUVEC) in a superoxide-dependent manner. This indicates that interference with superoxide dismutation can also affect signaling pathways involved in angiogenesis.<sup>346</sup> As both, sustaining of proliferative signaling and induction of angiogenesis, are two of the original 'hallmarks of cancer' proposed by Hanahan and Weinberg, such properties might support the anti-tumor effects of therapeutic strategies that target superoxide dismutation.<sup>109</sup> However, ATN-224 failed in a phase II clinical study for treatment of prostate cancer as no dose-response effect was observed.<sup>347</sup> Therefore,

the translation of such superoxide- increasing approaches into clinical application needs to be further investigated.

At this point, it is unclear, how DP68 mediates its cytotoxic effects. If DP68 indeed induces ROS accumulation via interference with superoxide dismutation, it might cause cytotoxicity in HeLa cells in a similar fashion as the SOD1 inhibitor LD100, because both trigger apoptosis. DP68 induced cytotoxic effects with similar potency in cancer cell lines and PBMCs. However, the significance of this finding may be limited, as the malignant cell lines were not derived from the hematopoietic system. A comparison to e.g. a lymphoma cell line might be more suitable to evaluate the ability of DP68 to induce cancer-selective cytotoxicity. Furthermore, the general cellular redox status will have a strong impact on the effectiveness of DP68-induced cytotoxicity. Thus, screening of a larger cell line panel might identify DP68-sensitive cell lines. As reported for ATN-224, small molecules that influence superoxide dismutation may also affect ROS-dependent signaling and could thereby suppress proliferation and activate cell death pathways. Considering the multifaceted roles of reactive oxygen species in a cellular environment, ROS-inducing compounds might facilitate anti-cancer properties by more than just elevating ROS levels above a lethal threshold.

## 7 Conclusion and perspectives

Reactive oxygen species are involved in a plethora of biological processes and consequentially play an important role in various diseases. Profound knowledge of cellular redox regulation is thus a prerequisite to develop new therapeutic approaches to address such pathologies, including cancer.

In the course of this thesis, novel, fast-acting inducers of cellular ROS accumulation were discovered by means of phenotypic screening. Biological characterization of selected hit compounds led to the identification of 4,5-dihalo-2-methylpyridazin-3-ones and 2,3,4,5(6)-tetrachloro-6(5)-methylpyridines as cytotoxic inducers of rapid cellular glutathione depletion.

Furthermore, an in-depth study of a diaminopyrimidine-based compound class was conducted. Chemical derivatization of the respective screening hit provided insights into the underlying structure-activity relationship and yielded a derivative with increased potency and water solubility. The ROS-inducing properties of the optimized compound DP68 were dissected using probes that selectively detect different reactive oxygen species. DP68 was found to strongly elevate superoxide levels without affecting hydrogen peroxide levels, indicating an interference with superoxide dismutation. However, the enzymatic activity of cellular superoxide dismutases was not affected by DP68.

A broad range of proteomics-based techniques and morphological profiling was employed to identify molecular targets of DP68 and to unravel its mode of action. The combined usage of the Cell Painting assay and thermal proteome profiling led to the identification of DP68 as novel antagonist of the  $\sigma_1$  receptor. Although this activity does not mediate ROS accumulation, it showcases the potential of integrating these two profiling techniques for target identification.

Affinity-based chemical proteomics revealed a putative interaction of DP68 with HEAT repeat domain-containing proteins, including phosphatidylinositol-3-kinase-like kinases, whose activity, however, was not influenced *in vitro*. A phosphoproteome analysis of DP68 predicted PPP2R1A, a HEAT repeat-domain-containing subunit of the protein phosphatase 2A, as upstream regulator. However, DP68 neither interacted with PPP2R1A nor inhibited its enzymatic activity *in vitro*. Alternatively, binding of DP68 to a protein's HEAT repeat domain could block a protein-protein interaction, which could be further investigated. In addition, DP68 induced SOD1 phosphorylation at S99, which is known to be involved in its nuclear localization. Therefore, the influence of the subcellular localization of SOD1 should be addressed.

Furthermore, DP68 induced cytotoxicity in different cancer cell lines, cancer cell spheroids and benign primary cells with micromolar potency. However, none of these models displayed outstanding sensitivity. Although an inactive derivative of DP68 was not cytotoxic, it is yet to be elucidated, if the cytotoxicity of DP68 is ROS-dependent. Co-treatments with superoxide-specific antioxidants may provide further insights. As cytotoxic effects of ROS-inducing compounds heavily depend on the cellular redox status, screening of a broad panel of cancer cell lines might identify DP68-sensitive cell lines.



## 8 References

1. Waldmann, H. Editorial: Drug Discovery – The Third in the Band! *Angewandte Chemie International Edition* **51**, 6284–6285 (2012).
2. Svatoš, A. Mass spectrometric imaging of small molecules. *Trends in Biotechnology* **28**, 425–434 (2010).
3. Ziegler, S. *et al.* Target Identification for Small Bioactive Molecules: Finding the Needle in the Haystack. *Angewandte Chemie International Edition* **52**, 2744–2792 (2013).
4. Jung, H. J. *et al.* Target deconvolution of bioactive small molecules: the heart of chemical biology and drug discovery. *Archives of Pharmacal Research* **38**, 1627–1641 (2015).
5. Schenone, M. *et al.* Target identification and mechanism of action in chemical biology and drug discovery. *Nature Chemical Biology* **9**, 232–240 (2013).
6. Arrowsmith, C. H. *et al.* The promise and peril of chemical probes. *Nature Chemical Biology* **11**, 536–541 (2015).
7. Rudmann, D. G. On-target and off-target-based toxicologic effects. *Toxicologic pathology* **41**, 310–314 (2013).
8. Eggert, U. S. The why and how of phenotypic small-molecule screens. *Nature Chemical Biology* **9**, 206–209 (2013).
9. Swinney, D. C. *et al.* How were new medicines discovered? *Nature Reviews Drug Discovery* **10**, 507–519 (2011).
10. Vincent, F. *et al.* Developing predictive assays: The phenotypic screening “rule of 3”. *Science Translational Medicine* **7**, 293ps15 (2015).
11. Futamura, Y. *et al.* Target identification of small molecules based on chemical biology approaches. *Molecular BioSystems* **9**, 897–914 (2013).
12. Kanoh, N. *et al.* Photo-Cross-Linked Small-Molecule Affinity Matrix for Facilitating Forward and Reverse Chemical Genetics. *Angewandte Chemie International Edition* **44**, 3559–3562 (2005).
13. Kawatani, M. *et al.* The identification of an osteoclastogenesis inhibitor through the inhibition of glyoxalase I. *Proceedings of the National Academy of Sciences of the United States of America* **105**, 11691–11696 (2008).
14. Murale, D. P. *et al.* Photo-affinity labeling (PAL) in chemical proteomics: a handy tool to investigate protein-protein interactions (PPIs). *Proteome Science* **15**, 1–34 (2016).
15. Li, Z. *et al.* Design and Synthesis of Minimalist Terminal Alkyne-Containing Diazirine Photo-Crosslinkers and Their Incorporation into Kinase Inhibitors for Cell- and Tissue-Based Proteome Profiling. *Angewandte Chemie International Edition* **52**, 8551–8556 (2013).
16. Laraia, L. *et al.* The cholesterol transfer protein GRAMD1A regulates autophagosome biogenesis. *Nature Chemical Biology* **15**, 710–720 (2019).
17. Ong, S.-E. *et al.* Stable Isotope Labeling by Amino Acids in Cell Culture, SILAC, as a Simple and Accurate Approach to Expression Proteomics. *Molecular & Cellular Proteomics* **1**, 376–386 (2002).
18. Ong, S.-E. *et al.* Identifying the proteins to which small-molecule probes and drugs bind in cells. *Proceedings of the National Academy of Sciences of the United States of America* **106**, 4617–4622 (2009).
19. Voigt, T. *et al.* A Natural Product Inspired Tetrahydropyran Collection Yields Mitosis Modulators that Synergistically Target CSE1L and Tubulin. *Angewandte Chemie* **125**, 428–432 (2013).
20. Lomenick, B. *et al.* Target identification using drug affinity responsive target stability (DARTS). *Proceedings of the National Academy of Sciences of the United States of America* **106**, 21984–21989 (2009).
21. West, G. M. *et al.* Quantitative proteomics approach for identifying protein–drug interactions in complex mixtures using protein stability measurements. *Proceedings of the National Academy of Sciences of the United States of America* **107**, 9078–9082 (2010).
22. Molina, D. M. *et al.* Monitoring Drug Target Engagement in Cells and Tissues Using the Cellular Thermal Shift Assay. *Science* **341**, 84–87 (2013).
23. Savitski, M. M. *et al.* Tracking cancer drugs in living cells by thermal profiling of the proteome. *Science* **346** (2014).
24. Reckzeh, E. S. *et al.* in *Systems Chemical Biology. Methods and Protocols*, edited by S. Ziegler & H. Waldmann (Springer New York, New York, NY, 2019), pp. 73–98.
25. Keiser, M. J. *et al.* Relating protein pharmacology by ligand chemistry. *Nature Biotechnology* **25**, 197–206 (2007).
26. Paull, K. D. *et al.* Identification of Novel Antimitotic Agents Acting at the Tubulin Level by Computer-assisted Evaluation of Differential Cytotoxicity Data. *Cancer research* **52**, 3892–3900 (1992).

27. Lamb, J. *et al.* The Connectivity Map: Using Gene-Expression Signatures to Connect Small Molecules, Genes, and Disease. *Science* **313**, 1929–1935 (2006).
28. Kawatani, M. *et al.* Identification of a Small-Molecule Inhibitor of DNA Topoisomerase II by Proteomic Profiling. *Chemistry & Biology* **18**, 743–751 (2011).
29. Kawatani, M. *et al.* Proteomic profiling reveals that collismycin A is an iron chelator. *Scientific Reports* **6**, 1–9 (2016).
30. Futamura, Y. *et al.* Morphobase, an Encyclopedic Cell Morphology Database, and Its Use for Drug Target Identification. *Chemistry & Biology* **19**, 1620–1630 (2012).
31. Bray, M.-A. *et al.* Cell Painting, a high-content image-based assay for morphological profiling using multiplexed fluorescent dyes. *Nature Protocols* **11**, 1757–1774 (2016).
32. Pahl, A. *et al.* in *Systems Chemical Biology. Methods and Protocols*, edited by S. Ziegler & H. Waldmann (Springer New York, New York, NY, 2019), pp. 115–126.
33. Christoforow, A. *et al.* Design, Synthesis, and Phenotypic Profiling of Pyrano-Furo-Pyridone Pseudo Natural Products. *Angewandte Chemie International Edition* **58**, 14715–14723 (2019).
34. Zimmermann, S. *et al.* A Scaffold-Diversity Synthesis of Biologically Intriguing Cyclic Sulfonamides. *Chemistry (Weinheim an der Bergstrasse, Germany)* **25**, 15498–15503 (2019).
35. Foley, D. J. *et al.* Phenotyping Reveals Targets of a Pseudo-Natural-Product Autophagy Inhibitor. *Angewandte Chemie International Edition* **59**, 12470–12476 (2020).
36. Laraia, L. *et al.* Image - Based Morphological Profiling Identifies a Lysosomotropic, Iron - Sequestering Autophagy Inhibitor. *Angewandte Chemie International Edition* **59**, 5721–5729 (2020).
37. Schneidewind, T. *et al.* Morphological Profiling Identifies a Common Mode of Action for Small Molecules with Different Targets. *Chembiochem : a European journal of chemical biology* (2020).
38. Bantscheff, M. *et al.* Quantitative chemical proteomics reveals mechanisms of action of clinical ABL kinase inhibitors. *Nature Biotechnology* **25**, 1035–1044 (2007).
39. Reker, D. *et al.* Identifying the macromolecular targets of de novo-designed chemical entities through self-organizing map consensus. *Proceedings of the National Academy of Sciences of the United States of America* **111**, 4067–4072 (2014).
40. Cheung, A. K. *et al.* in *Concepts and Case Studies in Chemical Biology*, edited by H. Waldmann & P. Janning (John Wiley & Sons, Ltd 2014), Vol. 1, pp. 249–264.
41. Robers, M. B. *et al.* Target engagement and drug residence time can be observed in living cells with BRET. *Nature Communications* **6**, 1–10 (2015).
42. Chessum, N. E. A. *et al.* Demonstrating In-Cell Target Engagement Using a Pirin Protein Degradation Probe (CCT367766). *Journal of Medicinal Chemistry* **61**, 918–933 (2018).
43. Trachootham, D. *et al.* Targeting cancer cells by ROS-mediated mechanisms: a radical therapeutic approach? *Nature Reviews Drug Discovery* **8**, 579–591 (2009).
44. Turrens, J. F. Mitochondrial formation of reactive oxygen species. *The Journal of Physiology* **552**, 335–344 (2003).
45. Tu, B. P. *et al.* Oxidative protein folding in eukaryotes mechanisms and consequences. *J Cell Biol* **164**, 341–346 (2004).
46. Jager, T. L. de *et al.* in *Ultraviolet light in human health, diseases and environment*, edited by S. I. Ahmad (Springer, Cham, Switzerland, 2017), pp. 15–23.
47. Pryor, W. A. *et al.* Oxidants in Cigarette Smoke. Radicals, Hydrogen Peroxide, Peroxynitrate, and Peroxynitrite. *Annals of the New York Academy of Sciences* **686** (1993).
48. Sagai, M. *et al.* Biological effects of diesel exhaust particles. I. in vitro production of superoxide and in vivo toxicity in mouse. *Free Radical Biology and Medicine* **14**, 37–47 (1993).
49. Stohs, S. J. *et al.* Oxidative mechanisms in the toxicity of metal ions. *Free Radical Biology and Medicine* **18**, 321–336 (1995).
50. Klotz, L.-O. *et al.* Cellular adaptation to xenobiotics: Interplay between xenosensors, reactive oxygen species and FOXO transcription factors. *Redox Biology* **13**, 646–654 (2017).
51. Martin, K. R. *et al.* Reactive oxygen species as double-edged swords in cellular processes: low-dose cell signaling versus high-dose toxicity. *Human & experimental toxicology* **21**, 71–75 (2002).
52. Paiva, C. N. *et al.* Are reactive oxygen species always detrimental to pathogens? *Antioxidants & redox signaling* **20**, 1000–1037 (2014).
53. Moloney, J. N. *et al.* ROS Signalling in the Biology of Cancer. *Seminars in cell & developmental biology* **80** (2018).
54. Singh, A. *et al.* Oxidative Stress: A Key Modulator in Neurodegenerative Diseases. *Molecules (Basel, Switzerland)* **24** (2019).



55. Newsholme, P. *et al.* Molecular Mechanisms of ROS Production and Oxidative Stress in Diabetes. *The Biochemical journal* **473** (2016).
56. Granger, D. N. *et al.* Reperfusion Injury and Reactive Oxygen Species: The Evolution of a Concept. *Redox Biology* **6** (2015).
57. Mittal, M. *et al.* Reactive Oxygen Species in Inflammation and Tissue Injury. *Antioxidants & redox signaling* **20** (2014).
58. Harman, D. Aging: A Theory Based on Free Radical and Radiation Chemistry. *J Gerontol* **11**, 298–300 (1956).
59. Liochev, S. I. Reactive oxygen species and the free radical theory of aging. *Free Radical Biology and Medicine* **60**, 1–4 (2013).
60. Murphy, M. P. How mitochondria produce reactive oxygen species. *Biochemical Journal* **417**, 1–13 (2009).
61. Turrens, J. F. Superoxide Production by the Mitochondrial Respiratory Chain. *Bioscience reports* **17** (1997).
62. Orr, A. L. *et al.* A Refined Analysis of Superoxide Production by Mitochondrial sn-Glycerol 3-Phosphate Dehydrogenase. *Journal of Biological Chemistry* **287**, 42921–42935 (2012).
63. Bunik, V. I. *et al.* Generation of superoxide and hydrogen peroxide by side reactions of mitochondrial 2-oxoacid dehydrogenase complexes in isolation and in cells. *Biological Chemistry* **399**, 407–420 (2018).
64. Mao, G. D. *et al.* Electron spin resonance study on the permeability of superoxide radicals in lipid bilayers and biological membranes. *FEBS Letters* **305**, 233–236 (1992).
65. Valko, M. *et al.* Free radicals and antioxidants in normal physiological functions and human disease. *The International Journal of Biochemistry & Cell Biology* **39**, 44–84 (2007).
66. Weisiger, R. A. *et al.* Superoxide Dismutase. Organelle Specificity. *The Journal of biological chemistry* **248** (1973).
67. Schrader, M. *et al.* Peroxisomes and oxidative stress. *Biochimica et Biophysica Acta - Molecular Cell Research* **1763**, 1755–1766 (2006).
68. Lubos, E. *et al.* Glutathione peroxidase-1 in health and disease: from molecular mechanisms to therapeutic opportunities. *Antioxidants & redox signaling* **15**, 1957–1997 (2011).
69. Klebanoff, S. J. Myeloperoxidase: friend and foe. *Journal of Leukocyte Biology* **77**, 598–625 (2005).
70. Gaschler, M. M. *et al.* Lipid peroxidation in cell death. *Biochemical and biophysical research communications* **482**, 419–425 (2017).
71. Dixon, S. J. *et al.* Ferroptosis: An Iron-Dependent Form of Nonapoptotic Cell Death. *Cell* **149**, 1060–1072 (2012).
72. Adams, L. *et al.* Reactive nitrogen species in cellular signaling. *Experimental biology and medicine (Maywood, N.J.)* **240**, 711–717 (2015).
73. Nauser, T. *et al.* The Rate Constant of the Reaction of Superoxide with Nitrogen Monoxide: Approaching the Diffusion Limit. *The Journal of Physical Chemistry A* **106**, 4084–4086 (2002).
74. Bedard, K. *et al.* The NOX family of ROS-generating NADPH oxidases: physiology and pathophysiology. *Physiological reviews* **87**, 245–313 (2007).
75. Nguyen, H. N. *et al.* Anti-oxidative effects of superoxide dismutase 3 on inflammatory diseases. *J Mol Med* **98**, 59–69 (2020).
76. Poole, L. B. The basics of thiols and cysteines in redox biology and chemistry. *Free Radical Biology and Medicine* **80**, 148–157 (2015).
77. Jung, T. *et al.* The proteasome and its role in the degradation of oxidized proteins. *IUBMB Life* **60**, 743–752 (2008).
78. Perkins, A. *et al.* Peroxiredoxins: guardians against oxidative stress and modulators of peroxide signaling. *Trends in Biochemical Sciences* **40**, 435–445 (2015).
79. Lu, J. *et al.* The thioredoxin antioxidant system. *Free Radical Biology and Medicine* **66**, 75–87 (2014).
80. Lillig, C. H. *et al.* Glutaredoxin systems. *Biochimica et Biophysica Acta - General Subjects* **1780**, 1304–1317 (2008).
81. Couto, N. *et al.* The role of glutathione reductase and related enzymes on cellular redox homeostasis network. *Free Radical Biology and Medicine* **95**, 27–42 (2016).
82. Stincone, A. *et al.* The return of metabolism: biochemistry and physiology of the pentose phosphate pathway. *Biological Reviews* **90**, 927–963 (2015).
83. Finkel, T. From Sulfenylation to Sulfhydration: What a Thiolate Needs to Tolerate. *Sci. Signal.* **5**, pe10-pe10 (2012).
84. Schieber, M. *et al.* ROS Function in Redox Signaling and Oxidative Stress. *Current Biology* **24**, R453–R462 (2014).
85. Bae, Y. S. *et al.* Epidermal Growth Factor (EGF)-induced Generation of Hydrogen Peroxide. Role in EGF Receptor-Mediated Tyrosine Phosphorylation. *The Journal of biological chemistry* **272** (1997).
86. Sundaresan, M. *et al.* Requirement for Generation of H<sub>2</sub>O<sub>2</sub> for Platelet-Derived Growth Factor Signal Transduction. *Science (New York, N.Y.)* **270** (1995).

87. Holmström, K. M. *et al.* Cellular mechanisms and physiological consequences of redox-dependent signalling. *Nature Reviews Molecular Cell Biology* **15**, 411–421 (2014).
88. Kwon, J. *et al.* Reversible oxidation and inactivation of the tumor suppressor PTEN in cells stimulated with peptide growth factors. *Proceedings of the National Academy of Sciences of the United States of America* **101**, 16419–16424 (2004).
89. Jena, N. R. DNA damage by reactive species: Mechanisms, mutation and repair. *Journal of Biosciences* **37**, 503–517 (2012).
90. Wang, Y. Bulky DNA Lesions Induced by Reactive Oxygen Species. *Chemical Research in Toxicology* **21**, 276–281 (2008).
91. Costa, V. *et al.* Protein oxidation, repair mechanisms and proteolysis in *Saccharomyces cerevisiae*. *IUBMB Life* **59**, 293–298 (2007).
92. Fedorova, M. *et al.* Protein carbonylation as a major hallmark of oxidative damage: Update of analytical strategies. *Mass Spectrometry Reviews* **33**, 79–97 (2014).
93. Tonelli, C. *et al.* Transcriptional Regulation by Nrf2. *Antioxidants & redox signaling* **29**, 1727–1745 (2018).
94. Kansanen, E. *et al.* The Keap1-Nrf2 Pathway: Mechanisms of Activation and Dysregulation in Cancer. *Redox Biology* **1** (2013).
95. Sasaki, H. *et al.* Electrophile Response Element-mediated Induction of the Cystine/Glutamate Exchange Transporter Gene Expression. *Journal of Biological Chemistry* **277**, 44765–44771 (2002).
96. Wild, A. C. *et al.* Regulation of  $\gamma$ -Glutamylcysteine Synthetase Subunit Gene Expression by the Transcription Factor Nrf2. *Journal of Biological Chemistry* **274**, 33627–33636 (1999).
97. Harvey, C. J. *et al.* Nrf2-regulated glutathione recycling independent of biosynthesis is critical for cell survival during oxidative stress. *Free Radical Biology and Medicine* **46**, 443–453 (2009).
98. Thimmulappa, R. K. *et al.* Identification of Nrf2-regulated Genes Induced by the Chemopreventive Agent Sulforaphane by Oligonucleotide Microarray. *Cancer research* **62**, 5196–5203 (2002).
99. McGrath-Morrow, S. *et al.* Nrf2 increases survival and attenuates alveolar growth inhibition in neonatal mice exposed to hyperoxia. *American Journal of Physiology - Lung Cellular and Molecular Physiology* **296**, L565-73 (2009).
100. Ishii, T. *et al.* Induction of murine intestinal and hepatic peroxiredoxin MSP23 by dietary butylated hydroxyanisole. *Carcinogenesis* **21**, 1013–1016 (2000).
101. Kim, Y.-C. *et al.* Thioredoxin-dependent redox regulation of the antioxidant responsive element (ARE) in electrophile response. *Oncogene* **22**, 1860–1865 (2003).
102. Chorley, B. N. *et al.* Identification of novel NRF2-regulated genes by ChIP-Seq: influence on retinoid X receptor alpha. *Nucleic Acids Research* **40**, 7416–7429 (2012).
103. Lane, D. P. p53, guardian of the genome. *Nature* **358**, 15–16 (1992).
104. Sablina, A. A. *et al.* The antioxidant function of the p53 tumor suppressor. *Nature Medicine* **11**, 1306–1313 (2005).
105. Bensaad, K. *et al.* TIGAR, a p53-Inducible Regulator of Glycolysis and Apoptosis. *Cell* **126**, 107–120 (2006).
106. Klotz, L.-O. *et al.* Redox regulation of FoxO transcription factors. *Redox Biology* **6**, 51–72 (2015).
107. Bae, I. *et al.* BRCA1 Induces Antioxidant Gene Expression and Resistance to Oxidative Stress. *Cancer research* **64**, 7893–7909 (2004).
108. Saha, T. *et al.* BRCA1 down - regulates cellular levels of reactive oxygen species. *FEBS Letters* **583**, 1535–1543 (2009).
109. Hanahan, D. *et al.* The Hallmarks of Cancer. *Cell* **100**, 57–70 (2000).
110. Hanahan, D. *et al.* Hallmarks of Cancer: The Next Generation. *Cell* **144**, 646–674 (2011).
111. Fisher, R. *et al.* Cancer heterogeneity: implications for targeted therapeutics. *British Journal of Cancer* **108**, 479–485 (2013).
112. Greaves, M. *et al.* Clonal evolution in cancer. *Nature* **481**, 306–313 (2012).
113. Szatrowski, T. P. *et al.* Production of Large Amounts of Hydrogen Peroxide by Human Tumor Cells. *Cancer research* **51**, 794–798 (1991).
114. Toyokuni, S. *et al.* Persistent oxidative stress in cancer. *FEBS Letters* **358**, 1–3 (1995).
115. Moloney, J. N. *et al.* ROS signalling in the biology of cancer. *Seminars in cell & developmental biology* **80**, 50–64 (2018).
116. Lim, J. K. M. *et al.* The impact of oncogenic RAS on redox balance and implications for cancer development. *Cell Death & Disease* **10**, 1–9 (2019).
117. Mitsushita, J. *et al.* The Superoxide-Generating Oxidase Nox1 Is Functionally Required for Ras Oncogene Transformation. *Cancer research* **64**, 3580–3585 (2004).
118. Ogrunc, M. *et al.* Oncogene-induced reactive oxygen species fuel hyperproliferation and DNA damage response activation. *Cell Death & Differentiation* **21**, 998–1012 (2014).

119. Kopnin, P. B. *et al.* Repression of Sestrin Family Genes Contributes to Oncogenic Ras-Induced Reactive Oxygen Species Up-regulation and Genetic Instability. *Cancer research* **67**, 4671–4678 (2007).
120. DeNicola, G. M. *et al.* Oncogene-induced Nrf2 transcription promotes ROS detoxification and tumorigenesis. *Nature* **475**, 106–109 (2011).
121. Koundouros, N. *et al.* Phosphoinositide 3-Kinase/Akt Signaling and Redox Metabolism in Cancer. *Frontiers in Oncology* **8**, 160 (2018).
122. Meng, T.-C. *et al.* Reversible Oxidation and Inactivation of Protein Tyrosine Phosphatases In Vivo. *Molecular Cell* **9**, 387–399 (2002).
123. Zhao, Y. *et al.* ROS signaling under metabolic stress: cross-talk between AMPK and AKT pathway. *Mol Cancer* **16**, 1–12 (2017).
124. Manning, B. D. *et al.* AKT/PKB Signaling: Navigating Downstream. *Cell* **129**, 1261–1274 (2007).
125. Son, Y. *et al.* Mitogen-Activated Protein Kinases and Reactive Oxygen Species: How Can ROS Activate MAPK Pathways? *Journal of Signal Transduction* **2011** (2011).
126. Taylor, C. A. *et al.* Role of p38 and JNK MAPK signaling pathways and tumor suppressor p53 on induction of apoptosis in response to Ad-eIF5A1 in A549 lung cancer cells. *Mol Cancer* **12**, 1–11 (2013).
127. Matsuzawa, A. *et al.* Redox control of cell fate by MAP kinase: physiological roles of ASK1-MAP kinase pathway in stress signaling. *Biochimica et Biophysica Acta - General Subjects* **1780**, 1325–1336 (2008).
128. Galanis, A. *et al.* Reactive oxygen species and HIF-1 signalling in cancer. *Cancer Letters* **266**, 12–20 (2008).
129. Bell, E. L. *et al.* The Qo site of the mitochondrial complex III is required for the transduction of hypoxic signaling via reactive oxygen species production. *J Cell Biol* **177**, 1029–1036 (2007).
130. Richard, D. E. *et al.* p42/p44 Mitogen-activated Protein Kinases Phosphorylate Hypoxia-inducible Factor 1 $\alpha$  (HIF-1 $\alpha$ ) and Enhance the Transcriptional Activity of HIF-1. *Journal of Biological Chemistry* **274**, 32631–32637 (1999).
131. Warburg, O. Über den Stoffwechsel der Carcinomzelle. *Naturwissenschaften* **12**, 1131–1137 (1924).
132. Liberti, M. V. *et al.* The Warburg Effect: How Does it Benefit Cancer Cells? *Trends in Biochemical Sciences* **41**, 211–218 (2016).
133. Rodic, S. *et al.* Reactive oxygen species (ROS) are a key determinant of cancer's metabolic phenotype. *International Journal of Cancer* **142**, 440–448 (2018).
134. Jung, Y. *et al.* Direct Cellular Responses to Platinum-Induced DNA Damage. *Chemical Reviews* **107**, 1387–1407 (2007).
135. Rowinsky, E. K. *et al.* Taxol: A Novel Investigational Antimicrotubule Agent. *Journal of the National Cancer Institute* **82**, 1247–1259 (1990).
136. Hsiang, Y. H. *et al.* Camptothecin induces protein-linked DNA breaks via mammalian DNA topoisomerase I. *Journal of Biological Chemistry* **260**, 14873–14878 (1985).
137. Druker, B. J. *et al.* Effects of a selective inhibitor of the Abl tyrosine kinase on the growth of Bcr–Abl positive cells. *Nature Medicine* **2**, 561–566 (1996).
138. Slamon, D. J. *et al.* Use of chemotherapy plus a monoclonal antibody against HER2 for metastatic breast cancer that overexpresses HER2. *The New England journal of medicine* **344**, 783–792 (2001).
139. World Health Organization. Model list of essential medicines: 21st list 2019. Available at <https://apps.who.int/iris/bitstream/handle/10665/325771/WHO-MVP-EMP-IAU-2019.06-eng.pdf?ua=1> (2019).
140. Volkan I. S. *et al.* Antioxidants Accelerate Lung Cancer Progression in Mice. *Science Translational Medicine* **6**, 221ra15 (2014).
141. van Zandwijk, N. *et al.* EUROSCAN, a Randomized Trial of Vitamin A and N-Acetylcysteine in Patients With Head and Neck Cancer or Lung Cancer. *J Natl Cancer Inst* **92**, 977–986 (2000).
142. Klein, E. A. *et al.* Vitamin E and the Risk of Prostate Cancer: The Selenium and Vitamin E Cancer Prevention Trial (SELECT). *JAMA* **306**, 1549–1556 (2011).
143. Lawenda, B. D. *et al.* Should Supplemental Antioxidant Administration Be Avoided During Chemotherapy and Radiation Therapy? *J Natl Cancer Inst* **100**, 773–783 (2008).
144. Kong, Q. *et al.* A threshold concept for cancer therapy. *Medical Hypotheses* **55**, 29–35 (2000).
145. Chou, W.-C. *et al.* Role of NADPH oxidase in arsenic-induced reactive oxygen species formation and cytotoxicity in myeloid leukemia cells. *Proceedings of the National Academy of Sciences of the United States of America* **101**, 4578–4583 (2004).
146. Litzow, M. R. Arsenic trioxide. *Expert Opinion on Pharmacotherapy* **9**, 1773–1785 (2008).

147. Trachootham, D. *et al.* Selective killing of oncogenically transformed cells through a ROS-mediated mechanism by  $\beta$ -phenylethyl isothiocyanate. *Cancer Cell* **10**, 241–252 (2006).
148. Shaw A. T. *et al.* Selective killing of K-ras mutant cancer cells by small molecule inducers of oxidative stress. *Proceedings of the National Academy of Sciences of the United States of America* **108**, 8773–8778 (2011).
149. Dolma, S. *et al.* Identification of genotype-selective antitumor agents using synthetic lethal chemical screening in engineered human tumor cells. *Cancer Cell* **3**, 285–296 (2003).
150. Yang, W. S. *et al.* Synthetic Lethal Screening Identifies Compounds Activating Iron-Dependent, Nonapoptotic Cell Death in Oncogenic-RAS-Harboring Cancer Cells. *Chemistry & Biology* **15**, 234–245 (2008).
151. Dixon, S. J. *et al.* Pharmacological inhibition of cystine–glutamate exchange induces endoplasmic reticulum stress and ferroptosis. *eLife Sciences Publications, Ltd* (2014).
152. Yang, W. S. *et al.* Regulation of Ferroptotic Cancer Cell Death by GPX4. *Cell* **156**, 317–331 (2014).
153. Guan, J. *et al.* The xc<sup>-</sup> cystine/glutamate antiporter as a potential therapeutic target for small-cell lung cancer: use of sulfasalazine. *Cancer Chemotherapy and Pharmacology* **64**, 463–472 (2009).
154. Dethmers, J. K. *et al.* Glutathione export by human lymphoid cells: depletion of glutathione by inhibition of its synthesis decreases export and increases sensitivity to irradiation. *Proceedings of the National Academy of Sciences of the United States of America* **78**, 7492–7496 (1981).
155. Magda, D. *et al.* Motexafin gadolinium: A novel redox active drug for cancer therapy. *Seminars in Cancer Biology* **16**, 466–476 (2006).
156. Marzano, C. *et al.* Inhibition of thioredoxin reductase by auranofin induces apoptosis in cisplatin-resistant human ovarian cancer cells. *Free Radical Biology and Medicine* **42**, 872–881 (2007).
157. Li, N. *et al.* Mitochondrial Complex I Inhibitor Rotenone Induces Apoptosis through Enhancing Mitochondrial Reactive Oxygen Species Production. *Journal of Biological Chemistry* **278**, 8516–8525 (2003).
158. Ogita, M. *et al.* Antimycin A-induced cell death depends on AIF translocation through NO production and PARP activation and is not involved in ROS generation, cytochrome c release and caspase-3 activation in HL-60 cells. *The Journal of Antibiotics* **62**, 145–152 (2009).
159. Djavaheri-Mergny, M. *et al.* 2-Methoxyestradiol induces apoptosis in Ewing sarcoma cells through mitochondrial hydrogen peroxide production. *Oncogene* **22**, 2558–2567 (2003).
160. Kato, S. *et al.* 2-methoxyestradiol mediates apoptosis through caspase-dependent and independent mechanisms in ovarian cancer cells but not in normal counterparts. *Reproductive sciences (Thousand Oaks, Calif.)* **15**, 878–894 (2008).
161. Ling, Y.-H. *et al.* Reactive Oxygen Species Generation and Mitochondrial Dysfunction in the Apoptotic Response to Bortezomib, a Novel Proteasome Inhibitor, in Human H460 Non-small Cell Lung Cancer Cells. *Journal of Biological Chemistry* **278**, 33714–33723 (2003).
162. Doroshow, J. H. Mechanisms of Anthracycline-Enhanced Reactive Oxygen Metabolism in Tumor Cells. *Oxidative Medicine and Cellular Longevity* **2019** (2019).
163. Chiu, W.-H. *et al.* Vinca alkaloids cause aberrant ROS-mediated JNK activation, Mcl-1 downregulation, DNA damage, mitochondrial dysfunction, and apoptosis in lung adenocarcinoma cells. *Biochemical Pharmacology* **83**, 1159–1171 (2012).
164. Casares, C. *et al.* Reactive Oxygen Species in Apoptosis Induced by Cisplatin: Review of Physiopathological Mechanisms in Animal Models. *European Archives of Oto-Rhino-Laryngology* **269** (2012).
165. Hwang, P. M. *et al.* Ferredoxin reductase affects p53-dependent, 5-fluorouracil-induced apoptosis in colorectal cancer cells. *Nature Medicine* **7**, 1111–1117 (2001).
166. Kosaka, T. *et al.* Reactive oxygen species induction by cabazitaxel through inhibiting Sestrin-3 in castration resistant prostate cancer. *Oncotarget* **8**, 87675–87683 (2017).
167. Zhang, Y.-W. *et al.* Cardiomyocyte death in doxorubicin-induced cardiotoxicity. *Archivum immunologiae et therapiae experimentalis* **57**, 435–445 (2009).
168. Dixon, S. J. *et al.* The Hallmarks of Ferroptosis. *Annual Review of Cancer Biology* **3**, 35–54 (2019).
169. Berger, I. *et al.* Baculovirus expression system for heterologous multiprotein complexes. *Nat Biotechnol (Nature Biotech)* **22**, 1583–1587 (2004).
170. Hashimoto, Y. *et al.* Ao38, a new cell line from eggs of the black witch moth, *Ascalapha odorata* (Lepidoptera: Noctuidae), is permissive for AcMNPV infection and produces high levels of recombinant proteins. *BMC biotechnology* **10**, 50 (2010).

171. Hu, J. J. *et al.* Fluorescent Probe HKSOX-1 for Imaging and Detection of Endogenous Superoxide in Live Cells and In Vivo. *Journal of the American Chemical Society* **137**, 6837–6843 (2015).
172. Lu, M. *et al.* 70 - Tracking Intriguing Lysosomal Superoxide Formation and Distribution in Multiple Cellular Models with a Highly Selective Fluorescent Probe. *Free Radical Biology and Medicine* **100**, S43 (2016).
173. Peng, T. *et al.* Molecular Imaging of Peroxynitrite with HKGreen-4 in Live Cells and Tissues. *Journal of the American Chemical Society* **136**, 11728–11734 (2014).
174. Sen Ye *et al.* Tandem Payne/Dakin Reaction: A New Strategy for Hydrogen Peroxide Detection and Molecular Imaging. *Angewandte Chemie* **130**, 10330–10334 (2018).
175. Carpenter, A. E. *et al.* CellProfiler: image analysis software for identifying and quantifying cell phenotypes. *Genome Biology* **7**, 1–11 (2006).
176. Cox, J. *et al.* MaxQuant enables high peptide identification rates, individualized p.p.b.-range mass accuracies and proteome-wide protein quantification. *Nature Biotechnology* **26**, 1367–1372 (2008).
177. Tyanova, S. *et al.* The Perseus computational platform for comprehensive analysis of (prote)omics data. *Nature Methods* **13**, 731–740 (2016).
178. Baumeister, S. *et al.* Synthesis and receptor binding of thiophene bioisosteres of potent GluN2B ligands with a benzo[7]annulene-scaffold. *Med. Chem. Commun.* **10**, 315–325 (2019).
179. Cheng, Y.-C. *et al.* Relationship between the inhibition constant (KI) and the concentration of inhibitor which causes 50 per cent inhibition (I50) of an enzymatic reaction. *Biochemical Pharmacology* **22**, 3099–3108 (1973).
180. Bradford, M. M. A rapid and sensitive method for the quantitation of microgram quantities of protein utilizing the principle of protein-dye binding. *Analytical Biochemistry* **72**, 248–254 (1976).
181. Adams, D. J. *et al.* Discovery of Small-Molecule Enhancers of Reactive Oxygen Species That are Nontoxic or Cause Genotype-Selective Cell Death. *ACS Chemical Biology* **8**, 923–929 (2013).
182. Kalyanaraman, B. *et al.* Measuring reactive oxygen and nitrogen species with fluorescent probes: challenges and limitations. *Free Radical Biology and Medicine* **52**, 1–6 (2012).
183. Fluorescence response of APF, HPF and H2DCFDA to various reactive oxygen species (ROS)—Table 18.4 | Thermo Fisher Scientific - DE. Available at <https://www.thermofisher.com/de/en/home/references/molecular-probes-the-handbook/tables/fluorescence-response-of-3-p-aminophenyl-fluorescein-afp-3-p-hydroxyphenyl-fluorescein-hpf-and-dichlorodihydrofluorescein-diacetate-h2dcfda-to-various-reactive-oxygen-species-ros.html> (2020).
184. Awasthi, Y. C. *et al.* Enzymatic Conjugation of Erythrocyte Glutathione With 1-chloro-2,4-dinitrobenzene: The Fate of Glutathione Conjugate in Erythrocytes and the Effect of Glutathione Depletion on Hemoglobin. *Blood* **58** (1981).
185. Kawamura, T. *et al.* Discovery of small-molecule modulator of heterotrimeric Gi-protein by integrated phenotypic profiling and chemical proteomics. *Bioscience, Biotechnology, and Biochemistry*, 1–7 (2020).
186. Švenda, J. *et al.* Biology-Oriented Synthesis of a Withanolide-Inspired Compound Collection Reveals Novel Modulators of Hedgehog Signaling. *Angewandte Chemie International Edition* **54**, 5596–5602 (2015).
187. Forman, H. J. *et al.* Glutathione: Overview of its protective roles, measurement, and biosynthesis. *Molecular Aspects of Medicine* **30**, 1–12 (2009).
188. Bauer, M. R. *et al.* 2-Sulfonylpyrimidines: Mild alkylating agents with anticancer activity toward p53-compromised cells. *Proceedings of the National Academy of Sciences of the United States of America* **113**, E5271–E5280 (2016).
189. Mervin, L. H. *et al.* Understanding Cytotoxicity and Cytostaticity in a High-Throughput Screening Collection. *ACS Chemical Biology* **11**, 3007–3023 (2016).
190. Griffith, O. W. *et al.* Potent and specific inhibition of glutathione synthesis by buthionine sulfoximine (S-n-butyl homocysteine sulfoximine). *The Journal of biological chemistry* **254** (1979).
191. Kawamura, T. *et al.* A small molecule that induces reactive oxygen species via cellular glutathione depletion. *Biochemical Journal* **463**, 53–63 (2014).
192. Robke, L. *et al.* Discovery of the novel autophagy inhibitor aumitin that targets mitochondrial complex I. *Chemical Science* **9**, 3014–3022 (2018).
193. Lardy, H. A. *et al.* Antibiotics as tools for metabolic studies. I. A survey of toxic antibiotics in respiratory, phosphorylative and glycolytic systems. *Archives of Biochemistry and Biophysics* **78**, 587–597 (1958).
194. Heytler, P. G. *et al.* A new class of uncoupling agents — Carbonyl cyanide phenylhydrazones. *Biochemical and biophysical research communications* **7**, 272–275 (1962).

195. Brown, G. C. *et al.* Mitochondrial proton and electron leaks. *Essays Biochem* **47**, 53–67 (2010).
196. Palmer, G. *et al.* Studies on the respiratory chain-linked reduced nicotinamide adenine dinucleotide dehydrogenase. XIV. Location of the sites of inhibition of rotenone, barbiturates, and piericidin by means of electron paramagnetic resonance spectroscopy. *The Journal of biological chemistry* **243** (1968).
197. Kim, H. *et al.* Structure of Antimycin A1, a Specific Electron Transfer Inhibitor of Ubiquinol–Cytochrome c Oxidoreductase. *Journal of the American Chemical Society* **121**, 4902–4903 (1999).
198. Mai, T. T. *et al.* Salinomycin kills cancer stem cells by sequestering iron in lysosomes. *Nature Chem* **9**, 1025–1033 (2017).
199. Lu, S. *et al.* Lysosomal adaptation: How cells respond to lysosomotropic compounds. *PLoS one* **12**, e0173771 (2017).
200. Polster, B. M. *et al.* in *Methods in Enzymology : Mitochondrial Function*, edited by A. N. Murphy & D. C. Chan (Academic Press 2014), pp. 225–250.
201. Johnston, P. A. Redox cycling compounds generate H<sub>2</sub>O<sub>2</sub> in HTS buffers containing strong reducing reagents—real hits or promiscuous artifacts? *Current Opinion in Chemical Biology* **15**, 174–182 (2011).
202. Soares, K. M. *et al.* Profiling the NIH Small Molecule Repository for compounds that generate H<sub>2</sub>O<sub>2</sub> by redox cycling in reducing environments. *Assay and drug development technologies* **8**, 152–174 (2010).
203. Yang, M. *et al.* Cytotoxicity of Air Pollutant 9,10-Phenanthrenequinone: Role of Reactive Oxygen Species and Redox Signaling. *BioMed Research International* **2018** (2018).
204. Brand, M. D. Mitochondrial generation of superoxide and hydrogen peroxide as the source of mitochondrial redox signaling. *Free Radical Biology and Medicine* **100**, 14–31 (2016).
205. Robb, E. L. *et al.* Control of mitochondrial superoxide production by reverse electron transport at complex I. *J. Biol. Chem.* **293**, 9869–9879 (2018).
206. Watson, M. A. *et al.* Use of S1QELs and S3QELs to link mitochondrial sites of superoxide and hydrogen peroxide generation to physiological and pathological outcomes. *Biochem Soc Trans* **47**, 1461–1469 (2019).
207. Altenhöfer, S. *et al.* Evolution of NADPH Oxidase Inhibitors: Selectivity and Mechanisms for Target Engagement. *Antioxidants & redox signaling* **23**, 406–427 (2015).
208. Probst, B. L. *et al.* Cancer Cell Growth Is Differentially Affected by Constitutive Activation of NRF2 by KEAP1 Deletion and Pharmacological Activation of NRF2 by the Synthetic Triterpenoid, RTA 405. *PLoS one* **10**, e0135257 (2015).
209. Su, S. *et al.* Lowering Endogenous Cathepsin D Abundance Results in Reactive Oxygen Species Accumulation and Cell Senescence. *Molecular & Cellular Proteomics* **16**, 1217–1232 (2017).
210. Antognelli, C. *et al.* Glyoxalase 1–419C>A Variant Is Associated with Oxidative Stress: Implications in Prostate Cancer Progression. *PLoS one* **8**, e74014 (2013).
211. Laurent-Matha, V. *et al.* Processing of Human Cathepsin D Is Independent of Its Catalytic Function and Auto-Activation: Involvement of Cathepsins L and B. *The Journal of Biochemistry* **139**, 363–371 (2006).
212. Chu, U. B. *et al.* Biochemical Pharmacology of the Sigma-1 Receptor. *Molecular pharmacology* **89**, 142–153 (2016).
213. Vaupel, D. B. Naltrexone fails to antagonize the sigma effects of PCP and SKF 10,047 in the dog. *European journal of pharmacology* **92**, 269–274 (1983).
214. Tam, S. W. *et al.* Sigma opiates and certain antipsychotic drugs mutually inhibit (+)-3H SKF 10,047 and 3Hhaloperidol binding in guinea pig brain membranes. *Proceedings of the National Academy of Sciences of the United States of America* **81**, 5618–5621 (1984).
215. Tesei, A. *et al.* Sigma Receptors as Endoplasmic Reticulum Stress “Gatekeepers” and their Modulators as Emerging New Weapons in the Fight Against Cancer. *Frontiers in Pharmacology* **9** (2018).
216. Vilner, B. J. *et al.* Sigma-1 and sigma-2 receptors are expressed in a wide variety of human and rodent tumor cell lines. *Cancer research* **55**, 408–413 (1995).
217. Hudkins, R. L. *et al.* M1 muscarinic antagonists interact with  $\sigma$  recognition sites. *Life Sciences* **49**, 1229–1235 (1991).
218. Kedjouar, B. *et al.* Structural similitudes between cytotoxic antiestrogen-binding site (AEBS) ligands and cytotoxic sigma receptor ligands. evidence for a relationship between cytotoxicity and affinity for AEBS or sigma-2 receptor but not for sigma-1 receptor. *Biochemical Pharmacology* **58**, 1927–1939 (1999).
219. Rao, T. S. *et al.* Neurochemical characterization of dopaminergic effects of opipramol, a potent sigma receptor ligand, in vivo. *Neuropharmacology* **29**, 1191–1197 (1990).
220. Perregaard, J. *et al.*  $\sigma$  Ligands with Subnanomolar Affinity and Preference for the  $\sigma_2$  Binding Site. 1. 3-( $\omega$ -Aminoalkyl)-1H-indoles. *Journal of Medicinal Chemistry* **38**, 1998–2008 (1995).

221. Lee, I. T. *et al.* An unambiguous assay for the cloned human sigma<sub>1</sub> receptor reveals high affinity interactions with dopamine D<sub>4</sub> receptor selective compounds and a distinct structure–affinity relationship for butyrophenones. *European journal of pharmacology* **578**, 123–136 (2008).
222. Tam, S. W. Naloxone-inaccessible sigma receptor in rat central nervous system. *Proceedings of the National Academy of Sciences of the United States of America* **80**, 6703–6707 (1983).
223. Brent, P. J. Kappa opioid receptor agonists inhibit sigma-1 (σ<sub>1</sub>) receptor binding in guinea-pig brain, liver and spleen: autoradiographical evidence. *Brain Research* **725**, 155–165 (1996).
224. Narita, N. *et al.* Interactions of selective serotonin reuptake inhibitors with subtypes of σ receptors in rat brain. *European journal of pharmacology* **307**, 117–119 (1996).
225. McLarnon, J. *et al.* The actions of L-687,384, a sigma receptor ligand, on NMDA-induced currents in cultured rat hippocampal pyramidal neurons. *Neuroscience letters* **174**, 181–184 (1994).
226. Ishima, T. *et al.* Interaction of new antidepressants with sigma-1 receptor chaperones and their potentiation of neurite outgrowth in PC12 cells. *European journal of pharmacology* **727**, 167–173 (2014).
227. Cobos, E. J. *et al.* Phenytoin differentially modulates the affinity of agonist and antagonist ligands for σ<sub>1</sub> receptors of guinea pig brain. *Synapse* **55**, 192–195 (2005).
228. Hayashi, T. *et al.* Sigma-1 receptor ligands: potential in the treatment of neuropsychiatric disorders. *CNS drugs* **18**, 269–284 (2004).
229. Pal, A. *et al.* The sigma-1 receptor protects against cellular oxidative stress and activates antioxidant response elements. *European journal of pharmacology* **682**, 12–20 (2012).
230. Gogvadze, N. *et al.* Sigma-1 Receptor Agonists Induce Oxidative Stress in Mitochondria and Enhance Complex I Activity in Physiological Condition but Protect Against Pathological Oxidative Stress. *Neurotoxicity Research* **35**, 1–18 (2019).
231. Entrena, J. M. *et al.* Sigma-1 Receptor Agonism Promotes Mechanical Allodynia After Priming the Nociceptive System with Capsaicin. *Sci Rep* **6**, 1–12.
232. Entrena, J. M. *et al.* Antagonism by haloperidol and its metabolites of mechanical hypersensitivity induced by intraplantar capsaicin in mice: role of sigma-1 receptors. *Psychopharmacology* **205**, 21–33 (2009).
233. Lolignier, S. *et al.* Mechanical allodynia. *Pflugers Arch - Eur J Physiol* **467**, 133–139 (2015).
234. Matsumoto, R. R. *et al.* Conformationally restricted analogs of BD1008 and an antisense oligodeoxynucleotide targeting σ<sub>1</sub> receptors produce anti-cocaine effects in mice. *European journal of pharmacology* **419**, 163–174 (2001).
235. Powell, N. A. *et al.* Optimization of highly selective 2,4-diaminopyrimidine-5-carboxamide inhibitors of Sky kinase. *Bioorganic & medicinal chemistry letters* **23**, 1051–1055 (2013).
236. Qin, Q. *et al.* Discovery of 2,4-diaminopyrimidine derivatives targeting p21-activated kinase 4: Biological evaluation and docking studies. *Archiv der Pharmazie*, e2000097 (2020).
237. Párrizas, M. *et al.* Specific inhibition of insulin-like growth factor-1 and insulin receptor tyrosine kinase activity and biological function by tyrphostins. *Endocrinology* **138**, 1427–1433 (1997).
238. Wilson, C. *et al.* ALK and IGF-1R as independent targets in crizotinib resistant lung cancer. *Sci Rep* **7**, 13955 (2017).
239. Wittman, M. *et al.* Discovery of a 1 H -Benzoimidazol-2-yl)-1 H -pyridin-2-one (BMS-536924) Inhibitor of Insulin-like Growth Factor I Receptor Kinase with in Vivo Antitumor Activity. *J. Med. Chem.* **48**, 5639–5643 (2005).
240. Carboni, J. M. *et al.* BMS-754807, a small molecule inhibitor of insulin-like growth factor-1R/IR. *Molecular cancer therapeutics* **8**, 3341–3349 (2009).
241. Sabbatini, P. *et al.* GSK1838705A inhibits the insulin-like growth factor-1 receptor and anaplastic lymphoma kinase and shows antitumor activity in experimental models of human cancers. *Molecular cancer therapeutics* **8**, 2811–2820 (2009).
242. Mitsiades, C. S. *et al.* Inhibition of the insulin-like growth factor receptor-1 tyrosine kinase activity as a therapeutic strategy for multiple myeloma, other hematologic malignancies, and solid tumors. *Cancer Cell* **5**, 221–230 (2004).
243. García-Echeverría, C. *et al.* In vivo antitumor activity of NVP-AEW541—A novel, potent, and selective inhibitor of the IGF-IR kinase. *Cancer Cell* **5**, 231–239 (2004).
244. Mulvihill, M. J. *et al.* Discovery of OSI-906: a selective and orally efficacious dual inhibitor of the IGF-1 receptor and insulin receptor. *Future medicinal chemistry* **1**, 1153–1171 (2009).
245. Gable, K. L. *et al.* Diarylureas are small-molecule inhibitors of insulin-like growth factor I receptor signaling and breast cancer cell growth. *Molecular cancer therapeutics* **5**, 1079–1086 (2006).

246. Quinlan, C. L. *et al.* The 2-oxoacid dehydrogenase complexes in mitochondria can produce superoxide/hydrogen peroxide at much higher rates than complex I. *J. Biol. Chem.* **289**, 8312–8325 (2014).
247. Bonnet, S. *et al.* A mitochondria-K<sup>+</sup> channel axis is suppressed in cancer and its normalization promotes apoptosis and inhibits cancer growth. *Cancer Cell* **11**, 37–51 (2007).
248. Morrell, J. A. *et al.* AZD7545 is a selective inhibitor of pyruvate dehydrogenase kinase 2. *Biochem Soc Trans* **31**, 1168–1170 (2003).
249. Tso, S.-C. *et al.* Structure-guided development of specific pyruvate dehydrogenase kinase inhibitors targeting the ATP-binding pocket. *J. Biol. Chem.* **289**, 4432–4443 (2014).
250. Campos, C. *et al.* Evaluation of the copper(II) reduction assay using bathocuproinedisulfonic acid disodium salt for the total antioxidant capacity assessment: The CUPRAC–BCS assay. *Analytical Biochemistry* **392**, 37–44 (2009).
251. Smith, G. C.M. *et al.* in *Handbook of cell signaling*, edited by R. A. Bradshaw & E. A. Dennis (Elsevier/Academic Press, Amsterdam, Boston, 2010), Vol. 2, pp. 575–580.
252. Perry, J. *et al.* The ATRs, ATMs, and TORs Are Giant HEAT Repeat Proteins. *Cell* **112**, 151–155 (2003).
253. Yoshimura, S. H. *et al.* HEAT repeats – versatile arrays of amphiphilic helices working in crowded environments? *J Cell Sci* **129**, 3963–3970 (2016).
254. The UniProt Consortium. UniProt: a worldwide hub of protein knowledge. *Nucleic Acids Res* **47**, D506–D515 (2019).
255. Tsang, C. K. *et al.* SOD1 Phosphorylation by mTORC1 Couples Nutrient Sensing and Redox Regulation. *Molecular Cell* **70**, 502–515.e8 (2018).
256. Edwards, S. R. *et al.* The Rapamycin-binding Domain of the Protein Kinase Mammalian Target of Rapamycin Is a Destabilizing Domain. *J. Biol. Chem.* **282**, 13395–13401 (2007).
257. Liu, Q. *et al.* Discovery of 9-(6-Aminopyridin-3-yl)-1-(3-(trifluoromethyl)phenyl)benzo[h][1,6]naphthyridin-2(1H)-one (Torin2) as a Potent, Selective, and Orally Available Mammalian Target of Rapamycin (mTOR) Inhibitor for Treatment of Cancer. *Journal of Medicinal Chemistry* **54**, 1473–1480 (2011).
258. Siegel, D. *et al.* NAD(P)H:quinone oxidoreductase 1: role as a superoxide scavenger. *Molecular pharmacology* **65**, 1238–1247 (2004).
259. Juarez, J. C. *et al.* Copper binding by tetrathiomolybdate attenuates angiogenesis and tumor cell proliferation through the inhibition of superoxide dismutase 1. *Clinical cancer research : an official journal of the American Association for Cancer Research* **12**, 4974–4982 (2006).
260. Horning, B. D. *et al.* Chemical Proteomic Profiling of Human Methyltransferases. *Journal of the American Chemical Society* **138**, 13335–13343 (2016).
261. Savitski, M. M. *et al.* Measuring and Managing Ratio Compression for Accurate iTRAQ/TMT Quantification. *Journal of Proteome Research* **12**, 3586–3598 (2013).
262. Lau, L. F. CCN1/CYR61: the very model of a modern matricellular protein. *Cellular and molecular life sciences : CMLS* **68**, 3149–3163 (2011).
263. Xu, H. *et al.* Acyl-CoA synthetase short-chain family member 2 (ACSS2) is regulated by SREBP-1 and plays a role in fatty acid synthesis in caprine mammary epithelial cells. *Journal of cellular physiology* **233**, 1005–1016 (2018).
264. Fink, M. *et al.* Cholesterogenic lanosterol 14 $\alpha$ -demethylase (CYP51) is an immediate early response gene. *Endocrinology* **146**, 5321–5331 (2005).
265. Prabhu, A. V. *et al.* The sterol-based transcriptional control of human 7-dehydrocholesterol reductase (DHCR7): Evidence of a cooperative regulatory program in cholesterol synthesis. *Biochimica et biophysica acta* **1842**, 1431–1439 (2014).
266. Lewis, C. A. *et al.* SREBP maintains lipid biosynthesis and viability of cancer cells under lipid- and oxygen-deprived conditions and defines a gene signature associated with poor survival in glioblastoma multiforme. *Oncogene* **34**, 5128–5140 (2015).
267. Dong, X. *et al.* Regulation of FADS2 transcription by SREBP-1 and PPAR- $\alpha$  influences LC-PUFA biosynthesis in fish. *Sci Rep* **7**, 40024 (2017).
268. Ericsson, J. *et al.* Synergistic binding of sterol regulatory element-binding protein and NF-Y to the farnesyl diphosphate synthase promoter is critical for sterol-regulated expression of the gene. *The Journal of biological chemistry* **271**, 24359–24364 (1996).



269. Dooley, K. A. *et al.* Sterol regulation of 3-hydroxy-3-methylglutaryl-coenzyme A synthase gene through a direct interaction between sterol regulatory element binding protein and the trimeric CCAAT-binding factor/nuclear factor Y. *The Journal of biological chemistry* **273**, 1349–1356 (1998).
270. Sakakura, Y. *et al.* Sterol regulatory element-binding proteins induce an entire pathway of cholesterol synthesis. *Biochemical and biophysical research communications* **286**, 176–183 (2001).
271. Streicher, R. *et al.* SREBP-1 mediates activation of the low density lipoprotein receptor promoter by insulin and insulin-like growth factor-I. *The Journal of biological chemistry* **271**, 7128–7133 (1996).
272. Sharpe, L. J. *et al.* Controlling cholesterol synthesis beyond 3-hydroxy-3-methylglutaryl-CoA reductase (HMGCR). *J. Biol. Chem.* **288**, 18707–18715 (2013).
273. Lagace, T. A. PCSK9 and LDLR degradation: regulatory mechanisms in circulation and in cells. *Current opinion in lipidology* **25**, 387–393 (2014).
274. Tabor, D. E. *et al.* Identification of conserved cis-elements and transcription factors required for sterol-regulated transcription of stearyl-CoA desaturase 1 and 2. *The Journal of biological chemistry* **274**, 20603–20610 (1999).
275. Guan, G. *et al.* Differential transcriptional regulation of the human squalene synthase gene by sterol regulatory element-binding proteins (SREBP) 1a and 2 and involvement of 5' DNA sequence elements in the regulation. *The Journal of biological chemistry* **273**, 12526–12535 (1998).
276. Bartz, F. *et al.* Identification of cholesterol-regulating genes by targeted RNAi screening. *Cell metabolism* **10**, 63–75 (2009).
277. Kuzu, O. F. *et al.* Effect of lysosomotropic molecules on cellular homeostasis. *Pharmacological research* **117**, 177–184 (2017).
278. Blazek, M. *et al.* Analysis of fast protein phosphorylation kinetics in single cells on a microfluidic chip. *Lab on a chip* **15**, 726–734 (2015).
279. Li, M. *et al.* The myeloid leukemia-associated protein SET is a potent inhibitor of protein phosphatase 2A. *The Journal of biological chemistry* **271**, 11059–11062 (1996).
280. Junttila, M. R. *et al.* CIP2A inhibits PP2A in human malignancies. *Cell* **130**, 51–62 (2007).
281. Seshacharyulu, P. *et al.* Phosphatase: PP2A structural importance, regulation and its aberrant expression in cancer. *Cancer Letters* **335**, 9–18 (2013).
282. Lu, Q. *et al.* Regulation of Estrogen Receptor  $\alpha$ -mediated Transcription by a Direct Interaction with Protein Phosphatase 2A. *J. Biol. Chem.* **278**, 4639–4645 (2003).
283. Ramos, F. *et al.* Role of protein phosphatases PP1, PP2A, PP4 and Cdc14 in the DNA damage response. *CST* **3**, 70–85 (2019).
284. Margolis, S. S. *et al.* Role for the PP2A/B56delta phosphatase in regulating 14-3-3 release from Cdc25 to control mitosis. *Cell* **127**, 759–773 (2006).
285. Ahn, J.-H. *et al.* Protein kinase A activates protein phosphatase 2A by phosphorylation of the B56 subunit. *J Biochem* **104**, 2979–2984 (2007).
286. Nobumori, Y. *et al.* HEAT Repeat 1 Motif Is Required for B56 $\gamma$ -containing Protein Phosphatase 2A (B56 $\gamma$ -PP2A) Holoenzyme Assembly and Tumor-suppressive Function. *J. Biol. Chem.* **287**, 11030–11036 (2012).
287. Ohama, T. The multiple functions of protein phosphatase 6. *Biochimica et Biophysica Acta (BBA) - Molecular Cell Research* **1866**, 74–82 (2019).
288. Tsang, C. K. *et al.* Superoxide dismutase 1 acts as a nuclear transcription factor to regulate oxidative stress resistance. *Nat Commun* **5**, 1–11.
289. Bordoni, M. *et al.* Nuclear Phospho-SOD1 Protects DNA from Oxidative Stress Damage in Amyotrophic Lateral Sclerosis. *Journal of clinical medicine* **8** (2019).
290. Freeman, A. K. *et al.* Negative regulation of CHK2 activity by protein phosphatase 2A is modulated by DNA damage. *Cell cycle (Georgetown, Tex.)* **9**, 736–747 (2010).
291. Zanoni, M. *et al.* 3D tumor spheroid models for in vitro therapeutic screening: a systematic approach to enhance the biological relevance of data obtained. *Scientific Reports* **6**, 1–11 (2016).
292. Belmokhtar, C. A. *et al.* Staurosporine induces apoptosis through both caspase-dependent and caspase-independent mechanisms. *Oncogene* **20**, 3354–3362 (2001).
293. Jiang, X. *et al.* Quantitative Imaging of Glutathione in Live Cells Using a Reversible Reaction-Based Ratiometric Fluorescent Probe. *ACS Chemical Biology* **10**, 864–874 (2015).

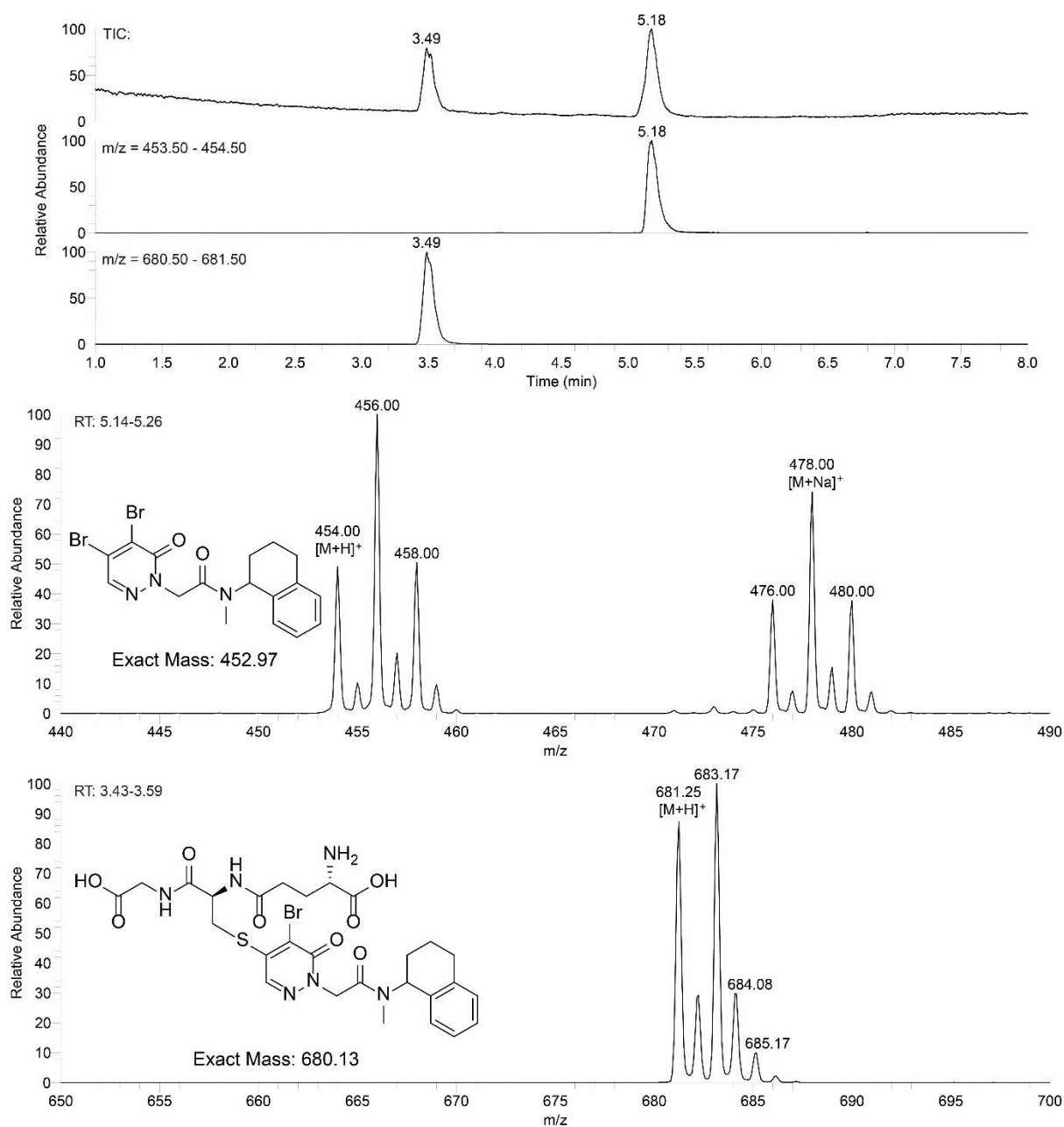
294. Xu, K. *et al.* Involvement of glutathione metabolism in the cytotoxicity of the phenethyl isothiocyanate and its cysteine conjugate to human leukaemia cells in vitro. *Biochemical Pharmacology* **61**, 165–177 (2001).
295. Bartels, P. G. *et al.* Inhibition of Carotenoid Synthesis by Fluridone and Norflurazon. *Weed Science* **26**, 198–203 (1978).
296. Somwar, R. *et al.* Identification and preliminary characterization of novel small molecules that inhibit growth of human lung adenocarcinoma cells. *Journal of biomolecular screening* **14**, 1176–1184 (2009).
297. Somwar, R. *et al.* Superoxide dismutase 1 (SOD1) is a target for a small molecule identified in a screen for inhibitors of the growth of lung adenocarcinoma cell lines. *Proceedings of the National Academy of Sciences of the United States of America* **108**, 16375–16380 (2011).
298. Landeta, C. *et al.* Compounds targeting disulfide bond forming enzyme DsbB of Gram-negative bacteria. *Nat Chem Biol* **11**, 292–298 (2015).
299. Ma, Y. *et al.* Novel CHOP activator LGH00168 induces necroptosis in A549 human lung cancer cells via ROS-mediated ER stress and NF- $\kappa$ B inhibition. *Acta Pharmacol Sin* **37**, 1381–1390 (2016).
300. Fayad, W. *et al.* Identification of Agents that Induce Apoptosis of Multicellular Tumour Spheroids: Enrichment for Mitotic Inhibitors with Hydrophobic Properties. *Chemical Biology & Drug Design* **78**, 547–557 (2011).
301. Lattmann, E. *et al.* Synthesis and evaluation of 5 - arylated 2(5H) - furanones and 2 - arylated pyridazin - 3(2H) - ones as anti - cancer agents. *Journal of Pharmacy and Pharmacology* **55**, 1259–1265 (2003).
302. Vandekerckhove, S. *et al.* Synthesis and antiplasmodial evaluation of aziridine –(iso)quinoline hybrids and their ring-opening products. *MedChemComm* **4**, 724–730 (2013).
303. Kaminski, J. *et al.* Microwave - Assisted Synthesis and Antiprotozoal Activity of Pyridazines Carrying Polyfluoro Substituents. *Synthetic Communications* **36**, 2719–2725 (2006).
304. Rao, K. S. *et al.* A Collection of Guinea Pig Sensitization Test Results — Grouped by Chemical Class. *Drug and Chemical Toxicology* **4**, 331–351 (1981).
305. Lynch, R. E. *et al.* Permeation of the erythrocyte stroma by superoxide radical. *J. Biol. Chem.* **253**, 4697–4699 (1978).
306. Hawkins, B. J. *et al.* Superoxide flux in endothelial cells via the chloride channel-3 mediates intracellular signaling. *Molecular biology of the cell* **18**, 2002–2012 (2007).
307. Kono, Y. *et al.* Superoxide radical inhibits catalase. *The Journal of biological chemistry* **257**, 5751–5754 (1982).
308. Blum, J. *et al.* Inactivation of glutathione peroxidase by superoxide radical. *Archives of Biochemistry and Biophysics* **240**, 500–508 (1985).
309. Zhu, H. *et al.* The highly expressed and inducible endogenous NAD(P)H:quinone oxidoreductase 1 in cardiovascular cells acts as a potential superoxide scavenger. *Cardiovascular toxicology* **7**, 202–211 (2007).
310. Collin, F. Chemical Basis of Reactive Oxygen Species Reactivity and Involvement in Neurodegenerative Diseases. *International journal of molecular sciences* **20** (2019).
311. Banks, W. A. *et al.* Small molecules as central nervous system therapeutics: old challenges, new directions, and a philosophic divide. *Future medicinal chemistry* **11**, 489–493 (2019).
312. Marceau, F. *et al.* Cation trapping by cellular acidic compartments: Beyond the concept of lysosomotropic drugs. *Toxicology and Applied Pharmacology* **259**, 1–12 (2012).
313. Gustafsdottir, S. M. *et al.* Multiplex Cytological Profiling Assay to Measure Diverse Cellular States. *PLOS ONE* **8**, e80999 (2013).
314. Agard, N. J. *et al.* A strain-promoted 3 + 2 azide-alkyne cycloaddition for covalent modification of biomolecules in living systems. *Journal of the American Chemical Society* **126**, 15046–15047 (2004).
315. Trinkle-Mulcahy, L. *et al.* Identifying specific protein interaction partners using quantitative mass spectrometry and bead proteomes. *J Cell Biol* **183**, 223–239 (2008).
316. González-Álvarez, M. *et al.* Mixed-ligand copper(II)-sulfonamide complexes: effect of the sulfonamide derivative on DNA binding, DNA cleavage, genotoxicity and anticancer activity. *Dalton transactions* **42**, 10244–10259 (2013).
317. Tommasino, J.-B. *et al.* Multi-biofunctional complexes combining antiseptic copper(II) with antibiotic sulfonamide ligands: Structural, redox and antibacterial study. *Polyhedron* **30**, 1663–1670 (2011).
318. Kaplan, J. H. *et al.* How Mammalian Cells Acquire Copper: An Essential but Potentially Toxic Metal. *Biophysical journal* **110**, 7–13 (2016).
319. Rae, T. D. *et al.* Undetectable intracellular free copper: the requirement of a copper chaperone for superoxide dismutase. *Science (New York, N.Y.)* **284**, 805–808 (1999).

320. Shao, S. *et al.* Structure and assembly pathway of the ribosome quality control complex. *Molecular Cell* **57**, 433–444 (2015).
321. Sato, S. *et al.* Biochemical Target Isolation for Novices: Affinity-Based Strategies. *Chemistry & Biology* **17**, 616–623 (2010).
322. O'Hare, T. *et al.* In vitro activity of Bcr-Abl inhibitors AMN107 and BMS-354825 against clinically relevant imatinib-resistant Abl kinase domain mutants. *Cancer research* **65**, 4500–4505 (2005).
323. Hargrove, J. L. *et al.* The kinetics of mammalian gene expression. *BioEssays : news and reviews in molecular, cellular and developmental biology* **13**, 667–674 (1991).
324. Obr, A. E. *et al.* Insulin-like growth factor receptor signaling in breast tumor epithelium protects cells from endoplasmic reticulum stress and regulates the tumor microenvironment. *Breast cancer research : BCR* **20**, 138 (2018).
325. Bondeson, D. P. *et al.* Targeted Protein Degradation by Small Molecules. *Annual review of pharmacology and toxicology* **57**, 107–123 (2017).
326. Rawson, R. B. The SREBP pathway—insights from Insigs and insects. *Nat Rev Mol Cell Biol* **4**, 631–640 (2003).
327. Zhitomirsky, B. *et al.* Lysosomotropic drugs activate TFEB via lysosomal membrane fluidization and consequent inhibition of mTORC1 activity. *Cell Death Dis* **9**, 1–15.
328. Peterson, T. R. *et al.* mTOR Complex 1 Regulates Lipin 1 Localization to Control the SREBP Pathway. *Cell* **146**, 408–420 (2011).
329. Giandomenico, V. *et al.* Coactivator-dependent acetylation stabilizes members of the SREBP family of transcription factors. *Molecular and cellular biology* **23**, 2587–2599 (2003).
330. Clark, A. R. *et al.* Protein phosphatase 2A as a therapeutic target in inflammation and neurodegeneration. *Pharmacology & therapeutics* **201**, 181–201 (2019).
331. Shang, Z. *et al.* DNA-PKcs activates the Chk2–Brca1 pathway during mitosis to ensure chromosomal stability. *Oncogenesis* **3**, e85–e85 (2014).
332. Wang, X. Q. *et al.* ATR dependent activation of Chk2. *Journal of cellular physiology* **208**, 613–619 (2006).
333. Meyer, C. *et al.* Are high-affinity progesterone binding site(s) from porcine liver microsomes members of the  $\sigma$  receptor family? *European journal of pharmacology* **347**, 293–299 (1998).
334. Gupta, P. *et al.* Phenethyl isothiocyanate: A comprehensive review of anti-cancer mechanisms. *Biochimica et Biophysica Acta (BBA) - Reviews on Cancer* **1846**, 405–424 (2014).
335. Jackson, P. A. *et al.* Covalent Modifiers: A Chemical Perspective on the Reactivity of  $\alpha,\beta$ -Unsaturated Carbonyls with Thiols via Hetero-Michael Addition Reactions. *Journal of Medicinal Chemistry* **60**, 839–885 (2017).
336. Aruoma, O. I. *et al.* The antioxidant action of N-acetylcysteine: Its reaction with hydrogen peroxide, hydroxyl radical, superoxide, and hypochlorous acid. *Free Radical Biology and Medicine* **6**, 593–597 (1989).
337. Gutteridge, J. M. C. Lipid peroxidation initiated by superoxide - dependent hydroxyl radicals using complexed iron and hydrogen peroxide. *FEBS Letters* **172**, 245–249 (1984).
338. Radi, R. *et al.* Peroxynitrite-induced membrane lipid peroxidation: the cytotoxic potential of superoxide and nitric oxide. *Archives of Biochemistry and Biophysics* **288** (1991).
339. Gutteridge, J. M. C. *et al.* Inhibition of the iron-catalysed formation of hydroxyl radicals from superoxide and of lipid peroxidation by desferrioxamine. *Biochem J* **184**, 469–472 (1979).
340. Pédebosq, S. *et al.* Non-Antioxidant Properties of  $\alpha$ -Tocopherol Reduce the Anticancer Activity of Several Protein Kinase Inhibitors In Vitro. *PloS one* **7**, e36811 (2012).
341. Lee, K. *et al.* The copper chelator ATN-224 induces peroxynitrite-dependent cell death in hematological malignancies. *Free Radical Biology and Medicine* **60**, 157–167 (2013).
342. Dong, X. *et al.* The rational design of specific SOD1 inhibitors via copper coordination and their application in ROS signaling research. *Chem. Sci.* **7**, 6251–6262 (2016).
343. Li, X. *et al.* The Specific Inhibition of SOD1 Selectively Promotes Apoptosis of Cancer Cells via Regulation of the ROS Signaling Network. *Oxidative Medicine and Cellular Longevity* **2019** (2019).
344. Glasauer, A. *et al.* Targeting SOD1 reduces experimental non–small-cell lung cancer. *J Clin Invest* **124**, 117–128 (2014).
345. Juarez, J. C. *et al.* Superoxide dismutase 1 (SOD1) is essential for H<sub>2</sub>O<sub>2</sub>-mediated oxidation and inactivation of phosphatases in growth factor signaling. *PNAS* **105**, 7147–7152 (2008).
346. Juarez, J. C. *et al.* Copper Binding by Tetrathiomolybdate Attenuates Angiogenesis and Tumor Cell Proliferation through the Inhibition of Superoxide Dismutase 1. *Clin Cancer Res* **12**, 4974–4982 (2006).

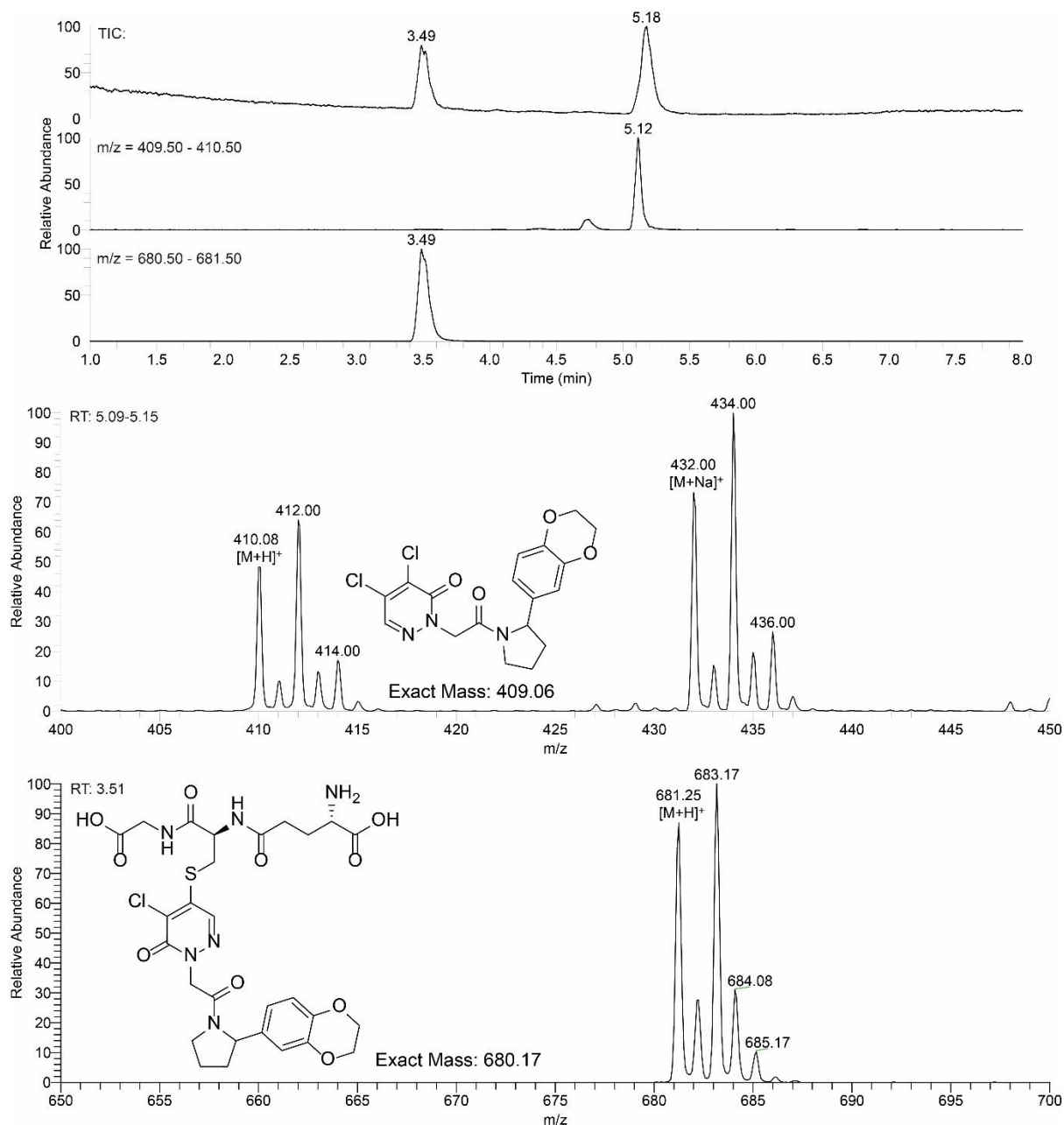
347. Lin, J. *et al.* A non-comparative randomized phase II study of 2 doses of ATN-224, a copper/zinc superoxide dismutase inhibitor, in patients with biochemically recurrent hormone-naïve prostate cancer. *Urologic Oncology: Seminars and Original Investigations* **31**, 581–588 (2013).
348. Pontén, F. *et al.* The Human Protein Atlas - a tool for pathology. *The Journal of Pathology* **216**, 387–393 (2008).

## 9 Appendix

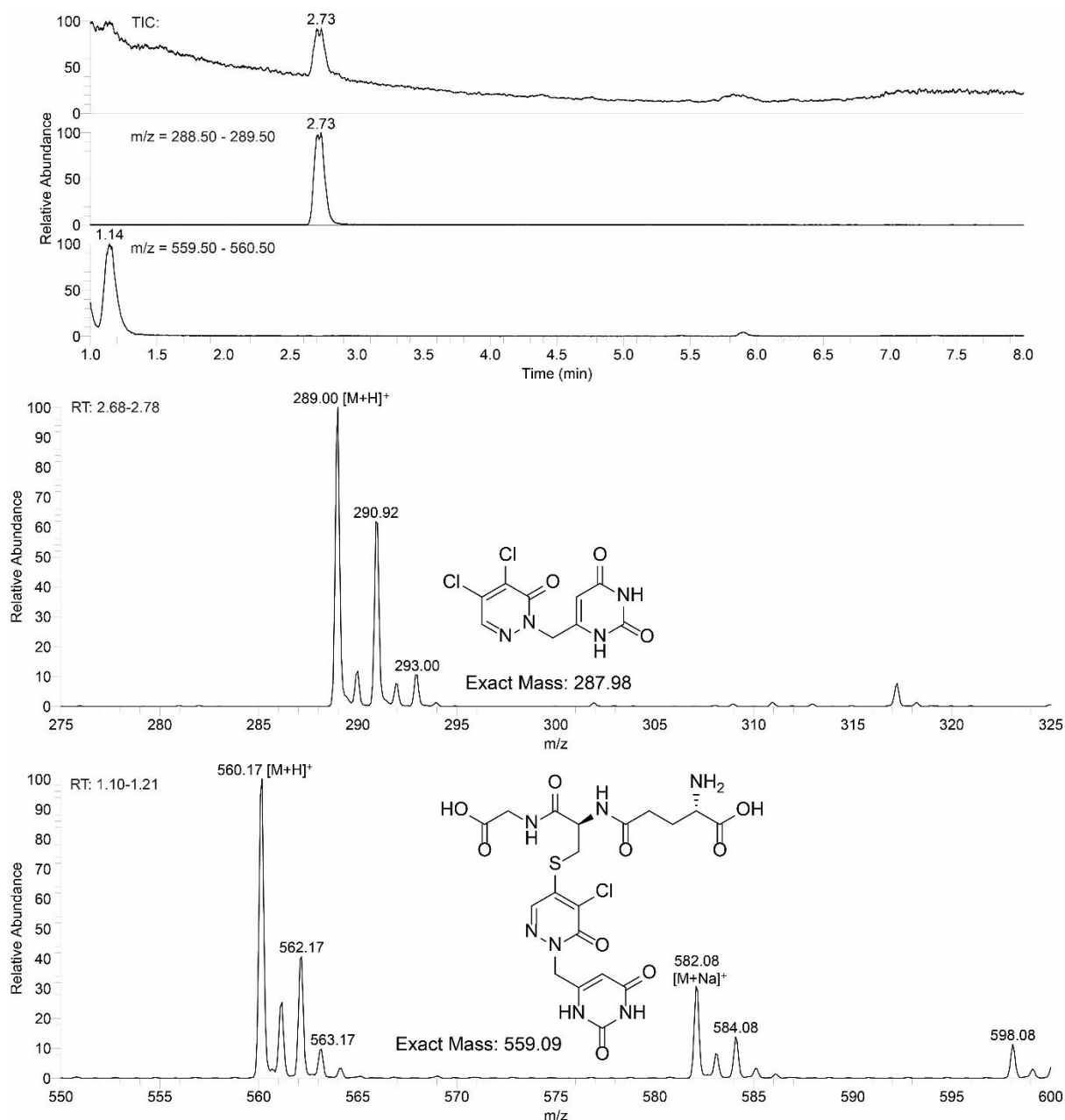
### 9.1 Supplementary data



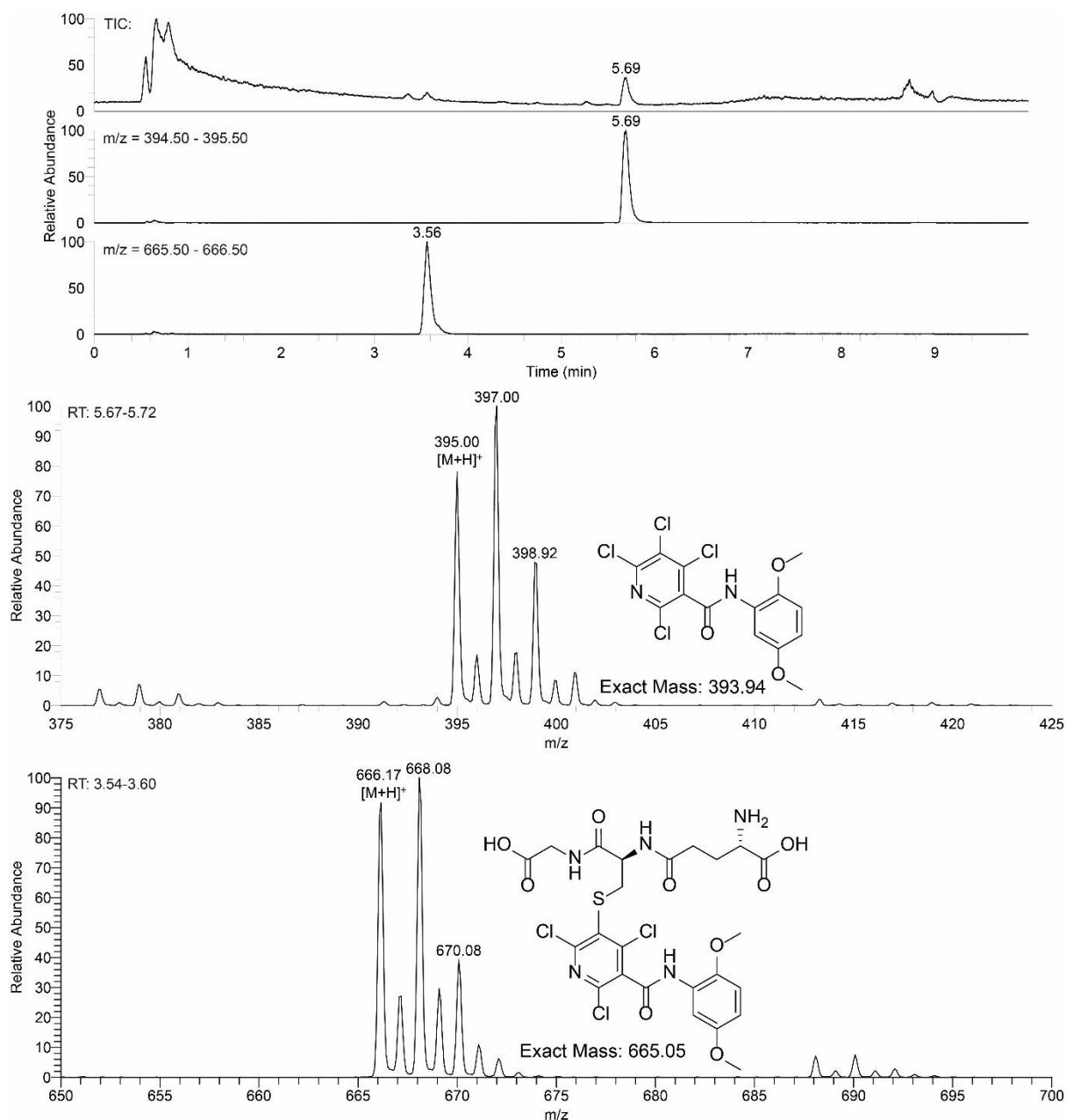
**Supplementary Figure 1: DHMP-1 reacts spontaneously with GSH in solution.** 100  $\mu$ M DHMP-1 was incubated in PBS for 1 h at 37  $^{\circ}$ C in the presence or absence of GSH (5 mM) and analyzed via HPLC-MS. Liquid chromatograms (C18 column; buffer A: H<sub>2</sub>O + 0.1 % formic acid; buffer B: acetonitrile + 0.1 % formic acid; 10-95 % gradient in 5 min) and mass spectra of DHMP-1 and its putative GSH-conjugate shown. Only one possible GSH conjugate is shown for each compound.



**Supplementary Figure 2: DHMP-2 reacts spontaneously with GSH in solution.** 100  $\mu$ M DHMP-2 was incubated in PBS for 1 h at 37  $^{\circ}$ C in the presence or absence of GSH (5 mM) and analyzed via HPLC-MS. Liquid chromatograms (C18 column; buffer A: H<sub>2</sub>O + 0.1 % formic acid; buffer B: acetonitrile + 0.1 % formic acid; 10-95 % gradient in 5 min) and mass spectra of DHMP-2 and its putative GSH-conjugate shown. Only one possible GSH conjugate is shown for each compound.

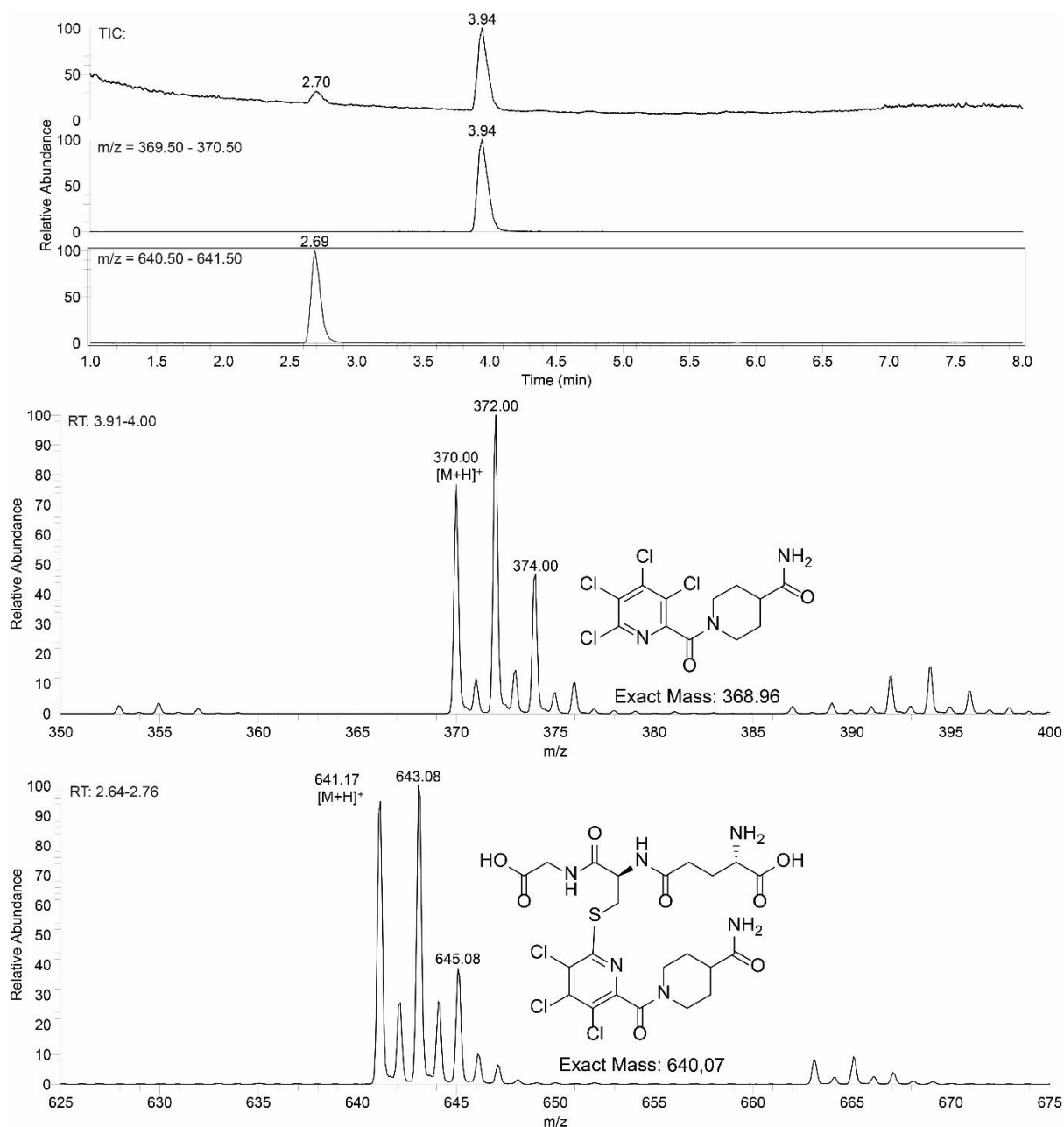


**Supplementary Figure 3: DHMP-3 reacts spontaneously with GSH in solution.** 100  $\mu$ M DHMP-3 was incubated in PBS for 1 h at 37  $^{\circ}$ C in the presence or absence of GSH (5 mM) and analyzed via HPLC-MS. Liquid chromatograms (C18 column; buffer A: H<sub>2</sub>O + 0.1 % formic acid; buffer B: acetonitrile + 0.1 % formic acid; 10-95 % gradient in 5 min) and mass spectra of DHMP-3 and its putative GSH-conjugate shown. Only one possible GSH conjugate is shown for each compound.

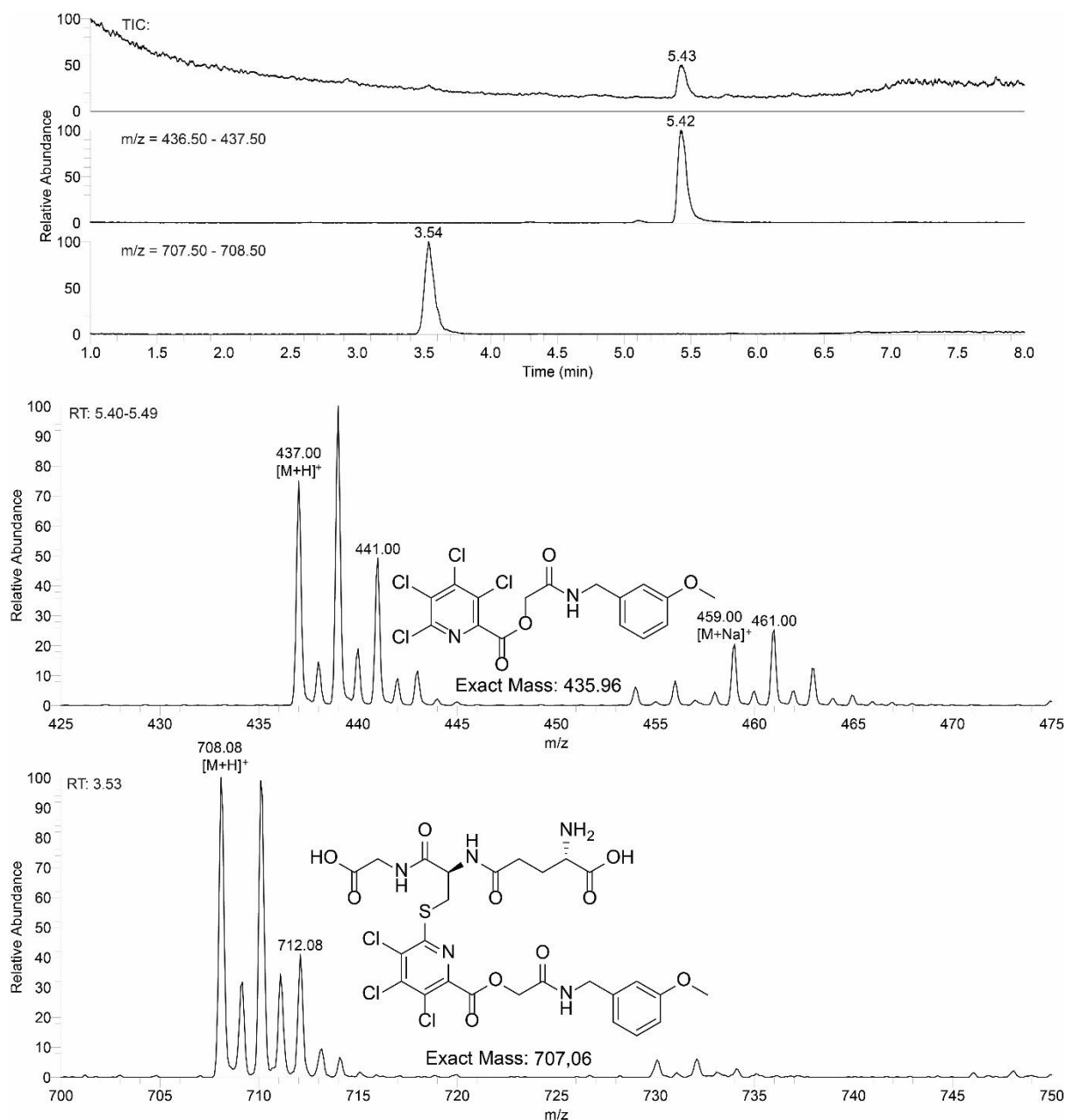


**Supplementary Figure 4: TCMP-1 reacts spontaneously with GSH in solution.** 100  $\mu\text{M}$  TCMP-1 was incubated in PBS for 1 h at 37  $^{\circ}\text{C}$  in the presence or absence of GSH (5 mM) and analyzed via HPLC-MS. Liquid chromatograms (C18 column; buffer A:  $\text{H}_2\text{O}$  + 0.1 % formic acid; buffer B: acetonitrile + 0.1 % formic acid; 10-95 % gradient in 5 min) and mass spectra of TCMP-1 and its putative GSH-conjugate shown. Only one possible GSH conjugate is shown for each compound.





**Supplementary Figure 5: TCMP-2 reacts spontaneously with GSH in solution.** 100  $\mu$ M TCMP-2 was incubated in PBS for 1 h at 37  $^{\circ}$ C in the presence or absence of GSH (5 mM) and analyzed via HPLC-MS. Liquid chromatograms (C18 column; buffer A: H<sub>2</sub>O + 0.1 % formic acid; buffer B: acetonitrile + 0.1 % formic acid; 10-95 % gradient in 5 min) and mass spectra of TCMP-2 and its putative GSH-conjugate shown. Only one possible GSH conjugate is shown for each compound.



**Supplementary Figure 6: TCMP-3 reacts spontaneously with GSH in solution.** 100  $\mu\text{M}$  TCMP-3 was incubated in PBS for 1 h at 37  $^{\circ}\text{C}$  in the presence or absence of GSH (5 mM) and analyzed via HPLC-MS. Liquid chromatograms (C18 column; buffer A:  $\text{H}_2\text{O}$  + 0.1 % formic acid; buffer B: acetonitrile + 0.1 % formic acid; 10-95 % gradient in 5 min) and mass spectra of TCMP-3 and its putative GSH-conjugate shown. Only one possible GSH conjugate is shown for each compound.

```

Query      1  MATKAVCVLKGDPVQGIINFEQKESNGPVKVWGSIKGLTEGLHGFHVHEFGDNTAGCTS  60
          MATKAVCVLKGDPVQG I+FE K      V V GSI GLTEG HGFHVH+FGDNT GCTS
Subject    1  MATKAVCVLKGDPVQGTIIHFEAKGDT--VVVTGSITGLTEGDHGFHVHQFGDNTQGCTS  58

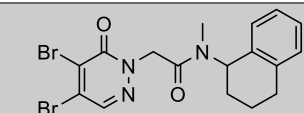
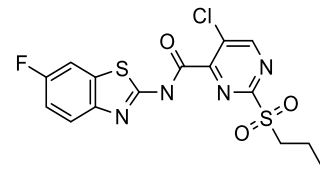
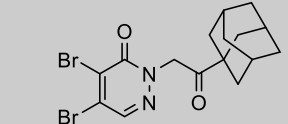
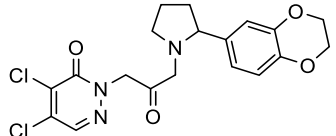
Query     61  AGPHFNPLSRKHGGPKDEERHVGD LGNVTADKDG VADVSIEDSVISLSGDHCIIGRTL VV 120
          AGPHFNPLS+KHGGPKDEERHVGD LGNVTADK+GVA V I D +ISLSG++ IIGRT+VV
Subject   59  AGPHFNPLSKKHGGPKDEERHVGD LGNVTADKNGVAIVDIVDPLISLSGEYSIIGRTMVV 118

Query    121  HEKADDLKGKGGNEESTKKTGNAGSRLACGVIGIAQ  154
          HEK DDLG+GGNEESTKKTGNAGSRLACGVIGIA+
Subject  119  HEKPDDLGRGGNEESTKKTGNAGSRLACGVIGIAK  152

```

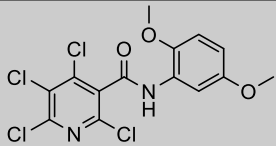
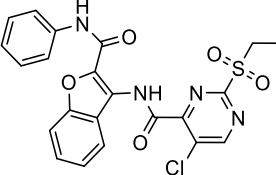
**Supplementary Figure 7: Protein sequence alignment of human and bovine SOD1.** Sequence alignment of human SOD1 (Uniprot ID: P00441) and bovine SOD1 (P00442) using Standard Protein BLAST (blast.ncbi.nlm.nih.gov) with a blastp algorithm. Range 1 to 152, Score: 246 bits (628), identities: 126/154 (82 %), positives: 136/154 (88 %) and gaps 2/154 (1 %).

**Supplementary Table 1: Most potent GSH-depleting compounds identified during the screening campaign for ROS-inducing small molecules.** The thirty most potent GSH-depleting compounds among the 704 preliminary screening hits are listed. ROS activity was determined after 90 min of compound incubation in U-2 OS cells and normalized to values of DMSO (0 %) and 10  $\mu$ M CDNB (100 %), N = 1, n = 1. GSH content relative to cells treated with DMSO (100 %) was determined after 120 min compound incubation in U-2 OS cells, N = 1, n = 1. Data were obtained by COMAS, Dortmund.

ID	Chemical structure	ROS activity [%]	GSH content [%]
158885		60	9.6
206181		97	11.2
153177		88	13.2
133479		163	19.2

ID	Chemical structure	ROS activity [%]	GSH content [%]
156807		67	20.4
183903		82	22.3
136450		79	22.6
206178		130	23.2
122281		55	24.2
141065		129	24.3
105833		110	24.4
118007		116	25.5
162152		52	29.5
191284		87	30.4
206170		107	30.7
161932		98	30.8

ID	Chemical structure	ROS activity [%]	GSH content [%]
109511		113	31.0
154954		111	31.9
128407		100	32.8
208036		92	34.3
154261		104	35.3
129456		95	35.5
154733		75	35.8
191285		91	36.1
208117		106	37.2
113130		77	37.5
206172		127	37.5
129559		70	38.9

ID	Chemical structure	ROS activity [%]	GSH content [%]
191462		69	39.3
206175		83	39.6

**Supplementary Table 2: Cell Painting assay reference list for DP68.** List of all reference compounds that displayed a profile similarity >85 % to the profile obtained for DP68 at 1  $\mu\text{M}$  with an induction range between 5-85 % and a cell count >80 % are shown. For each compound only the profile with the highest similarity values is listed. ROS inducing activity at 10  $\mu\text{M}$  in the U-2 OS cell-based screening is listed, N = 1, n = 1. n.d. = not determined. Data were obtained by COMAS, Dortmund.

Well ID	Trivial name	Concentration [ $\mu\text{M}$ ]	Cell Count [%]	Induction [%]	Similarity [%]	ROS induction [%]
247234:02:03_10.00	Promazine hydrochloride	10	101	24.5	94.1	9
280128:01:07_01.00	U-73343	1	101	27.1	94.1	10
392731:01:09_02.00	EHop-016	2	101	61.5	94.1	n.d.
247108:01:07_03.00	Clomiphene citrate (Z,E)	3	99	60.6	94.0	1
245492:03:03_10.00	Haloperidol	10	93	68.4	93.9	-1
347246:01:08_01.00	SB 216641	1	94	44.7	93.9	n.d.
410921:01:03_02.00	MI-463	2	106	76.2	93.9	n.d.
280575:01:09_01.00	GR 127935 hydrochloride	1	99	40.9	93.8	20
280492:01:03_10.00	Dilazep hydrochloride	10	91	72.7	93.8	19
247045:01:04_30.00	Ifenprodil tartrate	30	107	37.7	93.6	-1
247331:01:04_30.00	Ethopropazine hydrochloride	30	97	54.2	93.5	7
280968:01:03_10.00	Trifluoperidol hydrochloride	10	91	35.8	93.5	-3
280581:01:03_10.00	GBR-12935 dihydrochloride	10	94	32.6	93.5	13
246746:01:04_30.00	Cyproheptadine hydrochloride	30	99	67.9	93.4	0
247369:02:05_01.00	Fluspirilene, R 6218	1	108	29.9	93.4	28
280177:01:03_10.00	Aprindine hydrochloride	10	100	32.1	93.4	9
407863:01:06_01.00	AZ82	1	98	29.5	93.4	n.d.
247165:02:03_10.00	Fluoxetine hydrochloride	10	101	47.5	93.3	5
246344:01:04_30.00	Drofenine hydrochloride	30	98	63.6	93.2	16
246940:01:04_30.00	Alverine citrate	30	96	40.9	93.2	-3
247164:01:04_10.00	Bromperidol	10	101	60.1	93.2	14

Well ID	Trivial name	Concentration [ $\mu$ M]	Cell Count [%]	Induction [%]	Similarity [%]	ROS induction [%]
280104:01:03_10.00	N-Desmethylozapine	10	98	40.1	93.0	1
280161:01:03_10.00	LP 12 hydrochloride hydrate	10	101	41.3	93.0	-5
350306:01:04_03.00	SAG	3	97	43.9	93.0	n.d.
247177:02:03_10.00	Triflupromazine hydrochloride	10	100	45.3	92.9	6
280850:01:03_10.00	Propionylpromazine hydrochloride	10	90	43.2	92.8	29
280639:01:03_30.00	ML-7	30	108	57.9	92.6	-2
409887:01:03_03.00	DDR1-IN-1 (hydrat)	3	96	73.2	92.6	n.d.
409831:02:03_02.00	JQEZ5	2	100	55.4	92.6	n.d.
382185:04:03_10.00	Aumitin	10	93	69.8	92.6	n.d.
246739:01:09_01.00	Sertraline	1	102	14.0	92.6	2
245383:02:04_30.00	Xylometazoline hydrochloride	30	102	16.8	92.5	8
247242:01:04_30.00	Diphenylpyraline hydrochloride	30	98	27.3	92.5	-1
391878:01:02_02.00		2	93	78.4	92.5	n.d.
409916:01:03_03.00	TP-064	3	107	22.1	92.5	n.d.
246921:01:04_30.00	Erythromycin	30	88	43.2	92.5	1
247423:01:04_30.00	Pizotyline malate	30	102	59.9	92.4	17
246405:01:04_10.00	Thiopropazine dimesylate	10	96	50.3	92.3	36
247050:03:03_10.00	Fluphenazine dihydrochloride	10	108	56.5	92.2	6
247241:01:04_30.00	Chlorcyclizine hydrochloride	30	93	51.8	92.2	-6
409870:01:02_10.00	Tazemetostat	10	99	34.2	92.2	n.d.
409883:01:02_10.00	GSK484 (hydrochloride)	10	93	58.2	92.2	n.d.
246754:01:04_30.00	Piperidolate hydrochloride	30	97	35.2	92.1	2
247196:01:04_30.00	Acepromazine maleate	30	105	63.6	92.0	1
247214:04:02_10.00	Chlorpromazine hydrochloride	10	91	43.4	92.0	10
280219:01:03_30.00	Aminobenzotropine	30	97	64.2	92.0	4
247135:02:03_10.00	Cyclobenzaprine hydrochloride	10	103	37.0	91.9	4
280121:01:03_10.00	N-Methylhistaprodifen dioxalate salt	10	86	72.7	91.9	-8
280665:01:03_10.00	L-741,626	10	106	52.8	91.9	0
392794:01:09_02.00	KN-62	2	94	40.8	91.9	n.d.
409873:01:03_01.00	LLY-507	1	100	51.6	91.9	n.d.
246604:01:04_30.00	Penbutolol sulfate	30	91	79.3	91.8	-5
246764:01:04_30.00	(S)-Propranolol hydrochloride	30	98	24.4	91.8	5
409856:02:03_02.00	GSK343	2	98	45.6	91.8	n.d.
246481:01:04_10.00	DO 897/99	10	94	56.5	91.7	-2
280918:01:08_01.00	Cortexolone maleate	1	92	16.6	91.6	17

Well ID	Trivial name	Concentration [μM]	Cell Count [%]	Induction [%]	Similarity [%]	ROS induction [%]
408212:01:06_03.00	Deltarasin	3	81	85.5	91.6	n.d.
246896:01:04_30.00	Olanzapine	30	94	39.0	91.5	15
410685:01:03_02.00	(S)-crizotinib	2	93	46.6	91.5	n.d.
410846:01:03_02.00	Tenovin-6	2	97	67.0	91.5	n.d.
247293:01:04_30.00	SKF-525A hydrochloride	30	97	68.2	91.4	15
246877:01:04_30.00	(±)-Verapamil hydrochloride	30	94	49.6	91.3	14
247251:02:03_10.00	Imipramine hydrochloride	10	100	13.1	91.3	0
246889:01:05_10.00	Loperamide hydrochloride	10	98	63.7	91.2	17
247361:01:04_30.00	Promethazine hydrochloride	30	99	57.2	91.2	8
280342:01:03_30.00	BRL 52537 hydrochloride	30	95	57.3	91.0	-3
410917:01:03_02.00	UNC 0631	2	100	38.9	90.9	n.d.
409814:01:03_03.00	MRK-740	3	108	18.0	90.9	n.d.
245373:02:04_30.00	Oxybutynin Chloride	30	94	42.8	90.8	3
246461:01:04_10.00	Dosulepin hydrochloride	10	92	24.4	90.8	6
247072:02:03_10.00	Maprotiline hydrochloride	10	97	36.6	90.8	2
246828:02:03_10.00	Carvedilol	10	104	56.0	90.7	5
246988:01:04_30.00	Orphenadrine hydrochloride	30	102	25.7	90.7	6
280718:01:10_03.00	Metergoline	3	103	24.4	90.7	8
246631:01:04_30.00	Pirlindole mesylate	30	96	21.2	90.7	11
280789:01:03_10.00	(±)-Octoclothebin maleate	10	103	52.3	90.6	16
409918:01:02_10.00	GSK6853	10	91	49.9	90.6	n.d.
247425:01:04_30.00	Fluvoxamine maleate	30	97	35.6	90.6	5
280751:01:03_30.00	Naltrindole hydrochloride	30	105	37.1	90.5	7
410147:01:04_06.00	Ozanimod (RPC1063)	6	98	78.1	90.5	n.d.
287906:02:15_30.00	Pipinib	30	91	65.3	90.4	-20
409849:01:04_01.00	UNC0638	1	96	55.4	90.4	n.d.
246456:01:04_10.00	Cisapride	10	97	35.8	90.3	28
351488:03:09_10.00	MK-2206 2HCl	10	89	71.8	90.3	n.d.
392584:01:09_02.00	NVP-BHG712	2	100	48.0	90.3	
246784:01:04_10.00	Azelastine hydrochloride	10	94	56.1	90.2	16
280690:01:03_10.00	Methiothepin mesylate	10	97	53.4	90.2	15
409908:01:04_03.00	Bafetinib	3	97	68.7	90.2	n.d.
411147:01:03_10.00	BLU-285	10	98	75.1	90.2	n.d.
410868:01:03_00.20	MI-503	0.2	100	36.1	90.2	n.d.
247307:02:03_10.00	Trimipramine maleate	10	94	13.8	90.2	7
246478:01:04_30.00	Mesoridazine besylate	30	100	42.3	90.1	7



Well ID	Trivial name	Concentration [µM]	Cell Count [%]	Induction [%]	Similarity [%]	ROS induction [%]
280321:01:03_10.00	BW 723C86	10	102	33.2	90.1	3
280944:01:03_10.00	SKF 95282 dimaleate	10	96	48.7	90.1	-10
246897:02:03_30.00	Opipramol, dihydrochloride	30	92	60.1	90.0	-1
280660:01:03_10.00	L-703,606, oxalate	10	86	63.9	90.0	43
246567:01:04_10.00	Deptropine citrate	10	103	36.3	90.0	23
412258:01:03_10.00	ACBI1	10	101	50.4	90.0	n.d.
280767:01:03_30.00	NAN-190 hydrobromide	30	106	16.9	89.9	5
410043:01:04_00.60	ERK5-IN-1	0.6	107	50.9	89.9	n.d.
281022:01:03_30.00	(-)-cis-(1S,2R)-U-50488 tartrate	30	104	52.8	89.9	-2
410142:01:04_10.00	PRT-060318 2HCl	10	74	66.8	89.8	n.d.
410285:02:03_02.00	Nemiralisib, GSK2269557	2	98	43.5	89.8	n.d.
409872:01:04_30.00	GSK-LSD1 (Hydrochloride)	30	87	23.5	89.8	n.d.
410082:01:03_02.00	4-Hydroxytamoxifen	2	96	24.0	89.8	n.d.
280621:01:04_10.00	Indatraline hydrochloride	10	93	55.1	89.8	16
280438:01:03_10.00	Clemastine fumarate	10	91	52.5	89.7	8
247155:01:04_10.00	Propafenone hydrochloride	10	92	32.8	89.7	1
409861:01:04_01.00	UNC1999	1	100	47.3	89.7	n.d.
409868:01:02_10.00	OICR-9429	10	103	24.4	89.7	n.d.
247000:02:03_10.00	Nortriptyline hydrochloride	10	98	44.2	89.7	11
392624:01:09_02.00	PHA-665752	2	100	42.8	89.6	n.d.
246383:01:13_03.00	Itraconazole	3	96	73.1	89.6	10
246562:01:04_30.00	Alfadolone acetate	30	88	28.7	89.6	1
246430:01:04_10.00	Pimethixene maleate	10	94	30.4	89.5	9
246464:01:04_10.00	Metixene hydrochloride	10	100	55.3	89.5	8
280153:01:08_03.00	LP44	3	101	53.2	89.5	19
280198:01:03_10.00	GW405833 hydrochloride	10	86	50.9	89.5	39
246805:01:04_10.00	Toremifene	10	86	61.0	89.5	1
247073:01:04_10.00	Chlorprothixene hydrochloride	10	88	53.4	89.4	-2
280811:01:03_30.00	Phenamyl methanesulfonate	30	94	68.2	89.4	-2
280729:01:04_10.00	Mibefradil dihydrochloride	10	89	73.4	89.2	10
280583:01:04_10.00	Hexahydro-sila-difenidol hydrochloride	10	92	48.2	89.1	7
280874:01:09_30.00	Quinidine sulfate	30	87	66.3	89.1	7
280571:01:03_10.00	GW2974	10	103	36.4	89.1	86
409864:01:03_30.00	(R)-PFI-2	30	98	63.9	89.1	n.d.
246330:01:04_30.00	Dihydroergotamine tartrate	30	100	68.9	89.0	12

Well ID	Trivial name	Concentration [μM]	Cell Count [%]	Induction [%]	Similarity [%]	ROS induction [%]
247419:01:04_30.00	Naftopidil dihydrochloride	30	101	52.2	89.0	8
246899:02:04_10.00	Tamoxifen citrate	10	92	69.3	89.0	8
392056:01:02_02.00		2	93	73.4	89.0	n.d.
409860:01:04_01.00	UNC0642	1	93	45.8	89.0	n.d.
247122:01:14_03.00	Suloctidil	3	105	47.5	89.0	-2
280318:02:03_10.00	(±)-Butaclamol hydrochloride	10	104	43.5	88.9	-4
392545:02:03_02.00	Aurora A Inhibitor I	2	93	56.1	88.9	n.d.
246466:01:07_03.00	Terconazole	3	102	42.1	88.9	5
410714:01:03_02.00	Mardepodect (PF-2545920)	2	96	26.6	88.9	n.d.
412270:01:02_10.00	cis-ACB11	10	85	50.1	88.9	n.d.
247035:01:04_10.00	Benzydamine hydrochloride	10	103	18.7	88.8	4
247178:02:03_10.00	Pirenperone	10	104	15.2	88.8	7
280672:01:03_10.00	L-765,314	10	101	45.8	88.8	6
280360:01:03_10.00	CGS-12066A maleate	10	105	19.3	88.7	2
247346:02:03_10.00	Raloxifene hydrochloride	10	94	87.7	88.7	32
247042:02:03_10.00	Pimozide	10	92	66.8	88.6	48
410516:01:04_10.00		10	95	39.7	88.6	n.d.
281012:01:03_30.00	Tomoxetine	30	88	28.3	88.6	22
246371:01:04_30.00	Methoxy-6-harmalan	30	95	43.4	88.5	11
280097:01:03_10.00	Ebastine	10	89	63.2	88.5	9
281013:01:04_10.00	3-Tropanyl-3,5-dichlorobenzoate	10	89	35.8	88.5	1
246433:01:04_30.00	Diperodon hydrochloride	30	102	56.1	88.5	10
280215:01:03_10.00	TMB-8 hydrochloride	10	106	20.0	88.5	7
392705:02:05_03.00	JNK-IN-8	3	94	69.4	88.5	n.d.
280407:01:03_30.00	CNS-1102	30	96	53.7	88.4	10
246439:01:04_10.00	Lidoflazine	10	103	70.1	88.4	43
392479:02:03_10.00	Imatinib Mesylate (STI571)	10	90	75.5	88.4	n.d.
246895:01:04_30.00	Nylidrin	30	102	41.3	88.3	-1
280754:01:03_30.00	Naltriben methanesulfonate	30	99	82.4	88.3	-2
108102:02:03_10.00	Trequinsin hydrochloride	10	93	29.5	88.3	27
246360:01:04_30.00	Hydroxyzine dihydrochloride	30	90	37.5	88.2	3
246868:01:04_30.00	Terfenadine	30	84	80.3	88.2	0
280509:01:03_30.00	(±) trans-U-50488 methanesulfonate	30	108	68.9	88.2	10
246491:01:04_30.00	Benoxinate hydrochloride	30	103	16.1	88.2	19
382169:02:09_02.00	Ponatinib	2	63	64.6	88.2	n.d.

Well ID	Trivial name	Concentration [µM]	Cell Count [%]	Induction [%]	Similarity [%]	ROS induction [%]
392740:02:05_10.00	WZ4003	10	90	75.3	88.2	n.d.
280171:05:03_01.00	BIX01294 (hydrochloride hydrate)	1	90	53.7	88.2	38
247101:01:04_10.00	Ketoconazole	10	99	27.5	88.2	17
281030:01:03_10.00	U-74389G maleate	10	91	32.8	88.2	18
246494:01:04_30.00	Zimelidine dihydrochloride monohydrate	30	101	24.2	88.1	-3
246559:01:04_10.00	S(-)Eticlopride hydrochloride	10	93	47.2	88.1	-3
410083:01:03_02.00	Endoxifen HCl	2	94	37.8	88.1	n.d.
247014:02:03_10.00	Clomipramine hydrochloride	10	94	53.7	88.1	0
247033:02:03_10.00	Trazodone hydrochloride	10	101	17.4	88.1	-3
280802:01:03_30.00	(±)-PPHT hydrochloride	30	95	44.0	88.0	6
245325:02:04_30.00	Reserpine	30	81	74.1	88.0	58
280678:01:03_10.00	L-687,384 hydrochloride	10	101	25.7	87.8	-3
246537:01:04_10.00	Dimethisoquin hydrochloride	10	95	28.2	87.7	9
246835:01:04_30.00	Bupirone hydrochloride	30	99	16.2	87.7	5
247342:01:05_30.00	Doxazosin mesylate	30	99	87.6	87.7	7
280580:01:03_30.00	GR 4661	30	96	68.2	87.7	15
410614:01:04_10.00	Cinacalcet HCl	10	102	76.0	87.7	n.d.
392582:01:09_02.00	SGI-1776 free base	2	96	42.7	87.7	n.d.
246465:01:04_10.00	Norcyclobenzaprine	10	96	67.0	87.7	17
280225:01:03_30.00	Alaproclate hydrochloride	30	91	40.2	87.7	1
247067:01:04_30.00	Domperidone	30	95	72.9	87.6	9
280125:01:03_30.00	GR 5562 dihydrobromide	30	100	87.7	87.6	1
280349:01:03_10.00	Benztropine mesylate	10	100	7.4	87.5	4
392675:01:09_02.00	IKK-16 (IKK Inhibitor VII)	2	101	48.0	87.5	n.d.
392793:02:04_06.00	AZD9291	6	79	88.4	87.5	n.d.
246509:01:04_10.00	Methotrimeprazine maleat salt	10	96	28.2	87.5	27
280815:01:03_30.00	Progesterone	30	94	46.3	87.5	14
410906:01:03_02.00	MIR96-IN-1	2	70	88.1	87.5	n.d.
247148:01:04_30.00	Dicyclomine hydrochloride	30	102	42.1	87.4	4
280525:01:03_10.00	FLB 131	10	101	11.6	87.4	14
280627:01:04_30.00	3-(1H-Imidazol-4-yl) propyl-di(p-fluorophenyl)methyl ether hydrochloride	30	95	33.9	87.4	10
410919:01:03_02.00	666-15	2	94	79.6	87.4	n.d.
245372:01:05_03.00	Perphenazine	3	91	10.7	87.3	8
246538:01:04_30.00	Dipivefrin hydrochloride	30	90	50.6	87.3	0

Well ID	Trivial name	Concentration [ $\mu$ M]	Cell Count [%]	Induction [%]	Similarity [%]	ROS induction [%]
280466:01:04_30.00	Dihydroergocristine methanesulfonate	30	102	72.2	87.3	32
246606:01:04_10.00	Piperacetazine	10	100	54.1	87.3	15
409617:01:04_03.00	Siramesine fumarate salt	3	89	78.1	87.3	n.d.
382128:02:09_02.00	PD173074	2	92	24.2	87.2	n.d.
409991:01:04_10.00	AZ 3146	10	92	64.4	87.2	n.d.
410017:01:03_02.00	Tepotinib	2	94	37.3	87.2	n.d.
246664:01:04_30.00	Escitalopram	30	104	16.1	87.2	-3
247391:01:04_10.00	Protriptyline hydrochloride	10	101	32.1	87.2	1
280552:01:04_10.00	Fiduxosin hydrochloride	10	100	24.7	87.1	31
280961:01:03_10.00	SR 59230A oxalate	10	102	52.5	87.1	7
410118:01:06_10.00	VPS34 inhibitor 1	10	100	77.7	87.0	n.d.
246628:01:04_10.00	Zuclopenthixol hydrochloride	10	102	58.4	86.9	20
281024:01:03_30.00	(-)-trans-(1S,2S)-U-50488 hydrochloride	30	92	61.8	86.9	-5
247008:01:04_10.00	Doxepin hydrochloride	10	108	5.2	86.9	5
246421:01:04_10.00	Homochlorcyclizine dihydrochloride	10	95	42.0	86.8	21
280353:01:03_30.00	BP 897	30	81	84.6	86.8	-3
280545:01:03_10.00	cis-(Z)-Flupenthixol dihydrochloride	10	102	35.6	86.8	8
281035:01:03_30.00	VER-3323 hemifumarate salt	30	91	59.1	86.8	3
410699:01:04_06.00	PRT062607 (P505-15, BIIB057) HCl	6	74	79.1	86.6	n.d.
246615:01:04_30.00	Rifabutin	30	95	36.4	86.6	62
246346:01:04_10.00	Thiethylperazine malate	10	103	59.4	86.5	27
246453:01:04_10.00	Benperidol	10	99	20.9	86.5	16
246861:01:05_10.00	Astemizole	10	90	86.9	86.5	18
247410:02:03_30.00	Guanabenz acetate	30	96	42.0	86.5	-2
282109:02:03_10.00	Dibucaine hydrochloride	10	98	17.1	86.4	14
392660:01:09_02.00	NVP-AEW541	2	102	29.7	86.4	n.d.
247044:01:04_10.00	Mebeverine hydrochloride	10	110	18.1	86.4	30
280387:01:03_30.00	ML-9	30	99	70.8	86.3	7
390582:02:09_00.20	PIK-93	0.2	96	28.8	86.3	n.d.
246761:01:04_30.00	(R)-Propranolol hydrochloride	30	102	47.5	86.2	6
410039:02:03_02.00	SGI-1027	2	72	86.4	86.2	n.d.
280482:01:03_30.00	Dextromethorphan hydrobromide monohydrate	30	90	31.8	86.2	4
394277:01:05_10.00	Golvatinib (E7050)	10	81	78.6	86.1	n.d.
408552:01:08_03.00	Azaquindole-1	3	90	67.5	86.1	n.d.
409854:02:04_06.00	SGC0946	6	97	45.9	86.1	n.d.

Well ID	Trivial name	Concentration [ $\mu$ M]	Cell Count [%]	Induction [%]	Similarity [%]	ROS induction [%]
247099:02:03_10.00	Carbetapentane citrate	10	98	12.3	86.0	-2
280760:01:10_03.00	NNC 55-0396	3	103	38.2	86.0	7
394207:03:03_02.00	HTH-01-015	2	102	53.5	86.0	n.d.
410925:01:03_02.00	(rac)-BAY1238097	2	90	75.1	86.0	n.d.
247386:01:04_30.00	Trimeprazine tartrate	30	88	87.7	85.9	24
410518:01:04_10.00	Crobenetine	10	94	46.5	85.9	n.d.
410106:01:04_06.00	MS023	6	100	49.7	85.9	n.d.
410961:01:03_02.00	Pinometostat	2	106	9.8	85.9	n.d.
246690:01:04_10.00	Zotepine	10	101	52.7	85.8	15
247070:05:04_06.00	Desipramine hydrochloride	6	101	20.7	85.8	8
280858:01:03_10.00	Pergolide methanesulfonate	10	95	23.3	85.7	21
280861:01:10_03.00	Prochlorperazine dimaleate	3	99	21.1	85.7	14
410708:01:04_10.00	AM1241	10	103	49.7	85.7	n.d.
407970:01:04_10.00	A-395	10	92	31.3	85.7	n.d.
247233:02:03_30.00	Citalopram hydrobromide	30	102	29.4	85.7	0
246378:01:04_30.00	Nefazodone HCl	30	97	52.5	85.6	6
280302:01:03_30.00	5-(N,N-hexamethylene)amiloride	30	86	85.5	85.6	-1
392440:01:02_02.00		2	99	11.2	85.6	n.d.
392746:01:09_02.00	KN-93 Phosphate	2	96	9.3	85.6	n.d.
410667:01:03_06.00	GSK126	6	95	76.5	85.5	n.d.
280740:01:04_30.00	MDL 28170	30	95	44.0	85.5	19
410154:01:04_10.00	Asciminib (ABL001)	10	97	35.8	85.4	n.d.
246435:02:03_02.00	Amodiaquin dihydrochloride dihydrate	2	104	12.6	85.4	14
280753:01:03_30.00	Nylidrin hydrochloride	30	95	66.1	85.3	-3
246486:01:04_10.00	Prenylamine lactate	10	86	59.9	85.3	-7
392453:01:07_01.00	Bafilomycin A1, Baf-A1	1	91	79.3	85.3	n.d.
390583:01:08_10.00	T-00127-HEV1	10	104	38.3	85.3	n.d.
392742:02:04_00.60	VE-822	0.6	108	51.6	85.3	n.d.
246304:01:04_10.00	Cloperastine hydrochloride	10	100	27.6	85.2	17
410825:01:03_02.00	Birabresib	2	90	70.3	85.2	n.d.
245386:02:04_10.00	Clozapine	10	103	18.0	85.1	5
246872:01:04_30.00	Desloratidine	30	93	57.3	85.0	18
393774:02:03_02.00	VPS34-IN1	2	98	44.9	85.0	n.d.
411125:01:03_10.00	Miransertib HCl	10	87	88.8	85.0	n.d.

**Supplementary Table 3: Expression levels (mRNA) as normalized expression (NX) of dopamine and serotonin receptors in U-2 OS and HeLa cells.** Data originate from the Human Protein Atlas, Version 19.3 ([www.proteinatlas.org](http://www.proteinatlas.org)).<sup>348</sup> HSP90AA1 was included as high-abundant reference protein.

Name	Gene	U-2 OS [NX]	HeLa [NX]	Source
Dopamine receptor D1	DRD1	4.9	0.0	<a href="http://proteinatlas.org/ENSG00000184845-DRD1/cell">proteinatlas.org/ENSG00000184845-DRD1/cell</a>
Dopamine receptor D2	DRD2	0.0	0.0	<a href="http://proteinatlas.org/ENSG00000149295-DRD2/cell">proteinatlas.org/ENSG00000149295-DRD2/cell</a>
Dopamine receptor D3	DRD3	0.0	0.0	<a href="http://proteinatlas.org/ENSG00000151577-DRD3/cell">proteinatlas.org/ENSG00000151577-DRD3/cell</a>
Dopamine receptor D4	DRD4	0.6	0.3	<a href="http://proteinatlas.org/ENSG00000069696-DRD4/cell">proteinatlas.org/ENSG00000069696-DRD4/cell</a>
Dopamine receptor D5	DRD5	0.9	0.0	<a href="http://proteinatlas.org/ENSG00000169676-DRD5/cell">proteinatlas.org/ENSG00000169676-DRD5/cell</a>
5-HT1A receptor	HTR1A	0.0	0.0	<a href="http://proteinatlas.org/ENSG00000178394-HTR1A/cell">proteinatlas.org/ENSG00000178394-HTR1A/cell</a>
5-HT1B receptor	HTR1B	0.0	0.0	<a href="http://proteinatlas.org/ENSG00000135312-HTR1B/cell">proteinatlas.org/ENSG00000135312-HTR1B/cell</a>
5-HT1D receptor	HTR1D	7.4	5.1	<a href="http://proteinatlas.org/ENSG00000179546-HTR1D/cell">proteinatlas.org/ENSG00000179546-HTR1D/cell</a>
5-HT1E receptor	HTR1E	0.0	0.0	<a href="http://proteinatlas.org/ENSG00000168830-HTR1E/cell">proteinatlas.org/ENSG00000168830-HTR1E/cell</a>
5-HT1F receptor	HTR1F	0.0	0.0	<a href="http://proteinatlas.org/ENSG00000179097-HTR1F/cell">proteinatlas.org/ENSG00000179097-HTR1F/cell</a>
5-HT2A receptor	HTR2A	2.9	0.0	<a href="http://proteinatlas.org/ENSG00000102468-HTR2A/cell">proteinatlas.org/ENSG00000102468-HTR2A/cell</a>
5-HT2B receptor	HTR2B	0.0	0.0	<a href="http://proteinatlas.org/ENSG00000135914-HTR2B/cell">proteinatlas.org/ENSG00000135914-HTR2B/cell</a>
5-HT2C receptor	HTR2C	0.9	0.2	<a href="http://proteinatlas.org/ENSG00000147246-HTR2C/cell">proteinatlas.org/ENSG00000147246-HTR2C/cell</a>
5-HT3A receptor	HTR3A	0.4	0.0	<a href="http://proteinatlas.org/ENSG00000166736-HTR3A/cell">proteinatlas.org/ENSG00000166736-HTR3A/cell</a>
5-HT3B receptor	HTR3B	1.1	1.9	<a href="http://proteinatlas.org/ENSG00000149305-HTR3B/cell">proteinatlas.org/ENSG00000149305-HTR3B/cell</a>
5-HT3C receptor	HTR3C	0.0	0.0	<a href="http://proteinatlas.org/ENSG00000178084-HTR3C/cell">proteinatlas.org/ENSG00000178084-HTR3C/cell</a>
5-HT3D receptor	HTR3D	0.0	0.0	<a href="http://proteinatlas.org/ENSG00000186090-HTR3D/cell">proteinatlas.org/ENSG00000186090-HTR3D/cell</a>
5-HT3E receptor	HTR3E	0.0	0.0	<a href="http://proteinatlas.org/ENSG00000186038-HTR3E/cell">proteinatlas.org/ENSG00000186038-HTR3E/cell</a>
5-HT4 receptor	HTR4	0.0	0.0	<a href="http://proteinatlas.org/ENSG00000164270-HTR4/cell">proteinatlas.org/ENSG00000164270-HTR4/cell</a>
5-HT5A receptor	HTR5A	0.0	0.0	<a href="http://proteinatlas.org/ENSG00000157219-HTR5A/cell">proteinatlas.org/ENSG00000157219-HTR5A/cell</a>
5-HT6 receptor	HTR6	0.1	0.0	<a href="http://proteinatlas.org/ENSG00000158748-HTR6/cell">proteinatlas.org/ENSG00000158748-HTR6/cell</a>
5-HT7 receptor	HTR7	0.0	0.0	<a href="http://proteinatlas.org/ENSG00000148680-HTR7/cell">proteinatlas.org/ENSG00000148680-HTR7/cell</a>
Heat shock protein 90 alpha family class A member 1	HSP90AA1	53.4	67.5	<a href="http://proteinatlas.org/ENSG00000080824-HSP90AA1/cell">proteinatlas.org/ENSG00000080824-HSP90AA1/cell</a>

**Supplementary Table 4: List of proteins significantly enriched during detergent-free affinity-based chemical proteomics experiments using DP73 and DP74 as affinity probes.** Affinity beads were incubated with HeLa cell lysates for 2 h and washed to remove loosely bound proteins. Bound proteins were subjected to a tryptic digestion and identification and label-free quantification (LFQ) via HPLC-MS/MS. Mean LFQ ratios of proteins significantly enriched by DP73 in both replicates, FDR = 0.01, N = 3, n = 2

Protein names	Gene	LFQ ratio DP73/DP74	
		n = 1	n = 2
S-methyl-5-thioadenosine phosphorylase	MTAP	97.96	77.96
Nicotinate phosphoribosyltransferase	NAPRT	50.85	119.11
Acyl-protein thioesterase 1	LYPLA1	20.97	148.12
Prosaposin	PSAP	82.73	49.63
Aldehyde dehydrogenase, dimeric NADP-preferring	ALDH3A1	15.66	74.05
Long-chain-fatty-acid--CoA ligase 1	ACSL1	26.46	62.21
Phospholipase DDHD2	DDHD2	20.72	66.74
Acid ceramidase	ASAH1	20.01	44.21
Ubiquitin carboxyl-terminal hydrolase 22	USP22	22.54	38.17
Ubiquinone biosynthesis monooxygenase COQ6, mitochondrial	COQ6	47.74	12.21
Preylcysteine oxidase 1	PCYOX1	8.69	47.71
Retinoid-inducible serine carboxypeptidase	SCPEP1	29.49	26.41
Ubiquinone biosynthesis O-methyltransferase, mitochondrial	COQ3	26.51	27.68
FAD synthase	FLAD1	19.60	32.53
Desumoylating isopeptidase 1	DESI1	35.48	9.39
DnaJ homolog subfamily C member 13	DNAJC13	14.41	30.04
Peroxisomal multifunctional enzyme type 2	HSD17B4	34.95	8.88
Lysosome-associated membrane glycoprotein 1	LAMP1	30.85	7.78
NADH dehydrogenase [ubiquinone] iron-sulfur protein 2, mitochondrial	NDUFS2	12.30	26.11
Sphingomyelin phosphodiesterase	SMPD1	8.27	29.48
Atlastin-3	ATL3	16.14	18.15
NADH dehydrogenase [ubiquinone] 1 alpha subcomplex subunit 5	NDUFA5	19.87	13.42
Prostaglandin E synthase 2	PTGES2	6.77	26.33
Ubiquilin-1	UBQLN1	25.78	5.78
Preylated Rab acceptor protein 1	RABAC1	9.05	21.30
Palmitoyl-protein thioesterase 1	PPT1	22.19	8.02
Pyridine nucleotide-disulfide oxidoreductase domain-containing protein 2	PYROXD2	6.50	21.48
Oxidoreductase HTATIP2	HTATIP2	3.99	23.49
Carboxypeptidase	CTSA	9.61	17.29
Metaxin-1	MTX1	6.49	18.99
Carboxymethylenebutenolidase homolog	CMBL	20.12	4.71
Long-chain-fatty-acid--CoA ligase 3	ACSL3	14.26	10.42

Protein names	Gene	LFQ ratio DP73/DP74	
		n = 1	n = 2
1-acylglycerol-3-phosphate O-acyltransferase ABHD5	ABHD5	7.71	16.76
NAD-dependent protein deacetylase sirtuin-2	SIRT2	13.30	7.94
Peroxisomal acyl-coenzyme A oxidase 1	ACOX1	15.21	4.86
Voltage-dependent anion-selective channel protein 1	VDAC1	9.33	9.95
Calnexin	CANX	12.82	5.99
Ubiquilin-4	UBQLN4	2.84	15.95
2-methoxy-6-polyprenyl-1,4-benzoquinol methylase, mitochondrial	COQ5	7.89	9.56
Apolipoprotein B-100	APOB	11.34	5.44
Tubulin-specific chaperone D	TBCD	7.69	8.98
HLA class I histocompatibility antigen, A-69 alpha chain	HLA-A	4.81	11.10
EGF-like repeat and discoidin I-like domain-containing protein 3	EDIL3	9.55	6.29
Reticulon-3	RTN3	6.65	9.16
SEC23-interacting protein	SEC23IP	3.41	12.07
Retinoic acid receptor RXR-beta	RXRB	4.04	11.43
Epoxide hydrolase 1	EPHX1	10.86	4.54
Epimerase family protein SDR39U1	SDR39U1	6.72	8.65
Lanosterol synthase	LSS	4.65	10.25
ER degradation-enhancing alpha-mannosidase-like protein 3	EDEM3	4.13	10.08
E3 ubiquitin-protein ligase TRIM4	TRIM4	11.25	2.81
PRA1 family protein 3	ARL6IP5	7.75	6.08
Protein disulfide-isomerase	P4HB	7.71	6.00
ATPase ASNA1	ASNA1	6.06	6.98
Patatin-like phospholipase domain-containing protein 4	PNPLA4	4.45	8.45
Beta-2-microglobulin	B2M	5.06	7.72
5-demethoxyubiquinone hydroxylase, mitochondrial	COQ7	9.00	3.76
Nucleobindin-1	NUCB1	5.01	7.62
Monoglyceride lipase	MGLL	4.49	8.09
Farnesyl pyrophosphate synthase	FDPS	5.95	5.81
Nucleoporin Nup43	NUP43	6.35	5.37
NADH dehydrogenase [ubiquinone] iron-sulfur protein 3, mitochondrial	NDUFS3	5.97	5.56
Methionine--tRNA ligase, cytoplasmic	MARS	3.95	6.89
Peroxisomal biogenesis factor 19	PEX19	5.28	5.47
Reticulon-4	RTN4	3.96	6.74
Glucosylceramidase	GBA	3.08	7.37
Mid1-interacting protein 1	MID1IP1	3.86	6.51
Secretory carrier-associated membrane protein 3	SCAMP3	4.29	6.06
COBW domain-containing protein 1	CBWD2	4.48	5.75



Protein names	Gene	LFQ ratio DP73/DP74	
		n = 1	n = 2
Acyl-CoA desaturase	SCD	5.15	4.33
Nucleoporin Nup37	NUP37	4.39	4.86
NADH dehydrogenase [ubiquinone] 1 alpha subcomplex subunit 8	NDUFA8	2.44	6.68
Choline-phosphate cytidyltransferase A	PCYT1A	5.32	3.55
Collagen type IV alpha-3-binding protein (Ceramide transfer protein)	COL4A3BP	3.37	5.46
Perilipin-3	PLIN3	6.45	2.34
NADH-cytochrome b5 reductase 3	CYB5R3	4.20	4.57
2,4-dienoyl-CoA reductase, mitochondrial	DECR1	4.51	4.20
Citrate synthase;Citrate synthase, mitochondrial	CS	5.10	3.60
Protoporphyrinogen oxidase	PPOX	3.53	5.15
E3 ubiquitin-protein ligase RNF115	RNF115	3.15	5.40
Trifunctional enzyme subunit beta, mitochondrial;3-ketoacyl-CoA thiolase	HADHB	3.55	4.98
Cytosolic phospholipase A2	PLA2G4A	3.62	4.69
Ubiquinone biosynthesis protein COQ9, mitochondrial	COQ9	4.27	3.99
Sepiapterin reductase	SPR	2.69	5.24
Acyl-CoA dehydrogenase family member 9, mitochondrial	ACAD9	3.96	3.90
Nucleoporin SEH1	SEH1L	3.69	4.13
DnaJ homolog subfamily B member 6	DNAJB6	2.99	4.77
Vesicle-trafficking protein SEC22b	SEC22B	3.38	4.23
Asparagine--tRNA ligase, cytoplasmic	NARS	2.67	4.65
HAUS augmin-like complex subunit 4	HAUS4	3.29	3.98
Chloride intracellular channel protein 1	CLIC1	2.82	4.35
Trifunctional enzyme subunit alpha, mitochondrial	HADHA	3.20	3.90
UDP-glucose:glycoprotein glucosyltransferase 2	UGGT2	3.44	3.66
Basic leucine zipper and W2 domain-containing protein 2	BZW2	3.57	3.19
[Pyruvate dehydrogenase (acetyl-transferring)] kinase isozyme 3, mitochondrial	PDK3	3.44	3.29
ATP synthase subunit gamma, mitochondrial	ATP5C1	2.58	4.14
Vesicle-associated membrane protein-associated protein A	VAPA	3.41	3.30
Focadhesin	FOCAD	2.69	3.89
Surfeit locus protein 4	SURF4	2.76	3.78
Intraflagellar transport protein 56	TTC26	2.27	3.59
Glutamate dehydrogenase 1, mitochondrial	GLUD1	2.77	2.75
Nuclear pore complex protein Nup160	NUP160	2.18	3.29
Clathrin heavy chain;Clathrin heavy chain 1	CLTC	2.08	3.08
Protein NipSnap homolog 1	NIPSNAP1	2.71	2.43
Phosphoglycerate kinase 1	PGK1	2.39	2.55
Activator of 90 kDa heat shock protein ATPase homolog 1	AHSA1	2.14	2.70

**Supplementary Table 5: List of proteins significantly enriched during affinity-based chemical proteomics experiments using GE NHS beads.** 75 Proteins were found enriched on DP79 beads in experiments using GE NHS beads. FDR = 0.0001, LFQ ratios (DP79/DP80) of technical replicates, N = 4, n = 2.

Protein names	Gene	LFQ ratio DP79/DP80	
		n = 1	n = 2
Translational activator GCN1	GCN1L1	1475.77	1462.36
Serine/threonine-protein kinase mTOR	MTOR	109.11	1718.26
Exportin-2	CSE1L	1094.50	301.01
Exportin-1	XPO1	334.72	898.79
DNA-dependent protein kinase catalytic subunit	PRKDC	129.16	556.91
Importin-11	IPO11	190.73	402.07
Exportin-5	XPO5	211.38	194.25
Importin-7	IPO7	42.73	280.47
Prohibitin	PHB	24.49	271.29
Importin-5	IPO5	72.24	162.85
Transportin-1	TNPO1	114.85	110.49
Exportin-7	XPO7	107.21	102.53
Transportin-3	TNPO3	65.01	116.77
Serine/threonine-protein kinase ATR	ATR	94.59	32.26
Sigma non-opioid intracellular receptor 1	SIGMAR1	33.82	79.71
Thyroid adenoma-associated protein	THADA	39.91	72.41
Prohibitin-2	PHB2	14.84	89.75
Tubulin beta-6 chain	TUBB6	48.35	54.48
Importin-8	IPO8	36.65	64.64
D-3-phosphoglycerate dehydrogenase	PHGDH	49.59	50.26
Conserved oligomeric Golgi complex subunit 5	COG5	12.40	82.47
Importin-9	IPO9	42.73	47.28
Signal transducer and activator of transcription 3	STAT3	67.07	20.55
Conserved oligomeric Golgi complex subunit 7	COG7	36.49	48.84
Exportin-6	XPO6	39.40	42.19
Importin-4	IPO4	43.38	35.08
7-dehydrocholesterol reductase	DHCR7	34.50	43.36
Sterol O-acyltransferase 1	SOAT1	13.25	63.66
Basic leucine zipper and W2 domain-containing protein 1	BZW1	52.98	23.33
Stomatin-like protein 2, mitochondrial	STOML2	64.61	11.35
Fanconi anemia group I protein	FANCI	45.09	30.19
Surfeit locus protein 4	SURF4	36.58	34.62
Exportin-4	XPO4	14.08	55.07
Fatty aldehyde dehydrogenase	ALDH3A2	46.80	20.07

Protein names	Gene	LFQ ratio DP79/DP80	
		n = 1	n = 2
Transportin-2	TNPO2	30.57	33.84
Very-long-chain enoyl-CoA reductase	TECR	32.07	29.17
Exportin-T	XPOT	27.36	31.48
Target of rapamycin complex subunit LST8	MLST8	40.61	17.15
Importin subunit beta-1	KPNB1	18.00	36.56
Conserved oligomeric Golgi complex subunit 8	COG8	9.57	44.55
Gem-associated protein 4	GEMIN4	32.97	17.56
BRCA1-associated ATM activator 1	BRAT1	25.02	25.02
Flotillin-2	FLOT2	10.90	36.82
Proteasome-associated protein ECM29 homolog	KIAA0368	21.41	23.23
Conserved oligomeric Golgi complex subunit 6	COG6	21.22	22.72
Conserved oligomeric Golgi complex subunit 2	COG2	5.11	38.38
Voltage-dependent anion-selective channel protein 2	VDAC2	8.32	33.00
E3 ubiquitin-protein ligase listerin	LTN1	12.75	25.92
Flotillin-1	FLOT1	18.21	18.34
Brefeldin A-inhibited guanine nucleotide-exchange protein 2	ARFGEF2	10.50	22.57
Alkyldihydroxyacetonephosphate synthase, peroxisomal	AGPS	24.71	6.51
Conserved oligomeric Golgi complex subunit 3	COG3	7.79	23.41
Nuclear pore complex protein Nup160	NUP160	20.73	10.25
Dynein assembly factor 5, axonemal	DNAAF5	16.88	10.72
Pachytene checkpoint protein 2 homolog	TRIP13	19.69	7.19
Conserved oligomeric Golgi complex subunit 1	COG1	6.88	19.77
Tubulin alpha-4A chain	TUBA4A	16.38	9.98
Dolichyl-diphosphooligosaccharide--protein glycosyltransferase subunit 1	RPN1	17.60	5.98
Serine-protein kinase ATM	ATM	17.57	5.83
Probable ATP-dependent RNA helicase DDX20	DDX20	8.48	14.38
Erlin-2	ERLIN2	13.66	8.92
Tubulin alpha-1C chain	TUBA1C	11.49	8.40
Long-chain-fatty-acid--CoA ligase 3	ACSL3	8.50	11.37
Voltage-dependent anion-selective channel protein 1	VDAC1	3.75	15.68
Conserved oligomeric Golgi complex subunit 4	COG4	5.07	13.73
Palmitoyl-protein thioesterase 1	PPT1	12.17	5.69
Tubulin alpha-1B chain	TUBA1B	8.67	8.14
Probable methyltransferase TARBP1	TARBP1	5.55	10.77
Probable arginine--tRNA ligase, mitochondrial	RARS2	5.78	8.02
Heme-binding protein 1	HEBP1	8.53	5.12
Fatty acid desaturase 2	FADS2	5.92	6.81

Protein names	Gene	LFQ ratio DP79/DP80	
		n = 1	n = 2
Tubulin beta-4B chain	TUBB4B	6.09	6.42
Tubulin beta chain	TUBB	6.21	5.76
Protein MON2 homolog	MON2	4.89	6.66
4F2 cell-surface antigen heavy chain	SLC3A2	4.42	6.72

**Supplementary Table 6: List of proteins significantly enriched during affinity-based chemical proteomics experiments using Pierce NHS beads.** 428 Proteins were found enriched on DP79 beads in experiments using GE NHS beads, top 100 proteins are listed. FDR = 0.0001, LFQ ratios (DP79/DP80) of technical replicates, N = 4, n = 2.

Protein names	Gene	LFQ ratio DP79/DP80	
		n = 1	n = 2
Exportin-1	XPO1	2744.85	1747.41
Translational activator GCN1	GCN1L1	3315.83	919.39
Serine/threonine-protein kinase mTOR	MTOR	3309.75	618.06
Fanconi anemia group I protein	FANCI	1511.55	979.15
Brefeldin A-inhibited guanine nucleotide-exchange protein 2	ARFGEF2	1308.79	678.35
Fanconi anemia group D2 protein	FANCD2	1229.40	333.55
Condensin complex subunit 1	NCAPD2	860.94	665.64
E3 ubiquitin-protein ligase listerin	LTN1	1366.73	129.72
Proteasome-associated protein ECM29 homolog	ECM29	554.15	789.63
Ubiquitin-protein ligase E3C	UBE3C	717.01	573.06
Serine/threonine-protein kinase ATR	ATR	1093.46	158.38
Protein NipSnap homolog 1	NIPSNAP1	988.97	167.35
Fatty aldehyde dehydrogenase	ALDH3A2	985.94	168.27
Lipase maturation factor 2	LMF2	700.14	434.44
Target of rapamycin complex subunit LST8	MLST8	889.24	210.58
Exportin-2	CSE1L	767.18	238.27
E3 ubiquitin-protein ligase UBR4	UBR4	375.44	582.52
Carnitine O-palmitoyltransferase 1, liver isoform	CPT1A	664.21	261.20
Exportin-5	XPO5	388.90	504.03
Fatty acid desaturase 1	FADS1	583.95	307.48
Dimethyladenosine transferase 2, mitochondrial	TFB2M	416.02	473.63
E3 ubiquitin-protein ligase RNF213	RNF213	657.64	223.13
Serine-protein kinase ATM	ATM	547.98	294.94
Golgi-specific brefeldin A-resistance guanine nucleotide exchange factor 1	GBF1	482.38	305.17
Dynamin-like 120 kDa protein, mitochondrial	OPA1	182.15	468.90
Cleft lip and palate transmembrane protein 1-like protein	CLPTM1L	467.79	166.73

Protein names	Gene	LFQ ratio DP79/DP80	
		n = 1	n = 2
Fatty acid desaturase 2	FADS2	338.86	281.75
Very-long-chain (3R)-3-hydroxyacyl-CoA dehydratase 3	HACD3	464.30	134.32
Protein NipSnap homolog 2	GBAS	378.21	219.29
Telomere length regulation protein TEL2 homolog	TELO2	353.91	236.41
Midasin	MDN1	269.13	202.94
Gamma-tubulin complex component 2	TUBGCP2	315.54	147.67
Chitobiosyldiphosphodolichol beta-mannosyltransferase	ALG1	310.12	147.35
Sigma non-opioid intracellular receptor 1	SIGMAR1	282.76	171.47
Monocarboxylate transporter 1	SLC16A1	201.62	251.29
NADH dehydrogenase [ubiquinone] 1 alpha subcomplex subunit 9, mitochondrial	NDUFA9	324.13	123.58
Phosphatidylinositol 4-kinase alpha	PI4KA	306.26	139.30
Ras GTPase-activating-like protein IQGAP3	IQGAP3	419.41	22.21
Acyl-CoA desaturase	SCD	286.18	150.69
DNA-dependent protein kinase catalytic subunit	PRKDC	406.95	27.04
Delta(24)-sterol reductase	DHCR24	374.96	49.60
Brefeldin A-inhibited guanine nucleotide-exchange protein 1	ARFGEF1	260.25	149.67
Tonsoku-like protein	TONSL	173.84	226.99
Transmembrane protein 33	TMEM33	314.58	82.40
Exportin-6	XPO6	245.12	150.42
Protein RER1	RER1	245.11	135.56
Serine/threonine-protein phosphatase 6 regulatory subunit 3	PPP6R3	175.01	196.05
7-dehydrocholesterol reductase	DHCR7	161.00	204.60
Serine/threonine-protein phosphatase 2A 56 kDa regulatory subunit delta isoform	PPP2R5D	146.72	208.28
Protein transport protein Sec61 subunit alpha isoform 1	SEC61A1	231.60	114.74
Monocarboxylate transporter 4	SLC16A3	120.67	219.60
TELO2-interacting protein 1 homolog	TTI1	227.37	96.91
Surfeit locus protein 4	SURF4	215.31	108.10
AarF domain-containing protein kinase 4	ADCK4	198.80	117.52
ATP-dependent 6-phosphofructokinase, muscle type	PFKM	259.99	48.84
Voltage-dependent anion-selective channel protein 1	VDAC1	67.47	233.81
Probable arginine--tRNA ligase, mitochondrial	RARS2	124.50	169.49
Probable methyltransferase TARBP1	TARBP1	152.91	140.50
Nucleoporin NDC1	NDC1	124.36	168.61
Signal transducer and activator of transcription 3	STAT3	151.37	134.50
PCI domain-containing protein 2	PCID2	134.54	145.34
Dual specificity protein kinase TTK	TTK	176.16	102.55
Large neutral amino acids transporter small subunit 1	SLC7A5	66.59	206.20

Protein names	Gene	LFQ ratio DP79/DP80	
		n = 1	n = 2
Deoxynucleoside triphosphate triphosphohydrolase SAMHD1	SAMHD1	163.50	105.15
Very-long-chain 3-oxoacyl-CoA reductase	HSD17B12	143.08	118.25
Voltage-dependent anion-selective channel protein 2	VDAC2	53.02	197.94
Cytoplasmic dynein 1 heavy chain 1	DYNC1H1	78.36	170.92
Dolichol-phosphate mannosyltransferase subunit 1	DPM1	220.46	17.72
Neurofibromin;Neurofibromin truncated	NF1	191.80	45.49
ATP-dependent 6-phosphofructokinase, platelet type	PFKP	174.98	54.53
Gamma-tubulin complex component 3	TUBGCP3	160.21	69.02
ADP/ATP translocase 3	SLC25A6	167.44	60.81
Fatty acid desaturase 3	FADS3	101.93	124.91
Calcineurin B homologous protein 1	CHP1	104.30	119.37
Importin-8	IPO8	93.83	129.71
ATP-dependent 6-phosphofructokinase, liver type	PFKL	113.26	108.68
Replication factor C subunit 3	RFC3	157.25	64.41
Serine/threonine-protein phosphatase 6 catalytic subunit	PPP6C	86.30	128.84
Exportin-7	XPO7	135.91	79.00
Glycerol-3-phosphate acyltransferase 4	AGPAT6	137.61	75.55
Exocyst complex component 7	EXOC7	187.96	23.33
Nuclear pore complex protein Nup205	NUP205	70.70	135.81
LMBR1 domain-containing protein 2	LMBRD2	115.44	88.12
Inactive ubiquitin thioesterase FAM105A	FAM105A	177.75	22.62
Serine/threonine-protein phosphatase 6 regulatory subunit 1	PPP6R1	92.60	107.53
Coatomer subunit gamma-2	COPG2	38.85	157.06
Importin-11	IPO11	96.31	99.53
Protein MON2 homolog	MON2	113.22	75.61
Peroxisome assembly factor 2	PEX6	108.86	73.42
Phosphate carrier protein, mitochondrial	SLC25A3	70.04	108.56
Importin-4	IPO4	100.53	77.09
Trifunctional enzyme subunit alpha, mitochondrial	HADHA	54.20	121.49
Sterol regulatory element-binding protein 1	SREBF1	127.75	46.64
Sister chromatid cohesion protein PDS5 homolog A	PDS5A	80.39	90.62
Solute carrier family 35 member E1	SLC35E1	95.50	74.70
Gem-associated protein 4	GEMIN4	127.43	41.57
Probable ATP-dependent RNA helicase DDX11	DDX11	85.31	81.20
26S proteasome non-ATPase regulatory subunit 3	PSMD3	69.86	96.58
Probable ATP-dependent RNA helicase DDX20	DDX20	80.92	84.97
Lymphoid-specific helicase	HELLS	140.79	17.54

**Supplementary Table 7: Diaminopyrimidine-based compound library.** ROS induction in HeLa cells. Quantification using the 'Imaging positive' read-out. Mean values  $\pm$  SD,  $n \geq 3$ . Data were obtained by COMAS, Dortmund.

Name	ID	ROS EC <sub>50</sub> [ $\mu$ M]	Structure
DP01	226028	2.9 $\pm$ 1.0	
DP02	406794	2.4 $\pm$ 0.8	
DP03	407168	6.1 $\pm$ 1.9	
DP04	407169	7.6 $\pm$ 0.2	
DP05	407167	25.4 $\pm$ 4.0	
DP06	407163	14.4 $\pm$ 2.0	
DP07	407164	>30	
DP08	407166	>30	
DP09	407165	>30	
DP10	406789	>30	
DP11	226032	4.7 $\pm$ 0.4	

Name	ID	ROS EC <sub>50</sub> [μM]	Structure
DP12	406785	23.9 ± 0.0	
DP13	406792	>30	
DP14	407424	1.2 ± 0.2	
DP15	406798	6.1 ± 0.8	
DP16	226033	7.5 ± 0.7	
DP17	407428	2.1 ± 0.3	
DP18	406796	8.0 ± 0.4	
DP19	226031	6.2 ± 1.1	
DP20	226030	25.1 ± 5.0	
DP21	406787	9.7 ± 0.9	
DP22	406791	24.6 ± 3.0	
DP23	406786	8.5 ± 0.0	



Name	ID	ROS EC <sub>50</sub> [μM]	Structure
DP24	407425	5.0 ± 0.9	
DP25	226029	9.5 ± 0.3	
DP26	407436	>30	
DP27	406799	>30	
DP28	226017	>30	
DP29	407431	2.7 ± 0.5	
DP30	226022	25.0 ± 4.0	
DP31	406788	13.2 ± 1.0	
DP32	260984	27.1 ± 0.0	
DP33	407427	9.2 ± 0.3	
DP34	406790	12.1 ± 1.0	
DP35	406797	13.2 ± 1.0	

Name	ID	ROS EC <sub>50</sub> [μM]	Structure
DP36	406793	23.2 ± 3.0	
DP37	407161	>30	
DP38	407435	>30	
DP39	407162	>30	
DP40	407434	7.6 ± 0.6	
DP41	382205	>30	
DP42	407432	7.7 ± 0.2	
DP43	407423	10.2 ± 0.0	
DP44	407429	14.9 ± 2.0	
DP45	226019	>30	
DP46	407426	21.3 ± 2.0	
DP47	226018	>30	

Name	ID	ROS EC <sub>50</sub> [μM]	Structure
DP48	407430	>30	
DP49	406795	>30	
DP50	226023	>30	
DP51	226016	>30	
DP52	407437	>30	
DP53	226021	>30	
DP54	226020	>30	
DP55	407433	0.9 ± 0.1	
DP56	407776	1.2 ± 0.3	
DP57	407777	>30	
DP58	407778	>30	
DP59	408227	>30	
DP60	407782	19.6 ± 5.0	

Name	ID	ROS EC <sub>50</sub> [μM]	Structure
DP61	408225	1.3 ± 0.3	
DP62	407779	>30	
DP63	408224	2.6 ± 1.0	
DP64	408231	16.3 ± 16.0	
DP65	408230	17.5 ± 10.0	
DP66	408233	>30	
DP67	408234	15.4 ± 6.0	
DP68	408239	0.7 ± 0.3	
DP69	408238	0.8 ± 0.4	
DP70	409124	2.4 ± 1.0	
DP71	409126	>30	
DP72	409125	>30	

Name	ID	ROS EC <sub>50</sub> [μM]	Structure
DP73	409934	0.4 ± 0.2	
DP74	409933	>30	
DP75	411716	2.1 ± 1.2	
DP76	411723	29.2 ± 18.3	
DP77	411717	15.1 ± 0.9	
DP78	411718	4.5 ± 1.3	
DP79	411725	9.8 ± 3.0	
DP80	411724	>30	

## 9.2 Abbreviations

<b>Abbreviation</b>	<b>Meaning</b>
2-ME	2-methoxyestradiol
ABP	Affinity-based chemical proteomics
ANOVA	Analysis of variance
APS	Ammonium persulfate
ARE	Antioxidant response element
ASK-1	Apoptosis signal-regulating kinase 1
ATM	Ataxia Telangiectasia Mutated
ATR	Ataxia telangiectasia and Rad3-related protein
ATRIP	ATR-interacting protein
BBG	S-p-bromobenzyglutathione
BCA	Bathocuproinedisulfonic acid
BRET	Bioluminescence resonance energy transfer
BSA	Bovine serum albumin
BSO	Buthionine sulphoximine
CAT	Catalase
CDNB	1-Chloro-2,4-dinitrobenzene
CETSA	Cellular thermal shift assay
CHOP	C/BEP homologous protein
CM-H <sub>2</sub> DCFDA	5'/6'-chloromethyl-2'-7'-dichlorodihydrofluorescein diacetate
CML	Chronic myelogenous leukemia
CNS	Central nervous system
COMAS	Compound management and screening center
CP	Chlorpromazine
CPA	Cell Painting assay
CSRS	Center for Sustainable Resource Science
CTSD	Cathepsin D
CUL-3	Cullin-3
Da	Dalton
DAPI	4',6-diamidino-2-phenylindole
DARTS	Drug affinity responsive target stability
DBCO	Dibenzocyclooctyne
DCF	Dichlorofluoresceine
DFO	Deferoxamine
DHMP	4,5-dihalo-2-methylpyridazin-3-one
DMEM	Dulbecco's Modified Eagle Medium
DMSO	Dimethyl sulfoxide
DNA	Deoxyribonucleic acid
DNA-PK	DNA-dependent protein kinase
DTE	Dithioerythritol
DTG	1,3-Di-(2-tolyl)-guanidine
DTT	Dithiotreitol
EC <sub>50</sub>	Half-maximal effective concentration
ECAR	Extracellular acidification rate
EDTA	Ethylene diamine tetraacetic acid
EGF	Epidermal growth factor
EGTA	Triethylene glycol diamine tetraacetic acid
Em	Emission wavelength
ER	Endoplasmic reticulum
ERK	Extracellular signal-related kinase

<b>Abbreviation</b>	<b>Meaning</b>
ERO	ER oxireductin
ESI	Electrospray ionization
ETC	Electron transport chain
EtOH	Ethanol
Ex	Excitation wavelength
FBS	Fetal bovine serum
FDR	False discovery rate
FITC	Fluorescein isothiocyanate
FLuc	Firefly luciferase
FOXO	Forkhead box protein O
FP	Fluorescence polarization
FRET	Fluorescence resonance energy transfer
G6PD	Glucose-6-phosphate dehydrogenase
GCL	Glutamate-cysteine ligase
GF	Growth factor
GLO1	Glyoxalase 1
GndHCl	Guanidine hydrochloride
GPCR	G-protein coupled receptor
GPDH	Glycerol-3-phosphate dehydrogenase
GPX	Glutathione peroxidase
GR	Glutathione reductase
GRB2	Growth factor receptor-bound protein 2
Grx	Glutaredoxin
GSH	Glutathione, reduced
GSH-S	Glutathione synthase
GSSG	Glutathione, oxidized
H <sub>2</sub> DCF	Dihydrodichlorofluorescein
HBSS	Hank's balanced salt solution
HEAT	Huntingtin, Elongation factor 3, protein phosphatase 2A subunit A and TOR1
HEPES	4-(2-hydroxyethyl)-1-piperazineethanesulfonic acid
HER2	Human epidermal growth factor receptor 2
HIF1- $\alpha$	Hypoxia-inducible factor 1-alpha
HPLC	High performance liquid chromatography
HRP	Horseradish peroxidase
HUVEC	Human umbilical vein endothelial cells
IB	Immunoblotting
IC <sub>50</sub>	Half-maximal inhibitory concentration
IGF1	Insulin-growth factor 1
IMDM	Iscove's Modified Dulbecco's Medium
IPA	Ingenuity Pathway Analysis
ITC	isothermal titration calorimetry
JNK	c-Jun N-terminal kinase
KEAP1	Kelch ECH associating protein 1
LCFA	Long-chain fatty acid
LFQ	Label-free quantification
LMNG	Lauryl maltose neopentyl glycol
MAD	Median absolute deviation
Maf	Musculoaponeurotic fibrosarcoma
MAM	Mitochondria-associated membrane
MAP	Mitogen-activated protein
MAPK	MAP kinase

<b>Abbreviation</b>	<b>Meaning</b>
MAPKK	MAP kinase kinase
ME	Malic enzyme
MEM	Minimum Essential Medium
MeOH	Methanol
MKP	MAP kinase phosphatase
MPO	Myeloperoxidase
MS	Mass spectrometry
MS/MS	Tandem mass spectrometry
mTOR	Mammalian target of rapamycin
mTORC	mTOR complex
NAC	N-acetylcysteine
NADH	Nicotinamide adenine dinucleotide
NADPH	Nicotinamide adenine dinucleotide phosphate
NanoLuc	Nano luciferase
NHS	N-hydroxysuccinimide
NOS	Nitric oxide synthase
NOX	NADPH oxidase
NPC	Nuclear pore complex
NQO1	NAD(P)H dehydrogenase (quinone 1)
NRF2	Nuclear factor erythroid 2-related factor 2
OADH	2-oxoacid dehydrogenase
OCR	Oxygen consumption rate
PAGE	Polyacrylamide gel electrophoresis
PAL	Photoaffinity labeling
PAQ	Phenanthrenequinone
PBMC	Peripheral blood mononuclear cells
PBS	Phosphate-buffered saline
PDGF	Platelet-derived growth factor
PDH	Pyruvate dehydrogenase
PDI	Protein disulfide isomerase
PDK1	3-phosphoinositide-dependent protein kinase 1
PEITC	Phenethyl isothiocyanate
Pep A	Pepstatin A
PHGDH	Phosphoglycerate dehydrogenase
PI	Propidium iodide
PIKK	Phosphatidylinositol 3-kinase related kinase
PIP <sub>3</sub>	Phosphoinositoltriphosphate
PIPES	Piperazine-N,N'-bis(2-ethanesulfonic acid)
PP2A	Protein phosphatase 2a
PPP	Pentose phosphate pathway
PROTAC	PuHplcroteolysis targeting chimera
Prx	Peroxiredoxin
PTEN	Phosphatase and tensin homolog
PTP	Protein tyrosine phosphatase
PVDF	Polyvinylidene difluoride
RET	Reverse electron transport
RNA	Ribonucleic acid
RNS	Reactive nitrogen species
ROS	Reactive oxygen species
RTK	Receptor tyrosine kinase
S1P	Site-1 protease



<b>Abbreviation</b>	<b>Meaning</b>
S2P	Site-2 protease
SAR	Structure-activity relationship
SCAP	SREBP cleavage-activating protein
SD	Standard deviation
SDS	Sodium dodecylsulfate
SEA	Similarity Ensemble Approach
SEM	Standard error of the mean
SILAC	Stable isotope labeling with amino acids in cell culture
SLG	S-D-lactoylglutathione
SOD	Superoxide dismutase
SOS	Son of sevenless homolog
SPR	Surface plasmon resonance
SPROX	Stability of proteins from rates of oxidation
SREBP	Sterol-responsive element binding protein
TAMRA	Carboxytetramethylrhodamine
t-BHQ	tert-butylhydroquinone
TBS	Tris-buffered saline
TCEP	Tris(2-cyboxethyl)phosphine)
TCMP	2,3,4,5(6)-tetrachloro-6(5)-methylpyridine
TEAB	Triethylammonium bicarbonate
TEMED	Tetramethylethylenediamine
TFA	Trifluoroacetic acid
TFE	Trifluoroethanol
THPTA	Tris((1-hydroxy-propyl-1H-1,2,3-triazol-4-yl)methyl)amine
TMT	Tandem mass tag
TPP	Thermal proteome profiling
Trx	Thioredoxin
TR	Thioredoxin reductase
Ub	Ubiquitin
UHPLC	Ultra-high performance liquid chromatography
ULA	Ultra-low attachment
VCL	Vinculin
VEGF	Vascular endothelial growth factor
xCT	Cystine-glutamate antiporter
XO	Xanthine oxidase
$\alpha$ -Toc	$\alpha$ -Tocopherol
$\beta$ -ME	$\beta$ -mercaptoethanol

### 9.3 Curriculum vitae

#### Personal information:

Name: Julian Wilke  
Date and place of birth: March, 2<sup>nd</sup> 1990 in Bonn, Germany  
Citizenship: German

#### Education:

2016-2021                    **Doctoral studies in Chemical Biology**  
Max Planck Institute of Molecular Physiology, Dortmund  
Department of Chemical Biology  
TU Dortmund University, Dortmund, Germany  
Faculty of Chemistry and Chemical Biology

2013-2015                    **Master studies in Life and Medical Sciences**  
University of Bonn, Germany  
Faculty of Mathematics and Natural Sciences

2010-2013                    **Bachelor studies in Molecular Biomedicine**  
University of Bonn, Germany  
Faculty of Mathematics and Natural Sciences

## 9.4 Publication list

- T. Kawamura, Y. Futamura, E. Shang, M. Muroi, P. Janning, M. Ueno, J. Wilke, S. Takeda, Y. Kondoh, S. Ziegler, N. Watanabe, H. Waldmann, H. Osada: *Discovery of small-molecule modulator of heterodimeric G<sub>i</sub>-protein by integrated phenotypic profiling and chemical proteomics* *Bioscience, Biotechnology, and Biochemistry*, 2020, **84**, 2484-2490
- L. Laraia, G. Garivet, D.J. Foley, N. Kaiser, S. Müller, S. Zinken, T. Pinkert, J. Wilke, D. Corkery, A. Pahl, S. Sievers, P. Janning, C. Arenz, Y. Wu, R. Rodriguez, H. Waldmann: *Image-based morphological profiling identifies a lysosomotropic, iron-sequestering autophagy inhibitor* *Angewandte Chemie (International Edition)*, 2019, **59**, 5721-5729
- J. Ceballos, M. Schwalfenberg, G. Karageorgis, E.S. Reckzeh, S. Sievers, C. Ostermann, A. Pahl, M. Sellstedt, J. Nowacki, M.A. Carnero Corrales, J. Wilke, L. Laraia, K. Tschapalda, M. Metz, DA. Sehr, S. Brand, K. Winklhofer, P. Janning, S. Ziegler, H. Waldmann: *Synthesis of Indomorphane Pseudo-Natural Product Inhibitors of Glucose Transporters GLUT-1 and -3* *Angewandte Chemie (International Edition)*, 2019, **58**, 17016-17025
- A. Christoforow, J. Wilke, A. Binici, A. Pahl, C. Ostermann, S. Sievers, H. Waldmann: *Design, Synthesis, and Phenotypic Profiling of Pyrano-Furo-Pyridone Pseudo-Natural Products* *Angewandte Chemie (International Edition)*, 2019, **58**, 14715-14723
- J. Wilke, T. Kawamura, N. Watanabe, H. Osada, S. Ziegler, H. Waldmann: *Identification of cytotoxic, glutathione-reactive moieties inducing accumulation of reactive oxygen species via glutathione depletion* *Bioorganic & Medicinal Chemistry*, 2018, **26**, 1453-1461
- L. Robke, Y. Futamura, G. Konstantinidis, J. Wilke, H. Aono, Z. Mahmoud, N. Watanabe, Y. Wu, H. Osada, L. Laraia, H. Waldmann: *Discovery of the novel autophagy inhibitor aumitin that targets mitochondrial complex I* *Chemical Science*, 2018, **9**, 3014-3022
- F. Tolle, J. Wilke, J. Wengel, G. Mayer: *By-Product Formation in Repetitive PCR Amplification of DNA Libraries during SELEX* *PLoS One*, 2014, **9**, e114693



## 9.5 Eidesstattliche Versicherung (Affidativ)

Wilke, Julian

Name, Vorname  
(Surname, first name)

190871

Matrikel-Nr.  
(Enrolment number)

Belehrung:

Wer vorsätzlich gegen eine die Täuschung über Prüfungsleistungen betreffende Regelung einer Hochschulprüfungsordnung verstößt, handelt ordnungswidrig. Die Ordnungswidrigkeit kann mit einer Geldbuße von bis zu 50.000,00 € geahndet werden. Zuständige Verwaltungsbehörde für die Verfolgung und Ahndung von Ordnungswidrigkeiten ist der Kanzler/die Kanzlerin der Technischen Universität Dortmund. Im Falle eines mehrfachen oder sonstigen schwerwiegenden Täuschungsversuches kann der Prüfling zudem exmatrikuliert werden, § 63 Abs. 5 Hochschulgesetz NRW.

Die Abgabe einer falschen Versicherung an Eides statt ist strafbar.

Wer vorsätzlich eine falsche Versicherung an Eides statt abgibt, kann mit einer Freiheitsstrafe bis zu drei Jahren oder mit Geldstrafe bestraft werden, § 156 StGB. Die fahrlässige Abgabe einer falschen Versicherung an Eides statt kann mit einer Freiheitsstrafe bis zu einem Jahr oder Geldstrafe bestraft werden, § 161 StGB.

Die oben stehende Belehrung habe ich zur Kenntnis genommen:

Official notification:

Any person who intentionally breaches any regulation of university examination regulations relating to deception in examination performance is acting improperly. This offence can be punished with a fine of up to EUR 50,000.00. The competent administrative authority for the pursuit and prosecution of offences of this type is the chancellor of the TU Dortmund University. In the case of multiple or other serious attempts at deception, the candidate can also be unenrolled, Section 63, paragraph 5 of the Universities Act of North Rhine-Westphalia.

The submission of a false affidavit is punishable.

Any person who intentionally submits a false affidavit can be punished with a prison sentence of up to three years or a fine, Section 156 of the Criminal Code. The negligent submission of a false affidavit can be punished with a prison sentence of up to one year or a fine, Section 161 of the Criminal Code.

I have taken note of the above official notification.

Ort, Datum  
(Place, date)

Unterschrift  
(Signature)

Titel der Dissertation:  
(Title of the thesis):

Identification and Characterization of Small Molecules Inducing Cellular Reactive Oxygen

Species Accumulation

Ich versichere hiermit an Eides statt, dass ich die vorliegende Dissertation mit dem Titel selbstständig und ohne unzulässige fremde Hilfe angefertigt habe. Ich habe keine anderen als die angegebenen Quellen und Hilfsmittel benutzt sowie wörtliche und sinngemäße Zitate kenntlich gemacht.

Die Arbeit hat in gegenwärtiger oder in einer anderen Fassung weder der TU Dortmund noch einer anderen Hochschule im Zusammenhang mit einer staatlichen oder akademischen Prüfung vorgelegen.

I hereby swear that I have completed the present dissertation independently and without inadmissible external support. I have not used any sources or tools other than those indicated and have identified literal and analogous quotations.

The thesis in its current version or another version has not been presented to the TU Dortmund University or another university in connection with a state or academic examination.\*

\*Please be aware that solely the German version of the affidavit ("Eidesstattliche Versicherung") for the PhD thesis is the official and legally binding version.

Ort, Datum  
(Place, date)

Unterschrift  
(Signature)